Cranfield University

Alessio Bonaldo

Experimental Characterisation of Swirl Stabilized Annular Stratified Flames

School of Engineering

PhD

Cranfield University
School of Engineering

PhD Thesis

Alessio Bonaldo

Experimental Characterisation of Swirl Stabilized Annular Stratified Flames

Supervisor: Professor D.A. Greenhalgh

January 2007

This thesis is submitted in partial fulfilment of the requirements for the Degree of Doctor of Philosophy.

Abstract

A burner for investigating lean stratified premixed flames propagating in intense isotropic turbulence has been developed. Lean pre-mixtures of methane at different equivalence ratios are divided between two concentric co-flows to obtain annular stratification. Turbulence generators are used to control the level of turbulence intensity in the oncoming flow. A third annular weakly swirling air flow provides the flame stabilization mechanism. A fundamental characteristic is that flame stabilization does not rely on flow recirculation. The flames are maintained at a position where the local mass flux balances the burning rate, the result is a freely propagating turbulent flame front. The absence of physical surfaces in the vicinity of the flame provides free access for laser diagnostics.

Stereoscopic Planar Image Velocimetry (SPIV) has been applied to obtain the three components of the instantaneous velocity vectors on a vertical plane above the burner outlet where the flames propagate. The instantaneous temperature fields have been determined through Laser Induced Rayleigh (LIRay) scattering. Planar Laser Induced Fluorescence (PLIF) on acetone has been used to calculate the average equivalence ratio distributions. Instantaneous turbulent burning velocities have been extracted from SPIV results, while flame curvature and flame thermal thickness values have been calculated using the instantaneous temperature fields. The probability distributions of these quantities have been compared considering the separate influence of equivalence ratio stratification and turbulence. It has been observed that increased levels of turbulence determine higher turbulent burning velocities and flame front wrinkling. Flames characterized by stronger fuel stratification showed higher values in turbulent burning velocities. From the curvature analysis emerged that increased fuel concentration gradients favour flame wrinkling, especially when associated with positive small radius of curvature. This determines an increased surface area available for reaction that promotes a faster propagation of the flame front in the oncoming combustible mixtures.

Acknowledgements

I would like to thank Monica for always being beside me during the long experience of the PhD, supporting me in the difficult moments and enjoying with me the happy ones. I would like to thank my parents, Maria and Valerio, and my sister Stefania for being always present when I needed them. I will never forget my office mates: Adam, Thierry, Dmitry, Nick, Edouard, Claudio, Fathia, Christelle and Eduardo. They have been helpful when I needed technical advices and when it was the moment for a good laugh. Both have been appreciated.

I would like to thank Dr James Kelman for supervising me during the all PhD, for his essential advice, his extremely valuable professional help, and for being always available in supporting me and my project.

I would like to thank EPSRC and Cranfield University for financially supporting my project, and Professor Douglas Greenhalgh for his help during the final months of my PhD.

List of Contents

List of Figures

List of Tables

Notation

Roman Symbols

Symbol	*Description*	*Unit*
A_{tg}	Total cross section area of the tangential inlets	
A_{th}	Sonic nozzle throat cross section area	
A_{ul}	Rate coefficient for spontaneous emission energy	s^{-1}
$A_{u'l'}$	Rate coefficient for relaxation and energy exchanges processes in the vibrational and rotational levels in the upper and lower states.	s^{-1}
$B_G(x, y)$	Laser induced background frame	
B_{lu}	Einstein coefficient for the rate of absorption of photons for excitations from level l to level u	$W^{-1}\,cm^2\,s^{-2}$
B_{ue}	Einstein coefficient for the rate of absorption of photons for excitations from level u to higher levels e	$W^{-1}\,cm^2\,s^{-2}$
c_p	Specific heat at constant pressure	$J\,kg^{-1}\,K^{-1}$
C	Venturi nozzle discharge coefficient	
C'	Venturi nozzle critical flow function	
d_p	Particles diameter	μm
ds	PIV seed particles displacement	$pixels$
dt	PIV laser pulses separation	μs
d_{th}	Sonic nozzle throat diameter	mm
Da	Damköhler number	
D_{th}	Thermal diffusivity	$m^2\,s^{-1}$
e_c	Absolute error for the radius of curvature calculation	mm
e_c^R	Relative error for the radius of curvature calculation	$\%$
e_{ds}	Absolute error for the identification of the PIV seed particles displacement ds	$pixels$
e_T^R	Relative error for the temperature measurements	$\%$
e_v	Absolute error for the absolute velocity measurements using PIV	m/s
E	Activation energy	J/mol
$E_B(x, y)$	Electronic bias frame	
$Er_{st}(w)$	Standard error	
f	In a combusting process: actual fuel/air mass ratio	

Symbol	*Description*	*Unit*
f_s	In a combusting process: stoichiometric fuel/air mass ratio	
F_i	Chemical symbol for species i	
$F_L(x, y)$	Light intensity function of the untreated image collected	
k	Flame strain rate	$1/s$
k_f	Forward reaction rate constant for the jth reaction	
k_b	Backward reaction rate constant for the jth reaction	
k_L	Laser energy fluctuation factor	
K	Turbulent kinetic energy	m^2/s^2
Ka	Karlovitz number	
K_I	Rayleigh signal parameter for error analysis	
K_{opt}	Calibration constant of the calibration optics	
h_s	Sensible enthalpy	$J\ kg^{-1}$
I_0	Intensity of incident light	
I_v	Laser spectral intensity	$W\,cm^{-2}\,Hz^{-1}$
I_v^{sat}	Saturation level of laser spectral intensity for a specific transition	$W\,cm^{-2}\,Hz^{-1}$
$I_R(x, y)$	Light intensity function of the Rayleigh scattering signal	
$I_{LIF}(x, y)$	Light intensity function of the acetone fluorescence signal	
$\hat{I}_{LIF}(x, y)$	Corrected light intensity function of the acetone fluorescence signal	
$\overline{\hat{I}_{LIF}}(x, y)$	Average function calculated over 200 corrected light intensity functions of the acetone fluorescence signal	
$\overline{\hat{I}_{LIF-ann}}(x, y)$	Average function of the acetone fluorescence signal for the annular flow seeded in the flames' operative conditions	
$\overline{I_{R-ann}}$	Average function of the acetone fluorescence signal for the annular flow seeded in the reference conditions	
$I_{N-ann}(x, y)$	Mass fraction function of annular flow in the flames' operative conditions	%
$\overline{\hat{I}_{LIF-inn}}(x, y)$	Average function of the acetone fluorescence signal for the inner flow seeded in the flames' operative conditions	
$\overline{I_{R-inn}}$	Average function of the acetone fluorescence signal for the inner flow seeded in the reference conditions	
$I_{N-inn}(x, y)$	Mass fraction function of inner flow in the flames' operative conditions	%
I_t	Turbulence intensity	
l_t	Integral length scale	mm
$\dot{m}$	Mass flow rate	$kg\ s^{-1}$

Symbol	*Description*	*Unit*
$\dot{m}_{ax}$	Axial mass flow rate before tangential jets injection point	$kg\ s^{-1}$
$\dot{m}_{tg}$	Total tangential jets mass flow rate	$kg\ s^{-1}$
mc_{f-ann}	Fuel molar function in the annular flow	
mc_{f-inn}	Fuel molar function in the inner flow	
M_{gas}	Gas molar weight	$a.m.u.$
M_n	Nominal magnification	
$Mc_f(x,y)$	Fuel molar fraction function	
n	Refractive index of the gas at standard temperature and pressure	
N	Number of chemical species	
N_o	Loschmidt number	$2.69\times10^{19}\ cm^{-3}$
N_l	Number density of absorbers in the lower state	
N_m	Total number of molecules contained in the measurement volume	
p	Pressure	Pa
P_{up}	Static pressure upstream the sonic nozzle	Pa
Q	Heat release by complete combustion per unit mass of fuel	$J\ kg^{-1}$
Q_{pre}	Rate coefficient for predissociation	s^{-1}
Q_{elec}	Rate coefficient for electronic quenching of the system	s^{-1}
q	Laser beam pulse energy	mJ
q_{ref}	Reference laser beam pulse energy	
r	Motion size	mm
$r_{ac}(x)$	Auto-correlation function	mm
r_c	Radius of curvature	mm
$[r_c]_C$	Radius of curvature calculated	mm
r_{im}	Image resolution	$\mu m / pixel$
r_{tg}	Radius of the tangential inlet	mm
R	Boltzmann's constant	$8.31\ J/mol\ K$
$R_{op}(x,y)$	Optical response frame	
Re	Reynolds number	
Re_t	Turbulence Reynolds number	
R_{ax}	Radius of the main flow duct	mm
R_f	Total rate coefficient for all events transferring molecules from level l to u	s^{-1}
R_{St}	Reaction steps	
s_a	Arc length	mm

Symbol	*Description*	*Unit*
s_c	Chord length	mm
s_d	Local displacement speed of the iso-surface Θ	m/s
s_L	Laminar flame speed	m/s
s_T	Turbulent flame speed	m/s
$\bar{s}_T$	Sub-grid scale turbulent flame speed	m/s
S	Swirl number	
$S_{st}(x, y)$	Laser stripes frame	
S_0	Ground state singlet of the photoemission processes	
S_1	First excited singlet of the photoemission processes	
t	Time	s
T	Temperature	K
T_b	Burnt gases temperature	K
T_u	Unburnt gases temperature	K
T_{HOT}	Burnt gases temperature	K
T_{AIR}	Cold gases temperature	K
T_{up}	Temperature upstream the sonic nozzle	K
T_3	First excited triplet of the photoemission processes	
u_i	Velocity component	m/s
$\bar{u}$	Average absolute velocity	m/s
u'	Absolute velocity RMS	m/s
$\overline{u'}$	Sub-grid scale turbulence level	m/s
$U'(r)$	Characteristic velocity of the motion of size r	m/s
$Var(w)$	Variance	
V_k	Diffusion velocity of the species k	
$w_1,...,w_N$	Values of a set of data	
Y_k	Mass fraction of species k	
X_i	Mole fraction	

Greek symbols

Symbol	*Description*	*Unit*
δ	Flame thickness	μm
δ_L	Laminar flame thickness	μm
δ^r	Uncertainty of the variable that follows	
Δ	Variation of the variable that follows	
ε	Dissipation of turbulent kinetic energy	m^2/s^3

Symbol	*Description*	*Unit*
ϕ	Equivalence ratio	
ϕ_1	Equivalence ratio Flow 1 (inner flow)	
ϕ_2	Equivalence ratio Flow 2 (annular flow)	
$\Phi(x, y)$	Equivalence ratio function	
γ'_{ij}	Stoichiometric coefficient for species i appearing as reactant in reaction j	
γ''_{ij}	Stoichiometric coefficient for species i appearing as product in reaction j	
η_K	Kolmogorov scale	mm
κ	Flame curvature	m^{-1}
λ	Wavelength	nm
λ_0	Incident wavelength	nm
λ_t	Taylor length scale	mm
ν	Flow kinematic viscosity	$m^2\ s^{-1}$
ν_I	Wave number of the incoming radiation	
ν_m	Raman shift of particular vibrational or rotational state of a molecule	
ν_R	Wave number of the Raman-scattered light	
ν_t	Turbulent kinematic viscosity	$m^2\ s^{-1}$
θ	Tangential angle	Rad
ρ	Density	kg/m^3
σ	Cross section	cm^2
σ_{eff}	Effective Rayleigh scattering cross-section for a mixture of gases	cm^2
σ_i	Rayleigh cross-section of the i-th gas in a mixture	cm^2
σ_P	Standard deviation	
σ_{PK}	Standard deviation of a known distribution	
σ_R	Differential Rayleigh cross-section of a gas	cm^2
σ_{R-AIR}	Differential Rayleigh cross-section of cold gases (mixture of air and methane)	cm^2
σ_{R-HOT}	Differential Rayleigh cross-section of burnt gases	cm^2
τ	Characteristic time	s
τ_{ij}	Viscous tensor	$N\ m^{-2}$
$\dot{\omega}$	Rate of reaction	$mol \cdot cm^{-3} \cdot s^{-1}$
Θ	Reduced temperature	
Ψ	LES filter	

Abbreviations

Symbol	*Description*
AFR	Air Fuel Ratio
CCD	Charged Coupled Device
DNS	Direct Numerical Simulation
FFT	Fast Furier Transformed
LDA	Laser Doppler Anemometry
LES	Large Eddy Simulation
LIF	Laser Induced Fluorescence
LIRam	Laser Induced Raman scattering
LIRay	Laser Induced Rayleigh scattering
PDF (or pdf)	Probability Density Function
PIV	Planar Image Velocimetry
PLIF	Planar Laser Induced Fluorescence
RMS (or rms)	Root Mean Square
RANS	Reynolds Averaged Navier Stokes
SNR	Signal-to-Noise Ratio
SPIV	Stereoscopic Planar Image Velocimetry
STP	Standard Temperature and Pressure
TCM	Turbulent Combustion Model
UV	Ultra Violet
VOC	Voltaic Organic Compound
2D2C	Two Dimension Two Components
2D3C	Two Dimension Three Components

1 INTRODUCTION

Experimental attempts to understand the nature of combustion date back to as early as the 16th century when a host of European scientists and philosophers observed that air had an active component that is vital to combustion. In 1772, Antonie Laurent Lavoisier discovered that the ashes produced from burning certain solids out-weighed the original substance and this was due to the fact that an active fraction of air had combined with the flammable substance during burning. He named the active gas "oxygen". Despite the numerous discoveries from experiments for more than a century, the materialistic theory of combustion lacked a clear concept of the critical role that energy plays in the explanation of combustion. It was not till the 19th century, which saw the development of kinetic theory of gases, thermodynamics and thermo-chemistry, that the energy aspect of combustion was finally elucidated.

Progress in industrialisation was a powerful stimulus in the search for clarification of flame phenomena. As the occurrence of industrial fires and explosions in places such as coal mines increased, fire safety has drawn attention to the mechanism of flame propagation. Environmental concerns also have direct bearing on the utilisation of combustion and flame as tools since the burning of fossil fuel generates pollution and depletes the irreplaceable supply of such fuel. The rapid development of industry saw the importance of controlling combustion in order to increase energy output and reduce the size of practical devices, to decrease the amount of hazardous by products generated by the devices, to reduce the possibilities of catastrophic fires and explosions, and to improve fuel efficiency of the working cycles. As scientists and engineers seek more understanding about the nature of the phenomena, the study of combustion and flame has progressively matured into an extensive branch of physical science.

Combustion science is multi-disciplinary, involving chemistry, fluid mechanics and thermodynamics. The task of trying to develop a complete theory for combustion is extremely complex because of the simultaneous interaction between molecular reaction, diffusion, flow turbulence of various scales, and heat transfer between thermal states. The general science of combustion encompasses a great variety of phenomena which can be classified in different categories, as seen in many monographs of combustion (Borman and Ragland, 1998; Glassman, 1996; Kuo, 1986; Libby and Williams, 1980; Peters, 2000; Williams, 1985). Very often flames are categorised as either premixed flames, where fuels are homogeneously mixed with an oxidant before combustion takes place, or as diffusion flames whose ingredients are not mixed prior the entering the burning zone. Most common of all classifications is the separate treatment of turbulent combustion from the laminar case, as turbulence considerably increases the complexity of flame behaviour. Premixed flames can be further divided in lean, rich and stoichiometric. This classification depends on the mass ratio between air and fuel. Stoichiometric combustion takes place when the correct quantity of air required to exactly burn the fuel is provided. The lean flames are characterized by an excess of air while rich flames are associated to an excess of fuel.

Of all different forms of flames to our knowledge and experience since antiquity, the premixed flame is perhaps one of the simplest, but one of the latest to be recognized and studied. The importance of premixed combustion is stressed here because many practical combustion devices require the fuel and oxidiser to be premixed before entering the burning phase. Devices like spark-ignition internal combustion engines, the new generation of dry low NO_x gas turbines and a range of industrial processes all require partial or full premixing of the fuel and air.

In recent years the emission goals imposed by the international community have determined an increased demand for gas turbines that operate in a lean premixed mode. In order to have low emissions the concentration of fuel in the combustible mixture should be as low as possible with the bound imposed by the extinction limit. However, reduction of fuel in combustible mixtures does not only infer advantages. Combustors working in lean conditions are subjected to instabilities generating pressure waves. This phenomenon can reduce performance and work life of combustors. The root cause of these detrimental instabilities has been identified in the non uniform fuel distribution in the combustible mixture (Lieuwen, 1998a; Lieuwen, 1998b; Lieuwen, 2001). In gas turbines it isn't possible to properly mix the fuel with air before entering the combustion chamber. The premixing process must be made in a short time before the high temperature of the system ignites the combustible mixture. Because of the short mixing time the fuel mixture coming in the combustor has a non uniform air fuel ratio (AFR) distribution (partially premixing). Experimental results are needed to understand the fundamental theory of flame front propagation in partially premixed mixtures.

Computational modeling is an important tool to design new combustor devices. Large eddy simulations (LES) have been demonstrated as a powerful computational method to simulate turbulent reacting flows. LES exactly resolves the Navier-Stokes equations in the grid scale after a filtering process, but on the sub-grid scale it is based on semi-empirical models. The flame front in premixed combustion is of the order of millimetres and it must be solved by sub-grid models. The propagation of the flame front is of the order of meters per second and it affects the system on the grid scale. It is fundamental then to model exactly the sub-grid scale in order to solve the system on the macro-scale. Experimental data must be provided in a suitable form to validate computational models. The computer is far from being a complete substitute for experimentation, either for the fundamental science or in the development of practical combustion systems. The continuing necessity to rely on experimental data is still caused by our imperfect knowledge of the fundamental individual processes, such as turbulence and reaction kinetics, and by our inability to deal with the strong coupling between these processes (Bilger, 1993).

With the increasing availability of lasers and their greatly improved reliability, laser probing is assuming an ever expanding role in the diagnostics of combustion processes. Most of the disadvantages of physical probes have been circumvented by laser optical techniques. The laser techniques provide spatially precise and high resolution measurements with typical probe volumes approaching $0.1\times0.1\times0.1\,mm^3$. Single pulse measurements are possible with pulse width of the order of 10^{-8} to 10^{-6} sec depending on the type of laser employed. Instantaneity of the measurements enables the combustion processes to be frozen for the examination of non-equilibrium phenomena. The techniques are remote and, almost always, non perturbing and therefore are ideal

for application to recirculation zones, boundary layers and confined locations such as the combustion zone of an internal combustion engine. As the laser probes are non-intrusive, there is no limitation on the maximum temperature in their applicability, thus they are ideally suited to highly exothermic reactive flows (Eckbreth, 1988).

Several laser based techniques are available to the experimentalists in combustion. Particle Image Velocimetry (PIV) is used to measure the velocity field over a plane by double-pulse imaging particle positions with a laser sheet as the light source. Instantaneous velocity fields obtained from PIV are of great importance in the understanding of the fundamentals of turbulent combustion. When two cameras are used in the stereoscopic configuration (SPIV), it is possible to obtain all three components of the velocity vectors. Laser Induced Rayleigh (LIRay) scattering is usually employed for total gas density measurements, or to infer temperature using the gas law in a constant pressure system. Planar imaging of LIRay is perhaps one of the most frequently used laser diagnostic techniques employed in combustion because of the readily detectable signal strength and the relatively simple optical setup required. Laser Induced Raman scattering (LIRam) is frequently applied to measure molecular concentration in clean flames since the Raman scattered signal is species specific and linearly proportional to species number density. Provided appropriate interference filters are used in detection, generally only one laser is necessary to detect all the major species. Unfortunately, Raman scattering is very weak and suffers from low signal-to-noise ratio (SNR) in practical combustion situations, even with low noise detectors and high energy lasers. Laser Induced Fluorescence (LIF) is a spectroscopic process typically utilised for the detection of molecules which are often employed as markers of the fuel or the reaction zones. Planar imaging of LIF in flames has become a popular supplement to planar Rayleigh and Raman imaging, although realising LIF measurements often requires specialised tunable lasers capable of delivering the correct excitation frequency.

The experimental research of this thesis aims at revealing some aspects of flame front propagation in partially premixed mixtures and providing suitable experimental data for computer models validation. The measurements not only offer important information for the developments of the models, but also reveal the limitations of the techniques used, so that the next generation of experimentation can be designed to address some of the resolvable questions. To fulfil these targets a burner that produces lean turbulent stratified flames stabilized by weak swirl has been built. The stratification of fuel concentration is a fundamental condition to understand the effect of partially premixing on flame propagation. The burner utilizes three annular co-flows. The two internal flows are turbulent with different values of AFR in order to produce the equivalence ratio stratification across the mixing layer. The third external flow of air stabilizes the flame above the burner outlet using weak swirl. In the flame region experimental data have been collected using PIV to obtain the instantaneous velocity fields, LIRay to gain the instantaneous temperature fields and LIF to determine the average fuel concentration. The oncoming flow has been experimentally analyzed inside the burner nozzle, before it comes out of the burner outlet. Velocity fields and equivalence ratio distributions have been measured. This data is of fundamental importance to sufficiently characterize the turbulence and concentration properties of the flow where the flames are propagating.

Chapter two provides an overview on the background theory that applies to the research undertaken in this thesis. The negative interactions of the emissions with the atmosphere

and the nitric oxides formation in combustors are described. The fundamental aspects of chemical reactions involving hydrocarbon and oxygen are presented along with the characteristic length scales, time scales and non-dimensional numbers used to identify the premixed turbulent combustion regimes. The computational approaches used to study turbulent combustion are analyzed, and the differences between Large Eddy Simulations (LES), Reynolds Averaged Navier Stokes (RANS) and Direct Numerical Simulation (DNS) are underlined. Particular attention is focused on the sub-grid models for LES. The last section of this chapter is dedicated on explaining the physical theory upon which the most common laser diagnostics techniques are based.

Chapter three describes the last developments of experimental research on turbulent combustion, and stratified flames. The various types of flame stabilization mechanisms are considered and a detailed analysis on the use of weak swirl is presented. After an overview on the last advancements on the study of flame front propagation in stratified flows, the objectives and novelty of the burner designed here are defined.

The first part of chapter four analyzes in detail all the characteristics of the burner designed. The description involves the technical solutions adopted to produce turbulent stratified flows in which flames are stabilized using weak swirl. The gas support system of the burner is presented along with all the operating conditions for the experiments.

Chapter five describes the experimental apparatus used for the Stereoscopic PIV measurements. The characteristics of the algorithm used for the vector field calculations are explained and examples of the results are presented. The procedure adopted to extrapolate the instantaneous turbulent burning velocities is described.

Chapter six details the experiments executed applying Laser Induced Rayleigh scattering. The experimental apparatus is described in detail. The image processing procedure used to extract the Rayleigh signal from the collected images and to convert it to temperature values is presented. The progress variable fields have been calculated. The flame front curvature and flame thermal thickness have been obtained using the progress variable fields.

Chapter seven presents the LIF experiments using acetone as a marker. The reasons that guided the choice of acetone as fuel tracer are explained. The experimental apparatus is described considering the optical setup and the modifications applied to the gas support system in order to seed acetone in the inner and annular combustible flows. The image processing procedure used to obtain the average equivalence ratio fields is presented.

Chapter eight describes the flames characterization using the data collected. The velocity fields, the turbulence properties and the average equivalence ratio distributions allowed studying the oncoming flow. The characteristic length scales, time scales and non-dimensional numbers have been calculated and the turbulent combustion regimes of the flames have been identified.

The values of turbulent burning velocity, flame front curvature and flame thermal thickness have been organized in probability distributions associated to each experimental condition. Chapter nine presents the analysis of these probability distributions to identify the influences of fuel stratification and turbulence on flame front propagation.

The final chapter summarises the observations made in this thesis and draws some conclusions concerning combustion in turbulent stratified fuel mixtures.

Recommendations are finally made in relation to enhancements on the experimental techniques in order to gain further important data.

2 BACKGROUND

2.1 Emissions

2.1.1 Negative Interactions with the Atmosphere

Combustion scientists have long been aware that the use of fossil fuels as energy sources leads to products that may be environmentally harmful. Some of those less than desirable effects involve interactions with the chemistry of the atmosphere.

The combustion of fossil fuels, whether coal, liquid hydrocarbons, or natural gas, is generally described chemically as:

$$C_x H_{2y} + (x + y/2) O_2 \Rightarrow y H_2O + x CO_2$$

Fuels are usually not pristine and contain fuel-bound sulphur, oxygen, nitrogen and perhaps some heavy metals. The oxidizer is usually air, so nitrogen is introduced in large quantities. Therefore the combustion process produces quantities of NO_x , SO_x and unburned or partially oxidized organic species as well as various other chemicals. Interestingly, while these are quite minor parts of the general combustion process, they are sufficient to cause very demonstrable effects on air quality. In the analysis that follows the effects of SO_x on the atmosphere is not going to be considered because the corrosive action of this type of compound is feared in gas turbines, so it is preferred to use fuels without dangerous concentrations of sulphur.

An important interaction of the combustion products with the atmosphere is the urban photochemical smog, manifesting itself with the production of unhealthy concentrations of ozone, other toxins and particulate matter. Smog (ozone) is now understood to originate with the interaction of sunlight, hydrocarbons and NO_x. A generalized mechanism, illustrating that the chemistry is in essence a low temperature photo chemically driven combustion process, can be represented as (Golden, 2000):

$$NO_2 + hv \rightarrow NO + O$$
$$O + O_2 + M \rightarrow O_3 + M$$
$$OH + RH \rightarrow R + H_2O$$
$$R + O_2 + M \rightarrow RO + NO_2$$
$$RO_2 + NO \rightarrow RO + NO_2$$
$$RO + O_2 \rightarrow HO_2 + RCHO$$
$$HO_2 + NO \rightarrow HO + NO_2$$

Los Angeles has been the model for so long that it has taken some time to realize that in some areas the natural or biogenic hydrocarbon concentration was so high that controlling anthropogenic sources would have no substantial effect. These regions are NO_x controlled. The chemistry is quite non linear and results of models, often tuned to match data from environmental chambers (smog chambers) are displayed as isopleths of ozone concentration such as in Figure 2.1. It becomes apparent that reducing NO_x in the NO_x limited region has a large effect on ozone, whereas the same reduction in a voltaic organic compound (VOC) limited region has only a small effect.

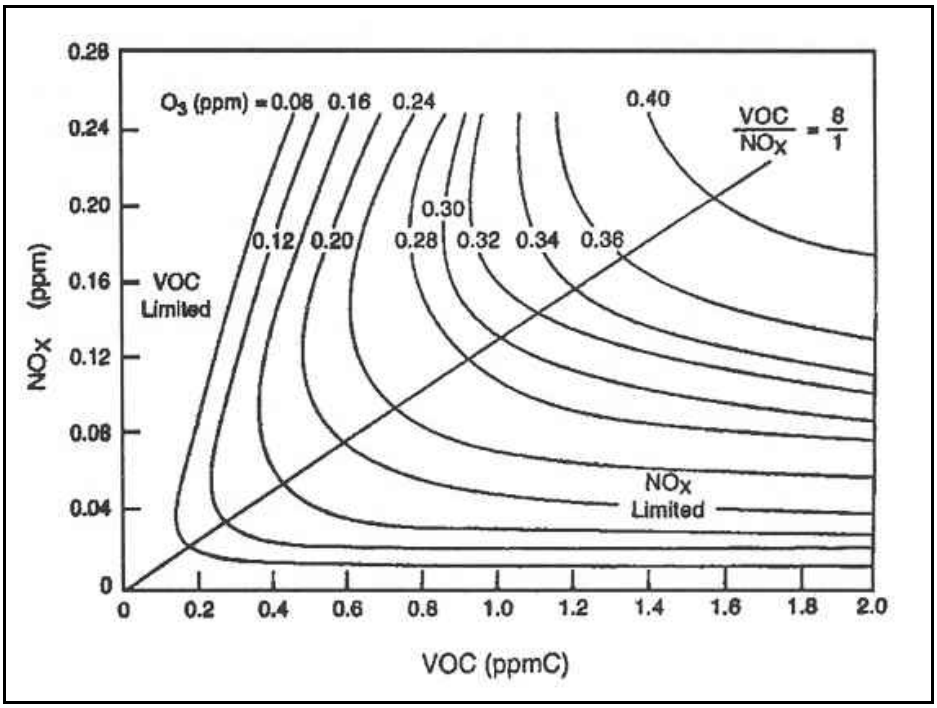

Figure 2.1. Typical peak ozone isopleths generated from initial mixtures of VOC and NO_x (Golden, 2000).

Emissions effect also precipitation. Normal rain is acidic, with pH of 5 to 6, due to dissolution of carbon dioxide and equilibrium formation of carbonic acid. Acid rains have pH values from 3 to 5. The extra acidity is a result of oxidation of SO_2 to H_2SO_4 (sulphuric acid) by H_2O_2 (hydrogen peroxide) in aqueous solution. Similar chemistry involving NO_x leads directly to HNO_3 (nitric acid) formation.

Nitric Oxide reacts also with ozone to deplete it in stratosphere. This is shown by the chemical reaction:

$$NO + O_3 \rightarrow NO_2 + O_2$$
$$NO_2 + O \rightarrow NO + O_2$$

The net result of these reactions ($O + O_3 \rightarrow 2O_2$) is a thinning of the ozone layer. This allows an increasing level of harmful ultraviolet radiation to penetrate the earth. It

contributes to global warming by increasing the perturbation to the vertical radiative flux in the troposphere.

2.1.2 Nitric Oxides Formation in Combustors

Stationary sources contribute a heavy fraction of the total NO_x emitted in the atmosphere (Figure 2.2). Consequently there has been great interest in predicting NO_x emissions and this interest has led to the formulation of various analytical models to predict specifically NO formation in combustion systems. The greatest number of analytical and experimental studies have been focused on NO formation alone and not on NO_2. Indeed the major portion of NO_x has been found to be NO (Glassman, 1996).

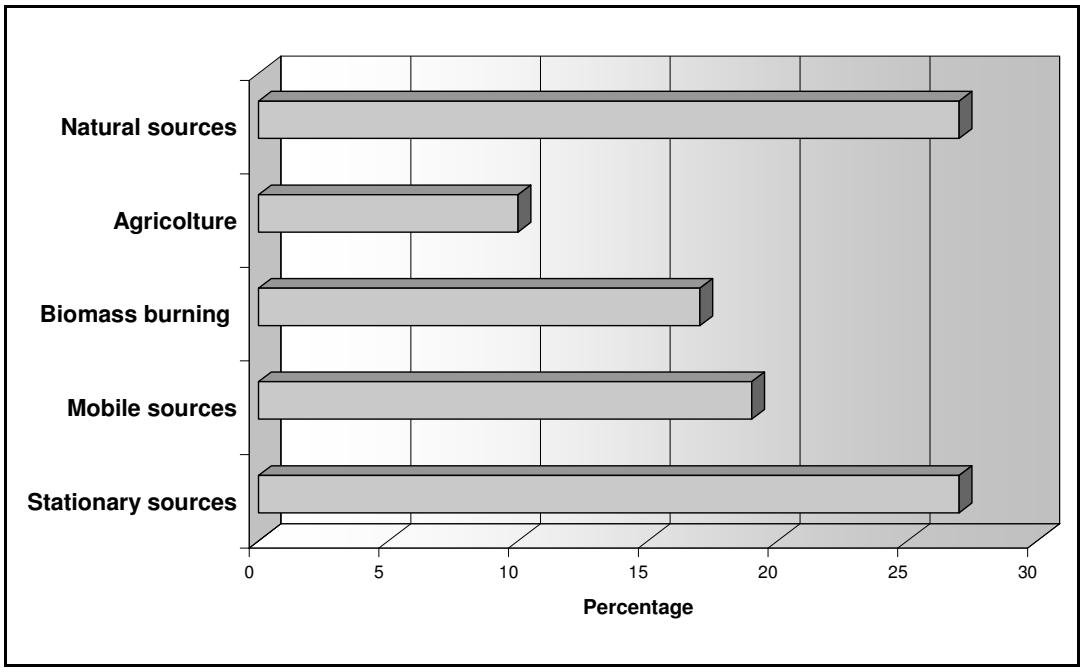

Figure 2.2. Estimated global NO_x percentage emission sources in 1994 (Golden,2000).

An important model of formation of nitric oxide is via the extended Zeldovich mechanism. Since it has high activity energy, it occurs when the temperature is raised above 1880 K (Edwards, 1974). It estimates that NO_x production increases by 1% each time the flame temperature is increased by one degree. The reaction proceeds with the dissociation of oxygen molecules into oxygen atoms within hot regions of the combustor. They react with nitrogen atoms forming nitric oxide and oxygen. This sets up the regenerative cycle:

$$O_2 \rightarrow 2O$$
$$O + N_2 \rightarrow N + NO$$
$$N + O_2 \rightarrow NO + O$$

The temperature and thus the mixture ratio, is the prime parameter in determining the quantities of NO formed. Ideally, as in equilibrium systems, the NO formation should peak at the stoichiometric value and decline on both the fuel-rich and fuel-lean sides, just as the temperature does.

However in partially premixed combustion systems, even though the overall mixture ratio may be lean and the fuel temperature could correspond to this overall mixture ratio, in some parts of the system the AFR could correspond to stoichiometric or rich values. Then more NO_x forms than would be expected.

2.2 Combustion Theory

2.2.1 Chemical Kinetics

Fundamental to all reacting flows is the presence of chemical reactions which take place at a definite rate, depending on the conditions of the system. The rate of reaction, $\dot{\omega}$, may be defined as the rate of increase of the product concentration and may have the molar unit of $mol \cdot cm^{-3} \cdot s^{-1}$. For a general system involving N chemical species and R_{St} reaction steps, the whole set of reversible chemical reactions can be represented by a symbolic stoichiometric equation of the form (Libby and Williams, 1980):

$$\sum_{i=1}^{N} \gamma'_{ij} F_i \Leftrightarrow \sum_{i=1}^{N} \gamma''_{ij} F_i \qquad j = 1,2,...,R_{St} \qquad (2.1)$$

Where F_i is the chemical symbol for species i, integers γ'_{ij} and γ''_{ij} are the stoichiometric coefficients for species i appearing as reactant and product respectively in reaction j. The forward reaction rate constant for the jth reaction is symbolised by k_f and that of the reverse direction is denoted as k_b. These rate constants are expressible in an exponential form involving temperature, T, for example, as:

$$k_f = \beta T^{\alpha} e^{-E/(RT)} \qquad (2.2)$$

Where β, α are constants with values specific to the jth reaction. The exponential term is the Arrhenius factor, containing the activation energy E, and the universal gas constant R.

Chemical source terms such as $\dot{\omega}_i$ appear in the equation for species and energy conservation. The overall reaction rate for a particular chemical species is derived from the contributions of all the reactions and may be expressed as $\dot{\omega}_i = \sum_{j=1}^{R_{St}} \dot{\omega}_{ij}$, where

$$\dot{\omega}_{ij} = (\gamma'_{ij} - \gamma''_{ij}) k_{fj} \prod_{i=1}^{N} [F_i]^{\gamma'_{ij}} \left(1 - \frac{k_{bj}}{k_{fj}} \prod_{i=1}^{N} [F_i]^{\gamma_{ij} - \gamma''_{ij}} \right) \qquad (2.3)$$

Is the mole rate of production per unit volume for the *ith* species by the *jth* reaction step and $[F_i]$ is the molar concentration of species i.

"Of all the different processes of chemical reactions, the most common types are the chain reactions which consist of a series of consecutive, competitive, and opposing reaction steps with different reaction rate constants" (Glassman, 1996). In chain reaction processes, the elementary reactions are chain-initiating, chain-terminating, chain-carrying or chain branching. Initiation of chain reaction involves the production of free radicals from the dissociation of molecules. A chain-carrying reaction has the same radicals in the product as there are in the reactant and a chain-branching reaction has more radicals in the product than there are in the reactants.

Detailed chemical kinetics composed of more than a hundred elementary reactions for simple hydrocarbons are commonplace. However, computations with a large mechanism are often time consuming and expensive, and a reduced mechanism for the chemical kinetics is necessary for reasons of practicality and improved understanding.

Reduced mechanisms can be developed empirically or from skeletal mechanisms that typically contain dozens of elementary reactions. In the latter approach, judiciously selected species are assumed to be at steady-state and selected reactions are assumed to be in equilibrium. These assumptions provide algebraic relationships that reduce the number of independent variables needed to describe the chemistry. Global reduced mechanisms must be used with caution because the assumptions or empiricism on which they are based may not be valid at all conditions (Brewster et al., 1999).

Several studies with reduced mechanisms have emphasized the role of hydrogen-containing free radicals such as H and OH in predicting CO. The following mechanism incorporates H and was use to analyze the inner structure of a methane–air premixed flame (Seshadri and Peters, 1990):

$$CH_4 + 2H + H_2O \leftrightarrow CO + 4H_2$$

$$CO + H_2O \leftrightarrow CO_2 + H_2$$

$$2H + M \leftrightarrow H_2 + M$$

$$O_2 + 3H_2 \leftrightarrow 2H + 2H_2O$$

This mechanism was derived using steady state assumptions for the intermediates OH , O , HO_2 , CH_3 , CH_2O , CHO , CH_3O and H_2O_2 .

2.2.2 Premixed Turbulent Combustion Regimes

Turbulent combustion is encountered in most practical combustion systems such as internal combustion, aircraft engines, industrial burners and gas turbines. Studying and modelling turbulent combustion processes is therefore an important issue to develop and improve practical systems (to increase efficiency and to reduce fuel consumption and pollutant formation). Turbulent flames are very difficult to handle using analytical techniques if it is considered that the full description of chemical mechanisms in flames may require hundreds of species and thousands of reactions. Turbulence itself is probably the most complex phenomenon in non-reacting fluid mechanics. Various length scales are involved and the structure and the description of turbulence remain incomplete. When a flame interacts with a turbulent flow, turbulence is modified by combustion because of the strong flow accelerations through the flame front induced by heat release, and because of the large changes in kinematic viscosity associated with temperature changes. Additionally, turbulence impacts the flame structure.

Important theoretical instruments for understanding turbulent combustion are the diagrams defining combustion regimes in terms of length and velocity scales ratios. Knowing the turbulence characteristics these diagrams indicate whether the flow contains flamelet, pockets or distributed reaction zones. This information is essential to build a turbulent combustion model. These diagrams are mainly based on intuitive arguments and introduce order of magnitude arguments rather than precise demonstrations.

Turbulence may be characterized by fluctuations of all local properties and occurs for sufficiently large Reynolds numbers, depending on the system geometry. Any property f is usually split into mean ($\bar{f}$) and fluctuating (f') contributions:

$$f = \bar{f} + f' \qquad (2.4)$$

The averaging process to calculate $\bar{f}$ is an ensemble average:

$$\bar{f} = \frac{1}{t}\int_0^t f(t')dt' \qquad (2.5)$$

The turbulence strength is generally characterized by the turbulence intensity I :

$$I = \frac{\sqrt{\overline{f'^2}}}{\bar{f}} \qquad (2.6)$$

A Reynolds number is introduced for each turbulent scale as:

$$\mathrm{Re}(r) = \frac{U'(r)\cdot r}{v} \qquad (2.7)$$

Where the quantity $U'(r)$ is the characteristic velocity of the motion of size r and v is the flow kinematic viscosity. When r corresponds to the integral scale l_t , the turbulent Reynolds number, Re_t, may also be expressed as

$$\mathrm{Re}_t = \frac{u' \cdot l_t}{v} \qquad (2.8)$$

Turbulence Reynolds number is usually high (100 to 2000 in most combustion devices). If turbulence is supposed to be homogeneous and isotropic, the speed $U'(r)$ and the size r of any eddy participating to the turbulence cascade are linked by the dissipation ε of turbulent kinetic energy K, estimated as the ratio of turbulent kinetic energy $U'^2(r)$ divided by the time scale $r/U'(r)$:

$$\varepsilon = \frac{U'(r)^3}{r} \qquad (2.9)$$

This assumption is useful to imagine how a turbulent flow may interact with a premixed front because it provides estimates of speeds and times variations with r. For example a typical turbulent time of an eddy of size r is:

$$\tau_m(r) = \frac{r}{U'(r)} = \frac{r^{2/3}}{\varepsilon^{1/3}} \qquad (2.10)$$

Along the cascade, the Reynolds number goes down from Re_t to values close to unity, where inertia and viscous forces balance. This limit determines the smallest scale found in the turbulent flow, the Kolmogorov scale:

$$\eta_K = \left(\frac{v^3}{\varepsilon} \right)^{1/4} \qquad (2.11)$$

The interaction between turbulence and premixed combustion may be described as the interaction between a flame front (flame thickness δ and laminar flame speed s_L) and an ensemble of eddies representing turbulence. These eddies have sizes ranging from the Kolmogorov scale, η_K, to the integral scale, l_t, and characteristic speeds ranging from the Kolmogorov speed, U'_K, to the integral characteristic velocity U'_t. An important parameter that links turbulence with combustion is the flame strain rate. It measures the fractional rate of increase of the flame front area and is directly linked to velocity gradients. To first order, the strain $k(r)$ induced on a flame front by an eddy of size r may be assumed to scale with $u'(r)/r$ which is the simplest estimate for velocity gradients created by the eddy. Then the Kolmogorov and the integral length scale induce strain values given by:

$$k(\eta_K) = \sqrt{\frac{\varepsilon}{v}} \qquad (2.12)$$

$$k(l_t) = \frac{\varepsilon}{U'^2} = \frac{\varepsilon}{K} \qquad (2.13)$$

Note that although the scales close to the Kolmogorov length have the smallest sizes and velocities, they generate the highest flame strain rate:

$$\frac{k(\eta_K)}{k(l_t)} = \sqrt{\frac{l_t U'}{\nu}} = \sqrt{\mathrm{Re}_t} \qquad (2.14)$$

The characteristic flame time scale can be defined by the following ratio:

$$\tau_C = \delta / s_L \qquad (2.15)$$

A reduced number can be calculated by comparing the characteristic time of an eddy of size r to a typical flame time scale:

$$Da(r) = \frac{\tau_m(r)}{\tau_C} \qquad (2.16)$$

This characteristic number suggests scenarios for flame-vortex interaction. For large values of $Da(r)$, chemical times are small compared to the eddy time and turbulence is not able to affect the flame inner structure in a significant way. On the other hand, low values of $Da(r)$ imply long chemical time scales and a flame strongly modified by the turbulent eddies. All these analyses are implicitly based on a single step irreversible reaction. Classical approaches introduce two reduced numbers corresponding to the limiting values of r. The Damköhler number Da is defined for the largest eddies and corresponds to the ratio of the integral time scale τ_t to the chemical time scale:

$$Da = Da(l_t) = \frac{\tau_t}{\tau_C} = \frac{l_t / U'(l_t)}{\delta / s_L} = \frac{l_t / u'}{\delta / s_L} \qquad (2.17)$$

The Karlovitz number, Ka, that corresponds to the smallest eddies (Kolmogorov) and is the ratio of the chemical time scale to Kolmogorov time:

$$Ka = \frac{1}{Da(\eta_K)} = \frac{\tau_C}{\tau_K} = \frac{U'(\eta_K)/\eta_K}{s_L/\delta} = \frac{\sqrt{\varepsilon/\nu}}{s_L/\delta} \qquad (2.18)$$

Using Damköhler and Karlovitz numbers, various combustion regimes may be identified in terms of length (l_t/δ) and velocity (U'/s_L) ratios as in Figure 2.3 using a log-log scale. The line separating corrugated flamelets and distributed reaction regimes corresponds to the condition $Ka = 1$ and is known as the Klimov-Williams criterion.

It has also been proposed to identify combustion regimes using two characteristic widths: the flame thickness δ, and the reaction zone thickness, $\delta_R (<< \delta)$ (Peters, 1999).

- When $\delta < \eta_K$ a "thin flame regime" is identified.

- When $\delta > \eta_K$, Kolmogorov scales are able to enter and to thicken the flame preheat zone. The Kolmogorov scales are also able to enter the reaction zone when the reaction thickness becomes larger than the Kolmogorov size, when the Karlovitz number reachs the transition value Ka_r, corresponding to $\delta_R = \eta_K$:

$$Ka_r = \left(\frac{\delta}{\eta_K}\right)^2 = \left(\frac{\delta}{\delta_R}\right)^2 \left(\frac{\delta_R}{\eta_K}\right)^2 = \left(\frac{\delta}{\delta_R}\right)^2 \qquad (2.19)$$

For most premixed flames, it is known that $\delta / \delta_R \approx 10$, corresponding to a transition for $Ka_r \approx 100$. Then two regimes are identified:

1. When $1 < Ka < Ka_r$, turbulent motions are able to enter and modify the flame preheat zone but not the reaction zone, which remains similar to a wrinkled laminar reaction zone. This regime is the "Thickened-wrinkled flame regime".
2. For $Ka > Ka_r$, both diffusion and reaction zone are affected by turbulent motions. No laminar structure can be identified. This regime is called the "thickened flame regime".

These regimes are identified in the diagram in Figure 2.4 and in the representation of three regimes plotted in Figure 2.5.

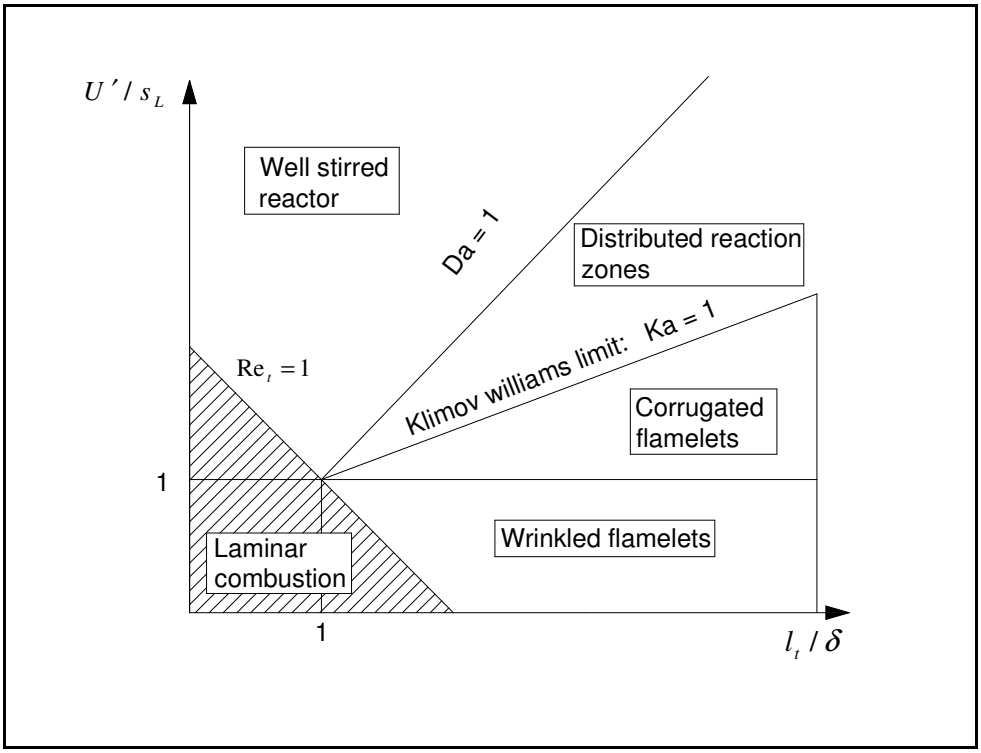

Figure 2.3. Classical turbulent combustion diagram. Combustion regimes are identified in terms of length and velocity ratios using a log-log scale (Peters,1986).

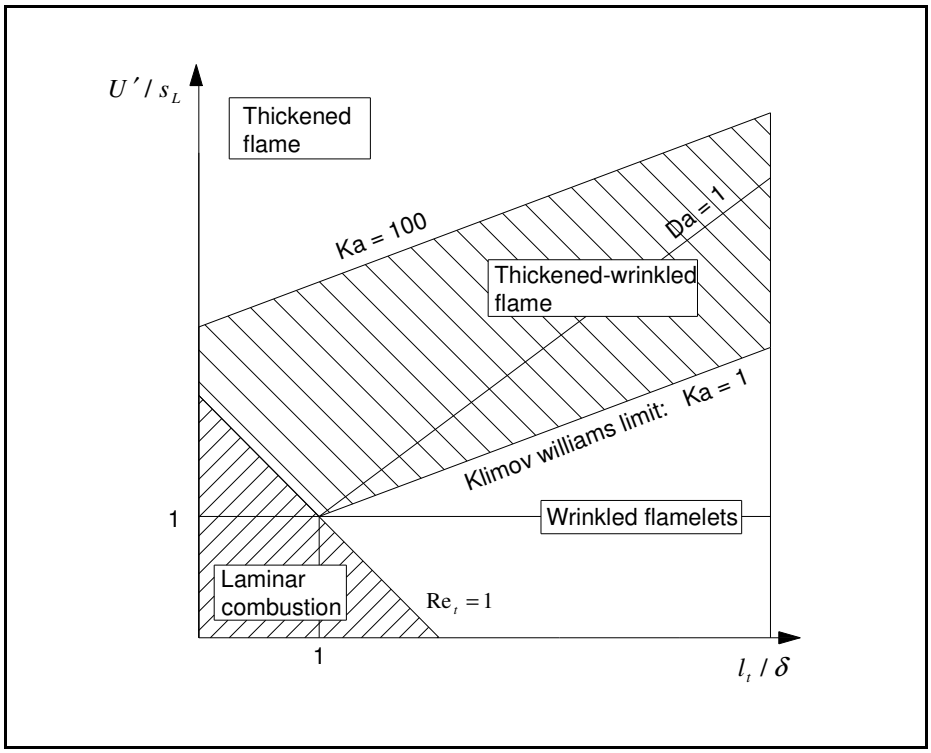

Figure 2.4. Modified turbulent combustion diagram (Peters, 1999). Combustion regimes are identified in terms of lengths and velocities ratios on a log-log scale.

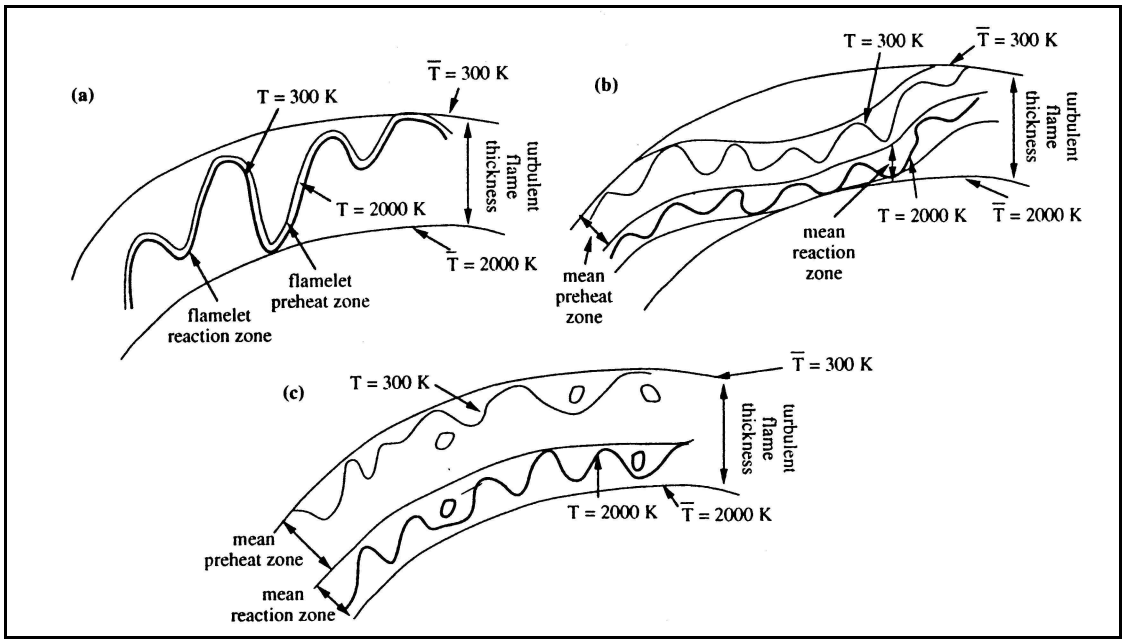

Figure 2.5. Turbulent premixed combustion regimes illustrated in a case where fresh and burnt gases temperatures are 300 K and 2000 K respectively: (a) wrinkled flamelet (thin wrinkled flame), (b) thickened wrinkled flame, (c) thickened flame (Poinsot and Veynante, 2001).

2.3 Computational Approaches for Turbulent Combustion

In this section a brief description is given of the computational approaches used for turbulent combustion in order to introduce the significance of the need for experimental results in order to validate theoretical models. The PhD project plan does not require a section in which the experimental conditions studied are also modelled using computation fluid dynamics tools, but it is within the PhD project objectives to provide experimental data in order to validate theoretical models that will be described in this section.

The starting points for a computational analysis of turbulent reacting flows are the instantaneous balance equations for mass, momentum, species and enthalpy (Poinsot and Veynante, 2001):

$$\frac{\partial \rho}{\partial t} + \frac{\partial}{\partial x_i}(\rho u_i) = 0 \qquad (2.20)$$

$$\frac{\partial \rho u_j}{\partial t} + \frac{\partial}{\partial x_i}(\rho u_i u_j) + \frac{\partial p}{\partial x_j} = \frac{\partial \tau_{ij}}{\partial x_i} \qquad (2.21)$$

$$\frac{\partial (\rho Y_k)}{\partial t} + \frac{\partial}{\partial x_i}(\rho u_i Y_k) = -\frac{\partial}{\partial x_i}(V_{k,i} Y_k) + \dot{\omega}_k \qquad \text{for } k = 1,2,\ldots,N \qquad (2.22)$$

$$\frac{\partial \rho h_s}{\partial t} + \frac{\partial}{\partial x_i}(\rho u_i h_s) = \dot{\omega}_T + \frac{Dp}{Dt} + \frac{\partial}{\partial x_i}(\lambda \frac{\partial T}{\partial x_i}) - \frac{\partial}{\partial x_i}\left(\rho \sum_{k=1}^{N} V_{k,i} Y_k h_{s,k}\right) + \tau_{ij} \frac{\partial u_i}{\partial x_j} \qquad (2.23)$$

The description of turbulent combustion processing using Computational Fluid Dynamics (CFD) may be achieved using a variety of numerical simulations. Three levels of turbulent reacting flow computations are distinguished:

The first level (RANS, for Reynolds Averaged Navier Stokes) has been developed to solve the mean values of all quantities. The balance equations for Reynolds or Favre (i.e. mass–weighted) averaged quantities are obtained by averaging the instantaneous balance equations. The averaged equations require closure rules: a turbulence model to deal with the flow dynamics in combination with a turbulent combustion model (TCM) to describe chemical species conversion and heat release.

The second level corresponds to large eddy simulations (LES). The turbulent large scales are explicitly calculated whereas the effects of smaller ones are modelled using sub-grid closure rules. The balance equations for large eddy simulations are obtained by filtering the instantaneous balance equations. LES of reacting flows determine the instantaneous position of a “large scale” resolved flame front but a sub-grid model is required to take into account the effects of small turbulent scales on combustion.

The third level of combustion simulations is based on direct numerical simulations (DNS) where the full instantaneous Navier-Stokes equations are solved without any model for turbulent motions: all turbulence scales are explicitly determined and their

effects on combustion are captured by the simulation. DNS are limited to simple academic flows (typically, combustion in a small cubic box).

Below RANS and LES simulations are going to be described more in detail.

2.3.1 RANS Simulations for Turbulent Combustion

Balance equations for mean quantities in RANS simulations are obtained by averaging the instantaneous balance equations. In constant density flows, Reynolds averaging consists in splitting any quantities into a mean and a fluctuating component. Reynolds averaging for variable density flows introduces many other unclosed correlations between any quantity f and density fluctuations ($\overline{\rho' f'}$). To avoid this difficulty, mass-weighted averages (called Favre averages) are usually preferred (Williams, 1985):

$$\widetilde{f} = \frac{\overline{\rho f}}{\overline{\rho}} \qquad (2.24)$$

Any component may be split into mean and fluctuating components as:

$$f = \widetilde{f} + f'' \qquad \text{with} \qquad \widetilde{f''} = 0 \qquad (2.25)$$

Using this formalism, the averaged balance equations become:

$$\frac{\partial \overline{\rho}}{\partial t} + \frac{\partial}{\partial x_i}(\overline{\rho}\widetilde{u}_i) = 0 \qquad (2.26)$$

$$\frac{\partial \overline{\rho}\widetilde{u}_i}{\partial t} + \frac{\partial}{\partial x_i}(\overline{\rho}\widetilde{u}_i\widetilde{u}_j) + \frac{\partial \overline{p}}{\partial x_j} = \frac{\partial}{\partial x_i}(\overline{\tau}_{ij} - \overline{\rho u_i'' u_j''}) \qquad (2.27)$$

$$\frac{\partial(\overline{\rho}\widetilde{Y}_k)}{\partial t} + \frac{\partial}{\partial x_i}\left(\overline{\rho}\widetilde{u}_i\widetilde{Y}_k\right) = -\frac{\partial}{\partial x_i}\left(\overline{V_{k,i}Y_k} + \overline{\rho}\,\widetilde{u_i''Y_k''}\right) + \overline{\dot{\omega}_k} \quad \text{for } k = 1,2,\ldots,N \qquad (2.28)$$

$$\frac{\partial \overline{\rho}\widetilde{h}_s}{\partial t} + \frac{\partial}{\partial x_i}(\overline{\rho}\widetilde{u}_i\widetilde{h}_s) = \overline{\dot{\omega}_T} + \overline{\frac{Dp}{Dt}} + \frac{\partial}{\partial x_i}\left(\overline{\lambda\frac{\partial T}{\partial x_i}} - \overline{\rho u_i'' h_s''}\right) + \overline{\tau_{ij}\frac{\partial u_i}{\partial x_j}} - \frac{\partial}{\partial x_i}\left(\overline{\rho\sum_{k=1}^{N} V_{k,i}Y_k h_{s,k}}\right) \qquad (2.29)$$

These equations are formally identical to the classical Reynolds averaged equations for constant density flows. Even though Favre averaging seems to offer a simple and efficient route for reacting flows, it has to be used with some care. There is no simple relation between Favre and Reynolds averages and comparisons between numerical simulations, providing Favre averages, with experimental data are not obvious. Most experimental techniques provide Reynolds averages.

A usual assumption in turbulent premixed combustion is to consider a single one-step, irreversible chemical reaction. The reactant mass fraction Y_F is non-dimensionalized using the initial reactant mass fraction in fresh gases $Y_F^1 : Y = Y_F / Y_F^1$. Y varies from 1 in the fresh gases to 0 in the burnt gases.

The reduce temperature is defined as:

$$\Theta = c_p (T - T_1) / (Q Y_F^1) \qquad (2.30)$$

Most turbulent combustion models assume constant pressure, unity Lewis number and adiabatic conditions. Under these three assumptions, the relation linking the reduced temperature to the reduced reactant mass fraction Y is:

$$\Theta + Y = 1 \qquad (2.31)$$

Therefore only the Θ (or the Y) equation needs to be retained. Θ, increasing from 0 in fresh gases to 1 in fully burnt gases, is called the progress variable. The system to solve for turbulent low-speed premixed flame then reduces to:

$$\frac{\partial \overline{\rho}}{\partial t} + \frac{\partial}{\partial x_i}(\overline{\rho}\,\widetilde{u_i}) = 0 \qquad (2.32)$$

$$\frac{\partial \overline{\rho}\,\widetilde{u_i}}{\partial t} + \frac{\partial}{\partial x_i}(\overline{\rho}\,\widetilde{u_i}\,\widetilde{u_j}) + \frac{\partial \overline{p}}{\partial x_j} = \frac{\partial}{\partial x_i}(\overline{\tau}_{ij} - \overline{\rho}\,\widetilde{u_i'' u_j''}) \qquad (2.33)$$

$$\frac{\partial (\overline{\rho}\,\widetilde{\Theta})}{\partial t} + \frac{\partial}{\partial x_i}\left(\overline{\rho}\,\widetilde{u_i}\,\widetilde{\Theta}\right) = -\frac{\partial}{\partial x_i}\left(\overline{\rho D}\,\frac{\partial \widetilde{\Theta}}{\partial x_i} + \overline{\rho}\,\widetilde{u_i'' \Theta''}\right) + \overline{\dot{\omega}_\Theta} \qquad (2.34)$$

Where $\dot{\omega}_\Theta = -\dot{\omega}_F / Y_F^1$ is the reaction rate for the reduced temperature Θ. The initial set of averaged equations is simplified since only $\overline{\rho}$, $\widetilde{u_i}$ and $\widetilde{\Theta}$ must be solved for. But the corresponding equations contain three unclosed terms requiring modelling:

The turbulent stress tensor: $\overline{\rho}\,\widetilde{u_i'' u_j''}$

The mean reaction rate: $\overline{\dot{\omega}_\Theta}$

The turbulent scalar transport: $\overline{\rho}\,\widetilde{u_i'' \Theta''}$

How these terms influence mean values is a key issue in turbulent combustion modelling. Such terms require closure assumptions and models to express them as functions of the solved mean quantities or as solutions of additional conservation equations.

Reynolds stresses in the momentum equation, $\overline{\rho}\,\widetilde{u_i'' u_j''}$ are usually viewed as additional stresses and modelled through a turbulent viscosity v_t (Boussinesq assumption). But the other two terms are specific due to the introduction of combustion in the Navier-Stokes equations. A large portion of literature in turbulent combustion focuses on the

modelling of the mean reaction rate. Models for scalar turbulent fluxes are generally closed using a gradient assumption.

2.3.2 Large Eddy Simulations

The objective of large eddy simulations is to explicitly compute the largest structures of the flow field, typically structures larger than the computational mesh size, whereas the effects of the smallest ones are modelled. This is the result of filtering the variables in spectral space or in physical space, using the filtered quantity defined as (Poinsot and Veynante, 2001):

$$\bar{f}(x) = \int f(x')\Psi(x-x')dx' \qquad (2.35)$$

where Ψ is the LES filter. The usual LES filters are shown in Figure 2.6 and reported below with their mathematical expression.

Cut-off filters in spectral space (case "a"):

$$\Psi(k) = \begin{cases} 1 & if\ k \le k_c = \pi/\Delta \\ 0 & otherwise \end{cases} \qquad (2.36)$$

where k is the spatial wave number. This filter keeps length scales larger than the cut-off length scale 2Δ, where Δ is the filter size.

Box filter in physical space (case "c"):

$$\Psi(x) = \Psi(x_1, x_2, x_3) = \begin{cases} 1/\Delta^3 & if\ \ |x_i| \le \Delta/2 \quad i = 1,2,3 \\ 0 & otherwise \end{cases} \qquad (2.37)$$

where (x_1, x_2, x_3) are the spatial coordinates of the location x. This filter corresponds to an averaging over a cubic box of size Δ.

Gaussian filter in physical space (case "c"):

$$\Psi(x) = \Psi(x_1, x_2, x_3) = \left(\frac{6}{\pi\Delta^2}\right)^{3/2} \exp\left[-\frac{6}{\Delta^2}(x_1^2 + x_2^2 + x_3^2)\right] \qquad (2.38)$$

All these filters are normalized:

$$\int_{-\infty}^{+\infty}\int_{-\infty}^{+\infty}\int_{-\infty}^{+\infty} \Psi(x_1, x_2, x_3)dx_1dx_2dx_3 = 1 \qquad (2.39)$$

For variable density ρ, a mass-weighted Favre filtering is introduced according to:

$$\bar{\rho}\,\widetilde{f(x)} = \int \rho\, f(x')\Psi(x-x')dx' \qquad (2.40)$$

The filtered quantity $\bar{f}$ is resolved in the numerical simulation whereas $f' = f - \bar{f}$ corresponds to the unresolved part.

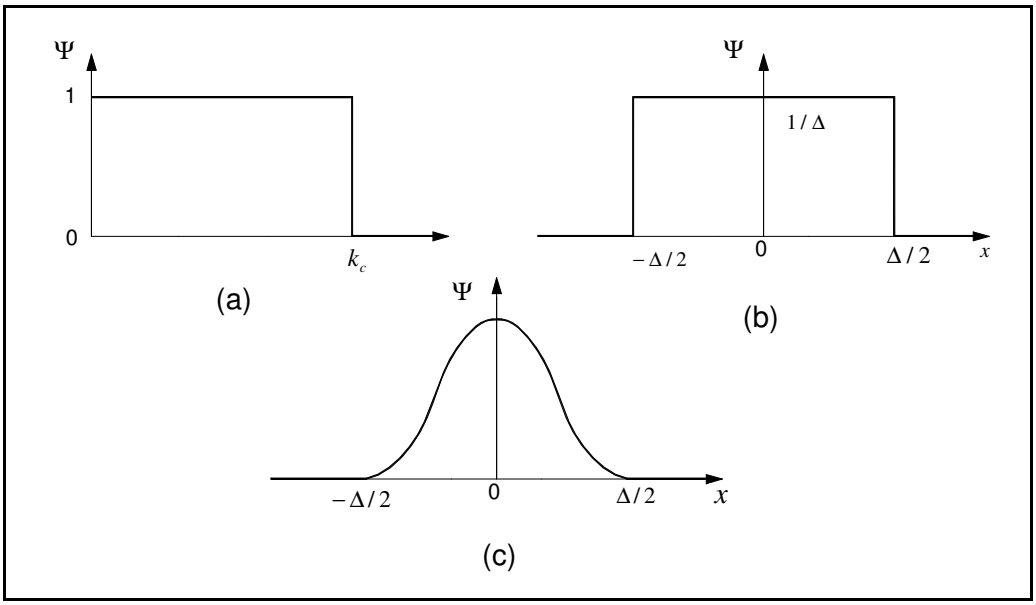

Figure 2.6. Common spatial filters used in large eddy simulations. Case (a): cut-off filter in spectral space. Case (b): box filter in physical space. Case (c): Gaussian filter in physical space.

Balance equation for large eddy simulations are obtained by filtering the instantaneous balance equations.

$$\frac{\partial \bar{\rho}}{\partial t} + \frac{\partial}{\partial x_i}(\bar{\rho}\,\tilde{u}_i) = 0 \qquad (2.41)$$

$$\frac{\partial \bar{\rho}\,\tilde{u}_i}{\partial t} + \frac{\partial}{\partial x_i}(\bar{\rho}\,\tilde{u}_i\,\tilde{u}_j) + \frac{\partial \bar{p}}{\partial x_j} = \frac{\partial}{\partial x_i}(\bar{\tau}_{ij} - \bar{\rho}(\widetilde{u_i\,u_j} - \tilde{u}_i\,\tilde{u}_j)) \qquad (2.42)$$

$$\frac{\partial(\bar{\rho}\,\tilde{Y}_k)}{\partial t} + \frac{\partial}{\partial x_i}\left(\bar{\rho}\,\tilde{u}_i\,\tilde{Y}_k\right) = \frac{\partial}{\partial x_i}\left(\overline{V_{k,i}Y_k} - \bar{\rho}(\widetilde{u_i''Y_k''} - \tilde{u}_i\,\tilde{Y}_k)\right) + \overline{\dot{\omega}_k} \qquad (2.43)$$

for k =1,2,…,N

$$\frac{\partial \bar{\rho}\,\tilde{h}_s}{\partial t} + \frac{\partial}{\partial x_i}(\bar{\rho}\,\tilde{u}_i\,\tilde{h}_s) = \overline{\dot{\omega}_T} + \overline{\frac{Dp}{Dt}} + \frac{\partial}{\partial x_i}\left(\overline{\lambda\frac{\partial T}{\partial x_i}} - \bar{\rho}\left(\widetilde{u_i\,h_s} - \tilde{u}_i\,\tilde{h}_s\right)\right) + \overline{\tau_{ij}\frac{\partial u_i}{\partial x_j}} - \frac{\partial}{\partial x_i}\left(\overline{\rho\sum_{k=1}^{N}V_{k,i}Y_k h_{s,k}}\right)$$

$$(2.44)$$

In this set of equations, the following unclosed quantities must be modelled:

Unresolved Reynolds stresses → $(\overline{\overline{u_i u_j}} - \overline{\overline{u}_i \overline{u}_j})$

Unresolved species flux → $\left(\overline{\overline{u_i Y_k}} - \overline{\overline{u}_i \overline{Y}_k}\right)$

Unresolved enthalpy flux → $\left(\overline{\overline{u_i h_s}} - \overline{\overline{u}_i \overline{h}_s}\right)$

Filtered laminar diffusion flux for species → $\overline{V_{k,i} Y_k}$

Filtered laminar diffusion flux for enthalpy → $\overline{\lambda \frac{\partial T}{\partial x_i}}$

Filtered chemical reaction rate → $\overline{\dot{\omega}_k}$

Finding models for the unknown terms in balance equations may follow concepts developed in RANS approaches, for example by using global quantities such as the sub-grid scale turbulent kinetic energy and its dissipation rate. Nevertheless, in large eddy simulations, additional information is available because large scale turbulent motions are numerically resolved. Closure models may be based on similarity assumptions, using the known largest structures to estimate the effects of the smaller ones.

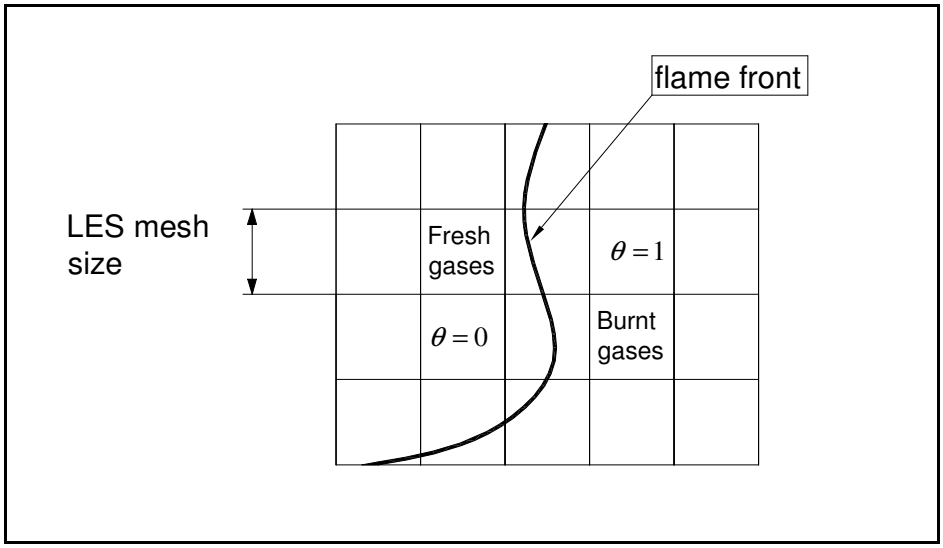

Figure 2.7. Comparison between premixed flame thickness and LES mesh size. The flame front separates fresh gases from burnt gases.

A difficult problem is encountered in large eddy simulations of premixed flames, the thickness δ_L of a premixed flame is about 0.1 to 1 mm and is generally much smaller than the LES mesh size Δ as plotted in Figure 2.7. The progress variable Θ is a very stiff variable and the flame front cannot be resolved in the computation, leading to

numerical problems. In fact, the most important contribution to the reaction rate probably occurs at the sub-grid scale level suggesting that LES could be impossible for reacting flows (Pope, 1990).

To overcome this difficulty, three main approaches have been proposed: simulation of an artificially thickened flame, use of a flame front tracking technique (G-equation), or filtering with Gaussian filter larger then the mesh size.

2.3.2.1 Artificially Thickened Flames

Butler proposed an attractive solution for the propagation of premixed flames on a coarse grid (Butler and O'Rourke, 1976). Following simple theories of laminar premixed flame (Williams, 1985), the flame speed s_L and the flame thickness δ_L may be expressed as:

$$s_L \propto \sqrt{D_{th} B} \qquad (2.45)$$

$$\delta_L \propto \frac{D_{th}}{s_L} = \sqrt{\frac{D_{th}}{B}} \qquad (2.46)$$

The symbol D_{th} is the thermal diffusivity and B the pre-exponential constant. For sufficiently large F values, if the thermal diffusivity is increased by a factor F, while the pre-exponential constant is decreased by F, the flame thickness δ_L is multiplied by F and the flame speed is maintained, the thickened flame front may be resolved on the LES computational mesh (Figure 2.8).

Unfortunately, when the flame is thickened from δ_L to $F\delta_L$, the interaction between turbulence and chemistry is modified because the Damköhler number is decreased by a factor F. An efficiency function E, corresponding to a sub-grid scale wrinkling factor, has been derived to account for this effect. In practice, the thickened flame approach is implemented by changing the diffusivity and the reaction rate.

Diffusivity:	D_{th}	$\rightarrow$	FD_{th}	$\rightarrow$	EFD_{th}
Pre-exponential constant:	B	$\rightarrow$	B/F	$\rightarrow$	EB/F
		thickening		wrinkling	

According to (2.45) and (2.46), the flame speed and the flame thickness are respectively replaced by:

$$s_T = E s_L \qquad (2.47)$$

$$\delta_T = F \delta_L \qquad (2.48)$$

where s_T is the sub-grid scale turbulent flame speed.

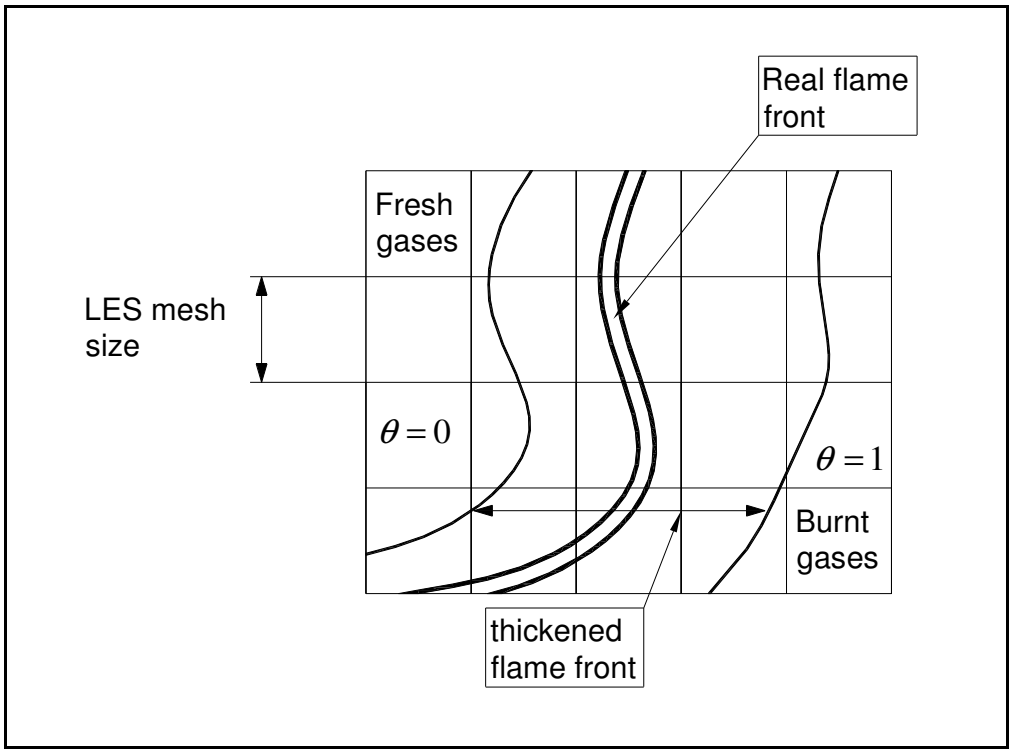

Figure 2.8. Thickened flame approach. The laminar flame is artificially thickened but its flame speed is preserved.

2.3.2.2 G-Equation

The G-equation formalism adopts a view which is opposite to the thickened flame approach: The flame thickness is set to zero and the flame front is described as a propagating surface tracked using a field variable G (Figure 2.9). In LES, the resolved flame brush is associated to the iso-level $G = G^*$. The resolved G field does not need to follow the progress variable (Θ) gradients and can be smoothed out to be resolved on the LES mesh. The G-equation is written as (Poinsot and Veynante, 2001):

$$\frac{\partial \overline{\rho} G}{\partial t} + \frac{\partial \overline{\overline{\rho u_i} G}}{\partial x_i} = \rho_0 \bar{s}_T \left| \nabla \overline{G} \right| \qquad (2.49)$$

A model for the sub-grid scale turbulent flame speed $\bar{s}_T$ is needed. This closure is generally based on the relation:

$$\frac{\bar{s}_T}{s_L} = 1 + \alpha \left(\frac{\overline{u'}}{s_L} \right)^n \qquad (2.50)$$

where $\overline{u'}$ is the sub-grid scale turbulence level, and the constants α and n have to be specified. The turbulent flame speed is not a well defined quantity and no universal

model is available. Despite this drawback, the G-equation is a popular technique for large eddy simulations of turbulent premixed combustion.

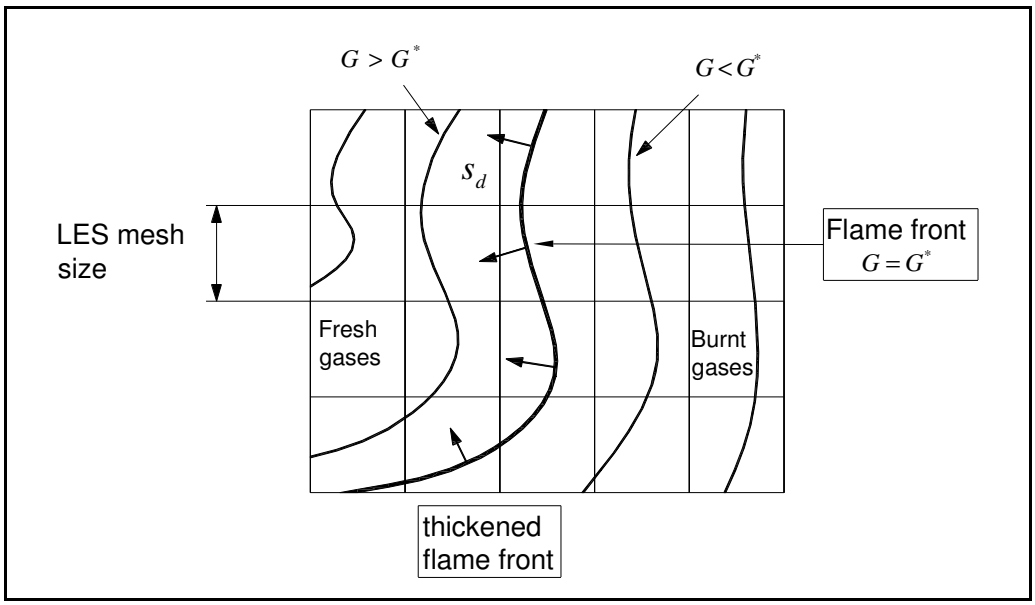

Figure 2.9. Flame front and G-field. The flame front is identified to a given surface $G = G^*$ of a G-field, generally related to the distance to the flame front.

2.3.2.3 Flame Surface Density LES Formulations

Another approach is to filter the Θ balance equation:

$$\frac{\partial \rho \Theta}{\partial t} + \frac{\partial \rho u_i \Theta}{\partial x_i} = \frac{\partial}{\partial x_i}\left(\rho D \frac{\partial \Theta}{\partial x_i}\right) + \dot{\omega}_\Theta = \rho s_d |\nabla \Theta| \qquad (2.51)$$

where s_d is the local displacement speed of the iso-surface Θ, leading to:

$$\frac{\partial \overline{\rho}\,\overline{\overline{\Theta}}}{\partial t} + \frac{\partial \overline{\rho}\,\overline{\overline{u_i}}\,\overline{\overline{\Theta}}}{\partial x_i} + \frac{\partial}{\partial x_i}\left(\overline{\rho}\,\overline{\overline{u_i\,\Theta}} - \overline{\rho}\,\overline{\overline{u_i}}\,\overline{\overline{\Theta}}\right) = \frac{\partial}{\partial x_i}\left(\overline{\rho D \frac{\partial \Theta}{\partial x_i}}\right) + \dot{\omega}_\Theta = \overline{\rho s_d |\nabla \Theta|} \qquad (2.52)$$

As already pointed out, the flame front (and the gradient of the progress variable Θ) is too thin to be resolved on the LES computational mesh. Nevertheless, the filtered progress variable $\overline{\overline{\Theta}}$ may be resolved using a physical space Gaussian filter with a filter size Δ larger than the computational mesh size Δ_m as displayed on Figure 2.10. Compared to an arbitrary G-field, the progress variable Θ has a main advantage: Θ and related quantities, such as flame surface densities, are physically defined and may be extracted from DNS or experimental measurements.

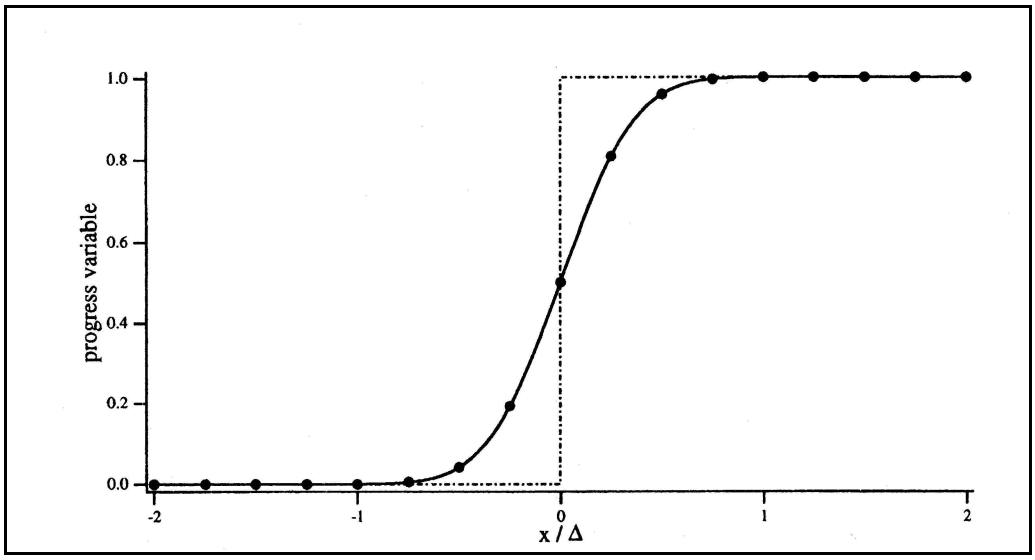

Figure 2.10. Effect of spatial Gaussian Filter defined with Equation (2.38) having a size Δ larger than the mesh size Δ_m (here $\Delta = 4\Delta_m$). Unfiltered Θ (dashed line -•-) and filtered progress variable $\overline{\overline{\Theta}}$ (continuous line—) versus x/Δ where x is the spatial coordinate. The progress variable Θ is not resolved on the computational mesh denoted by (•) whereas the filtered progress variable $\overline{\overline{\Theta}}$ is resolved with about $2\Delta/\Delta_m = 8$ grid points in the filtered flame front (Boger et al., 1998).

2.4 Laser Diagnostics Applied on Combustion

Much of the imperfect knowledge of fundamental combustion processes can be blamed on the difficulty of making measurements in the hostile combustion environment. Also to blame is the general impracticality of using scale modelling techniques in experiments. Laser diagnostics have created a revolution in the approach to experimentation in combustion. Essentially non-intrusive, they eliminate many of the concerns, such as flame holding and flow alteration, which arise when using thermocouples, pressure probes and sampling probes in flame and combustors. Lasers also allow measurements of high spatial and temporal resolution, greatly alleviating problems of spatial and temporal averaging that arise with intrusive probes. Thirdly, lasers allow great improvements in imaging so that the path integrated images can be replaced by images of a sheet section through the flow. Such images can even be used to produce three-dimensional “pictures”.

A general configuration for two dimensional optical techniques is shown in Figure 2.11. The laser beam is formed into a thin sheet of light that illuminates a cross-sectional area of the flow. Depending of the method used, light scattered or fluorescence from within the illuminated sheet is collected normal to the sheet, passed through optical filters, and imaged on to a two dimensional detector. The basic elements of the experimental

configuration include: the laser illumination sheet, the collection optics, the optical filters and the multichannel detector and its related electronics (including a computer).

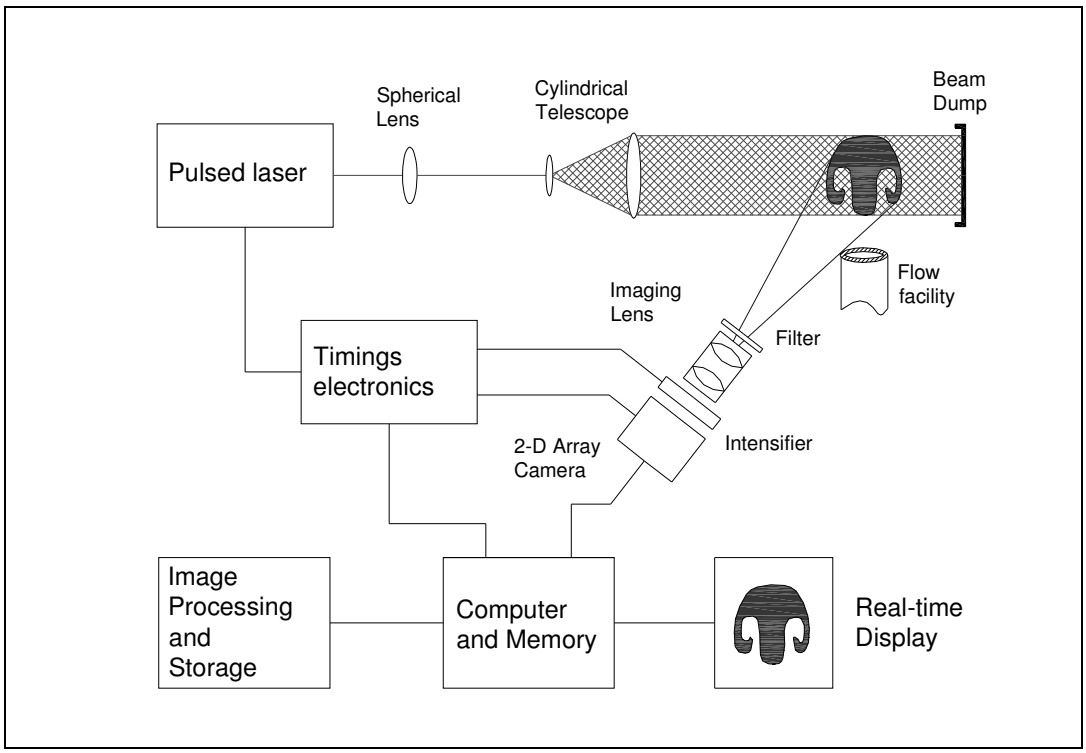

Figure 2.11. Typical experimental set-up for two dimensional laser diagnostic techniques.

The characteristics of the light emerging from the illuminated sheet depend on the type of interaction between the laser sheet and the molecules or particles of the flow. Listed below are several emission types, related to different diagnostic techniques:

1. Lorenz-Mie scattering (elastic scattering from particles)
2. Rayleigh scattering (elastic scattering from molecules)
3. Spontaneous Raman scattering (inelastic scattering from molecules)
4. Laser induced fluorescence (LIF)
5. Particle image velocimetry (PIV)

The different principles related with the emissions listed before will be expanded upon.

2.4.1 Lorentz-Mie Scattering

The Lorenz-Mie scattering theory is applicable to homogeneous spheres of arbitrary size illuminated by plane waves. If scatterers are either much smaller or much larger than the wavelength of the light, the full Lorenz-Mie scattering theory is needed to

accurately describe the scattering. This is the scattering regime involved for visible wavelength of light ($\lambda \approx 0.5\mu m$) and the largest aerosol particles that will remain entrained in gas phase flows ($d_p \approx 1\mu m$).

The basis of the Lorenz-Mie scattering technique involves using a dense aerosol to tag one component of a mixing flow. The intensity of the light scattered from the seeded flow will be proportional to the concentration of the seeded gas. Even if the coherence and monochromatic properties of the lasers are not essential, the convenient source of high-intensity illumination provided by lasers makes the measurements much easier and improves the signal-to-noise ratio. Of all the light scattering techniques, Lorenz-Mie scattering is often the easiest, because of the large elastic scattering from aerosol particles. The requirements of illumination intensity are greatly reduced as are the requirements of detector sensitivity.

One of the main limitations of Lorenz-Mie scattering is the noise related to the finite number of aerosol particles that exist within any volume. If too many particle are added, secondary scattering will become important and there will be errors imposed on the signal due to the fact that the scattered light must pass through an inhomogeneous, optically dense medium to reach the detector. If too few particles are present within the resolution volume, then the shot noise related to this finite number of particles (called marker shot noise) will become the dominant noise source.

Another consideration using aerosols to tag a flow relates to the ability of the particles to follow the fluid motion. It should be remembered that even though the seed particles may be able to follow the turbulent motion of the flow, aerosols are not subject to molecular diffusion. Thus, care must be taken whenever molecular diffusion effects are significant.

Lorenz-Mie scattering technique is used for obtaining concentration distribution. For example in premixed flame if flow is seeded with particles that are destroyed at the flame front (e. g. oil or sugar aerosol) the scattered intensity distribution is proportional to the concentration of non reacted fuel/oxidizer (Long, 1993).

2.4.2 Laser Induced Rayleigh Scattering (LIRay)

Rayleigh scattering is the elastic scattering of light from particles much smaller than the wavelength. Because the scattering cross-section is much smaller than that of aerosols, more laser energy must be used than for Lorenz-Mie scattering experiments and aerosols must not be present within the measurement volume in order to use Rayleigh scattering successfully.

The differential Rayleigh cross-section of a gas, σ_R , can be related to the index of refraction of the gas as follow:

$$\sigma_R = \frac{4\pi^2}{\lambda_0^4}\left[\frac{n-1}{N_0}\right]^2 \qquad (2.53)$$

where λ_0 is the incident wavelength, n is the refractive index of the gas at standard temperature and pressure (STP) and N_o is the Loschmidt number($2.69\times10^{19}\,cm^{-3}$). The Rayleigh scattering cross-section for different gases can vary by up to 2 orders of magnitude.

The expression of the intensity of Rayleigh scattered light from a mixture of gases is as follows:

$$I_R = K_{opt} I_0 N_m \sigma_{eff} \qquad (2.54)$$

where

$$\sigma_{eff} = \sum X_i \sigma_i \qquad (2.55)$$

K_{opt} is the calibration constant of the calibration optics, I_0 is the intensity of incident light and N_m is the total number of molecules contained in the measurement volume. The symbol σ_{eff} is the effective Rayleigh scattering cross-section for a mixture of gases determined from the mole-fraction-weighted sum of all the components. X_i is the mole fraction and σ_i the Rayleigh cross-section of the i th gas in the mixture.

Rayleigh scattering has been used to map out the temperature in flames. As seen from Equation (2.54), Rayleigh scattered intensity will depend only on the number of scatterers in each volume, if the term for the effective Rayleigh cross-section can be held nearly constant. In a reacting flow at constant pressure, N is inversely proportional to the temperature (Long, 1993).

2.4.3 Spontaneous Raman Scattering (LIRam)

Spontaneous Raman scattering is an inelastic scattering process involving the interaction of a photon with a specific vibrational-rotational state of a molecule. Since spontaneous Raman scattering is not a resonant process, it does not require the laser to be tuned to a specific wavelength. Thus, a single laser is capable of exciting Raman scattering from nearly all gases in a flame.

Because there is a transfer of energy between the electromagnetic wave and the scattering molecule, the energy and the wavelength of the scattered light differ from that of the incoming light. For spontaneous Raman scattering, the transfer of energy occurs between the photon and the quantized vibrational and rotational state of the molecule. If the wave number of the incoming radiation is ν_I, the wave number of the Raman-scattered light, ν_R, will be expressed as follows:

$$\nu_R = \nu_I \pm \nu_m \qquad (2.56)$$

where ν_m is the Raman shift of particular vibrational or rotational state of a molecule. The $\pm$ sign in the above expression allows energy to be transferred from

electromagnetic wave to the molecule (so called Stokes scattering) or from the molecule to the electromagnetic wave (anti-Stokes scattering).

Raman cross-sections are extremely small, for most gases are three orders of magnitude smaller than for Rayleigh scattering. This leads to extremely low signal levels, even with the best lasers currently available. Then its use is restricted to detection of major species.

The intensity of the Raman signal is directly proportional to the number of scatterers in a given vibrational-rotational state. Therefore, the intensity of the Raman spectrum is sensitive to both the number density and temperature of gas species. By appropriate selection of the spectral region and bandwidth of the detected Raman scattering, it is possible to minimize the temperature dependence of the detected signal, and thus Raman scattering has been used quite extensively to measure species concentrations. Similarly by measuring the spectral features of the Raman spectrum or the ratio of the Stokes to anti-Stokes scattering, Raman scattering has been used to measure temperatures (Long, 1993).

2.4.4 Laser Induced Fluorescence (LIF)

The term fluorescence is usually applied to the radiation emitted by an atom or molecule when it decays spontaneously from a higher to a lower energy level or state. In LIF the molecule is pumped to a higher level by a photon from a laser tuned to an electronic resonance. This process is illustrated in Figure 2.12, and for low intensities it is controlled by the product of laser intensity I_v, the number density of absorbers in the lower state, N_l, and the Einstein coefficient for the rate of absorption of photons, B_{lu}. Here l, denotes the lower electronic level and u the upper level. Once the molecule is excited there are several competing path ways for de-excitation of the upper level, six of these processes are illustrated in Figure 2.12.

Fluorescence can arise from spontaneous emission direct from the upper level to which the species is excited by the laser (A_{ul}). More typically, relaxation and energy exchange processes in the vibrational and rotational levels in the upper state, plus the opportunity to relax to other rotational and vibrational levels in the lower electronic state, cause the fluorescence to be shifted to longer wavelengths ($A_{u'l'}$). Other important competitor processes include: stimulated emission to the original lower state by the laser ($B_{ul}I_v$), further excitation by the laser to higher states or to an ionising level ($B_{ue}I_v$), predissociation (Q_{pre}) of the molecules and electronic quenching of the system (Q_{elec}). Electronic quenching, or just quenching as it is normally referred to, also arises from collisions with other bath gas molecules. Typically all processes are present in all systems, but quenching and rotational and vibrational relaxations are the most important.

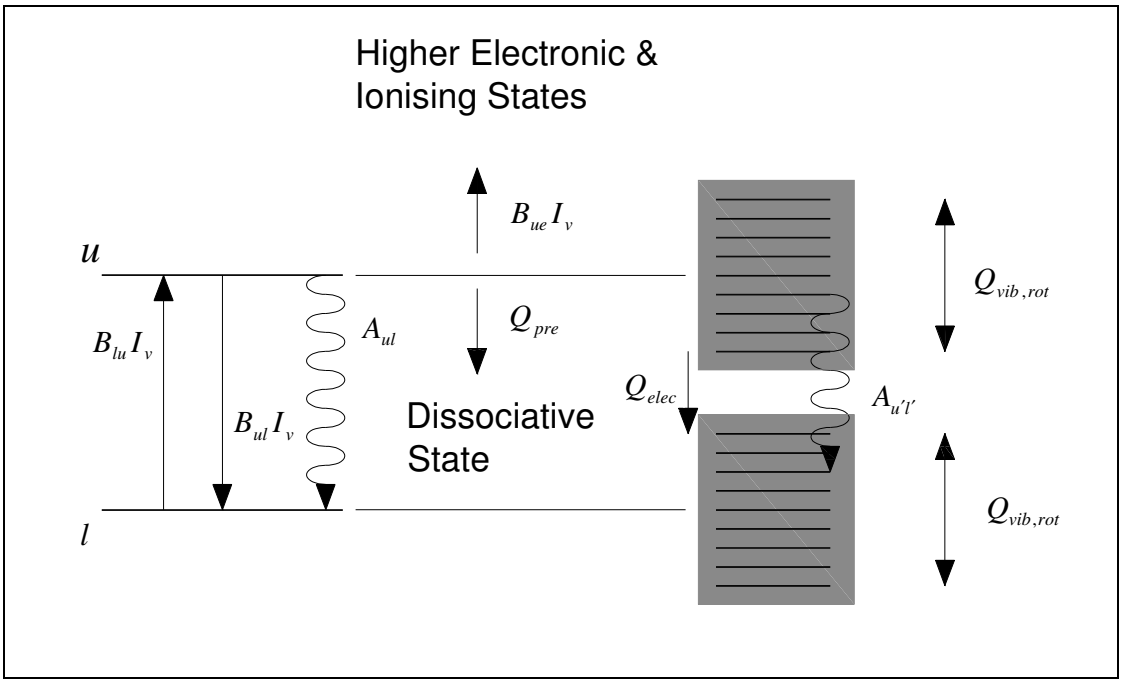

Figure 2.12. Diagram of energy transfers in LIF.

The total rate coefficient for all events transferring molecules from level l to u is R_f:

$$R_f = N_l B_{lu} I_v \left[\frac{A_{ul}}{A_{ul} + Q_{elec} + Q_{pre}} \right] \left[\frac{1}{1 + I_v / I_v^{sat}} \right] \qquad (2.57)$$

where I_v^{sat} is the saturation parameter for a specific transition. In the limit $I_v >> I_v^{sat}$ a constant number density of excited state is achieved irrespective of laser intensity. The attraction of saturation is that the effects of electronic quenching are eliminated. In practice this is very difficult to obtain because most lasers have an approximately Gaussian spatial intensity distribution and this cause both saturated, partially saturated and unsaturated fluorescence to be simultaneously generated and detected.

For accurate quantitative measurements, it is preferable to work in the low intensity limit or to have an accurate knowledge of the quenching. It is better to choose a system where quenching is essentially constant for all sensible variations of local gas composition.

One such strategy is to choose energy levels within the molecular system where predissociation is possible such that if $Q_{pre} >> Q_{elec}$ the rate of fluorescence emission becomes:

$$R_f = N_l B_{lu} I_v \left[\frac{A_{ul}}{A_{ul} + Q_{pre}} \right] \qquad (2.58)$$

Therefore changes in quenching due to local gas composition are eliminated.

In a combustion system oxygen and polar molecules such as H_2O are the most important quenching species. For fuel visualization, the quenching effect due to oxygen is usually the most important, and choosing a fluorescent fuel or fuel marker which is insensitive to quenching is therefore critical for quantitative measurements. Unfortunately most commonly used fuels are not suitable for detection by LIF since they either do not have a sufficiently strong absorption at an accessible wavelength or they dissociate in preference to fluorescing. For such fuels a carefully chosen fuel marker is preferable. For light fuels, markers based on certain ketones and aldehydes such as acetone, pentanone and acetaldehyde have proven to be very successful (Seitzman and Hanson, 1993).

2.4.5 Particle Image Velocimetry (PIV)

Particle Image Velocimetry (PIV) is a technique used to accurately determine the instantaneous velocity field across a planar area of a flow field. The flow is seeded with tiny, neutrally buoyant particles so called tracers (e.g. oil or water aerosols in air and solid particles in fluids or flames). Using a light sheet, formed by passing a double pulsed laser beam through an optical arrangement including cylindrical lenses, the particles in the flow are illuminated twice with a small time separation between pulses.

The displacement of particles in the time between the laser pulses is recorded as either a single image exposed twice or as a pair of two single exposure images. The recorded particle displacement field is measured locally across the whole field of view of the images, scaled by the image magnification and then divided by the known pulse separation to obtain flow velocity at each point. A camera positioned typically perpendicular to the plane of the light sheet is shuttered to capture the light scattered from the particles. The light is scattered according to the Lorenz-Mie theory. Depending on the flow velocity and the factor of magnification of the camera lenses the delay of the two pulses have to be chosen such that adequate displacements of the particle images on the CCD are obtained. From the time delay between the two illuminations and the displacement of the tracers velocity vectors can be calculated.

For the evaluation of the particle images it is assumed that the tracers follow the flow into the local flow velocity between the two illuminations. The (digital) PIV recording is divided in small subareas, so called interrogation windows. Using statistical correlation techniques one local displacement vector is determined for each interrogation window. For this reason the size of this interrogation cell is selected such that all particles within this area have moved homogeneously in the same direction and the same distance.

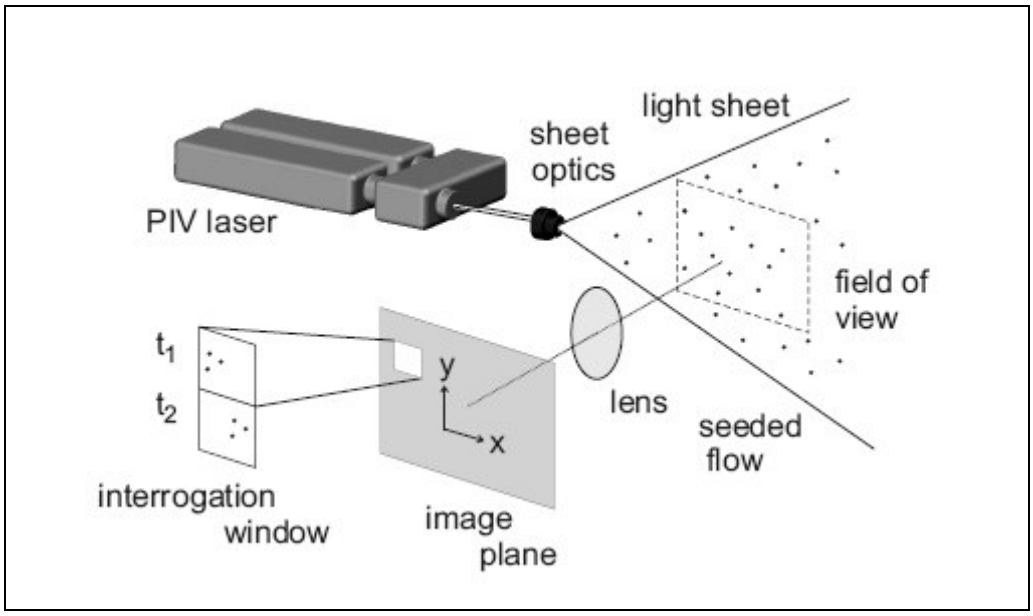

Figure 2.13. General setup of a 2D PIV system [La Vision Davis 7.1 Software Manual, pag. 15].

The evaluation of the particle images depends on the way these images have been recorded by the used camera. One possibility is to record the scattered light of both illuminations in one frame what is called 'single frame / double exposure'. These pictures can be evaluated by auto-correlation. The other possibility is to record the scattered light from the first illumination in one frame and the scattered light from the second illumination in another frame. This is called 'double frame / double exposure'. These double frame images can be evaluated by cross-correlation.

In the case of auto-correlation the scattered light from first and second exposure of the particles is recorded in one image. The complete image is subdivided in so called interrogation windows and each window is evaluated by auto correlation. The auto correlation function is characterized by two identical correlation peaks rotationally symmetrical about the highest central peak indicating zero displacement (Figure 2.14). This is a consequence as it is not possible to detect the sign of the displacement because it is not known which particle is illuminated by the first and the second laser pulse. So the information from the auto-correlation is ambiguous and not conclusive if there is no a priori information about the observed flow. Also the detection of very small displacements is a problem as in this case the correlation peaks are very close to the central peak. Compared to cross-correlation the auto-correlation peaks are significantly smaller. High noise increases the possibility that the displacement correlation peak disappears in the background.

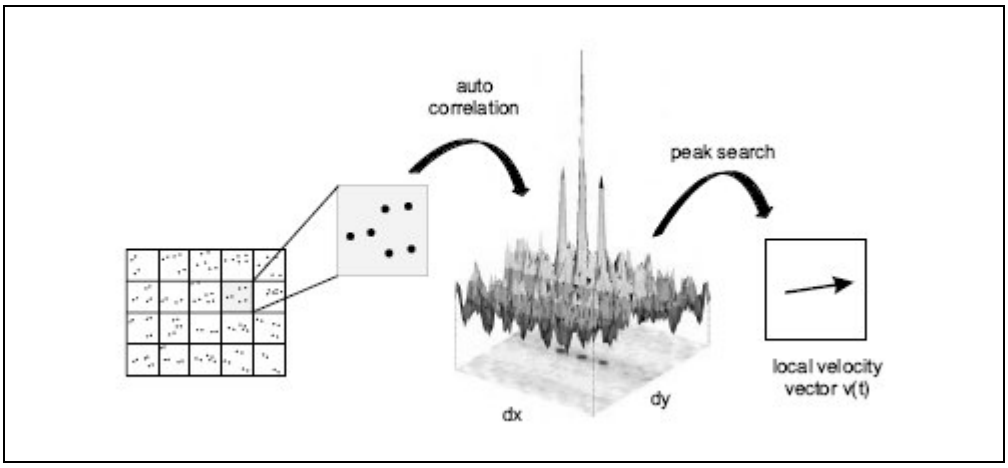

Figure 2.14. Evaluation of PIV recordings using auto-correlation [La Vision Davis 7.1 Software Manual pag. 17].

For the case of cross-correlation the scattered light from first and second exposure of the particles is recorded in two different images. The complete image is subdivided in interrogation windows and each window is evaluated by cross correlation. For cross-correlation a fast double shuttered CCD camera is typically used to record images with 'double frame / double exposure'. The minimum time delay between the two laser pulses is limited by the time necessary for the frame transfer of the camera. But compared to the auto-correlation it has a higher and unambiguous correlation peak (Figure 2.15).

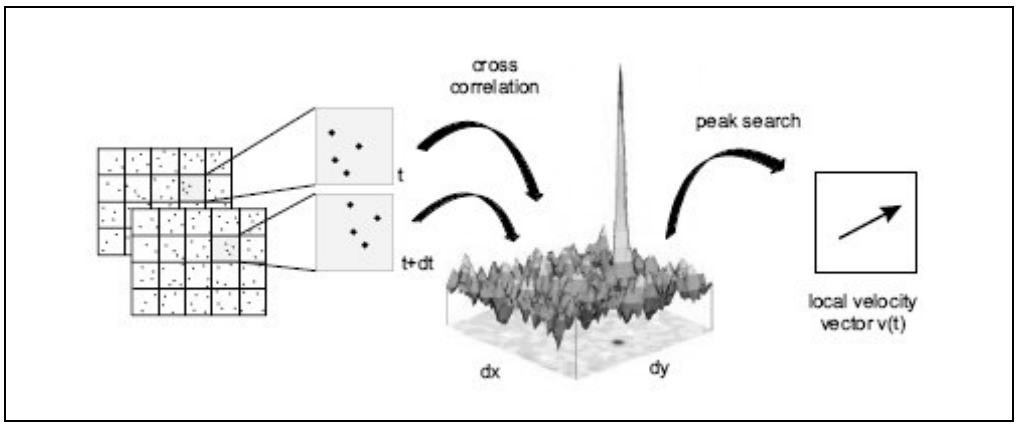

Figure 2.15. Evaluation of PIV recordings using cross-correlation [La Vision Davis 7.1 Software Manual pag. 18].

2.4.5.1 Stereoscopic Particle Image Velocimetry

"Stereoscopic particle image velocimetry employs two cameras to record simultaneous but distinct off-axis views of the same region of interest, illuminated plane within a flow

seeded with tracer particles" (Prasad, 2000). When measuring three-dimensional particle displacement, one may characterize this situation as having three unknowns (Δx, Δy , Δz) with the single view providing only two equations. The addition of a second, different view, provides two additional equations which may be used to solve for the three-dimensional information. All stereoscopic systems, despite the wide variety in configurations, must satisfy the basic requirement of recording two simultaneous, but different views of the same object. The two views are then combined using one of an assortment of algorithms to reconstruct the three-dimensional field. Figure 2.16 shows the conventional single camera PIV arrangement wherein the camera axis is perpendicular to the illuminated plane in order to obtain the in-plane velocity components. A particle with initial position $\overrightarrow{x_i} = (x, y, 0)$ forms an image at $\overrightarrow{X_i} = (-M_n x, -M_n y, 0)$ where the nominal magnification $M_n = d_i / d_O$. Here d_O is the object distance to the middle of the light sheet, and d_i is the corresponding image distance. It should be noted that Figure 2.16 depicts the motion of only one particle, and secondly, that this particle is initially located exactly on the object plane. In reality, each PIV measurement averages the motion of all particles in an interrogation volume, which is defined by the intersection of the light sheet with the back-projection of the interrogation spot onto the object plane. Second, these particles cannot obviously be constrained to start their motions from the object plane in a real flow.

However the process of integrating the contributions of multiple particles embedded uniformly throughout the interrogation volume reduces the physical problem of the situation depicted in Figure 2.16 with an error of order $(\Delta z_0 / d_O)^2$ where Δz_0 is the thickness of the light sheet. For a typical PIV recording, $\Delta z_0 \approx 1mm$ and d_O is hundreds of millimetres, so this error is negligible (Prasad and Adrian, 1993).

The relative error between the true and the apparent in-plane displacement is called perspective error. It can significantly contaminate in-plane measurements when the relative out-of-plane component is large, as well as when the angle subtended by the particle to the camera-axis, θ, is large. Stereoscopic PIV eliminate this problem acquiring two simultaneous views along different off-axis directions as shown in Figure 2.17. The apparent displacements recorded by each camera, $\Delta\overrightarrow{X_1}$ and $\Delta\overrightarrow{X_2}$, are later combined to obtain the correct in-plane displacement, $(\Delta x, \Delta y)$, and more importantly, the out-of-plane displacement, Δz.

Commonly used stereoscopic systems may be broadly classified according to translation systems, also known as lateral displacement, and rotational systems, also known as angular displacement.

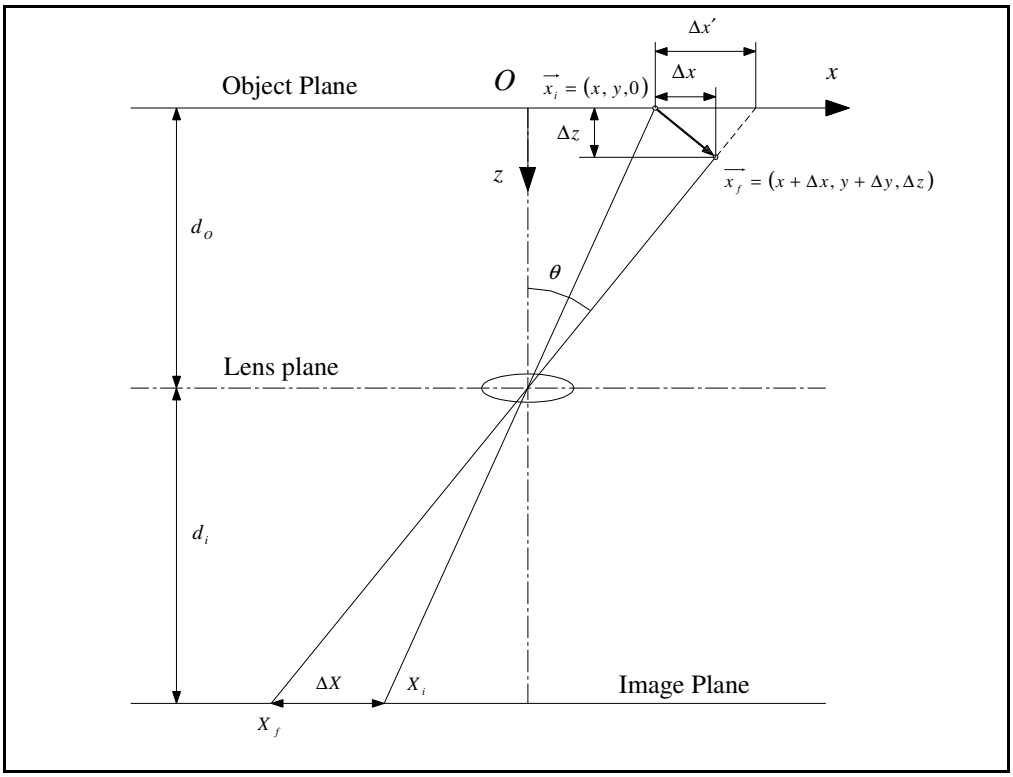

Figure 2.16. Error in measurement of in-plane displacements due out-of-plane motion using a single camera.

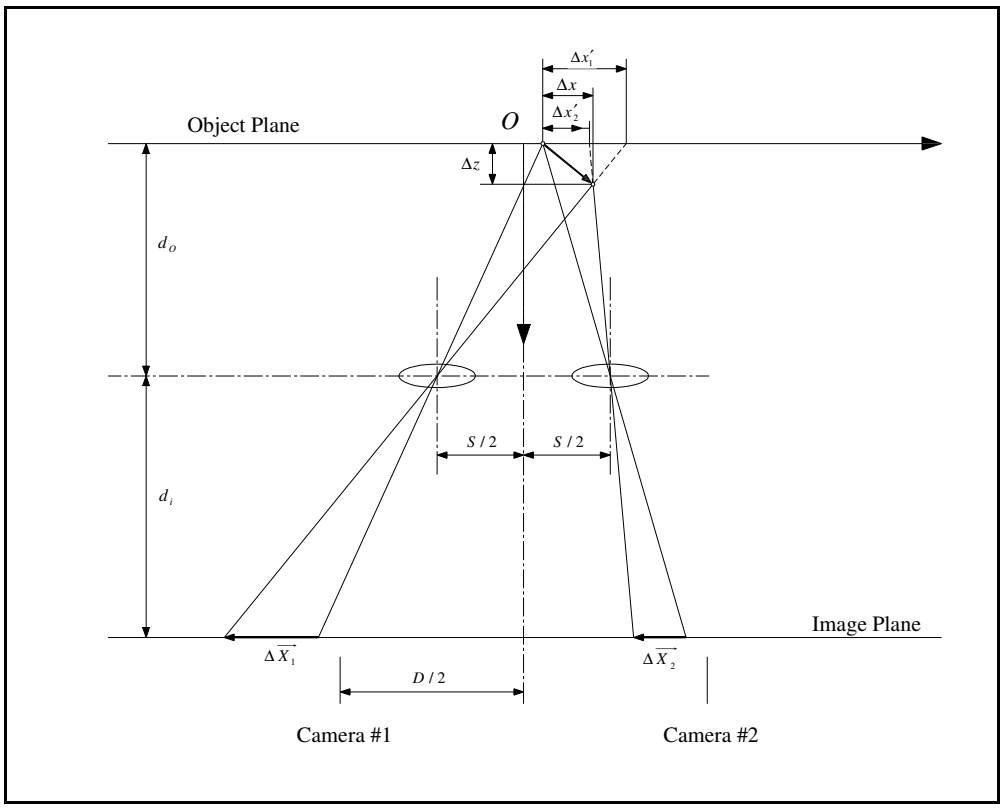

Figure 2.17. Scheme of stereoscopic configuration.

2.4.5.1.1 Translation Systems

In the translation system, the axes of both cameras are placed parallel to each other, such that they are both orthogonal to the light sheet. The primary advantage of the translation method is its simplicity. Because the object plane, lens plane and image plane are all parallel to each other, the image field enjoys uniform magnification. Good image focus is achieved without the need to reduce the aperture beyond what is used in single camera PIV (the depth of field requirement is unchanged). One of the objections raised to the translation method is the small common area viewed by each camera. However, the common area can be maximized by off-setting each sensor frame away from the lens-axis. It should be noted that such an off-set may be difficult to enforce with CCD cameras due to vignetting caused by the camera body.

A more serious difficulty with the translation system is that there is an upper bound to the off-axis angle θ subtended by the centre of the region of interest to the centre of the lens. This restriction arises purely from the design of the lens; if the lenses are separated by a value that is too large for a given d_O, the lens performance degrades as it is forced to operate at the outer limit of its specification.

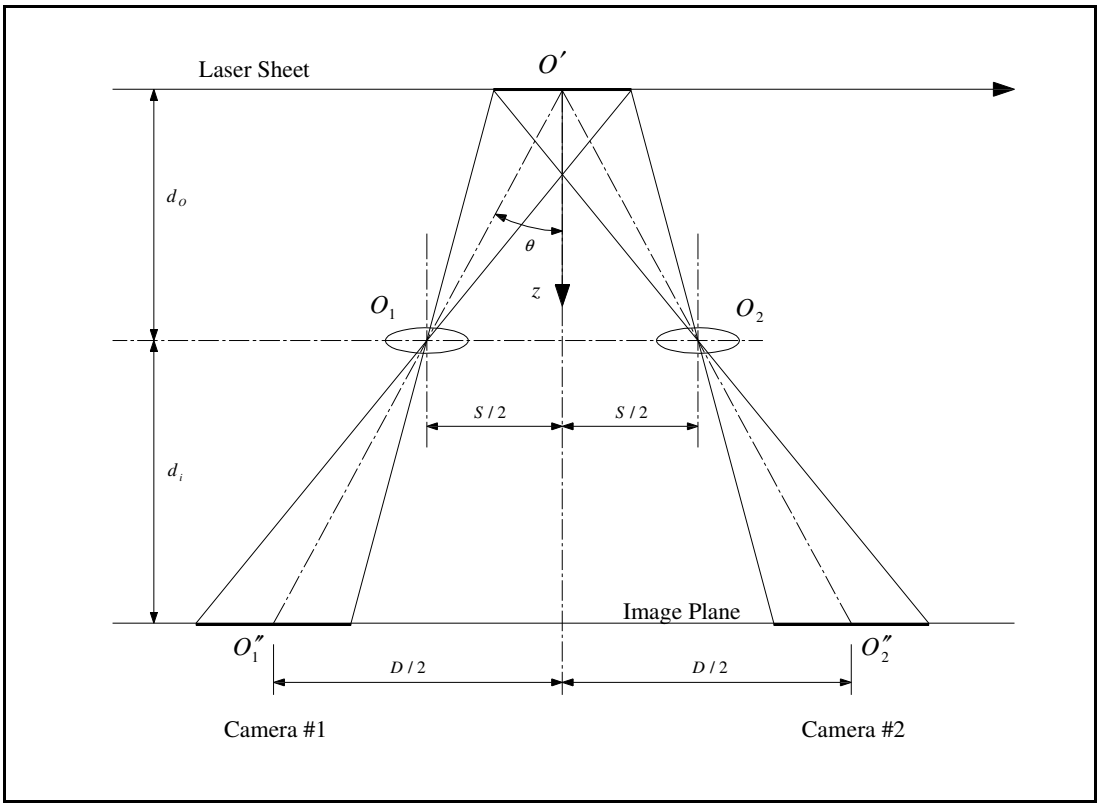

Figure 2.18. Scheme the stereoscopic translation system.

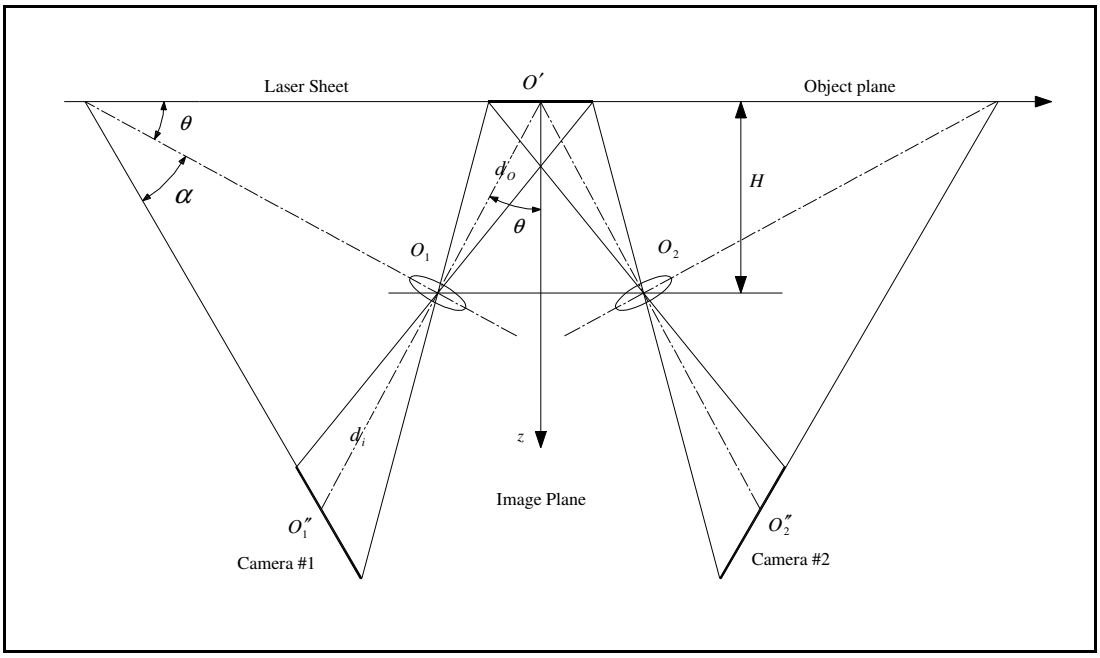

Figure 2.19. Scheme of the stereoscopic rotational system.

2.4.5.1.2 Rotational Systems

The restriction on θ imposed by the translation arrangement is removed in rotational systems. As shown in Figure 2.19 the two camera axes are no longer parallel to each other but are rotated such that the two axes intersect the object plane at the system axis. Now the angle θ may be increased to much larger values without incurring problems associated with lens performance, thereby allowing greater accuracy in the out-of-plane component. However, the magnification is no longer uniform over the field of view. Furthermore, as shown in Figure 2.19 the image plane has to be further rotated with respect of the lens plane by an angle α such that the object plane, lens plane and image plane are collinear. This requirement, known as the Scheimpflug condition, ensures that all particles in the object field will be in good focus in the image plane. However, the Scheimpflug condition exacerbates the non-uniformity in magnification.

In addition to non-uniformity, the angular displacement arrangement depicted in Figure 2.19 produces image fields which are oppositely stretched. It is impossible to directly combine information from each view in the image plane without first interpolating the data on to a common grid.

Several researchers suggested the use of the Scheimpflug condition (Hinsch, 1995). Willert used a variation of the Scheimpflug angular displacement system in which the two cameras were placed on either side of the light sheet (Willert, 1997). Two benefits accrue from this arrangement. First, by properly orienting the direction of propagation of the illuminating laser beam, it is possible to operate both cameras in forward scatter. Because scattering efficiency is significantly higher in forward scatter, both views can exploit higher (and equal) signal-to-noise ratios. Secondly, Willert's arrangement implies that both views will be stretched identically, rather than the opposite stretching

for cameras situated on the same side of the light sheet. However, the task of interpolating both views on to a Cartesian grid still remains.

3 DEVELOPMENT OF A NOVEL BURNER FOR TURBULENT PARTIALLY PREMIXED FLAMES ANALYSIS

The main objective of this thesis is to enhance the comprehension of stratified turbulent flame propagation using an open flame burner. For this reason this chapter describes the experimental research carried out to date on turbulent combustion and stratified flames using open flame burners. In the first section the various means of stabilization used on open flame burners are considered with particular attention to the weak swirl mechanism. In the second section the latest research on stratified flames propagation is described. In both sections the laser diagnostic tools used and the information gained on each research project are considered. The aim is to show the process for selecting the burner characteristics and the experimental tools for this thesis project.

3.1 Considerations on Flame Stabilization Methods used for Experimental Burners

Many laboratory burners of different configurations and flame geometries have been used for studying the fundamental properties of turbulent flame propagation. It has long been recognized that that these studies have made significant contributions to the understanding of turbulence-combustion interactions and have provided valuable experimental validation to support current turbulent combustion models. Since there is no general consensus on a standard configuration for studying turbulent flame propagation and making comparison with theoretical predictions, burners designed to provide flame zones closest to the idealized normal one-dimensional or inclined two-dimensional infinite planar flames are most often used. However, the selection of the burner geometry is sometimes restricted by other practical experimental concerns such as optical diagnostic access and stable operation under a wide range of flow and mixture conditions.

Plane symmetric v-flames and stagnation flow stabilized flame are generally used to validate models for planar flames. This family of burners is designed to produce relatively uniform incident turbulence intensity, which can be varied by the use of different turbulence generators. The turbulence produced by these means has no mean shear stress, and the behaviour is well understood. Flame propagation is not influenced by shear stresses, therefore by Kolmogorov scaling, the various length scales associated with the incident flow can be predicted from the RMS velocity fluctuations and integral length scales, and are used to estimate the Damköhler and Karlovitz numbers.

The significant feature of v-flames is that the flame brush is relatively planar. Though the flame zone is oblique to the flow, it has been shown that by a coordinate

transformation it is possible to compare the results with predictions of one-dimensional models for infinite planar flames.

The use of stagnation flow to stabilize turbulent flames is an extension of a method used to study laminar flame propagation. Due to the fact that the flame brush at the centreline is locally normal to the incident flow, this flame configuration provides a convenient means of determining the turbulent flame speed.

The tube stabilized conical flame burner is perhaps the simplest burner to design and construct. By use of a pilot flame at the exit rim, flames can be stabilized over a large range of mixture and flow conditions. In some studies long tubes typically less than 20 mm in diameter are used, and the turbulence at the exit is then non-uniform fully developed pipe turbulence.

Flame stabilization by swirl instead is a common feature of many turbines and furnaces. Varying the degree of swirl provides the control of their operation over a large range of conditions. The most distinct flow feature is the large recirculation zone or toroidal vortex which is vital to steady operation. Much can be learned from open swirl stabilized flames, because they are easily accessible to probing by laser diagnostics. Conditions of weak swirl provide a means of stabilizing freely propagating yet steady flames which are maintained at a distance above the burner exit without the presence of recirculation zones. Using this interesting and useful phenomenon of flame stabilization, the flow field is not influenced by physical boundaries, as in the cases of stagnation point flames, rod-stabilized v-flames and Bunsen flames. It gives free access to laser diagnostics and has the potential of being one of the most ideally suited configurations for investigating fundamental properties of premixed turbulent flames.

3.2 Previous Research on Turbulent Combustion using Weak Swirl Stabilized Flames

Cheng was the first to introduce the use of weak swirl as a means to stabilize freely propagating open premixed turbulent flames. The first task was analysis of the flow characteristics of this new burner configuration and their effects on flame speed (Chan et al., 1992; Cheng, 1995). The weak swirl burner has been further developed in order to generate intense isotropic turbulence. The result has been achieved using turbulent generators introduced by Videto and Santavicca (Videto and Santavicca, 1991). Laser Doppler anemometry and Rayleigh scattering techniques have been applied on the new configuration to determine the turbulence and scalar statistics (Bedat and Cheng, 1995). Measurements of the velocity statistics showed that the flames produced very little changes in the mean and RMS velocities of the flow. The high incident turbulence level seems to have obscured the flame acceleration introduced by the heat release and flame generated turbulence. The flame speed was found to increase linearly with turbulent kinetic energy. A schematic of the low-swirl burner designed by Cheng is presented in Figure 3.1.

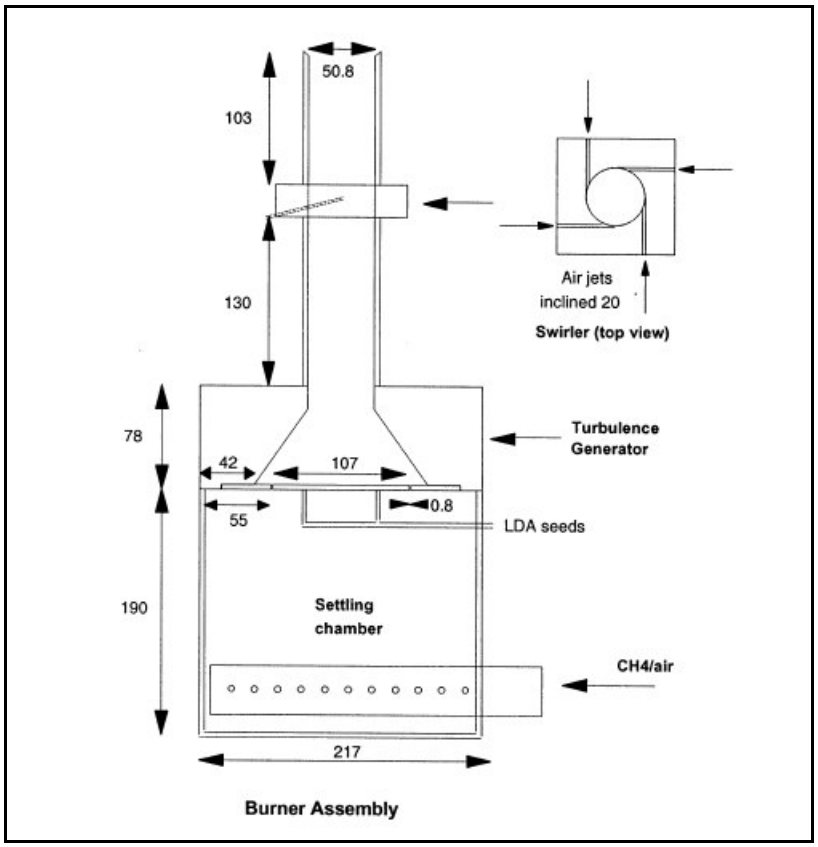

Figure 3.1. Schematics of the low-swirl burner with a circular slot turbulence generator used in the work of Cheng (Cheng et al., 2002).

The results showed that the burner was a useful tool to investigate systematically the variation in flame structures near the Klimov-Williams criterion. The goal of the following research using the same burner has been to gain a better insight into the flame structures at high turbulence and to test and verify the concept of the distributed reaction zones regime (Plessing et al., 2000). Experiments have been performed by Cheng using joint OH-PLIF and Rayleigh temperature as well as joint OH-PLIF and PIV measurements. The results allowed the analysis of the flame brush thickness under the effect of turbulence. The flame brush thickness was obtained from temperature images conditioned to OH-PLIF signal, while the turbulence information was gained through PIV. The measured turbulent burning velocities showed good agreement with the previous measurements obtained using Laser Doppler Anemometry.

The set of 200 OH-PLIF images obtained for each flame condition considered, clearly showed that flame wrinkling is a random process that requires statistical analysis of a sizable data set (Cheng et al., 2002). Due to this randomness, flame wrinkles at a given instance display only a limited range of turbulence scales. The probability of the flame showing the smallest wrinkles is relatively low. The important implication is that the penetration of small intense eddies into the flame sheet may be statistically an extremely rare event. Therefore, the distributed reaction zone regime of $Ka > 1$ should be interpreted as the regime where the probability for small intense turbulence to penetrate the flame sheet is finite. This interpretation confirmed the recent numerical and

theoretical results (Poinsot et al., 1990), suggesting that flamelets are resilient to penetration by small eddies. The OH-PLIF images were also processed to determine statistical properties of the mean flames curvatures and flame lengths for comparison with turbulence intensity and turbulence length scales.

O'Young and Bilger designed a burner similar to Cheng, that used vanes instead of tangential jets in order generate the swirl flow (Figure 3.2). A three dimensional imaging technique was used to provide instantaneous measurements of flame structures in turbulent premixed flames (O'Young and Bilger, 1997). The technique utilised two parallel laser light sheets closely spaced spatially and temporally to obtain two simultaneous images of Rayleigh scattering from the gas molecules. One of the images was used to provide information in two of the dimensions, while the second image was used to infer information in the third dimension. An instantaneous three-dimensional scalar gradient has been measured. Data taken in highly turbulent flames revealed that the magnitude of the local flame front gradient is not necessarily the same value as for a laminar flame, contradicting the assumption made by the flamelet hypothesis.

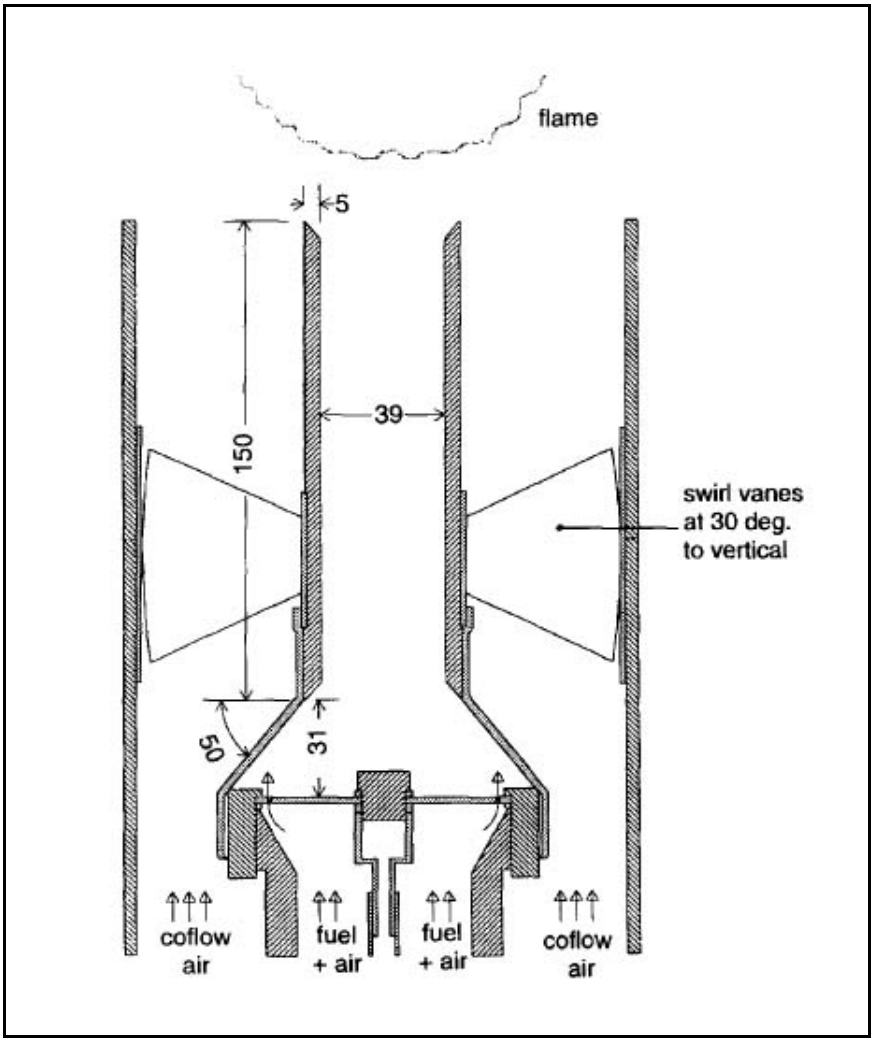

Figure 3.2. Turbulent swirl burner designed by O'Young and Bilger (O'Young and Bilger, 1997).

3.3 Current Experimental Research using Stratified Burners

Combustion in stratified medium where the reactants are not perfectly premixed can be presented as a relatively classical configuration in an industrial context, such as combustion in direct injection engines or in gas turbines. Research in the field of partially premixed combustion in the last 10 years has become of utmost importance since the effects of small and large scale heterogeneities of the reactant may have a significant impact on the pollutant emissions and combustion efficiency. Moreover, their effects on the flame dynamics (flame speed, local flame structure, heat release, etc.) are not well known and the positive or negative effects of fuel heterogeneities on the flame enhancement seem contradictory (Jimenez et al., 2002). Additionally, numerical results suggested that stratified methane flames propagating from stoichiometric to lean mixtures travel 20-30% faster than homogeneous ones because of heat feedback from already burnt mixtures (Pires Da Cruz et al., 2000). Experimental verification of these computations has been significantly hindered by difficulties in establishing a controllable and steady distribution of equivalence ratio (ϕ).

The objective of Kang's work was to use an experimental configuration, in which a steady compositional stratification of fuel-air mixture was established, in order to study the propagation of methane-air flames parallel to an equivalence ratio gradient (Kang and Kyritsis, 2005). The fuel stratification was achieved using the principle outlined in Figure 3.3. A mixture of constant equivalence ratio equal to ϕ flowed continuously over the top of the chamber where the stratification was established and the mixture was left to diffuse into the chamber through a series of staggered wire grids. This diffusion was counterbalanced by the slow convection of a mixture of different stoichiometry, which in Figure 3.3 is shown as pure air. The flame was ignited in the stratified mixture with a spark plug and propagated downward. An additional screen (indicated as "screen B" in Figure 3.3) was placed immediately above the spark plug to avoid upward propagation of the flame. The cross section of the chamber was $20X20\ mm^2$ and the flame propagated through a total length of $9\,cm$. A valve on the top of the chamber was opened right before ignition to avoid pressure build-up and effects of gas expansion during the propagation.

In order to experimentally measure the compositional stratification in the cold mixture, the methane was doped with acetone in a bubbler and measured using acetone planar laser induced fluorescence (PLIF). Flame speed was measured by monitoring the propagation with a Phantom V7.0 high speed camera at a rate of 1,000 frames per second and assuming that the front propagation speed was equal to the flame speed. This was a reasonable assumption given the small magnitude of the convective velocities used to establish the mixture stratification.

The flame was shown to propagate at a speed significantly higher than the adiabatic flame speed corresponding to the local equivalence ratio in areas of $0.5 < \phi < 0.7$. Also an extension of the flammability limit to $\phi = 0.4$ was observed for stratified

combustion. It was shown that these differences from quasi-homogeneous propagation at the local adiabatic flame speed were not controlled by the local equivalence ratio gradient, which measures the local variation of composition of the unburnt mixture. Rather, these differences were controlled by an integrated measure J of the large-scale compositional non-uniformities in the unburnt mixture that takes into consideration the whole history of flame propagation. The quantity J was defined as the product of the average equivalence ratio gradient times the ratio of the average over the local value of ϕ.

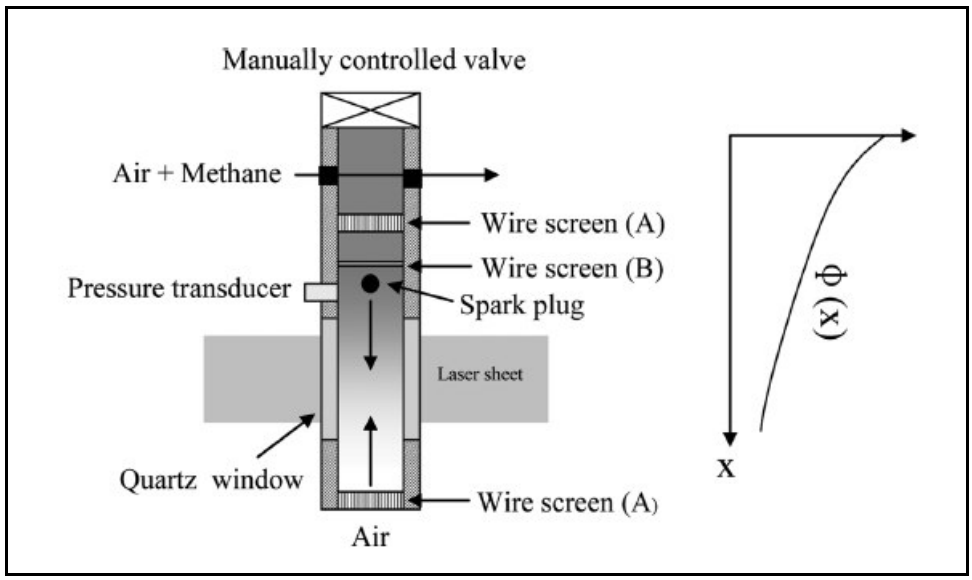

Figure 3.3. Optically accessible test chamber for stratified combustion (Kang and Kyritsis, 2005).

An experimental approach was developed by Galizzi, based on a laminar V-shaped flame configuration expanding in a non-homogeneously premixed flow. To study the influence of the stratification on flame front, the homogeneous case was first investigated as a reference. A lean premixed methane–air flame (equivalence ratio $\phi_0 = 0.58$) was stabilized on a 2 mm diameter rod at the exit of a wind tunnel. The V-shaped flame expanded in a laminar unconfined flow whose mean velocity was $5 m/s$ and residual turbulence intensity was about 0.4% (Galizzi and Escudie, 2006).

The stratified case, as shown in Figure 3.4, was obtained by means of a one-dimensional injection of pure methane, generated by an injection rail set in the upstream settling chamber at a fixed distance from the flame holder (ΔY). Because of the flame angle and the concentration profile in the stratification zone, the interaction evolved from a zone where the stratified front branch encountered a positive equivalence ratio gradient into a downstream region where the oblique front propagated in a field with negative equivalence ratio gradient.

Different techniques were employed to study the V-flame expanding in the stratified flow. Laser Doppler Anemometry (LDA) and PIV were used to gain the velocity field. The temperature field was detailed by means of Pt-Rh 30%/Pt-Rh6% thermocouple for

the burnt gas and a Ni-Cr/Ni-Al type for the temperature gradient zone. To describe the concentration field and the reaction zone location, a sampling probe connected to a probe analyzer was associated to CH* chemiluminescence measurements.

When the laminar V-shaped flame is expanded in the stratified flow defined previously, its shape was significantly modified. A particular pattern appeared as shown in Figure 3.5. The characteristic length scale δ_P, is of the same order of magnitude as the stratification thickness. The bulging shape called "peninsula", was separated from the oblique front by a vanishing strip of fresh gases. This particular shape was observed as a stationary topology. The first visible effect of the stratification was the increase in the flame surface by a flame front wrinkle.

The detailed analysis of temperature and CH* emission fields showed the existence of a diffusion branch inside the burnt gases. This diffusion front develops from an origin point that is located on the stratified front. It consumes excess fuel and oxygen. The oblique front evolves from a parallel to a normal interaction with the stratification. This transition is due to a change in flame speeds at the diffusion point. It induces an increase of the flame surface and the local reaction rate. The stabilized peninsula arises from the equilibrium between the tip location in a stoichiometric zone and the streamline deflection.

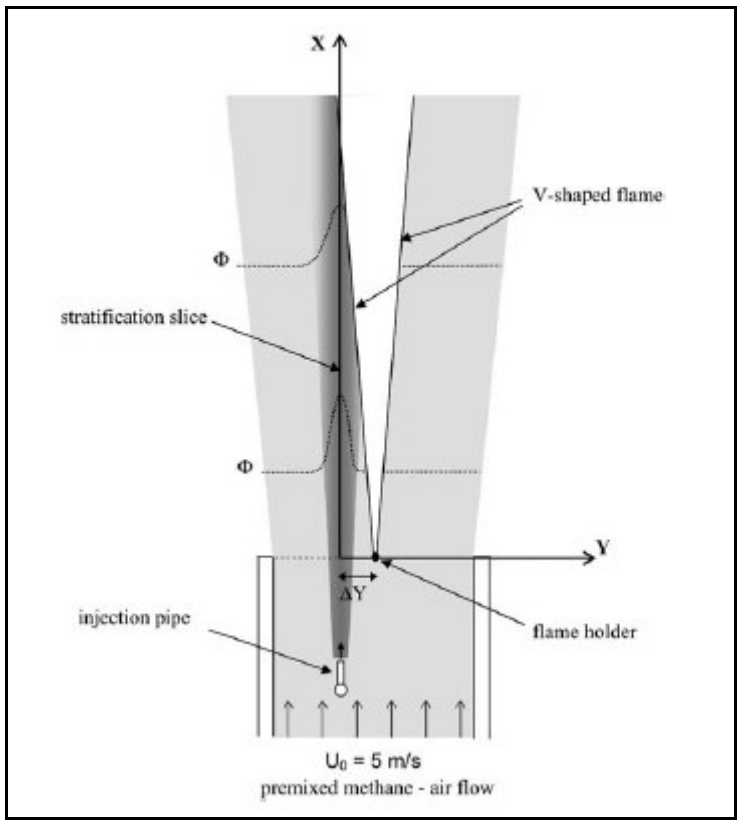

Figure 3.4. V-shaped flame burner (Galizzi and Escudie, 2006). The drawing shows the interaction between the stratified slice and the V-shaped flame.

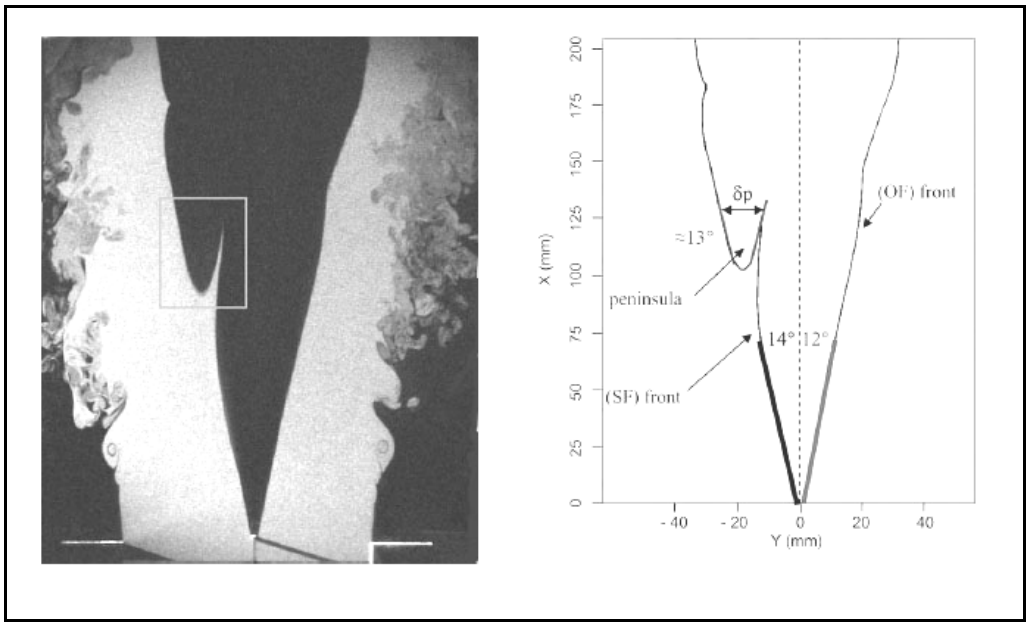

Figure 3.5. Visualization of the V-shaped flame for the stratified case (Galizzi and Escudie, 2006) and the mean characteristics of the stratified laminar premixed flame. With SF is indicated the stratified front while OF is used for opposite front.

Degardin too studied the effect of fuel concentration stratification on a V-shaped flame. "The experimental set-up (Figure 3.6) consisted of a vertical wind tunnel adapted to stationary combustion. An upstream mixing chamber composed of nine parallel vertical compartments enabled various equivalence ratios profiles to be obtained" (Degardin et al., 2006). Each compartment was made of 13 gas cooker injectors screwed up on the injection ramp. The free jets of gas were then mixed with air flow and homogenized with small glass marbles. The flow was laminarized with honeycomb structure and conducted to the study zone by a convergent nozzle. At the exit of the convergent, a V-shaped flame was stabilized on a heated rod situated on the central axis. Flames with fixed equivalence ratio were considered as reference conditions, then various decreasing equivalence ratio profiles were produced.

In these experiments simultaneous Rayleigh scattering technique and Acetone PLIF to measure the temperature and the fuel mole fraction fields in the preheat zone of the flame were used. The temperature dependence of the acetone fluorescence signal for a fixed excitation wavelength could be corrected by the local temperature. Simultaneously, the influence of the Acetone cross-section on the Rayleigh scattering measurements could be corrected by the local acetone fraction.

It has been observed that in the homogeneous conditions the flame thickness increased with a decreasing methane mole fraction and, by extension, equivalence ratio. For the stratified conditions, the flame thickness also increased with a decreasing methane mole fraction, but with a moderate slope. According to these results it can be assumed that the flame thickness becomes less sensitive to the methane mole fraction near the flame front (Degardin et al., 2006).

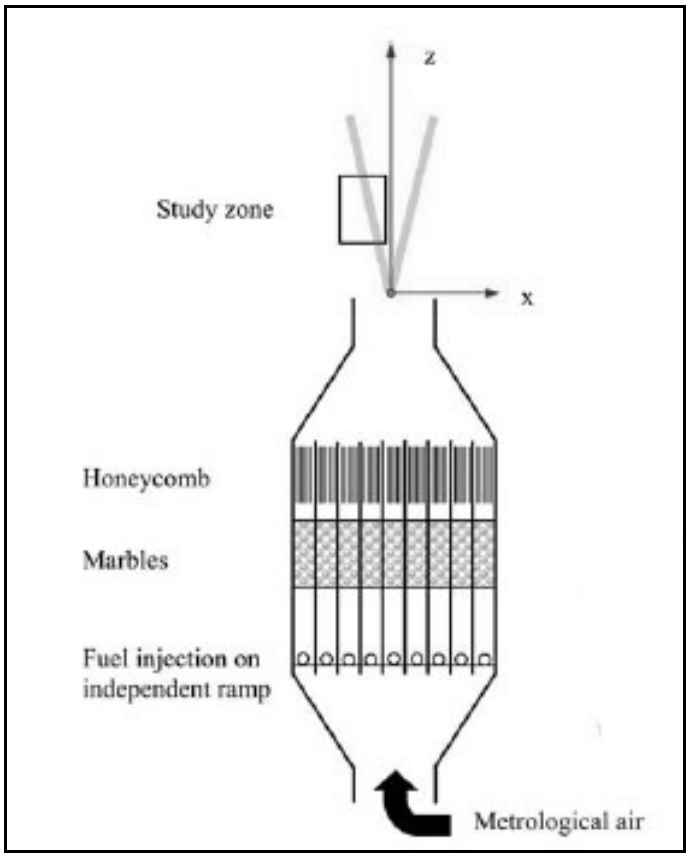

Figure 3.6. Schematic of the vertical wind tunnel used by Degardin to study the effects of equivalence ratio stratification on V-shaped flames (Degardin et al., 2006).

3.4 Objectives and Novelty of a Weak Swirl Stratified Burner

The understanding of lean partially premixed flames propagation is important because it is closely related with reduction of combustion emissions in turbines and direct injection engines. The flow conditions in industrial applications are turbulent, but the difficulty of generating stationary turbulent stratified flames, reduced the experimental analysis to the laminar case. Although the comprehension of fuel stratification effects on laminar flames is essential, also of fundamental importance is the consideration of the combined action of turbulence and equivalence ratio gradients. To answer these requirements, it has been necessary to build a burner capable of producing stationary flames propagating in lean stratified turbulent flows. The equivalence ratio stratification had to be controlled to consider various gradients in fuel concentration in a well defined area of the oncoming flow. At the same time, the burner needed to be capable of operating at various turbulence levels.

The choice of using an open flame burner to produce such flames has been driven by the convenience of avoiding any boundary surface that could reduce the optical access of laser diagnostics tools. This is the reason why previous sections have considered only the past research for open flame burners. The choices of experimental research examples in turbulent combustion have been further reduced by the choice of considering stationary flames propagating in isotropic turbulent conditions. There are several examples of open flame burners capable of producing stationary turbulent flames (Al-Abdeli and Masri, 2003a; Al-Abdeli and Masri, 2003b; Kalt et al., 2002; Landenfeld et al., 1998; Masri et al., 2000; Masri et al., 2004; Schmittel et al., 2000), but the flames are generally stabilized using recirculation zones with the main effect of producing anisotropic turbulence. The target has been of analyzing flame fronts as close as possible to the theoretical conditions of planar flame propagating in an isotropic turbulent oncoming flow, a further reason to avoid the consideration of burners characterized by recirculation.

The analysis presented in the previous sections showed that the best solution to produce stationary flames propagating in isotropic turbulence is the use of weak swirl as stabilization mechanism coupled with the turbulent generators presented by Videto and Santavicca (Videto and Santavicca, 1991). This has been the solution adopted by Cheng and O'Young (Cheng et al., 2002; O'Young and Bilger, 1997). To this configuration it has been necessary to implement the capability of generating stratified flows. The stratification in fuel concentration has been obtained splitting the oncoming flow in annular co-flows characterized by different values in equivalence ratio. The mixing region defined the stratification area characterized by a controlled fuel concentration gradient. In the following chapter a more detailed description is given of the design process and the construction solutions of the stratified turbulent burner.

The flames have been analyzed using laser diagnostics techniques. In order to define the characteristics of the oncoming flow, it has been fundamental to gain information about velocities and fuel concentration distribution. The first objective was accomplished using Stereoscopic PIV that allowed instantaneous velocity fields to be obtained. This data was necessary for a description of the turbulence characteristics of the oncoming flow and for the definition of the burning velocity. The fuel concentration was determined through PLIF using acetone as a fuel tracer. Instantaneous temperature fields have been obtained using Rayleigh scattering that allowed the analysis of flame front properties such as curvature and flame thermal thickness.

The information of velocities, equivalence ratio distribution and temperatures has been used to analyse the effects of different gradients of fuel concentration on quantities that characterize flame front propagation: burning velocity, flame front curvature and flame thermal thickness. Because the flame wrinkling is a random process (Cheng et al., 2002), it required a statistical analysis of a sizable data set. The experimental data have been collected in sets of minimum 200 images for each condition analyzed. The following chapters fully describe the experimental procedure that has been defined in its fundamental steps here.

4 BURNER DESIGN AND OPERATIONAL CONDITIONS

It has been explained in the previous chapter that for obtaining the needed experimental data on lean turbulent stratified flames, the burner must be capable of generating flames with the following characteristics:

1. Lean flames with a region in which the concentration of the combustible mixture is characterized by a controlled gradient.
2. Flames must be turbulent with high turbulence intensity, while it has to be possible to vary the level of turbulence intensity itself.
3. Flames must freely propagate in the flow without constraint to allow the application of laser diagnostic techniques.

Figure 4.1 presents the principle scheme of the burner capable to produce flames fulfilling the specifications listed above. The flame is stabilized using an external swirl flow of air generated by eight tangential jets. It is possible to control the flow rate through the tangential jets and this allows the change in the swirl number associated with the outlet flow. Turbulence plates are used to produce the high turbulence intensity required. They consist of a sleeve, a perforated plate which has a ring of holes at a defined diameter followed by a contraction. The combustible mixture is forced to travel through the holes and consequently to strike against the internal surface of the nozzle to produce high intensity turbulence. The turbulence intensity can be varied changing the flow rate through the turbulence plates. The two combustible mixture flows (indicated in the burner scheme as Flow 1 and Flow 2) are characterized by two different equivalence ratio values. An annular mixing layer is generated in the mixing region between the two flows. Changing the equivalence ratio values associated with the two flows it is possible to vary the gradient of the distribution of fuel concentration. Both flows are lean in fuel concentration.

In Figure 4.2 the vertical section of the burner assembly is shown. The three flows (Flow 1, Flow 2, and Air) follow three separate paths until they reach the mixing section just before the burner outlet. Flow 1 enters the inner sleeve through a single central pipe, while Flow 2 and Air are distributed into the respective sleeves using two manifolds. The manifold of Flow 2 is connected with 4 pipes while the manifold for Air with eight pipes. This solution allows a uniform distribution of the flow rate within the cross section area of the sleeves. Flow 1 and Flow 2 are forced through the turbulence plates and subsequently into the nozzles section. The external flow (Air) is forced to pass trough the glass beads in order to improve the flow distribution uniformity within the nozzle section. The turbulence generators and swirl section design are going to be explained in more detail.

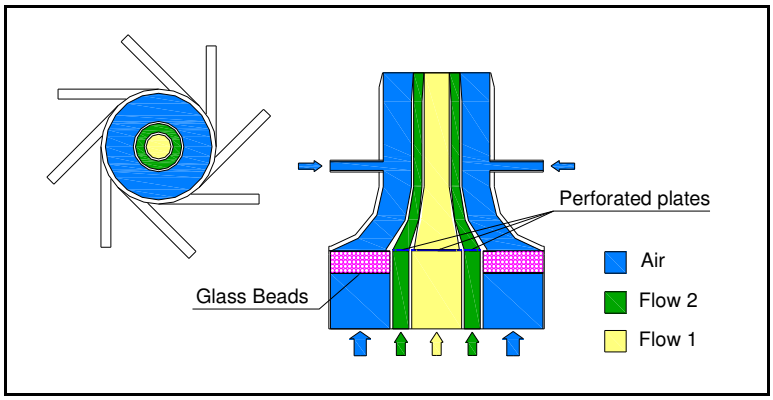

Figure 4.1. Burner principle scheme. Top view and vertical section of the burner nozzle.

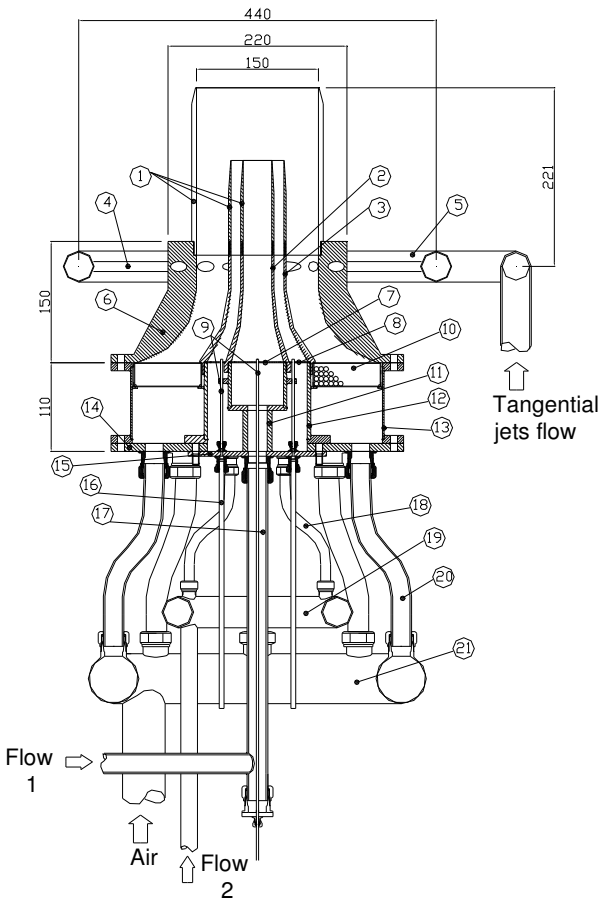

LEGEND	
N.	Description
1	Collars
2	Inner nozzle
3	Annular nozzle
4	Tangential jet
5	Tangential jets air manifold
6	Swirl generator main body
7	Inner turbulence plate
8	Annular turbulence plate
9	Seeding lines
10	Glass beads
11	Inlet sleeve
12	Annular sleeve
13	Outer sleeve
14	Air flow injection plate
15	Flows injection plate
16	External seeding line
17	Inner combustible flow pipe
18	Annular flow pipes
19	Annular combustible manifold
20	Air flow pipes
21	Air flow manifold

Figure 4.2. Vertical section of the burner assembly

4.1 Turbulence Generators

The first predecessor of the turbulence generator system designed is the turbulent flow system developed by Videto and Santavicca (Videto and Santavicca, 1991). Their device consists of a squared inlet section terminated by a blockage plate which has a pair of parallel, 0.8mm wide straight slots at 39 mm apart. Downstream of the slots there is a one-dimensional contraction in the horizontal direction which leads to a 150 mm long outlet section. An adaptation of the linear slot design was applied by Bedat and Cheng where the geometry of their burner is axis symmetric. It has a blockage plate with a 0.8 mm wide, 107 mm diameter circular slot. Downstream of the plate is a contraction of 140 mm diameter converging to a 50 mm diameter which leads to a straight nozzle 233 mm long (Bedat and Cheng, 1995). A further variation introduced by O'Young and Bilger the substitution of the circular slot by a ring of small holes (O'Young and Bilger, 1997).

The operating principle behind the turbulence generation is based upon the breaking up of large scale vertical motions (Videto and Santavicca, 1991). Premixed air and fuel flowing through the relative sleeve are forced through the perforated plate and vortices are formed by the high velocity jets exiting the ring of small holes. The jets turn inward due to their impact with the inner surface of the contraction. As the flow convects through the nozzle, the vortices breakdown and their energy are converted to turbulent fluctuations.

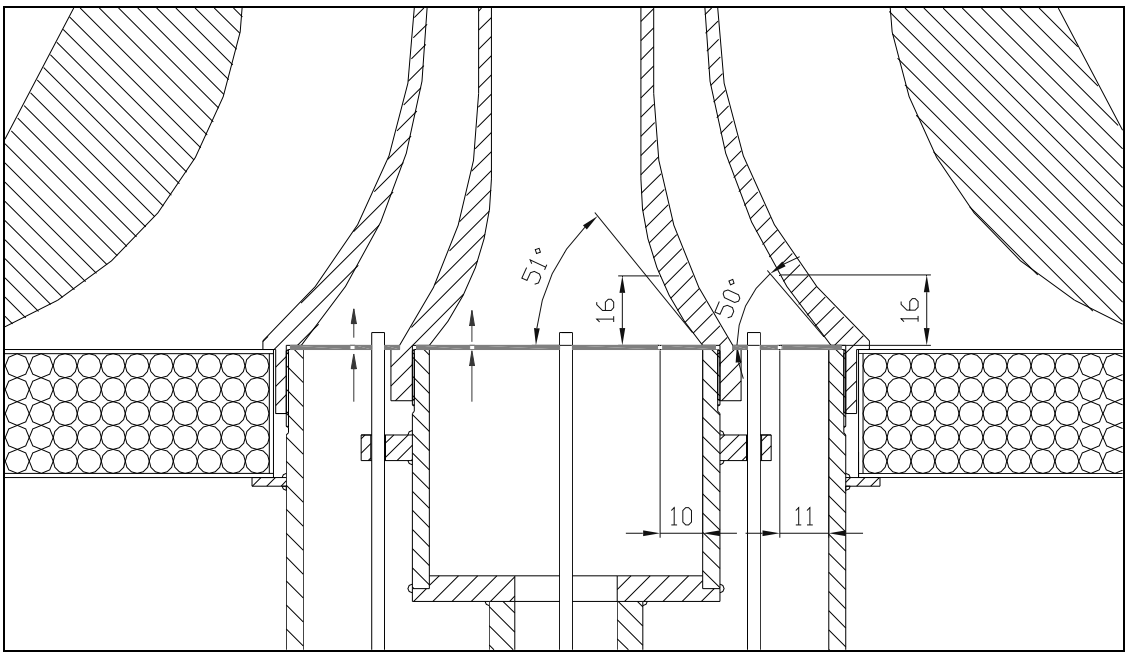

Figure 4.3 Turbulence generators vertical section.

In Figure 4.3 is presented the section on a vertical plane of the turbulence generators designed, while in Figure 4.4 are shown the turbulence plates dimensions. In Figure 4.5 are displayed the fundamental dimensions used in the three burner designs mentioned

previously. The objective has been to maintain, as close as possible, the same dimensions as other workers in order to generate high turbulence levels demonstrated by other researchers.

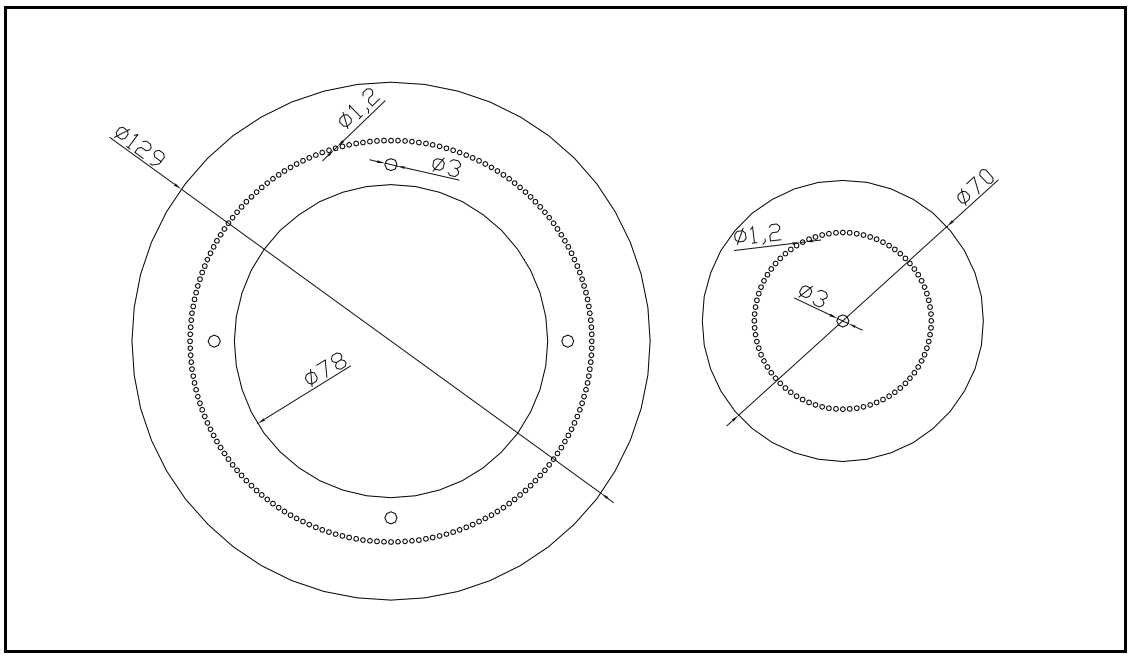

Figure 4.4 Turbulence plates dimensions and holes distribution.

	Videto	**Bédat**	**Current design Flow 1**	**Current design Flow 2**
Symmetry	Planar	Axial	Axial	Axial
Y-Section	Rectangular	Round	Round	Round
Dj (mm)	0.8	0.8	1.2	1.2
a (mm)	13	13	10	12
b (mm)	16.6	16.6	16	16
q (deg)	52	52	51	50

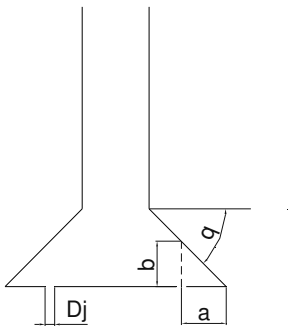

Figure 4.5. Comparison of the fundamental dimensions of the current burner with its predecessors.

4.2 Flame Stabilization using Weak Swirl

Flame stabilization by swirl is a common feature of many turbines and furnaces. Most of these enclosed combustors require relatively intense swirl to induce recirculation zones in order to steady reactive flows. When rotating motion is imparted to a fluid upstream of an orifice, the fluid flow emerging from the orifice has a tangential velocity component in addition to the axial and radial components of velocity (Beer and Chigier, 1972). The presence of the swirl results in the setting up of radial pressure gradients which, in turn, influence the flow field. In the case of strong swirl, the adverse axial pressure gradient is sufficiently large to result in reverse flow along the axis and a setting up of an internal recirculation zone (Schmittel et al., 2000).

In weak swirl the axial pressure gradients are insufficiently large to cause internal recirculation. Swirl has the effect of increasing the rate of velocity decay on the burner outlet section. For a region not far downstream of the burner it has been found that weak swirl causes the mean axial velocity to decrease almost linearly (Chan et al., 1992; Cheng, 1995; O'Young and Bilger, 1997; Starner and Bilger, 1986). This provides a stable environment for the flame ignited in the core flow of air and fuel mixture to maintain itself at a position where the local mass flux equals the burning rate (lifted flame). The flame flow field is not influenced by physical boundaries, as in the case of stagnation point flames, rod-stabilized v-flames or Bunsen flames and it gives free access to laser diagnostics.

Even though swirl is vital to flame stabilization, the flame zone and its properties are not affected by shear associated with swirl (Chan et al., 1992).The flame thus provides the closest approximation to the planar one-dimensional premixed turbulent flame on many theoretical models.

Two sectional drawings of the swirl generator of the burner designed are shown in Figure 4.6. The swirl number, S, for this configuration is given by the ratio of axial flux of angular momentum to axial flux of linear momentum divided by the burner radius (Beer and Chigier, 1972). Claypole and Syred had shown that with a similar configuration S can be conveniently obtained from the burner geometry and mass flow rate by (Claypole and Syred, 1980):

$$S = \frac{\pi r_{tg} R_{ax}}{A_{tg}} \left(\frac{m_{tg}}{m_{tg} + m_{ax}} \right)^2 \qquad (4.1)$$

where r_{tg} is the radius of the tangential inlet, R_{ax} is the radius of the burner outlet, A_{tg} is the total cross section area of the tangential inlets, m_{tg} and m_{ax} are the tangential and the axial mass flow rate respectively.

Varying the flow rate in the tangential jets it is possible to change the swirl number associated with the flow.

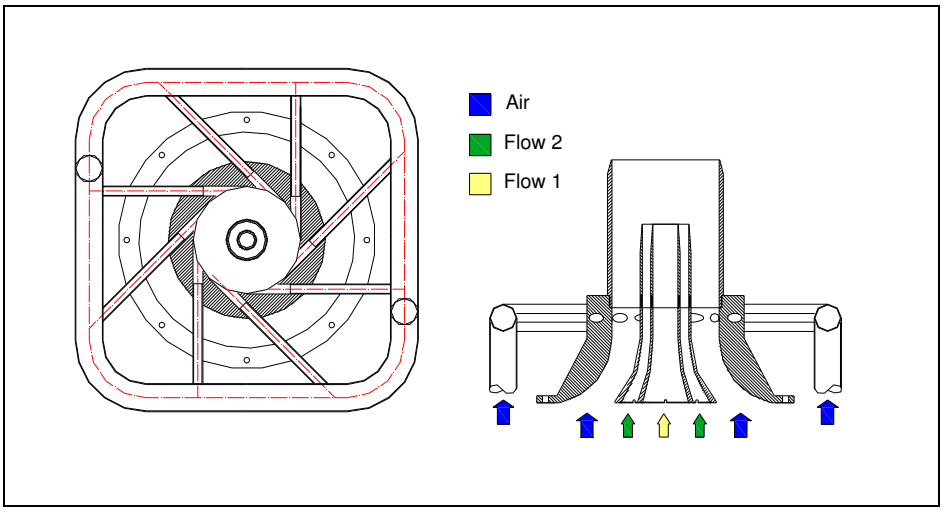

Figure 4.6. Section drawings of the swirl generator.

4.3 Outlet Configurations

The burner has been fitted with two outlets having different geometry. They are both shown in Figure 4.7. To simplify the notation they are identified with the names: Collar 1 and Collar 2.The configuration called Collar 1 has been the first solution adopted in the burner design. In order to have information about the oncoming flow characteristics enabling the comparison of experimental results with computer modelling, the second configuration adopts a collar made of transparent fused silica. In the case of Collar 2 it is then possible to collect data about velocities and equivalence ratio distribution before the flow exits from the burner outlet. In order to contain the cost of the experiments it has been decided to use components already available in the lab and for this reason Collar 2 does not have the same dimensions of Collar 1. Collar 2 is characterized by a smaller diameter and a longer vertical length. Two pictures of the two different configurations are presented in Figure 4.8.

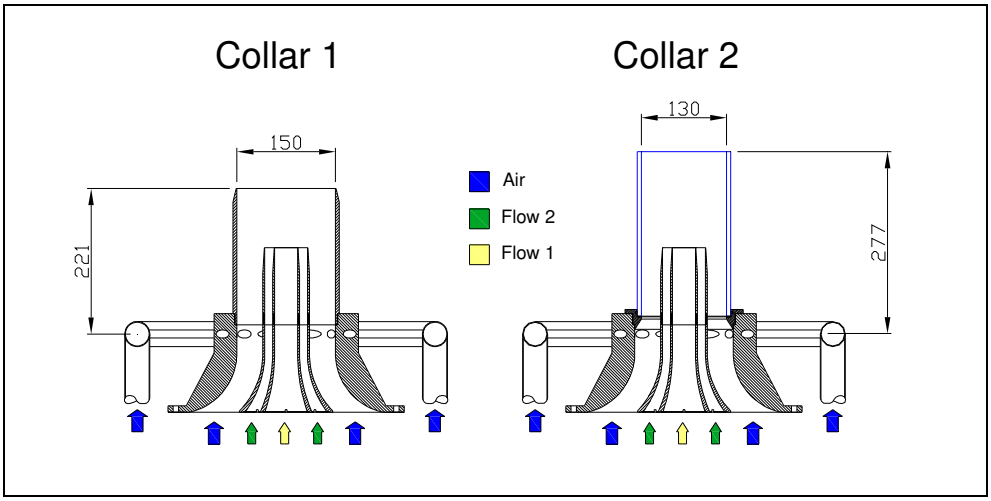

Figure 4.7. Outlet configurations dimensions.

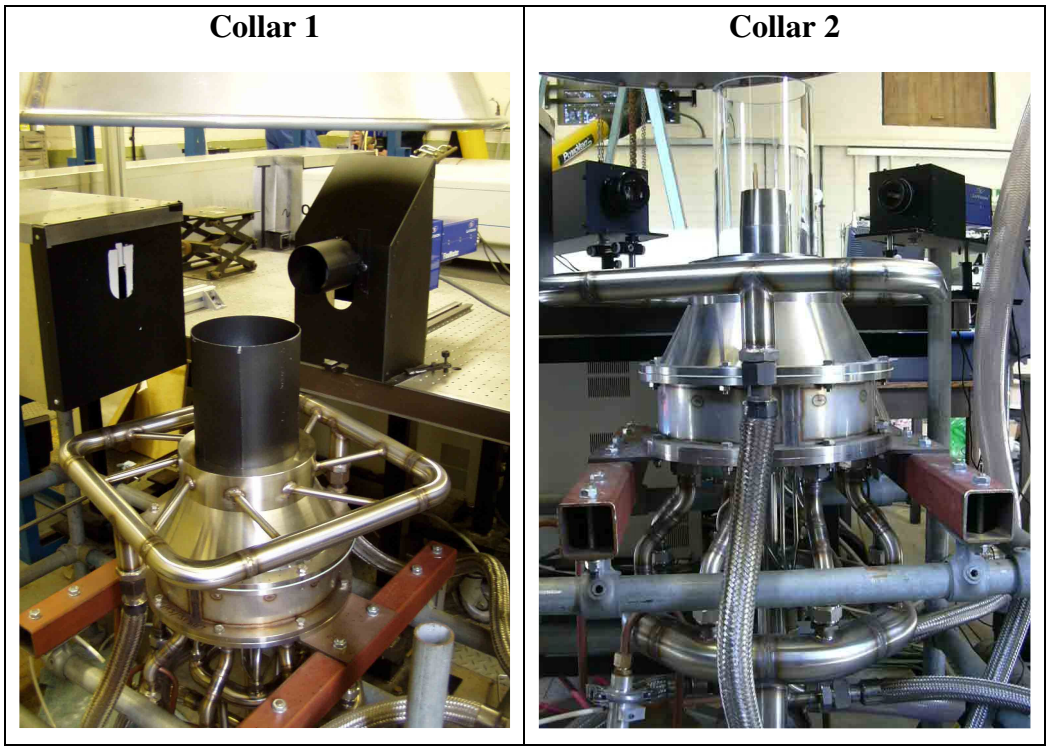

Figure 4.8. Pictures of the burner in both outlet configurations.

4.4 Gas Flow Support

The gas flow support supplies reactants to the burner. The burner head needs to be supplied by four different flows:

- Flow 1 at equivalence ratio ϕ_1
- Flow 2 at equivalence ratio ϕ_2
- Tangential jets air flow
- Axial component of the air swirl flow

Figure 4.9 presents the gas flow support scheme for supplying the combustible mixtures of Flow 1 and Flow 2. Methane is piped from a bottle source while the air comes from a compressor. The flow rate through each line is measured using critical flow nozzles. The required amount of methane and air is delivered in the two separate mixing chambers in order to produce the determined flow rates for Flow 1 and Flow 2. Non-return valves are included in order to prevent the reactants mixing before entering the mixing chamber.

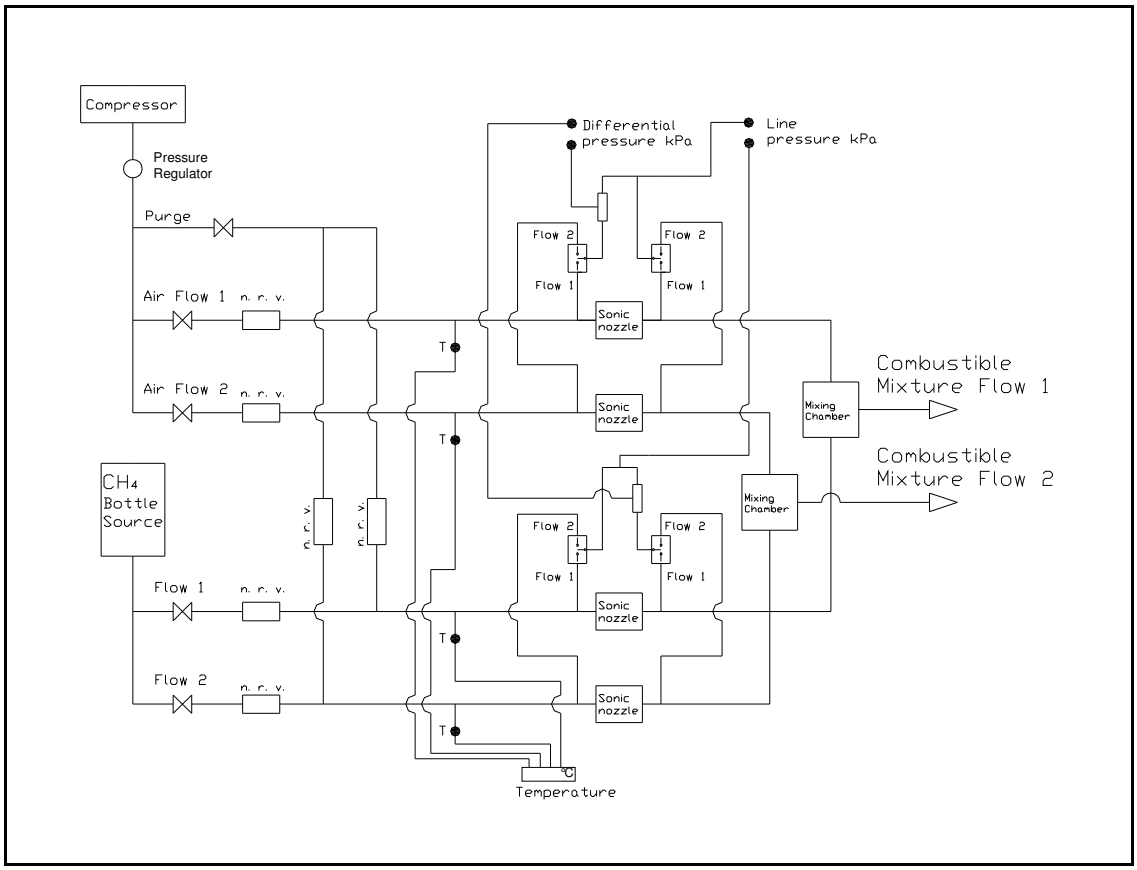

Figure 4.9 Gas flow support scheme for supplying the combustible mixtures of Flow 1 and Flow 2.

The tangential jets air flow is supplied from the compressor through a floating element flow-meter. The axial flow component of the swirl air is delivered from a blower. The flow rate is deducted measuring the pressure drop associated with a bell mouth installed on the blower intake (Figure 4.10).

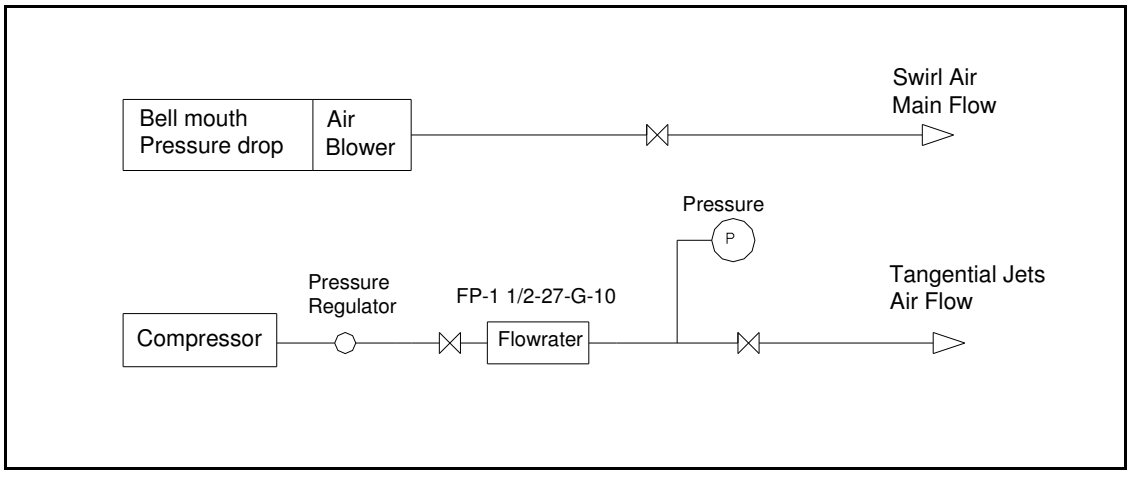

Figure 4.10 Gas flow support scheme for supplying the air flow components of the external swirl flow.

The main objective of the research is the analysis of the fuel stratification effects on flame front propagation. It is then of fundamental importance to accurately measure the reactants flow rates. Calibrated sonic nozzles can measure the flow rate with an error inferior to 1% while flow-meters with floating elements are associated with an error level of around 3%. The sonic nozzles have been designed according to British Standards indications. The flow rate is obtained by sending a compressed flow through a nozzle sized to accelerate the flow to mach one and measuring the static pressure upstream the nozzle. The static pressure downstream is also measured to ensure that the nozzle stays choked. In these conditions the flow rate depends only on the value of the upstream pressure. A thermocouple is fitted just upstream of the nozzle to measure the temperature of the flow.

The sizes of the sonic nozzles are calculated in relation of the flow rate needed and knowing the available range of pressure of the gas sources. The following equation has been applied (British Standards Institution 1991):

$$\dot{m} = A_{th} C C' P_{up} \Big/ \left(R T_{up} / M_{gas} \right)^{\frac{1}{2}} \qquad (4.2)$$

Where $\dot{m}$ is the mass flow rate, A_{th} is the cross section area of the nozzle throat, C is Venturi nozzle discharge coefficient, C' Venturi nozzle critical flow function, P_{up} is the upstream static pressure, R is Boltzmann's constant, T_{up} is the upstream temperature, M_{gas} is the gas molar weight. The relation between the diameter of the nozzle throat (d_{th}) and the cross section area A_{th} is:

$$A_{th} = \frac{\pi}{4} d_{th}^2 \qquad (4.3)$$

From Equation (4.2) it is possible then to obtain the diameter of the sonic nozzle throat:

$$d_{th} = \sqrt{\frac{4 \dot{m} \sqrt{T_{up} R / M_{gas}}}{\pi P_{up} C C'}} \qquad (4.4)$$

The values of the Venturi nozzle critical flow function C' are obtained using tables in the British Standards section for measurements in closed conduits (British Standards Institution 1991). This coefficient is related to the type of fluid considered and its thermodynamic conditions. It is displayed for different fluids against pressure and temperature.

The Venturi nozzle discharge coefficient C is related to the type of flux that is present in the nozzle throat and to the geometry of the nozzle throat. In the British Standards section for measurements in closed conduits a table that displays C against the Reynolds number is present and those values have been used in the design stage to select the throat diameter values (British Standards Institution 1991). These have been chosen in order to cover the whole range of flow rates necessary for the experiments. Once the sonic nozzles were built, they have been calibrated to associate to each of them a particular value of the discharge coefficient. For the calibration procedure the

gas flow rate through the sonic nozzle has been measured by a bell-prover. Using Equation (4.2) it is possible to calculate the value of the Venturi nozzle discharge coefficient:

$$C = \left(\frac{R T_{up}}{M_{air}} \right)^{\frac{1}{2}} \dot{m} / \left(P_{up} \, A_{th} \, C' \right) \qquad (4.5)$$

For each sonic nozzle the values of C have been calculated at different upstream static pressures through the range between 1 bar and 7 bar (gauge pressure). In Appendix A the results of the calibration procedure are reported. The measurement error has been calculated as the root mean square of the variance for the sample values of C collected for each nozzle. The error is the sum of two components. The first is related to the assumption that the value of C is constant for the range of pressure considered and it defines the precision of the sonic nozzle flow rate measure. The second component is associated with the bell-prover system. The error increase with bigger throat diameter because the flow rate associated is bigger and this infers an increased error in the measurements detected through the bell prover. This component is at its minimum for smaller diameters when the overall error is less than 1%. The first component of the error is the one associated to the precision of the sonic nozzle flow rate measurement, it does not depend on the size of the throat diameter and it is consequently less than 1%.

4.5 Burner Operational Conditions

The gas support system has been designed in order to control the following parameters:

- Volumetric flow rate
- Equivalence ratio ϕ_1 for Flow 1
- Equivalence ratio ϕ_2 for Flow 2
- Flow swirl number S

The volumetric flow rate allows control of the level of turbulence within the flow. The increase in volumetric flow rate determines the generation of higher turbulence because of the faster velocity at which the jets emerge from the perforated plates and strike on the nozzle inner surface. According to the working principle of the turbulence generators as the flow convects through the nozzle, the vortices breakdown and their energy is converted to turbulence fluctuations. It follows that jets emerging at higher speeds are associated with increased levels of kinetic energy to be converted into turbulence fluctuations.

In order to analyze the effect of fuel stratification on flame propagation at different values of turbulence intensity, three reference values of volumetric flow rate have been considered. These three conditions are associated with three different values of the average velocity at which Flow 1 and Flow 2 emerge from the respective collar before being mixed with the external swirl flow. After taking in consideration the volumetric flow rates used by previous researchers (Chan et al., 1992; O'Young and Bilger, 1997)

and the capabilities of the gas support system, the following velocities have been chosen: 6m/s, 7m/s and 9m/s. In order to simplify the explanation while referring to the three different conditions now defined, will be used this notation:

- Bulk Flow 1: flow average velocity 6m/s.
- Bulk Flow 2: flow average velocity 7m/s.
- Bulk Flow 3: flow average velocity 9m/s.

Once the reference conditions were defined for the volumetric flow rate, the next step was to determine the combinations of equivalence ratios (ϕ_1 and ϕ_2) that were compatible with a freely propagating flame. The swirl flow is a means to stabilize the flame and then the value of S varies according to this purpose. It is important to preserve the same characteristics of the incoming flow, to avoid variations on the values of the swirl number for the combinations of equivalence ratios considered. The results can be easily summarized using a matrix like output as presented in the following figures. They are called stability maps because they define in which condition it is possible to generate a freely propagating flame on the top of the burner outlet. The value of the swirl number that is associated with stable flames has been kept uniform at the value of S = 0.09. It has been used the letter "S" to indicate when a stable flame can be generated and the letter "X" otherwise. The empty cells are associated with combinations that have not been tested. For each "Bulk Flow" condition six flames have been chosen, they are differentiated by regular changes in the equivalence ratios associated with Flow 1 and Flow 2. The flames selected are indicated with letters from A to F for each bulk flow velocity considered.

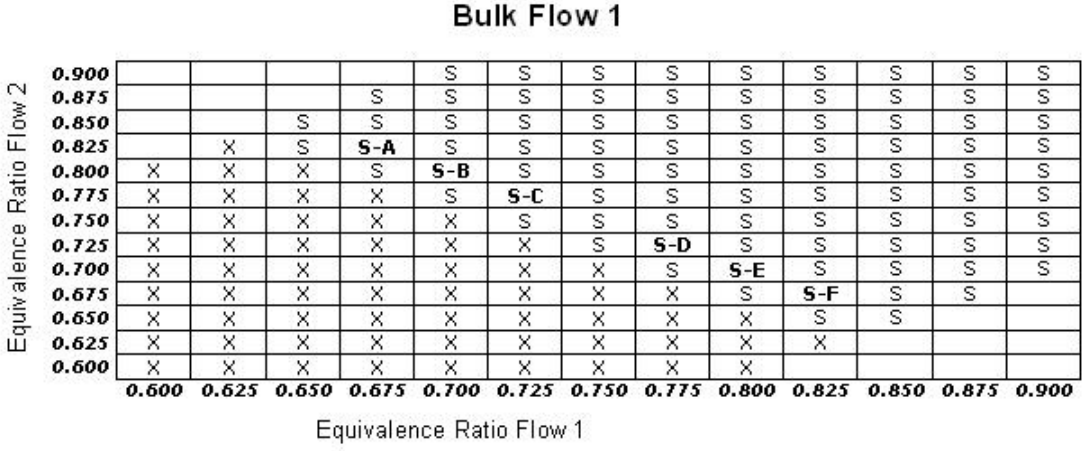

Figure 4.11. Flames stability map for Collar 1 in the conditions of Bulk Flow 1. "S" indicates stable flame and the letters from "A" to "F" the flames selection for the future analysis.

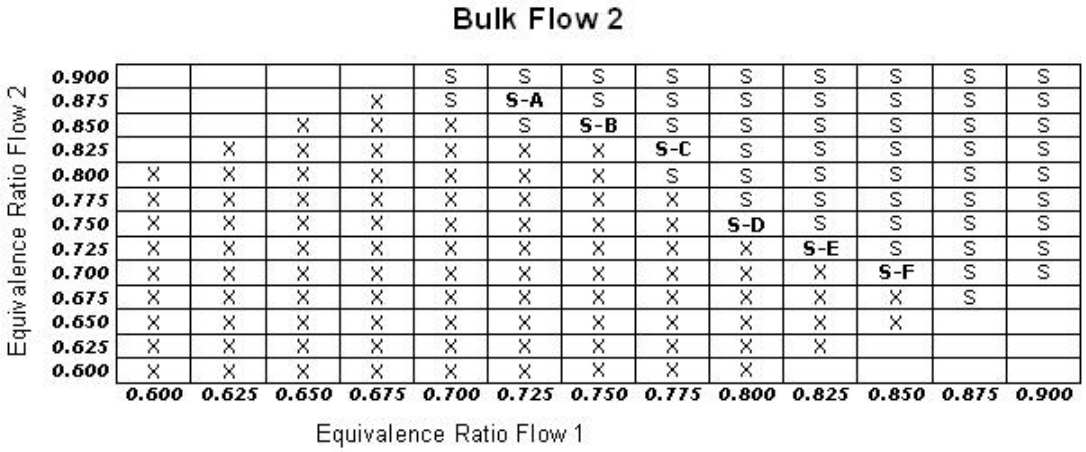

Figure 4.12. Flames stability map for Collar 1 in the conditions of Bulk Flow 2.

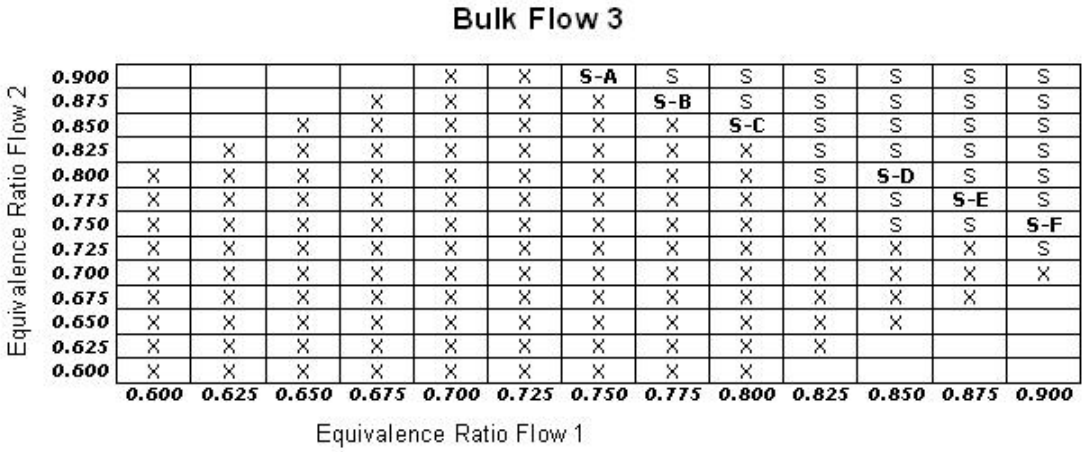

Figure 4.13. Flames stability map for Collar 1 in the conditions of Bulk Flow 3.

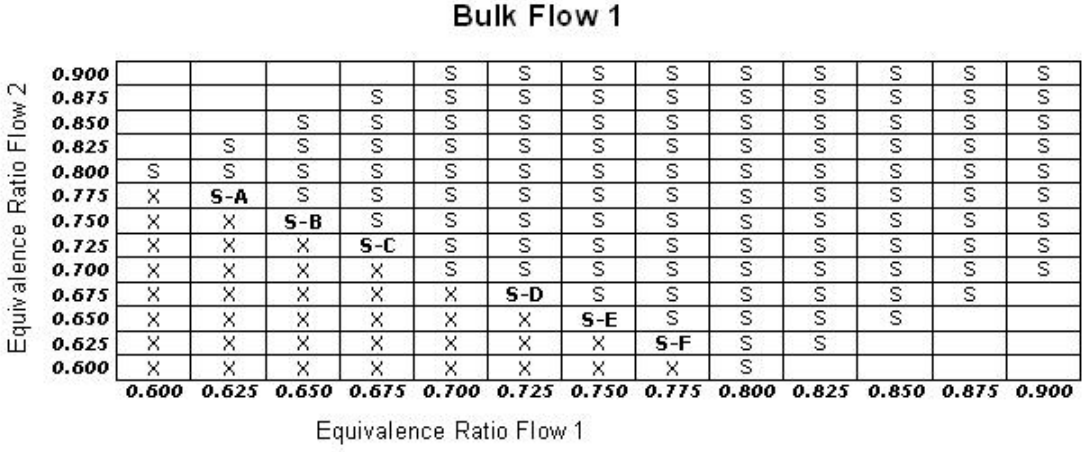

Figure 4.14. Flames stability map for Collar 2 in the conditions of Bulk Flow 1. "S" indicates stable flame and the letters from "A" to "F" the flames selection for the future analysis.

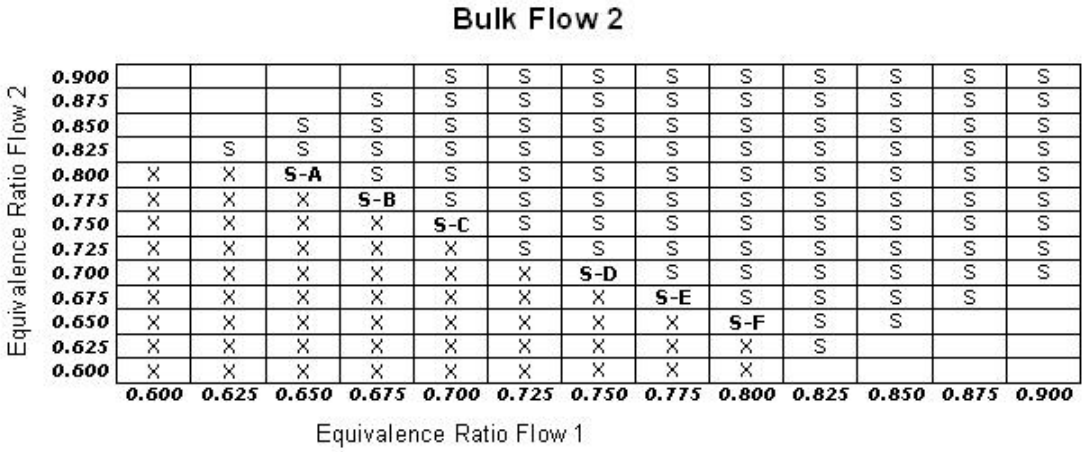

Figure 4.15. Flames stability map for Collar 2 in the conditions of Bulk Flow 2.

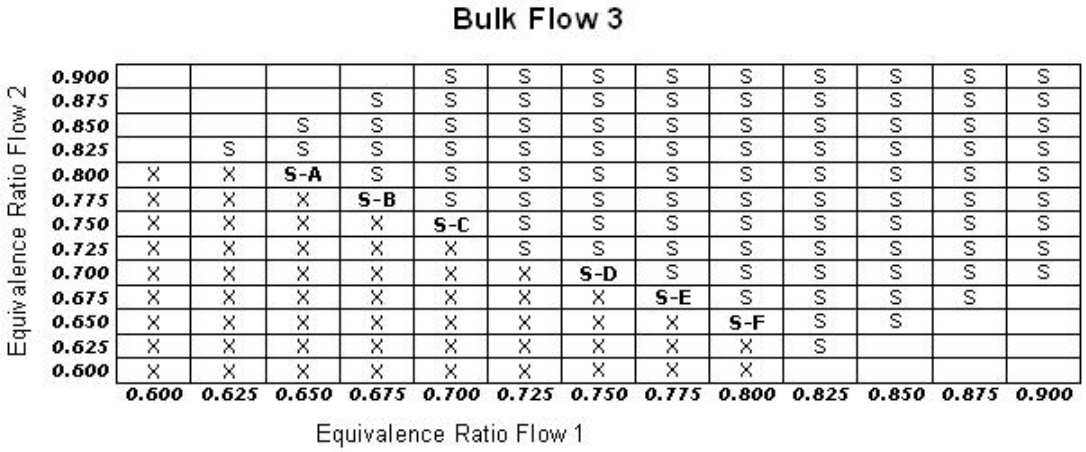

Figure 4.16. Flames stability map for Collar 2 in the conditions of Bulk Flow 3.

A picture of one of the flames produced by the burner is shown in Figure 4.17. The flames are lifted around 4 cm above the burner outlet. The flames freely propagate in the flow without constraint and this allows an easy access for application of laser diagnostics techniques.

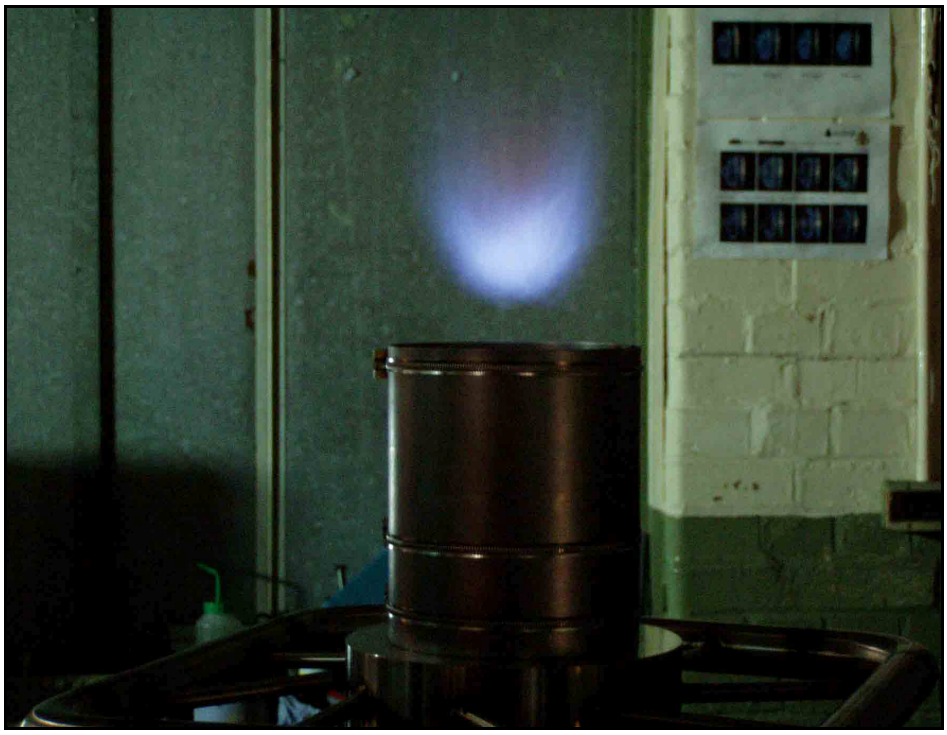

Figure 4.17. Picture that shows the nature of the flames produced by the burner.

5 PIV IMAGING

The chapter describes the application of PIV in order to gain the instantaneous velocity fields. For Collar 1, 2D-PIV has been used, while for Collar 2, stereoscopic PIV has been applied. For the latter the analysis has been performed at the flame height and inside the collar of fused silica. The experimental setup will be described along with the mathematical procedures used to process the raw images to obtain the velocity fields. The chapter concludes with the analysis of the oncoming flow kinematic characteristics. The chapter describes particularly the experimental approach used for the stereoscopic PIV because 2D-PIV can be considered as a reduced system that uses only one camera instead of two and produces velocity measurements that contain information only about two of the three components.

5.1 Experimental Apparatus

The experimental apparatus used for stereoscopic PIV is shown in Figure 5.1. It used a Nd:YAG Laser (Quanta Ray PIV-400-10) as laser source. The Nd:YAG Laser has been modified such that it can operate in a double pulse mode. The active medium is neodymium-doped yttrium aluminium garnet which, combining with wavelength-selective optics, emits laser light at 1064 nm (infrared) wavelength. An electro-optical Q-switch enables the laser to release short pulses of high intensity light at around 8ns pulse width and 300 mJ of energy. The output end of the Nd:YAG laser is coupled with a harmonic generator set for producing a second harmonic wavelength of 532nm (green). The final output beam has a diameter approximately 8 mm and 160 mJ per pulse (measured), with most of the light at 532 nm in addition to some residual infra-red light. The time between the two laser pulses was chosen to be $50\,\mu s$.

A front coated dichroic mirror at 45° incident angle is used to steer the output light from the second harmonic generator of the Nd:YAG laser. The 532 nm component of the beam is reflected horizontally in the perpendicular direction. This beam is reflected again perpendicularly by a second dichroic mirror of the same type mounted on an adjustable holder to steer the beam towards the burner at some 1.5 meters away. A fused silica positive cylindrical lens (150mm focal length) and a glass positive spherical lens (1000mm focal length) have been used to produce a laser sheet 40mm high with an average thickness of 1mm.

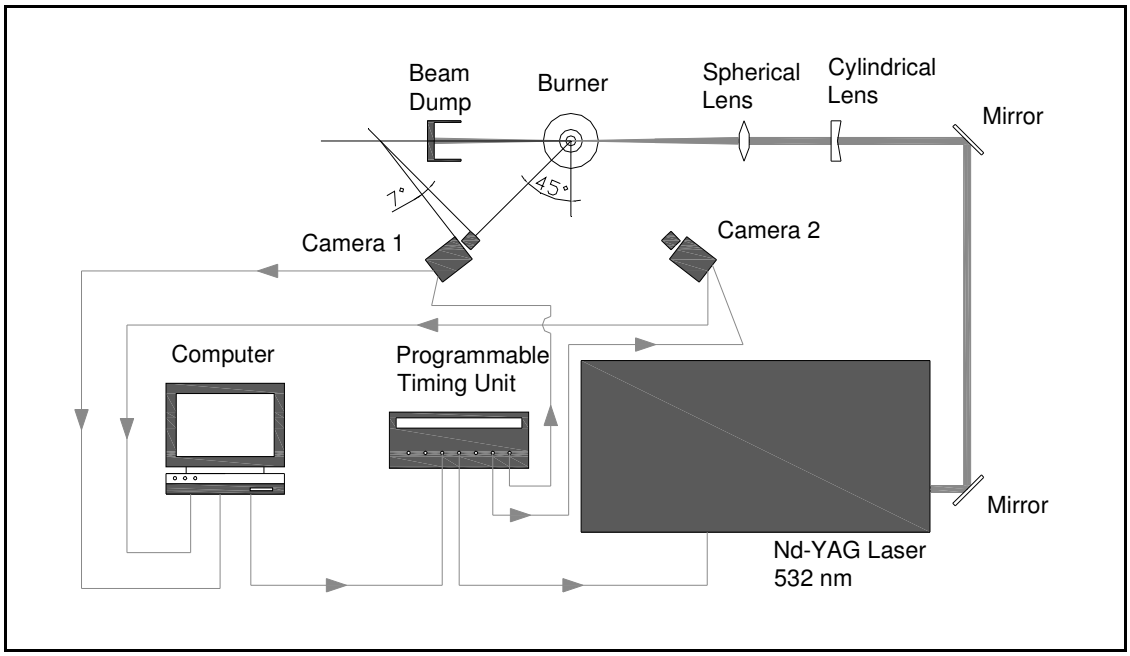

Figure 5.1. Experimental apparatus of the stereoscopic PIV system.

The images have been recorded using two La Vision Flow Master cameras with Nikon 50mm focal length multi-element lenses mounted on the camera head. The two cameras have been arranged in stereoscopic configuration with a 45° angle from a line perpendicular to the laser sheet plane and passing through the burner axis. The angle between the lenses plane and the chip plane was 7° according to the Scheimpflug criterion. Both cameras were on the same side of the laser sheet. For this reason the light scattered towards "Camera 1" was more intense than "Camera 2", two different apertures of the camera lenses have been used, respectively f/1.4 for the former and f/1.2 for the latter.

Seed particles of TiO_2 with an average diameter of $3\mu m$ were added to the flow. The TiO_2 particles have been injected only in the two combustible mixture flows just after the perforated plate of the turbulent generator. The seeding lines are shown in Figure 4.2 with part number 16. The software used for controlling the hardware while collecting the images was DaVis 7.1 from La Vision. The same software has been used for processing the raw images in order to gain the velocity vector fields.

For the burner configuration called "Collar 1", 2D-PIV experiments have been performed and only one camera pointing perpendicularly to the laser sheet has been used. Stereoscopic PIV has been used for outlet configuration "Collar 2", in this case two areas are imaged, above the burner outlet and inside the glass extension tube just above the annular collars. In Figure 5.3 is shown the position and the dimensions of the area imaged for the case of Collar 1. The imaged area considered is the portion of the raw image collected by the camera that is characterized by signal intensity levels high enough to extrapolate velocity vector fields. The laser sheet is fired horizontally from left to the right with reference to the image considered. While the horizontal dimension of the area imaged depends on the camera field of view, the vertical dimension depends on the height of the laser sheet.

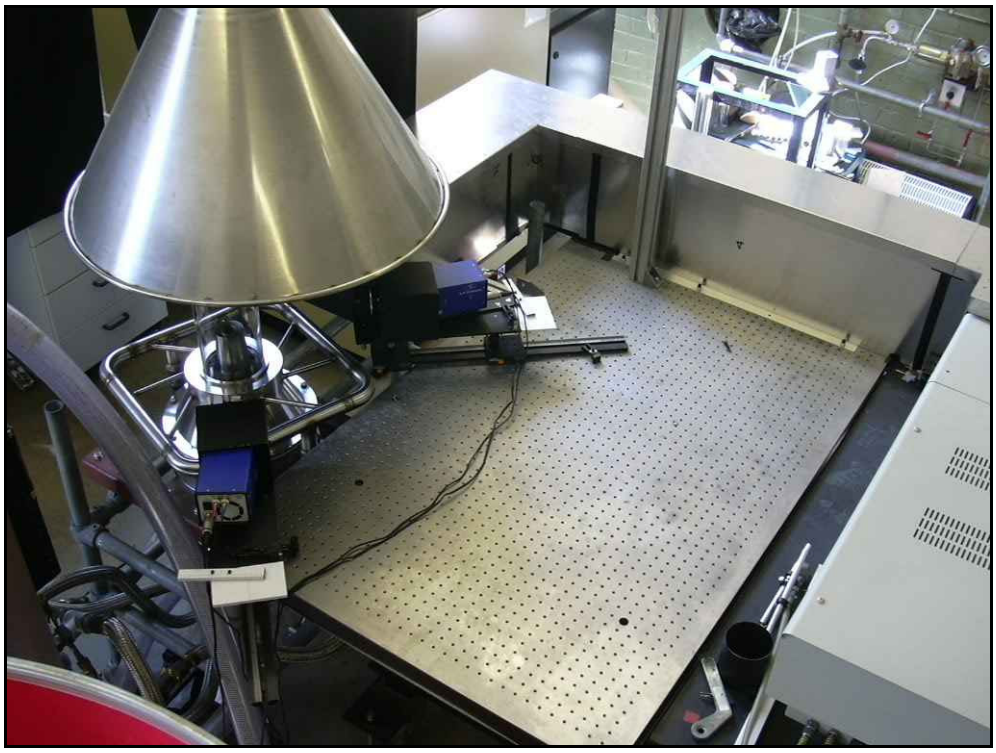

Figure 5.2. Stereoscopic PIV experimental apparatus used in Test House 1 at Cranfield University.

The position and dimensions of the areas imaged in the case of Collar 2 are presented in Figure 5.4 (just above the burner outlet) and Figure 5.5 (inside the glass tube below the burner outlet). The imaged areas for Collar 1 and Collar 2 just above the burner outlet are of similar dimensions. The laser sheet height is around 40 mm and field of view with horizontal dimension 96 mm. In the case of the area imaged inside the silica tube, the dimensions are reduced because the external swirl flow is not seeded with TiO_2 particles. The Mie scattering signal outside a diameter greater than 65 mm was negligible. The TiO_2 particles were seeded in the inner and annular flows only. In the mixing section before the burner outlet, TiO_2 particles were mixed with the external swirl flow component. However at the position of the imaged area inside the glass tube the mixing process was at its preliminary stage and it has not been possible to obtain velocity information concerning the swirl component.

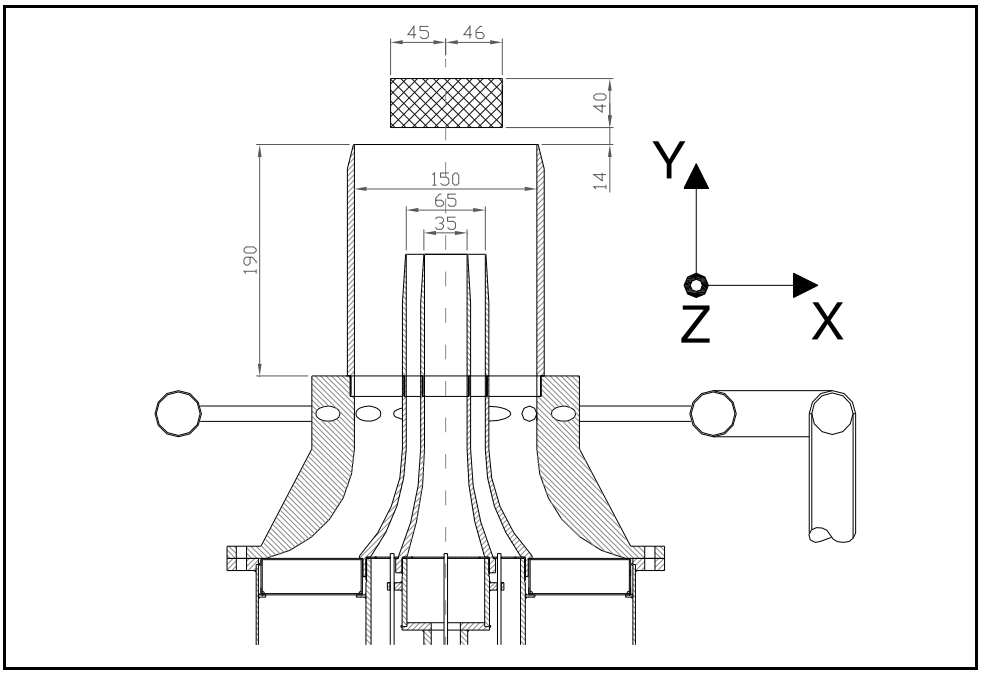

Figure 5.3. Dimensions and position of the area imaged using 2D PIV on burner outlet configuration Collar 1 (all measures are in mm). The reference system is shown and its origin must be considered coincident with the centre of the burner outlet circular rim (150 ID).

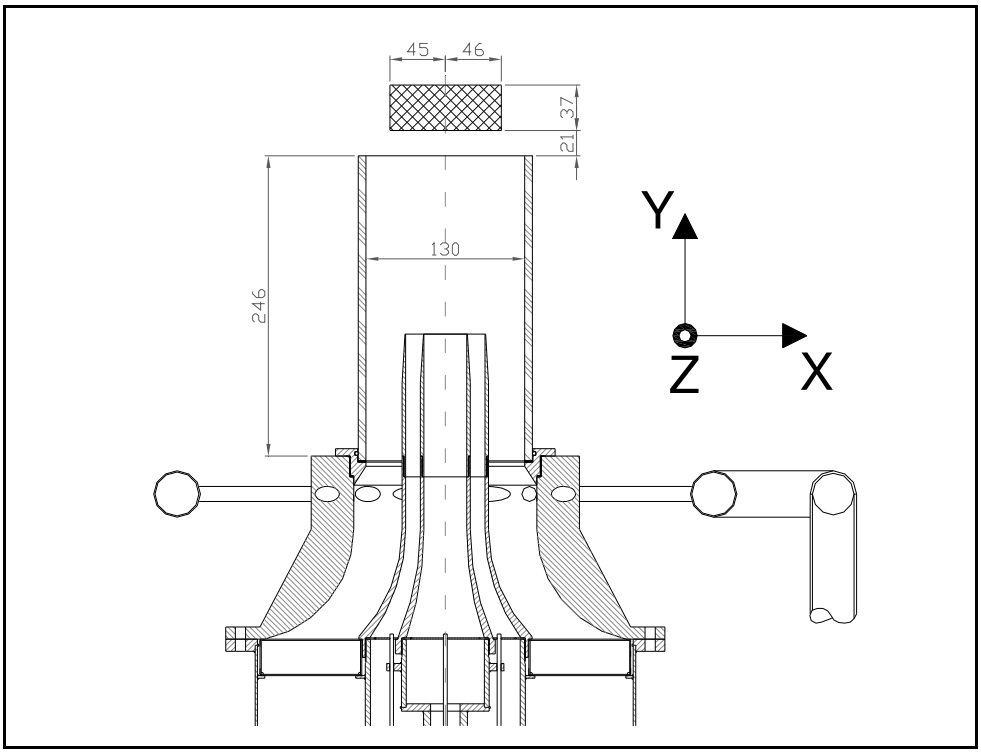

Figure 5.4. Dimensions and position of the area imaged using Stereoscopic PIV on burner outlet configuration Collar 2 outside the glass tube (all measures are in mm). The reference system is shown and its origin must be considered coincident with the centre of the burner outlet circular rim (130mm ID).

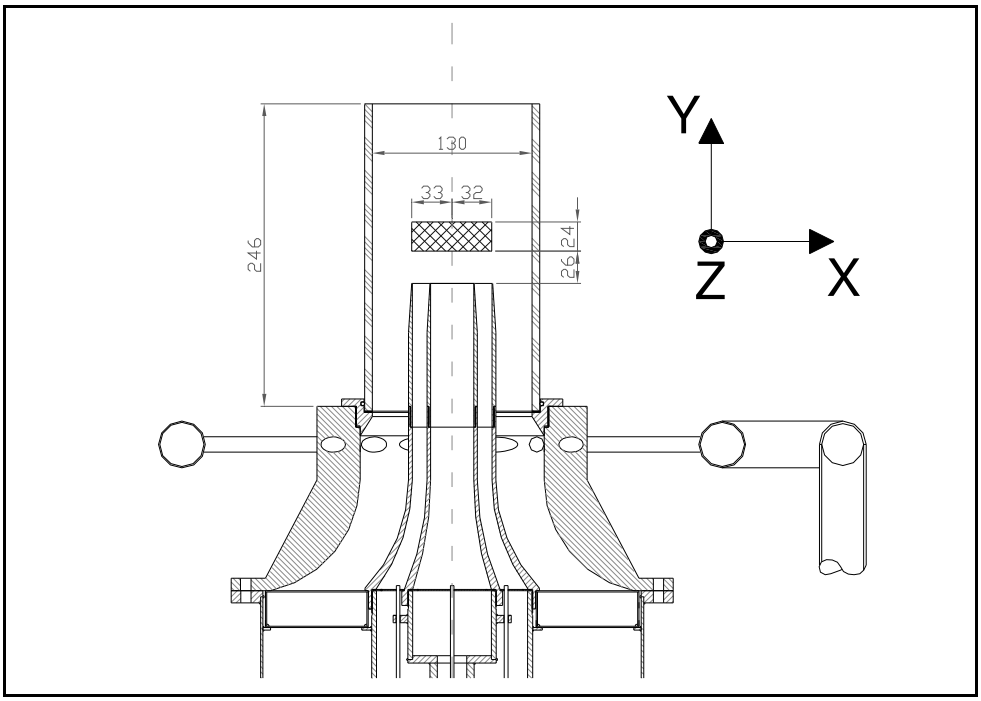

Figure 5.5. Dimensions and position of the area imaged using Stereoscopic PIV on burner outlet configuration Collar 2 inside the glass tube (all measures are in mm). The reference system is shown and its origin must be considered coincident with the centre of the annular collar circular rim (65mm ID).

5.2 Vector Field Computation

For the evaluation of images via correlation the complete image is divided in so-called interrogation windows. The correlation function operates on the intensities inside each interrogation window and passes through the complete PIV recording with a specified window shift. The evaluation will yield one velocity vector for each interrogation window. The window size defines the size of the interrogation window in width and height. The window size selected was a square 32X32. Each correlation operates only on the intensities inside the corresponding interrogation window. Considering that the image resolution was around $0.05\,mm/pixel$, the choice of an interrogation window size of 32X32 results in associating a velocity vector on squared interrogation windows with side 1.5 mm.

The window overlap defines the overlap among neighbouring interrogation windows. The bigger the specified overlap, the closer is the grid of computed velocity vectors (the number of pixels for each interrogation window is not affected). The interrogation window size and the window overlap determine the grid size of a vector field. This is the spacing between two neighbouring vectors in the vector field. In all the calculations a window size of 32×32 pixels and an overlap of 50% have been considered. This

choice allows the interrogation windows to be big enough for having a sufficient number of particles in the area considered in order to calculate efficiently the velocity value. At the same time 50% overlap provides an increased number of grid points where the velocity vectors are calculated. The distance between the centres of neighbouring interrogation windows is also reduced to 16 pixels and then $0.8\,mm$.

The raw images have been processed using the cross-correlation mode. The original image consists of two frames. The first frame (frame 0) contains the 1st exposure while the second frame (frame 1) contains the 2nd exposure. The algorithm computes the cross-correlation of all interrogation windows between frame 0 and frame 1. The highest peak in the cross-correlation image is the most likely displacement vector $\overrightarrow{ds}$. There is no peak at the zero-displacement. The multi pass option with decreasing window size has been used in the iteration.

The vector field is calculated by an arbitrary number of iterations with a decreasing interrogation window size. The initial interrogation window was 64X64 and the final interrogation window size was 32X32. The evaluation starts in the first pass with the initial interrogation window size and calculates a reference vector field. In the next pass the window size is half the size of the previous pass and the vector calculated in the first pass is used as a best-choice window shift. In this manner the window shift is adaptively improved to compute the vectors in the following steps more accurately and more reliably. This ensures the same particles are correlated with each other even if small interrogation windows are used where less particles enter into or disappear from the interrogation window. This helps to correlate the right particles and improves the signal-to-noise ratio.

The multi-pass with decreasing window size allows using a much smaller final interrogation window size than it would be possible without adaptive window shifting. This improves the spatial resolution of the vector field and produces less erroneous vectors. With a final interrogation window size of 32×32 pixels then with a fixed window shift of 0 pixels it is only possible to calculate vectors with ±16 pixels particle displacement maximum. In a vector field with large fluctuations vectors can still be computed in areas with big particle separation using the multi-pass algorithm since the window shift is locally adapted to the mean particle displacement. Using an initial 64 × 64 pixel window size even large vectors are calculated with high confidence. Those vectors are then used as a window shift for the final 32 × 32 calculation.

The algorithm used for the cross correlation was the standard function via FFT. This correlation uses the following equation, which is the standard cyclic FFT based algorithm that calculates a cyclic correlation of the interrogation window and is similar but not exactly the same as the mathematical true correlation:

$$C(dx,dy)=\frac{\sum_{x=0,y=0}^{x<n,y<n}\left(I_1(x,y)-I_{1avg}(x,y)\right)\left(I_2(x+dx,y+dy)-I_{2avg}(x+dx,y+dy)\right)}{RMS\left(I_1(x,y)-I_{1avg}(x,y)\right)RMS\left(I_2(x+dx,y+dy)-I_{2avg}(x+dx,y+dy)\right)} \qquad (5.1)$$

The symbols I_1 and I_2 are the image intensities of the 1st and 2nd interrogation window and the 2D-array C gives the correlation strength for all integer displacements (dx,dy)

between the two interrogation windows. The size of the interrogation window is n and usually also the size of the correlation plane, i.e. $\pm n/2$ is the maximum displacement computed.

'Cyclic' means that the correlation is computed as if the two interrogation windows of size $n \times n$ are repeated again in 2D-space and on this pattern the true correlation is computed. Mathematically from the two $n \times n$ interrogation windows the complex 2D-FFT is calculated, they are multiplied complex conjugated, and the inverse FFT is computed, which yields the cyclic correlation function. This is much faster (e.g. 50×) than directly computing the correlation according to the above equation except for very small interrogation windows.

A disadvantage is that this introduces a weighting of the correlation coefficients with an emphasis on the displacement (0,0) (assuming no additional window shift) with decreasing weighting toward larger displacement. For example, for an interrogation window of size 32×32 pixel the weighting is 1 for a displacement of (0,0) and 1/2 for a displacement of 16 pixels and 0 for a displacement of 32 pixels. This is because e.g. for a displacement of 16 pixel, only signal in left half of the first interrogation window really adds to the correlation strength. The other right half of the first interrogation window is actually correlated with the wrong left half of the other interrogation window, only adding unwanted false random correlation noise. Therefore this correlation function should only be used, when the displacement is less than about 1/3 of the interrogation window size. Or the other way around, the interrogation window size should be big enough to accommodate possible large vectors.

This weighting is not always a disadvantage. Using the multi-pass approach with iteratively smaller interrogation window sizes and adapted window shifts, this cyclic FFT-correlation performs very well, because the adapted window shift places the correlation peak of the true displacement always in the middle of the correlation plane and therefore gives the peak a large weighting factor.

One more disadvantage of the cyclic FFT-based correlation is that it introduces a bias toward smaller displacements. E.g. if the displacement is 10 pixel, calculated is actually 9.8 pixel. Again this is due to the above weighting feature which changes a perfect Gaussian correlation peak to one which is slightly shifted toward higher weighting functions, that is toward lower displacements. Using adaptive multi-pass this bias can be eliminated almost totally, because the relevant displacement is reduced to a range of less than ±1 pixel.

What is left is still a so called 'peak locking' bias effect, which shifts the measured displacement slightly toward the next integer. The peak locking effect depends on the size of the signal relative to the pixel dimensions on the CCD, the size of the interrogation window and the density of the signal. The effect is of the order of 0.1 pixels. The peak locking bias together with the always present RMS noise limits the possible maximum accuracy of the vector computation.

Once a vector field was calculated, vector validation algorithms were applied to eliminate spurious or false vectors. An allowed vector range was defined and a median filter applied. The allowed vector range restricts the filtered vectors to a specified range in units of velocity [m/s]. As the value of the bulk flow velocity was known, this value increased by 20% was used to define the upper limit for all the velocity components.

The median filter computes a median vector from the eight neighbouring vectors and compares the middle vector with this median vector ± deviation of the neighbouring vectors. The centre vector is rejected when it is outside the allowed range of the average vector ± deviation of the neighbour vectors. Note that each vector component is checked independently. The deviation is not computed on all components, rather the two most deviating values are ignored (only done if more than 5 neighbour vectors exist), such that up to one or two spurious vectors do not spoil the RMS calculated.

5.2.1 Unburnt Gases Mask Image Algorithm

A sudden drop of signal from seed particles was noticed in correspondence of the flame front. This phenomenon hindered the velocity vector calculation in the areas corresponding to burnt gases. Considering that the flames burning velocity is defined as the velocity of the oncoming unburnt gases just before the preheated zone, it follows that the unburnt gases flow characteristics are important for the understanding of flame propagation, therefore it has been decided to calculate the velocity vectors only for the interrogation windows of the unburnt gases. This choice has been implemented associating to each image the respective mask image created using an algorithm pipeline built in DaVis 7.1. This algorithm procedure allowed associating to the unburnt gases pixels the value 1 and the value 0 to the burnt gases pixels. The correlation function to calculate the velocity vectors has been applied only for interrogation windows associated with at least 60% of pixels equal to 1.

The procedure to distinguish the unburnt gases areas from the burnt gases consisted in five steps. The raw image is a detection of Mie signal coming from the surface of small particles, then signal RMS of a particular area is higher if several particles are involved. While it is lower if few particles are present. For this reason the first step has been the calculation of the signal RMS on a squared zone of 10 pixels side around each pixel. In Figure 5.6 image (a) is the raw image collected with the camera while image (b) is the correspondent image produced calculating the RMS of the signal in each pixel as explained before. It emerges that the RMS higher values are associated mostly with the unburnt gases.

On the image produced a sliding average filter over 20 pixels was applied and in Figure 5.6 (c) is shown the result. This filter computes a local average over a specified scale length by computing the average according to the following equations applied four times, by going from left to right, from right to left, from top to bottom and from bottom to top through the image:

$$S^{avg}(0) = I(0) \qquad (5.2)$$

$$S^{avg}(i) = \left((n-1)/n\right)S^{avg}(i-1) + \left(1/n\right)I(i) \qquad for\ i \geq 1 \qquad (5.3)$$

Where $I(i)$ is the pixel intensity at a certain pixel i and $S^{avg}(i)$ is the computed average at that pixel and $S^{avg}(i-1)$ is the computed average at the previous pixel. The

value n is the scale length (in the case considered 20), which corresponds about to the distance over which the average is computed. The effect is a sliding average, where each new pixel is added with a small weighting factor. This type of filter is much faster than any Fourier type of average filter or a linear filter, since very few multiplications are necessary for each pixel, independent on the scale length. There is a small edge effect at the image borders, but by far not as severe as when using a FFT-Filter. The only drawback is that the image intensities are shifted a bit in the direction of processing. But this is compensated by going not only from left to right, but also from right to left.

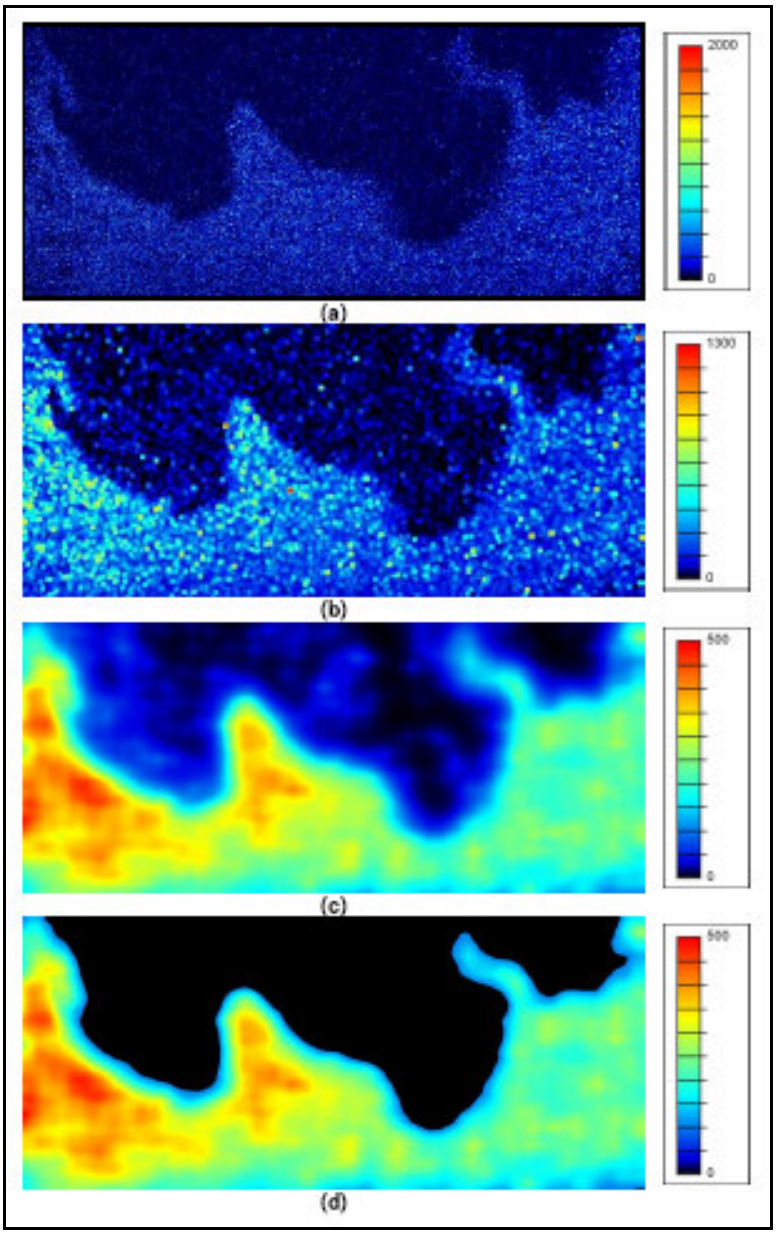

Figure 5.6. Intermediate images in the algorithm pipeline for calculating the cold gases mask image.

Coming back to the description of the mask calculation, after the sliding average filter the following step has been the application of a lower threshold. All the pixels with a number of counts below 20% of the image maximum were converted to 0. The consideration of a percentage of the maximum is related to the dependence of the signal intensity on laser power and seed particles density, both quantities were not guaranteed constant for technical reasons. The result of this operation on image (c) is image (d) in Figure 5.6. The final step was the conversion of all the pixels with an intensity value greater than 0 to 1.

5.2.2 Stereoscopic Vector Field Computation

The precondition for stereoscopic PIV is an accurate calibration of the two cameras. Correcting for off axis viewing is an essential part of stereoscopic PIV evaluation and must be done with care to ensure accurate results. LaVision employs a fully empirical calibration method, which does not involve measuring angles or distances. It has been proved to be highly accurate and reliable. The calibration plate was mounted on a multistage holder capable of movements of 1 mm with $\pm 10 \mu m$ error. The calibration plate was required to be placed in three parallel positions with a displacement of 1 mm. In each position two images were collected, one from each camera. The final set of six images were necessary to correct the off axis viewing and to allow the calculation of the off plane component of the velocity.

Different approaches for stereo vector computation have been proposed. In all cases 2D2C-vector fields are computed for each camera from which by stereoscopic reconstruction a 2D3C-vector field is computed (Prasad, 2000). One has the choice of following procedures:

1. Computing the 2D2C-field on a regular grid in the raw images and using the two interpolated vectors to compute a 3C-vector at regular world grid positions.
2. Computing the 2D2C-vectors in the raw image at a position corresponding to the correct world position.
3. Dewarping the images first and computing the 2D2C-vectors at the correct world grid position.

Method 1 has the disadvantage that the vectors are not computed at the correct world position and due to vector interpolation false or inaccurate vectors affect the final 3C-vectors. Method 2 has the disadvantage that the size and shape of the interrogation windows differ between the two cameras due to the perspective viewing. For method 3 the computed 2D2C-vectors are already computed at the world correct position and originate from the same interrogation window of equal size and shape, but a sub-pixel interpolation is required during the dewarping, which together with the sub-pixel interpolation necessary for the multi-pass window deformation scheme leads to added image degradation. Therefore DaVis 7.1 uses a modified method 3 approach where the dewarping and image deformation is done at once before each step in the multi-pass iterative scheme.

For the first vector computational pass the two frames (t0,t0 + dt) of each camera are dewarped and evaluated. This already provides vectors at the correct position in the world coordinate system. Also the size and shape of the interrogation windows for both cameras are the same, which means that the correlation is done on the same particles apart from effects due to the non-zero thickness of the light sheet. Then a preliminary 3C-reconstruction is done to remove corresponding vectors in the 2C-vector fields for which the reconstruction error is too large, e.g. larger than 0.5 or 1 pixel. This very effectively removes spurious vectors since two false vectors with random directions are rarely correlated. At the end of the first pass missing vectors are interpolated and the vector field is smoothed slightly for numerical stability.

The resulting vector field is used as a reference for deforming the interrogation windows in the next pass. Actually not each interrogation window is deformed individually, but the complete image is deformed at once with half the displacement in backward direction assigned to the first image at t0 and the other half in forward direction to the second image at t0 + dt. The image deformation is combined with the dewarping of the original image in one step. Usually after 3 or 4 passes at the final interrogation window size the 2D2C-vector fields have converged sufficiently. Then the 3C-reconstruction is done which consists of solving a system of 4 linear equations with three unknowns (u,v,w).

This is done by using the normal equation which distributes the error evenly over all three components. Computing from (u, v, w) again the (u1,v1)- and (u2,v2)-components the deviation from the measured (u1,v1) and (u2,v2) can be calculated ('reconstruction error'). Usually with a good calibration and 2C-vector errors of less than 0.1 pixels, the reconstruction error is well below 0.5 pixels. The 2D2C-vector fields are separately computed for camera 1 and 2. The multi-pass scheme used consists, of two passes with interrogation window size of 64×64 pixel and 50% overlap followed by 2 passes with 32×32 and 50% overlap. After each pass a 2D3C-reconstruction is done for the purpose of eliminating 2D2C-vectors with reconstruction errors above some threshold, but the 2D3C-vector field is not used further. Only at the end the reconstructed 2D3C field is taken and validated by a median filter. The detailed error analysis for the stereorscopic PIV measurements is reported in Appendix C.

In order to show a typical sample result, Figure 5.7 shows one of the four frames that compose the instantaneous image file collected during the stereoscopic PIV experiments. From the instantaneous image file referred to Figure 5.7 the vector field shown in Figure 5.8 has been calculated. The vectors in the image indicate the velocity components on the laser sheet plane. The x axis is considered in the horizontal direction from left to right, while the y axis is on the vertical direction pointing to the top. Consequently the z axis is on the direction that is orthogonal to the laser sheet plane, and according to the right hand rule it is pointing outside the paper plane (x-y plane). Comparing Figure 5.7 with Figure 5.8 it is possible to see the effects of the application of the mask algorithm in order to calculate the velocity vectors in the unburnt gases area only. Another difference is on the size of the two figures. Figure 5.7 is the image as it is collected from the camera without any type of perspective correction. It is referred to a laser sheet plane tilted 45° from the lenses plane. A correction needs to be applied in order make coincident the laser sheet plane with the image plane, this operation consequently increases the horizontal side of the image, this is the reason why the

horizontal side of Figure 5.8 is longer than the one of Figure 5.7. These images are referred to the imaged area shown in Figure 5.4.

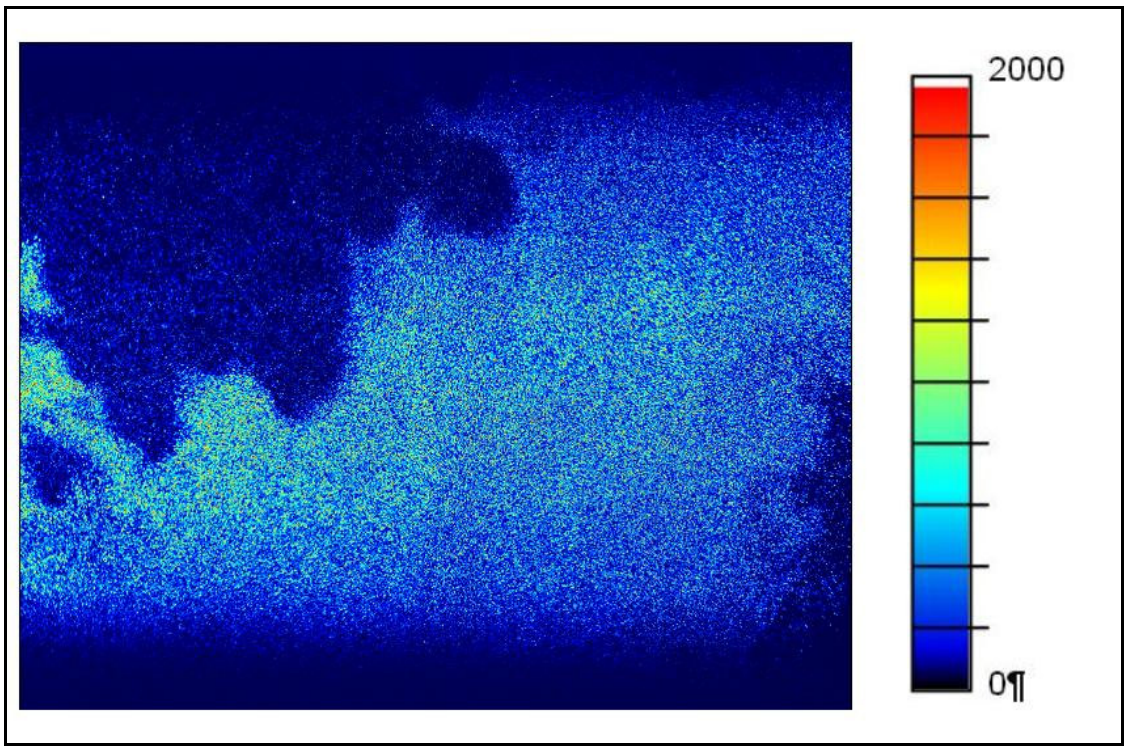

Figure 5.7. Every raw image is composed of four frames, two for each camera in correspondence of each laser pulse. In this figure is shown one of these frames. The coloured scale represents the light intensity measured in number of counted photons for each pixel.

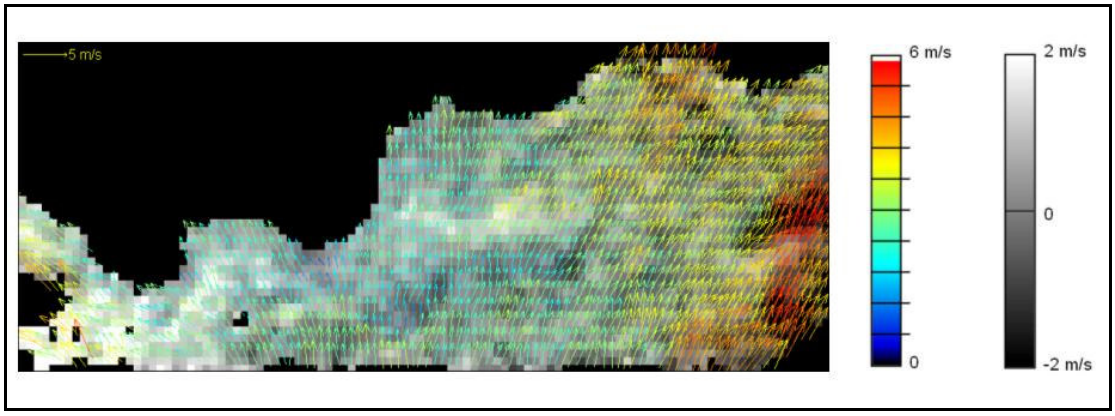

Figure 5.8. Velocity vectors calculated from the raw image related to Figure 5.7. The vectors are calculated only in the unburnt gases area using the mask algorithm. The vector length indicates the velocity vector component on the x-y plane, it is the sum of the x-component and the y-component. On the top left corner is indicated a 5 m/s reference vector. The out of plane z-component is indicated by the background black and white scale on the left of the image. The coloured scale is applied on the vectors and indicates the absolute value of the velocities.

5.3 Acquiring Burning Velocities

The flame velocity, which is also called the burning velocity, normal combustion velocity, or flame speed, is more precisely defined as the velocity at which unburnt gases move through the combustion wave in the direction normal to the wave surface (Glassman, 1996). The velocity fields have been used to extrapolate the burning velocities. The images obtained using the PIV system allowed calculation of the velocity vectors in the unburnt gases area for every image collected. Considering the definition of the burning velocity, all the interrogation windows at the borders of the unburnt gases region have been selected and the related velocity vectors have been associated with the flame speed. The only assumption is that the velocity of the cold gases just upstream the flame front is considered to be orthogonal to the flame front itself.

For each instantaneous absolute velocity field has been defined a computer code capable to detect the interrogation windows along the flame front. An example is shown in Figure 5.9 and Figure 5.10. For each flame condition, the burning velocities have been extrapolated and the related PDF distributions have been defined. The differences in their characteristics under the effect of various levels of turbulence and fuel stratification will be analyzed in Chapter 9.

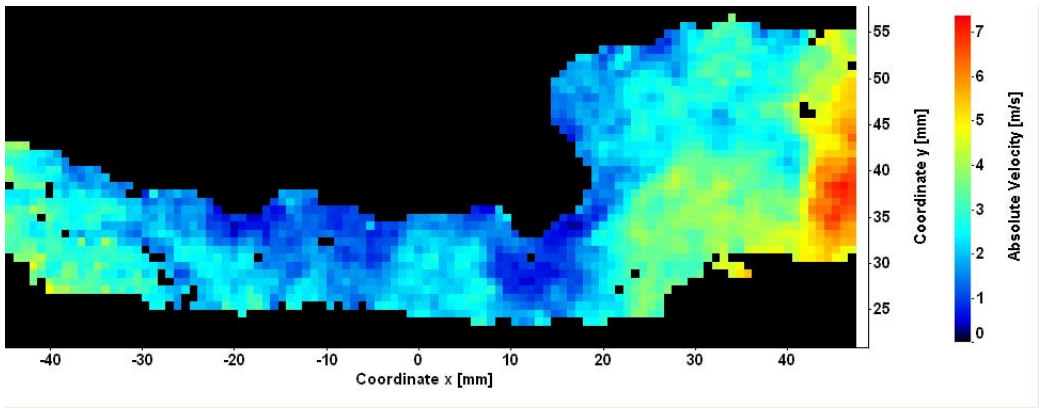

Figure 5.9. Instantaneous absolute velocity field calculated from an instantaneous 3D velocity vector field. The velocities are determined only in the cold gases area.

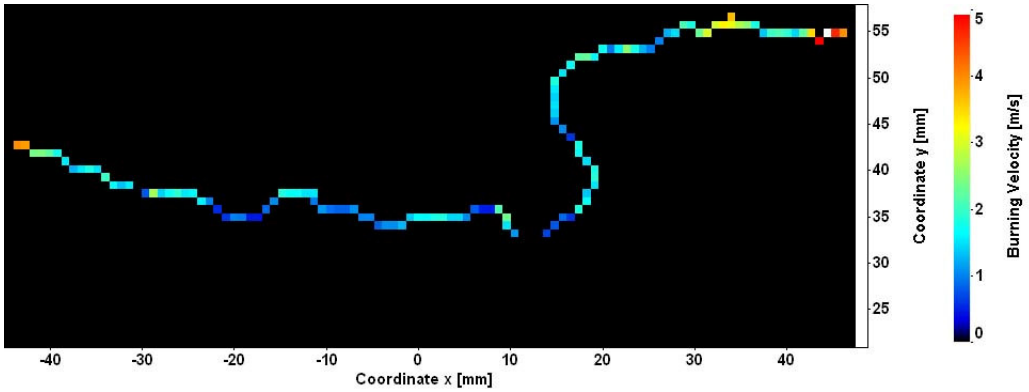

Figure 5.10. 3D-PIV interrogation windows selection along the flame front in order to isolate the burning velocities. The selection of interrogation windows shown in this figure has been obtained from the instantaneous absolute velocity field of Figure 5.9.

6 RAYLEIGH EXPERIMENTS AND ANALYSIS

This chapter describes the application of the laser diagnostic method using Rayleigh scattering to obtain the temperature fields for the imaged area. The experimental apparatus used is presented and then the processing procedure used to analyze the images collected is described. Both burner outlet configurations have been studied in the flame region. The instantaneous temperature fields are important in order to calculate the flame thickness and flame curvature. The procedures to extrapolate their values from the temperature fields are explained.

6.1 Experimental Apparatus

The experimental apparatus used for Rayleigh measurements is shown in Figure 6.1. It used a Nd:YAG Laser (Quanta Ray) as the laser source, the same laser used for PIV experiments. The Nd:YAG Laser has been modified such that it can operate in a double pulse mode, but in this case a single pulse was necessary and the time interval between the two laser pulses has been set to $0\mu s$. The final output beam has a diameter approximately 8 mm and 300 mJ per pulse (measured), with most of the light at 532 nm in addition to some residual infra-red light.

A front coated dichroic mirror at 45° incident angle is used to steer the output light from the second harmonic generator of the Nd:YAG laser. The 532 nm component of the beam is reflected horizontally in the perpendicular direction. This beam is reflected again perpendicularly by a second dichroic mirror of the same type mounted on an adjustable holder to steer the beam towards the burner at some 1.5 meters away. A fused silica positive cylindrical lens (150mm focal length) and a glass positive spherical lens (1000mm focal length) have been used to produce a laser sheet 40mm high with an average thickness of $160\mu m$.

The images have been recorded using a La Vision Flow Master camera connected to a La Vision Intensifier with a Nikon 50mm focal length multi-element lense. The use of an intensifier is required because of the low intensity of the Rayleigh signal. The lens aperture used for all the experiments has been f/1.2 and the intensifier gain has been set to 7.5, this combination showed to be characterized by the higher signal to noise ratio (≈ 25). The software used for controlling the hardware while collecting the images was DaVis 7.1 from La Vision. The same software has been used for processing the raw images in order to gain the temperature fields.

The Rayleigh scattering from the molecules is an elastic process as is the Mie scattering from particles but it is three orders of magnitude weaker, for this reason filters were applied on all gas flow supply lines in order to remove any dust particle present in the oncoming flow. The filters were capable of removing particles and liquid down to 0.01 μm. According to the standards of ISO 8573 Class of Dirt 2 the air has a residual of 10ppm for 1 μm particles.

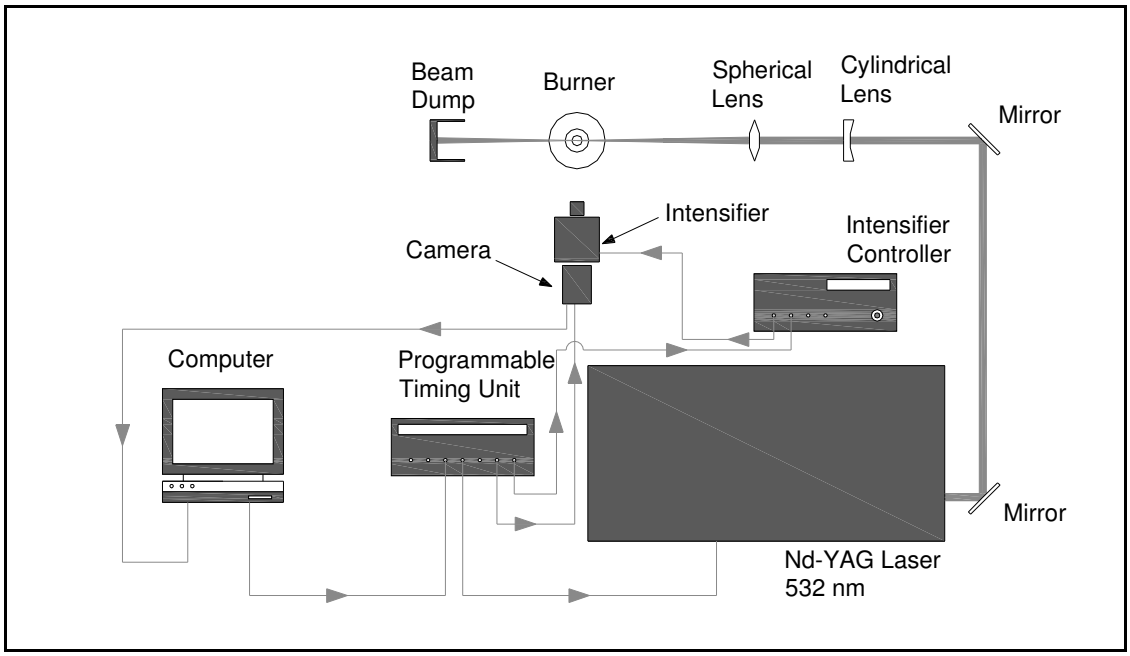

Figure 6.1. Experimental apparatus used for Rayleigh experiments. The laser source and the laser sheet forming optics are displayed. The electronic tools used for collecting the measurements and their connections are shown.

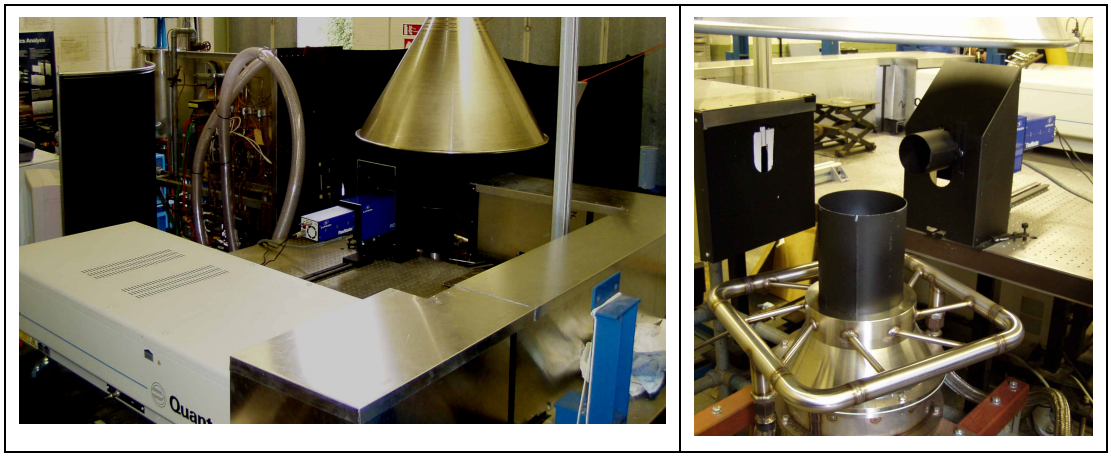

Figure 6.2. Pictures of Rayleigh experimental apparatus used in Test House 1 at Cranfield University.

The light is elastically scattered from the molecules and consequently it is at the same wavelength of the laser source. Any reflection of the laser sheet light on solid surfaces that enters the field of view of the collecting optics represents background noise that needs to be reduced to a minimum level. In order to do so, all the metal surfaces around the burner outlet have been painted in black and drapes of black velvet have been applied around the imaging area of the lab. Figure 6.2 shows two pictures of the experimental set up.

The position and the dimensions of the imaged area in the case of Collar 2 are presented in Figure 6.3 and for Collar 1 in Figure 6.4. The selection of the imaged area has been driven by the necessity of matching as close as possible the imaged areas used for PIV measurements in order to correlate the data collected with the two different techniques. The resolution for the images was $74 \mu m / pixel$ for Collar 1 while in the case of Collar 2 it was $77 \mu m / pixel$.

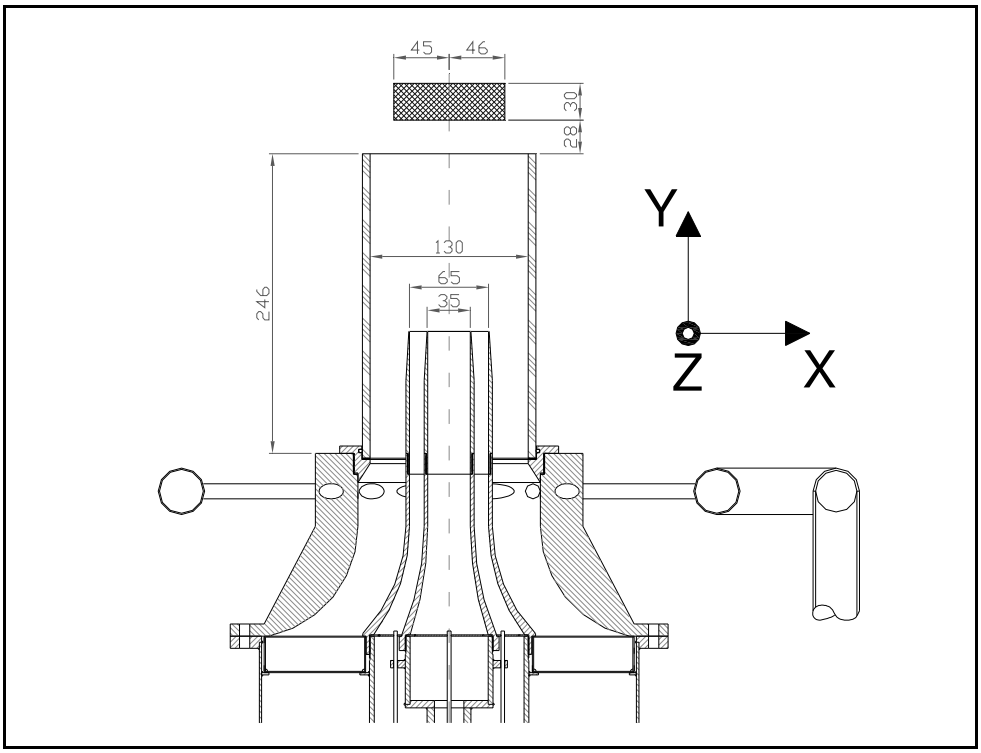

Figure 6.3. Dimensions and position of the area imaged using 2D Rayleigh scattering technique on burner outlet configuration Collar 2 (all measures are in mm). The reference system is shown and its origin should be considered coincident with the centre of the burner outlet rim (130mm I.D.).

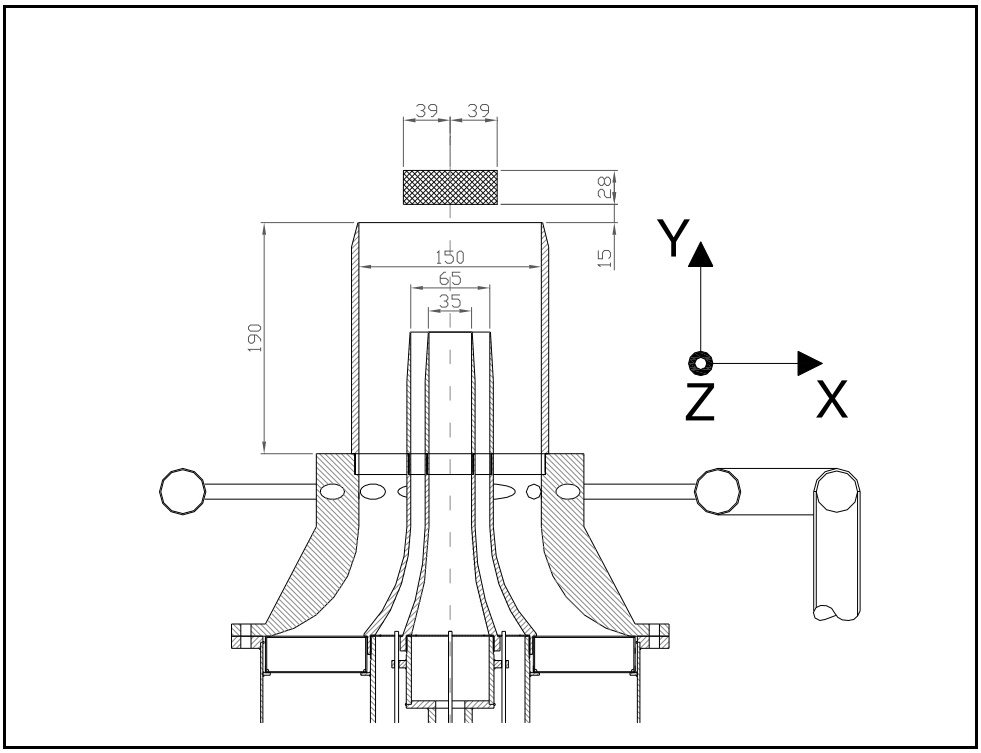

Figure 6.4. Dimensions and position of the area imaged using 2D Rayleigh scattering technique on burner outlet configuration Collar 1 (all measures are in mm). The reference system is shown and its origin should be considered coincident with the centre of the burner outlet rim (150 I.D.).

6.2 Image Processing

The raw images need to be corrected for inherent system characteristics in a similar manner irrespective of the type of light scattering processes involved. The correction process involves in dealing with the following six aspects:

1. electronic bias: $E_B(x, y)$
2. laser energy fluctuation: k_L
3. laser-induced background: $B_G(x, y)$
4. optical response: $R_{op}(x, y)$
5. laser beam stripes: $S_{st}(x, y)$

Note that only for the image processing procedure, the co-ordinate system is such that the laser sheets are parallel to the x-y plane, the x coordinate is parallel to the direction of beam travel, and the origin of the coordinates is at the top-left of the images. The units for the coordinate values of x and y are pixels.

Each untreated image is considered as a discrete light intensity function, $F_L(x, y)$, expressed algebraically as:

$$F_L(x, y) = k_L \; R_{op}(x, y) \left[S_{st}(x, y) \; I_R(x, y) + B_G(x, y) \right] + E_B(x, y) \qquad (6.1)$$

Where $I_R(x, y)$ is the light intensity of the Rayleigh scattering that we wish to obtain. By rearranging $I_R(x, y)$ is expressed as:

$$I_R(x, y) = \frac{\left[F_L(x, y) - E_B(x, y) \right] - k_L \; R_{op}(x, y) B_G(x, y)}{k_L \; R_{op}(x, y) S_{st}(x, y)} \qquad (6.2)$$

Others terms are explained in the following sections which describe the procedures for obtaining $\left[F_L(x, y) - E_B(x, y) \right]$, $S_{st}(x, y)$, $R_{op}(x, y) B_G(x, y)$, $R_{op}(x, y)$, k_L.

6.2.1 Electronic Bias

Subtraction of electronic bias is done before any manipulation is performed on the images. A bias frame, $E_B(x, y)$, taken with an imaging system in the absence of light, represents the system DC level plus any small structure exhibited by the CCD and image intensifier. With the lasers inoperative and the flames absent, twenty frames were taken by the detection system to be averaged to form the bias frame for the system. There is no apparent day-to-day variation in the intensity of the bias frames. The subtraction of bias is to yield a zero reference for the pixel intensities that remain, intensities that are laser induced irrespective of the type of light scattering.

6.2.2 Laser Energy Fluctuation and Laser Beam Stripes

The laser used is inherently unstable in its pulse to pulse energy and this is reflected in the images. Correcting for energy fluctuation is done simply by normalising each Rayleigh image by the value of k_L. The reference condition is the power associated with an average over 300 images in air at ambient temperature.

From Equation (6.1) it is possible to obtain an expression for the frame $S_{st}(x, y)$:

$$S_{st}(x, y) = \frac{\left[F_L(x, y) - E_B(x, y) - B_G(x, y) R_{op}(x, y) \right]}{R_{op}(x, y) I_R(x, y)} \qquad (6.3)$$

Laser beam stripes are seen as non-uniform spatial distribution of laser energy across the height of the beam. The distribution can be expressed by an image that for each stripe defines the relative laser power intensity. This is achieved by defining a determined number of mask images, each mask image defines an area of 3 pixels thickness in the direction (usually horizontal) of the laser stripes, they obviously cover the all area imaged. Each mask area is then associated with the relative laser power. The sum of these masks defines the laser beam stripes of the image considered. Because it carries only information about the laser energy distribution within the area considered, the average of all the pixel values applied on the image has to be equal to one for each instantaneous laser beam stripes image considered. It is k_L that defines the laser energy associated with the shot in relation with the reference conditions.

In order to calculate the frame $S_{st}(x, y)$ for each laser shot, it is necessary to define within the image, a region that is associated with a medium at uniform scattering properties, a so called uniform region. This region has to overlap at least in 300 pixels each mask associated with a single laser stripe. For this experiment two regions are selected in all the instantaneous images: the unburnt gas area and the burnt gas area. The burnt gas area signal has been converted in unburnt gas signal by using the known gas composition and the Rayleigh scattering cross section for the two conditions. This has been possible because the flame front chemical and thermodynamic evolution for the various equivalence ratios considered has been studied using the software CHEMKIN and the results are reported in Appendix B. One-dimensional laminar flame code has been applied to calculate the species concentration and temperature distribution in the flame front.

For each mask associated with a laser stripe a frame has been defined in which the pixels on the mask area all have the same value obtained by averaging the signal over the intersection of the mask with the uniform region. The frame sum of all these frames represents the laser power distribution. The laser energy fluctuation k_L is then calculated by dividing the average of all the pixel values of the laser power distribution by the average of the frame associated with the reference signal conditions of unburnt gases only. The frame of the laser power distribution has to be divided by the average laser power calculated over all the frame's pixels producing $S_{st}(x, y)$. After this operation the average value of the frame $S_{st}(x, y)$ is unity as required.

The steps followed in the procedure to calculate the laser beam stripes energy profiles are shown by Figure 6.5, Figure 6.6, Figure 6.7, Figure 6.8, Figure 6.9, and Figure 6.11. The starting point is the raw image collected during the experiments from which only the electronic bias has been removed (Figure 6.5), and is called FC. With the application of two threshold levels, one for the unburnt gases and one for the burnt gases signal, it has been possible to obtain the masks shown in Figure 6.6 and Figure 6.7, respectively called BG and UG. From the data reported in Appendix B it is possible to define the ratio $k_{b.u}$ between the Rayleigh signal of the unburnt gases and the Rayleigh signal of the burnt gases. The sample frame (SF) used to deduce the laser power distribution for the shot considered is then calculated by applying the following equation:

$$SF = FC \times BG \times k_{b.u} + FC \times UG \qquad (6.4)$$

The result of this operation is displayed in Figure 6.8, when it is applied on the instantaneous image shown in Figure 6.5. The laser stripes are approximated by 127 masks (M_{S-i} with $i = 0,...,126$) associated to 127 adjacent horizontal stripes 3 pixels width. The frame SF is used to calculate the average Rayleigh signal I_{S-i} associated to each laser stripe. The Rayleigh signal from a uniform media is linearly dependent on the laser power and consequently for each mask has been given a value I_{S-i} that is directly proportional to the laser power. It follows that the laser beam stripes power is directly proportional to the frame obtained by $\sum_{i=o}^{126} M_{S-i} \times I_{S-i}$. The normalization is applied by dividing by the average over the all frame. It can be concluded that the frame representing the normalized laser beam stripes power can be obtained using the following equation:

$$LP = \frac{\sum_{i=0}^{126} M_{S-i} \times I_{S-i}}{Avg\left(\sum_{0}^{126} M_{S-i} \times I_{S-i}\right)} \qquad (6.5)$$

With the notation $Avg(...)$ is indicated the average of the pixels' values over the frame that is the argument of the operation. Figure 6.9 displays the image of the laser beam stripes normalized power LP related to Figure 6.5. Figure 6.10 shows the profile of the values associated to a vertical line of the frame LP shown in Figure 6.9. The laser beam stripes profile is characterized by a higher power for the pixels in the central part of the beam, because a cylindrical lens is used to form a laser sheet from an originally circular laser beam section. The profile itself is not a smooth line and those irregularities are different every shot, for this reason it is important to calculate accurately the laser beam stripes power for every image collected.

Figure 6.11 shows the result of the correction process for the case of the raw image shown in Figure 6.5. This would be the signal collected by the camera if the laser energy profile was uniform along a vertical section of the laser sheet.

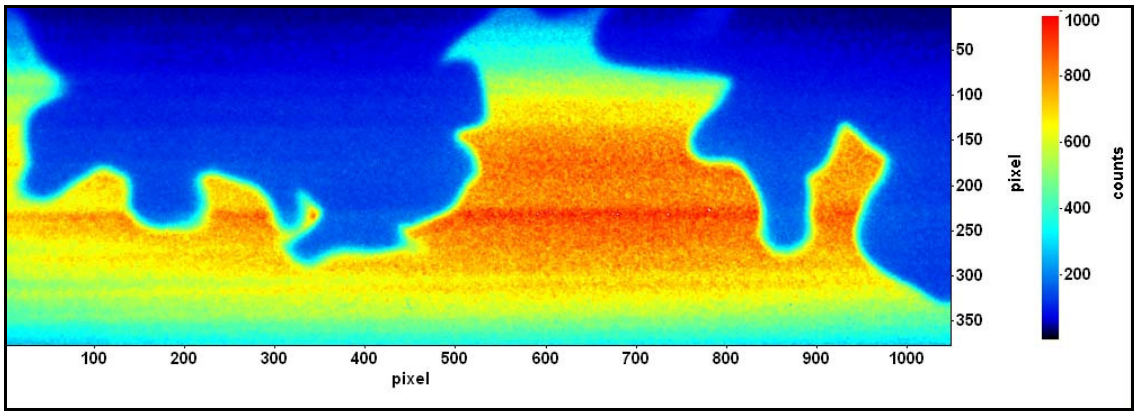

Figure 6.5. Example of image collected during the Rayleigh experiments. From the image shown it has been removed the electronic bias only.

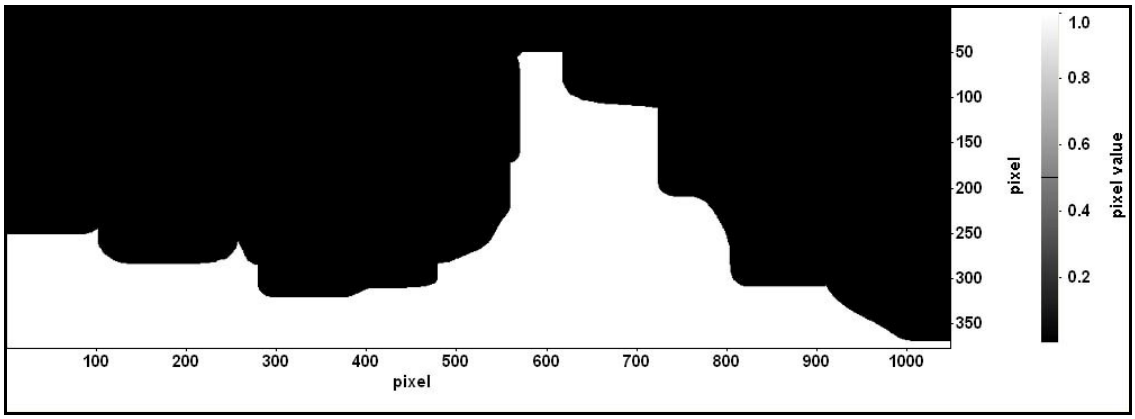

Figure 6.6. Mask of the unburnt gases obtained from the image shown in Figure 6.5.

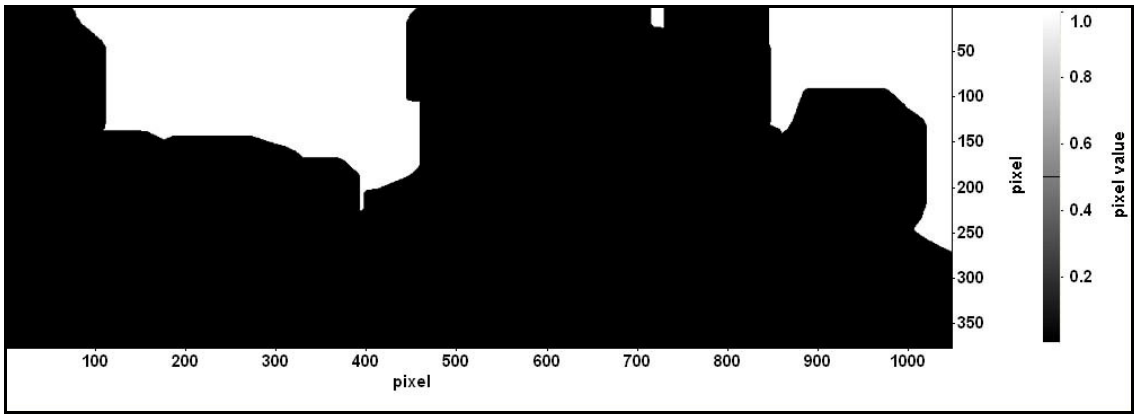

Figure 6.7. Mask of the burnt gases obtained from the image shown in Figure 6.5.

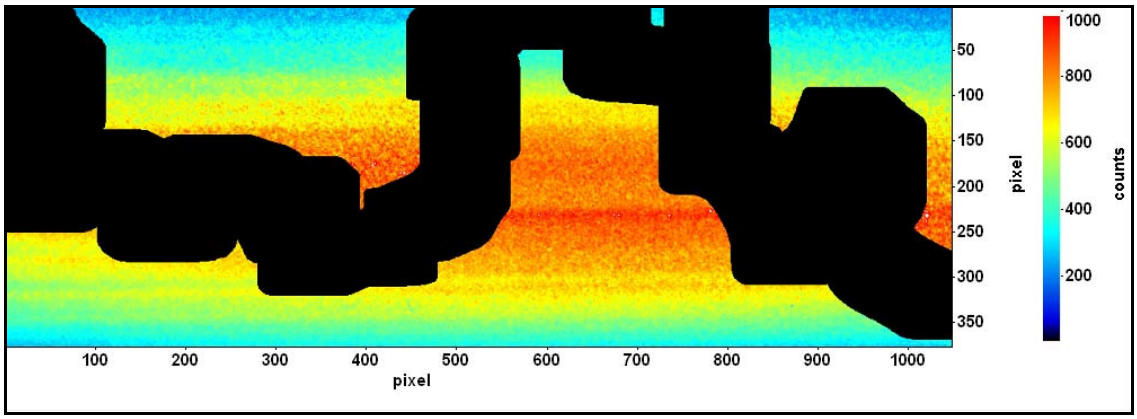

Figure 6.8. Image obtained by converting the burnt gases signal in unburnt gases signal for the mask region of Figure 6.7 and keeping the unburnt gases signal for the mask region of Figure 6.6. This is the sample image in order to calculate the laser stripes energy distribution.

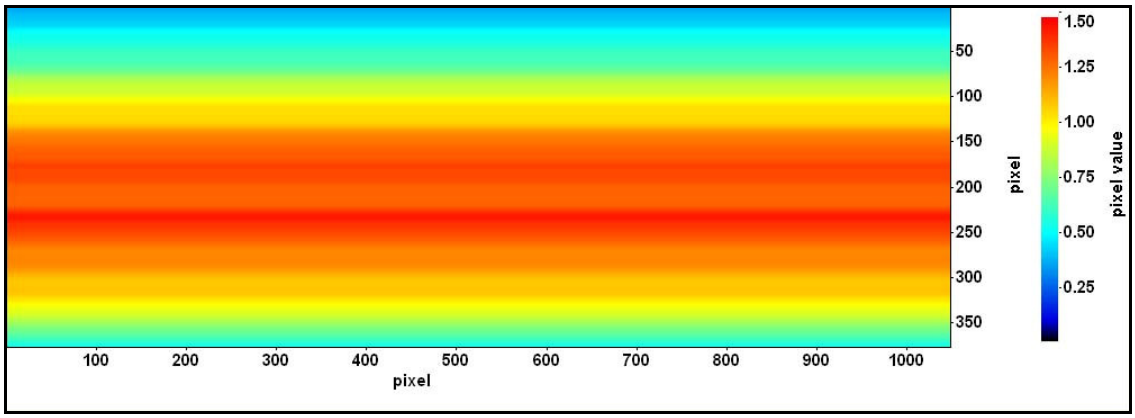

Figure 6.9. Laser stripes frame obtained from the sample image shown in Figure 6.8.

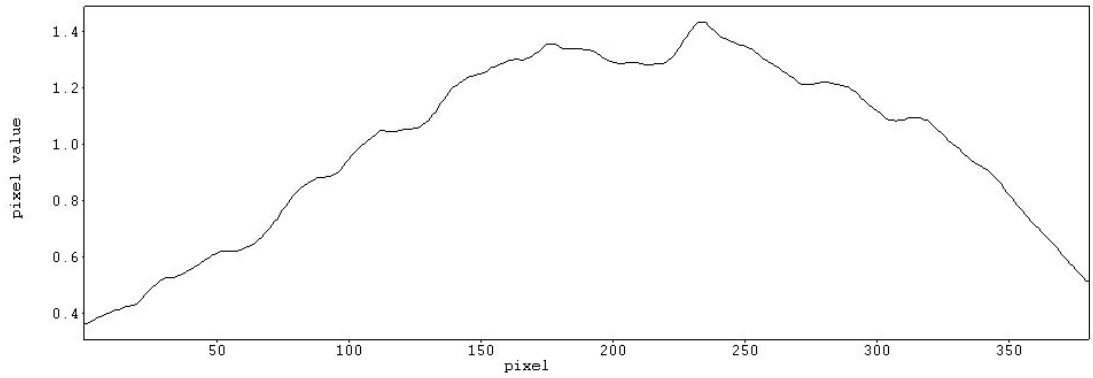

Figure 6.10. Profile along a vertical line of the frame shown in Figure 6.9. It is the normalized profile of the laser power stripes.

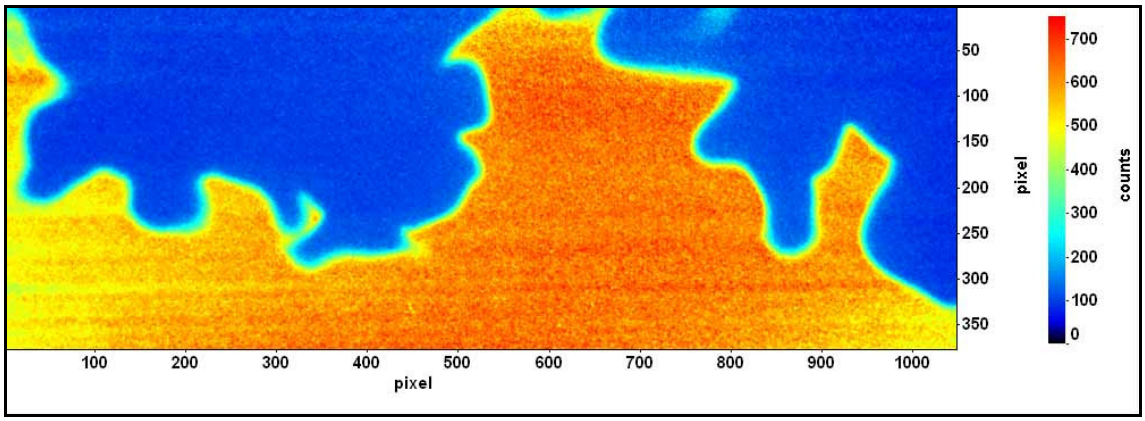

Figure 6.11. Result of the correction process when applied on the raw image shown in Figure 6.5.

6.2.3 Laser Induced Background

Background level, or laser induced background $B_G(x,y)$, is referred to here as the additional light intensity collected by the detection system because of the scattered laser light reflected by the environment surrounding the flame. Ideally the true Rayleigh background can be obtained if the probed volume is a vacuum, therefore no molecular scattering is present and only scattered background light is collected. As a vacuum is an impractical environment to achieve, a method has been developed using two gas mixtures at two different thermodynamic conditions, for which the Rayleigh cross-sections are known. The first gas is air at ambient temperature, the second medium is constituted by burnt gases. The second experimental condition is practically achieved by reducing the lift off height of the flame front until it is always placed under the bottom limit of the area imaged.

Equation (6.1) applied on the two conditions mentioned becomes:

$$F_{L-AIR}(x,y) = k_{L-AIR}\ R_{op}(x,y)\left[S_{st-AIR}(x,y)\ I_{R-AIR}(x,y) + B_G(x,y)\right] + E_B(x,y) \qquad (6.6)$$

$$F_{L-HOT}(x,y) = k_{L-HOT}\ R_{op}(x,y)\left[S_{st-HOT}(x,y)\ I_{R-HOT}(x,y) + B_G(x,y)\right] + E_B(x,y) \qquad (6.7)$$

These two equations apply on images that are averages of 300 images. Because (6.6) is applied to the reference condition for the laser power coefficient, it follows that $k_{L-AIR} = 1$. The frame $F_{L-HOT}(x,y)$ is an average over 300 images. The laser power fluctuates from shot to shot, however the laser energy fluctuation factor can be considered equal to one when 300 shots are considered ($k_{L-HOT} = 1$).

In order to simplify the expression for the mathematical equations the frames will be indicated only with a capital letter, without the expression (x,y), while cursive letters will be used for coefficients and parameters.

From the physical theory of Rayleigh scattering the relation between the light intensity of molecular scattering for the two conditions considered can be written as:

$$I_{R-HOT} = I_{R-AIR}\frac{T_{AIR}\ \sigma_{R-HOT}}{T_{HOT}\ \sigma_{R-AIR}} \qquad (6.8)$$

where T stands for temperature in Kelvin and σ_R is the Rayleigh cross-section. The value of σ_{R-AIR} is easy to obtain because the air composition is well known, while for the case of the burnt gases it has been necessary to use a chemical code to calculate the mixture fractions of the molecules produced by the combustion process and the final temperature of the burnt gases (T_{HOT}). The software CHEMKIN has been used to overcome this problem and the results are reported in Appendix B. Substituting (6.8) in (6.7) obtains:

$$F_{L-HOT} = R_{op}\left[S_{st-HOT}\ I_{R-AIR}\ \frac{T_{AIR}\sigma_{R-HOT}}{T_{HOT}\sigma_{R-AIR}} + B_G\right] + E_B \qquad (6.9)$$

Obtaining $(R_{op}\ I_{R-AIR})$ from (6.6) and substituting it in (6.9):

$$F_{L-HOT} = \frac{S_{st-HOT}\ T_{AIR}\ \sigma_{R-HOT}}{S_{st-AIR}\ T_{HOT}\ \sigma_{R-AIR}}\left(F_{L-AIR} - E_B - R_{op}\ B_G\right) + R_{op}\ B_G + E_B \qquad (6.10)$$

Defining the frame K_{LR} as:

$$K_{LR} = \frac{S_{st-HOT}\ T_{AIR}\ \sigma_{R-HOT}}{S_{st-AIR}\ T_{HOT}\ \sigma_{R-AIR}} \qquad (6.11)$$

The frame K_{LR} carries the information about the ratio $\left(\frac{T_{AIR}\ \sigma_{R-HOT}}{T_{HOT}\ \sigma_{R-AIR}}\right)$, which is the same for any pixel considered, and the ratio S_{st-HOT}/S_{st-AIR} that is invariant for each individual laser stripe mask.

From (6.10) it is now possible to produce an expression for the product $(R_{op}\ B_G)$:

$$R_{op}\ B_G = \frac{\left(F_{L-HOT} - E_B\right) - K_{LR}\left(F_{L-AIR} - E_B\right)}{1 - K_{LR}} \qquad (6.12)$$

6.2.4 Optical Response

Shading corrections are required to compensate for variations in system responsivity. A shading correction may include variations due to the detector responsivity, variations in the illumination pattern from the light source and vignetting due to optics. Usually optical responsivity is visible from a shading correction frame, $R_{op}(x, y)$, or "flat field", whereby a uniformly illuminated flat surface is imaged with the system in question.

The reference flat field image has been considered the average over 300 images collected when imaging air at room temperature, because it represents a media at uniform Rayleigh scattering cross section. This case is described by Equation (6.6), from which it is possible to obtain the frame R_{op} that represents the optical response:

$$R_{op} = \frac{F_{L-AIR} - E_B - R_{op}\ B_G}{S_{st-AIR}\ I_{R-AIR}} \qquad (6.13)$$

The frame I_{R-AIR} is the theoretic molecular scattering from a uniform medium (air in this case), assuming that the laser energy distribution is uniform in the region imaged. This is then a frame with the same value in each pixel. This value is coincident with the average over the frame obtained by ($F_{L-AIR} - E_B - R_{op}\ B_G$), while imaging a uniform region filled with air.

6.2.5 Acquiring Temperature and Progress Variable

All the frames necessary to calculate $I_R(x, y)$ for the instantaneous shot are defined now and it can be applied (6.2). According to the theory associated with Rayleigh scattering as previously described, it is possible to correlate the Rayleigh signal with the gas temperature. This correlation has been defined for several values of equivalence ratios under the form of an equation in which the variables are temperature, T , and ratio between Rayleigh scattering for the instantaneous condition (I_{R-i}) and Rayleigh scattering at the reference conditions of air at ambient temperature, $\left(\frac{I_{R-i}}{I_{R-AIR}} \right)$. The mathematical form of the equation is:

$$T = a \left(\frac{I_{R-i}}{I_{R-AIR}} \right)^b \qquad (6.14)$$

The parameters a and b have been calculated using the results obtained by the software CHEMKIN and reported in Appendix B. One-dimensional laminar flame code has been applied to calculate the species concentration and temperature distribution in the flame front. From these data it is possible to define the intensity of the Rayleigh scattering assuming a reference value for the cold gases condition (in Appendix B the reference value considered is $I_{R-AIR} = 500$).

It is important to state that a high-accuracy Rayleigh scattering thermometry system has been developed by calibrating a McKenna premixed flat-flame burner applying corrections for the temperature dependence of the scattering cross section (Sutton et al., 2006). For the purpose of this analysis it has been assumed sufficient the approximation of the flame front species and temperature distribution using the results obtain by CHEMKIN computations.

The temperature and Rayleigh signal ratios results obtained from CHEMKIN computations have been plotted on log-log scale diagrams in order to obtain the equation of the linear interpolation function. In Figure 6.12 is shown the case for equivalence ratio 0.7. From the values of the slope and the intercept of the least square interpolation trendline it is possible to obtain the values for the parameters a and b used in Equation (6.14).

Figure 6.13 shows the plot of the results for a premixed flame with equivalence ratio 0.7 on a coordinate system using the temperature as ordinate and the ratio I_{R-i}/I_{R-AIR} as abscissa. All those points can be correlated with the function expressed in (6.14) and the values of the coefficients a and b can be calculated using the least square interpolation applied on the log-log scale diagram. In the case of Figure 6.13 with $\phi = 0.7$ the interpolation function equation is displayed. The same procedure has been applied for all the equivalence ratio values considered by the one-dimensional laminar flame code in order to define the coefficients a and b from the data reported in Appendix B. In Table 6.1 are shown the values of the parameters a and b for the various equivalence ratios considered, the errors associated to the least square fitting are also indicated for a, b and temperature.

It emerges that the temperature measurement error associated to the least square fitting applied to the results of CHEMKIN computations in very low (~1 K). The main source of error is associated with the quality of the Rayleigh signal detected by the optical system. It has been observed a signal to noise ratio equal to 25. It follows that the error of Rayleigh signal measurements is 4% ($\delta(I_{R-i})/I_{R-i}$). Equation (6.14) defines the correlation between temperature and Rayleigh signal. It follows that the temperature measurement uncertainty is given by:

$$e_T^R = \frac{\delta^r(T)}{T} = \pm\sqrt{\left(K_I \frac{\delta^r(I_{R-i})}{I_{R-i}}\right)^2} \qquad (6.15)$$

With

$$K_I = \frac{I_{R-i}}{T}\frac{\partial T}{\partial I_{R-i}} = b \qquad (6.16)$$

Substituting Equation (6.16) in Equation (6.15) and using the value previously defined for $\delta(I_{R-i})/I_{R-i}$, temperature measurement error can be defined as:

$$e_T^R = b \times 4\% \cong 4\% \qquad (6.17)$$

The value of b can be approximated with 1 because the values in Table 6.1 are considered.

The progress variable c is a scalar quantity that is defined as a normalized temperature.

$$c = \frac{T - T_u}{T_b - T_u} \qquad (6.18)$$

Once the temperature fields are calculated it is straight forward to define the progress variable c in each point of the image applying Equation (6.18). Where T is the temperature in the pixel where the progress variable has to be calculated while T_u is the unburnt gases temperature and T_b is the burnt gases temperature, both obtained from the CHEMKIN data in Appendix B.

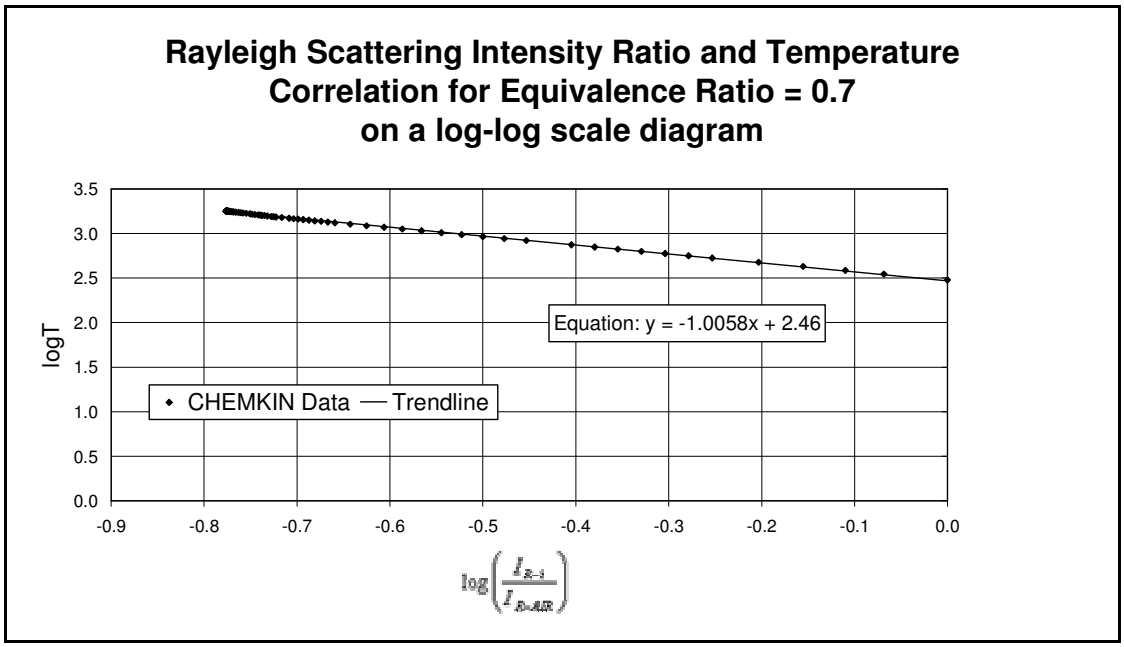

Figure 6.12. Rayleigh scattering intensity ratio and temperature correlation on a log-log scale diagram. The linear trendline that interpolate the results obtained using the one-dimensional laminar flame code data is shown with its equation.

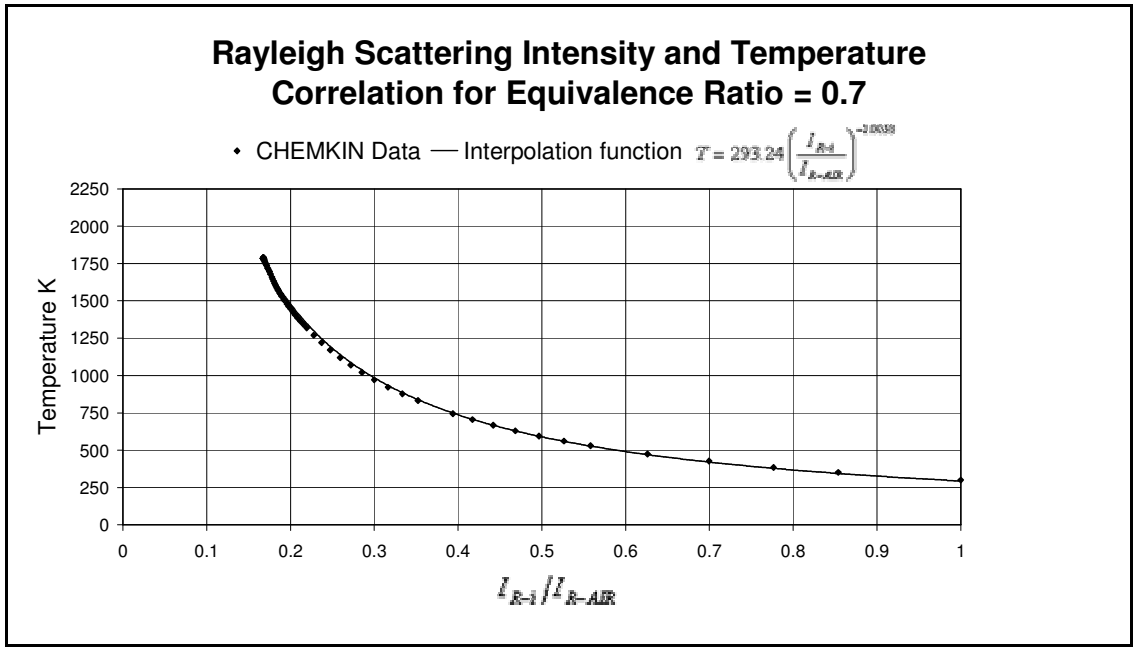

Figure 6.13. Rayleigh scattering intensity and temperature correlation interpolating the results obtained using the one-dimensional laminar flame code data.

Equivalence Ratio	a	b	a error	b error	Temperature (K)
0.7	293.24	-1.0058	1.005	0.0032	1.01
0.725	292.91	-1.005	1.006	0.0035	1.01
0.75	293.14	-1.0038	1.006	0.0036	1.02
0.775	292.55	-1.0043	1.007	0.0040	1.02
0.8	288.36	-0.9989	1.006	0.0039	1.02

Table 6.1. Values of the parameters a and b used for the least square fitting procedure regarding the various equivalence ratios considered in Appendix B. In the table are also indicated the errors for a, b and temperature.

6.2.6 Temperature and Progress Variable Fields

In this section the temperature and progress variable fields obtained with the processing procedure explained will be analyzed. At this stage it is not necessary to make any difference between Collar 1 and Collar 2, because common features of the instantaneous temperature fields are going to be considered. In the following figures from Figure 6.14 to Figure 6.19 are shown some examples of instantaneous temperature fields related to the same flame conditions. The case considered is Flame B, Bulk Flow 1 for the outlet configuration Collar 1, the figures show temperature fields obtained from six consecutive images collected with a frequency of $\approx 4Hz$. The cold gases are associated with black or blue colour while the hot gases with red. From the instantaneous temperature fields it can be observed the position and the shape of the flame front because it is characterized by a rapid increase of temperature and then a sudden change in colours. Comparing all the six images it emerges that the flame front position is always changing as is its' shape. Even if the temperature fields have been obtained by six consecutive images, there is no straight forward correlation between the flame front characteristics and the image temporal order. It is clear that the analysis of the flame front needs to be performed on a statistical basis. In order to do that the following sections explain how to manipulate the temperature fields in order to obtain the flame curvature and flame thermal thickness.

Examining the six instantaneous flame fronts figures it is possible to see the flame wrinkling produced by the oncoming turbulence. The PDF distributions of the flame curvature and flame thermal thickness will be analyzed for the effects of turbulence and fuel stratification, and will be correlated with the flame front propagation.

Figure 6.20 shows the temperature profile along the segment AB indicated in Figure 6.19. The line AB is perpendicular to the flame front in the position where they intersect. At the flame front there is a steep increase of temperature due to the combustion process. The temperature profile plotted in Figure 6.22 is obtained along the y axis of the average temperature field over 200 images for the experimental conditions

associated with Collar 1, Bulk Flow 1 and Flame B (Figure 6.21). The average temperature profile is not characterized by a steep increase as in the instantaneous case, instead the temperature gradually increases as a linear function of the coordinate y.

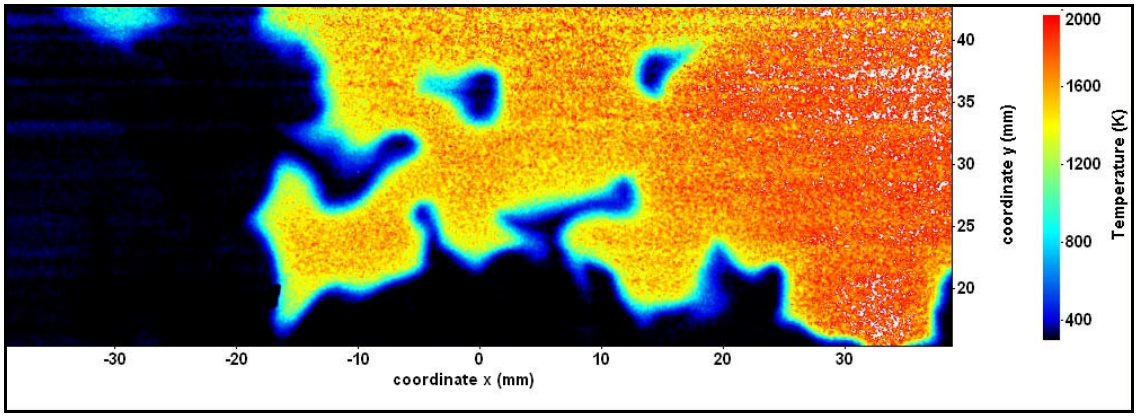

Figure 6.14. Instantaneous temperature field for the experimental conditions defined by the following characteristics: Collar 1, Bulk Flow 1, Flame B, Image number 10.

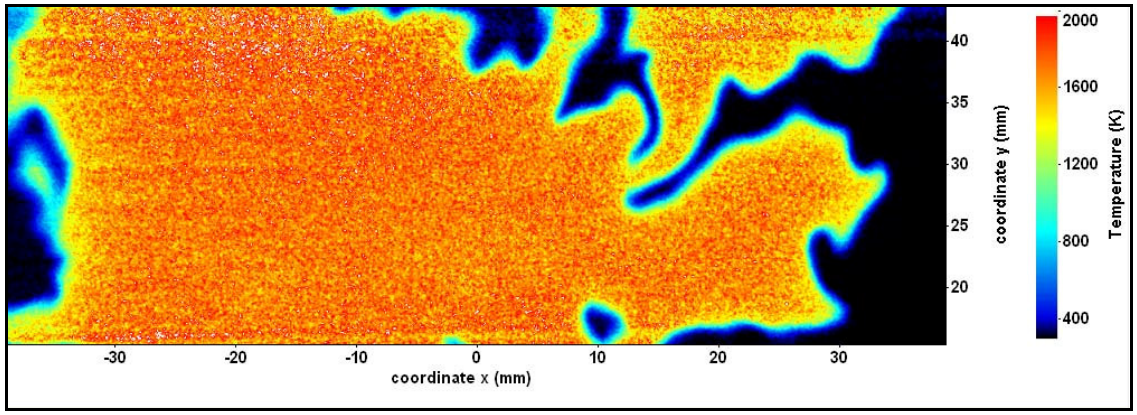

Figure 6.15. Instantaneous temperature field for the experimental conditions defined by the following characteristics: Collar 1, Bulk Flow 1, Flame B, Image number 11.

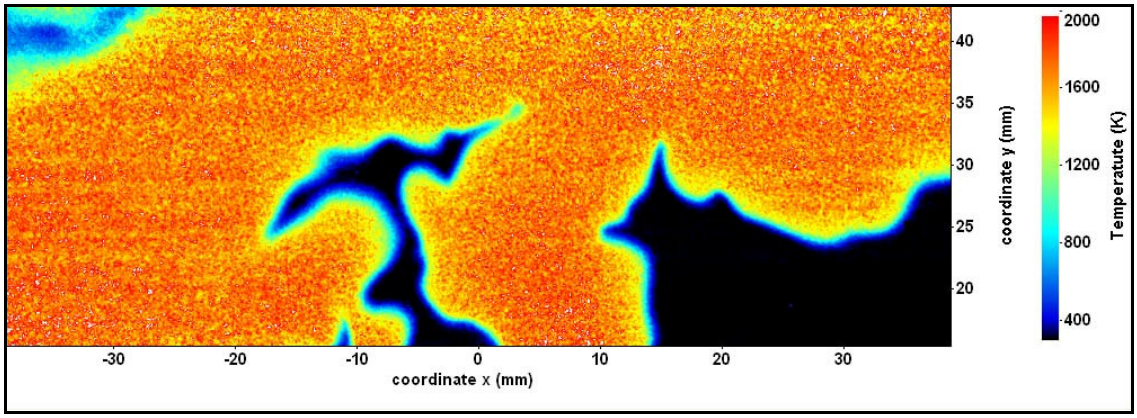

Figure 6.16. Instantaneous temperature field for the experimental conditions defined by the following characteristics: Collar 1, Bulk Flow 1, Flame B, Image number 12.

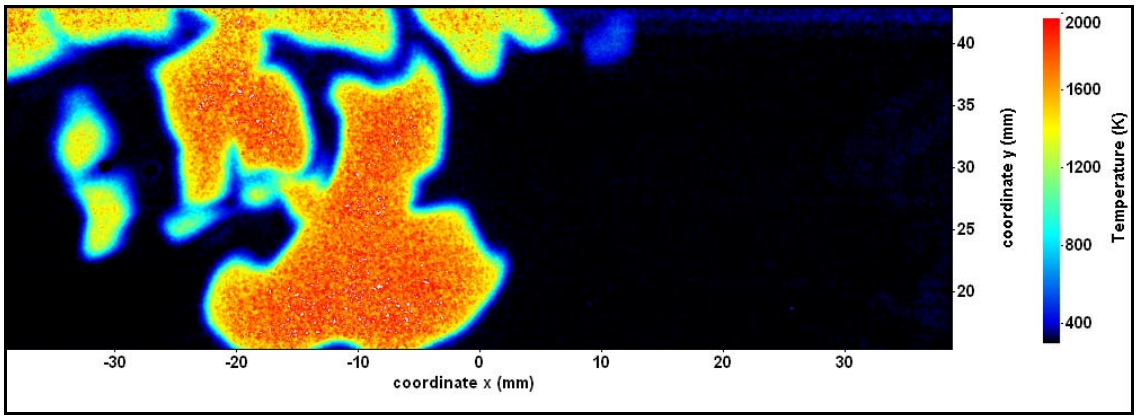

Figure 6.17. Instantaneous temperature field for the experimental conditions defined by the following characteristics: Collar 1, Bulk Flow 1, Flame B, Image number 13.

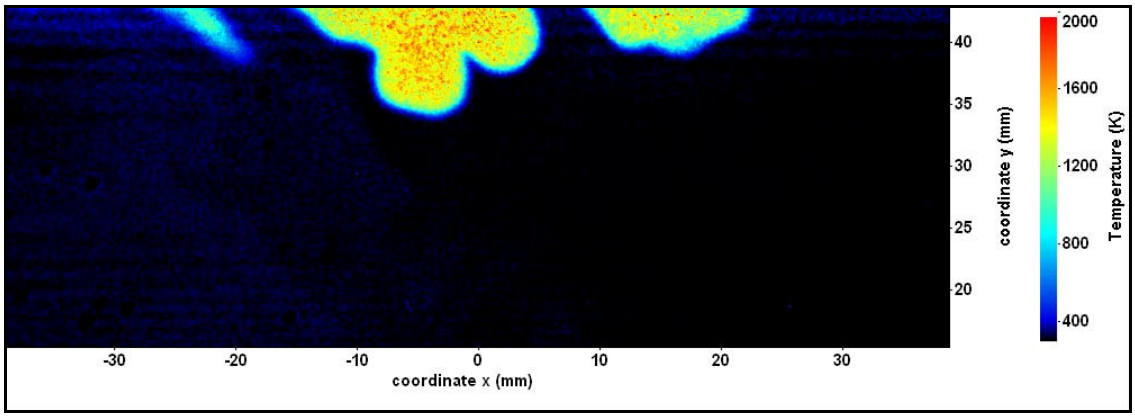

Figure 6.18. Instantaneous temperature field for the experimental conditions defined by the following characteristics: Collar 1, Bulk Flow 1, Flame B, Image number 14.

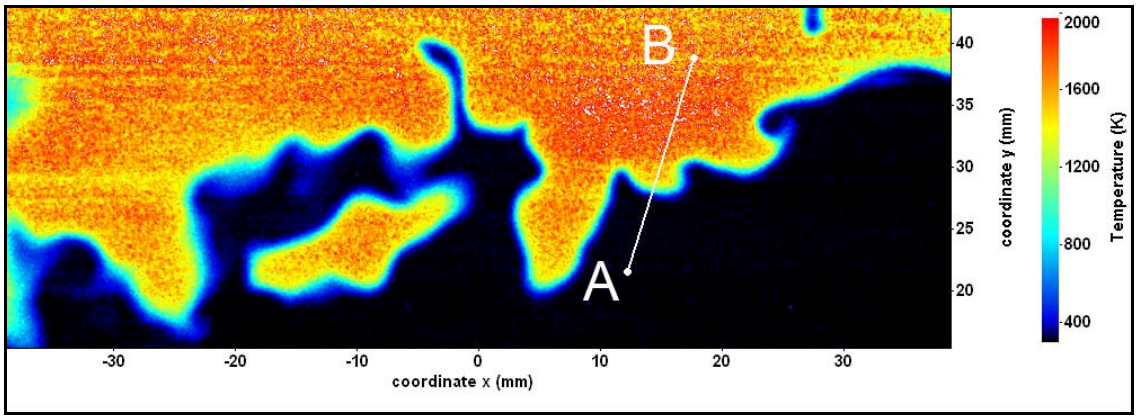

Figure 6.19. Instantaneous temperature field for the experimental conditions defined by the following characteristics: Collar 1, Bulk Flow 1, Flame B, Image number 15.

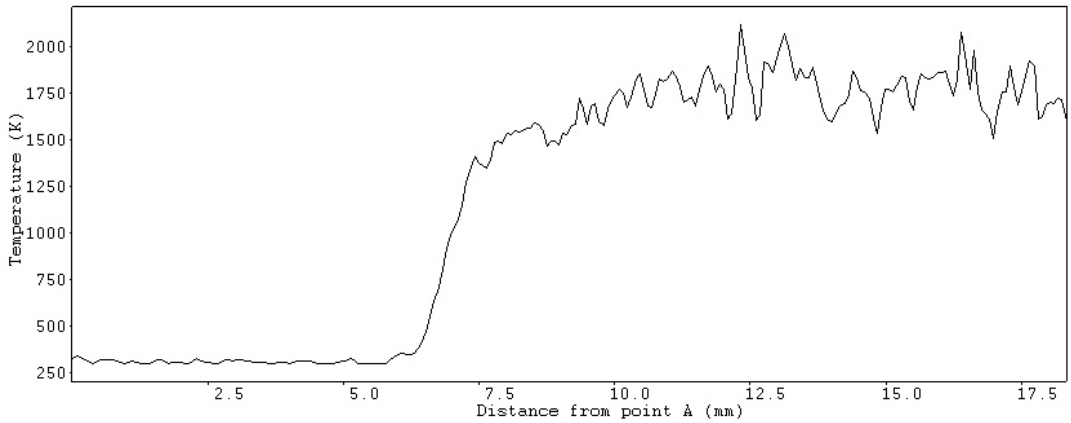

Figure 6.20. Plot of the temperature profile along the line AB shown in Figure 6.19. The line passes across the flame front that in the profile plot is identified by the steep increase in temperature.

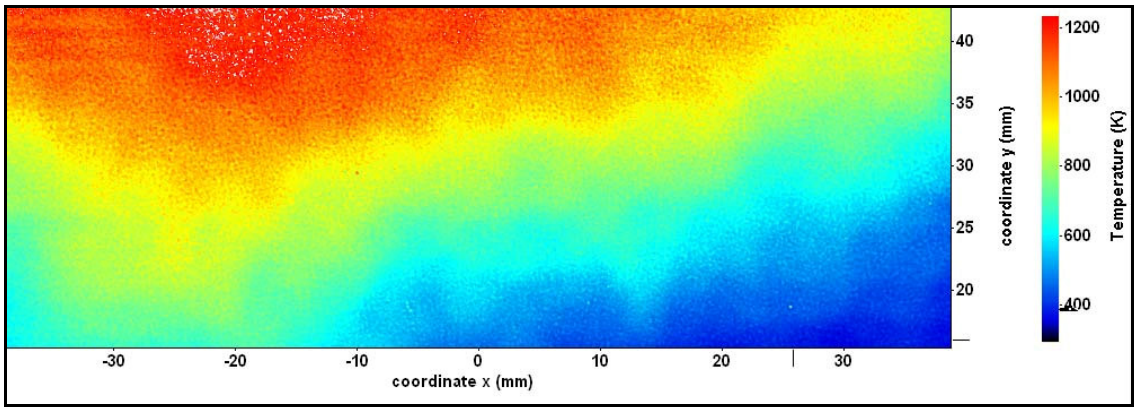

Figure 6.21. Average temperature field over 200 images for the experimental conditions defined by the following characteristics: Collar 1, Bulk Flow 1, Flame B.

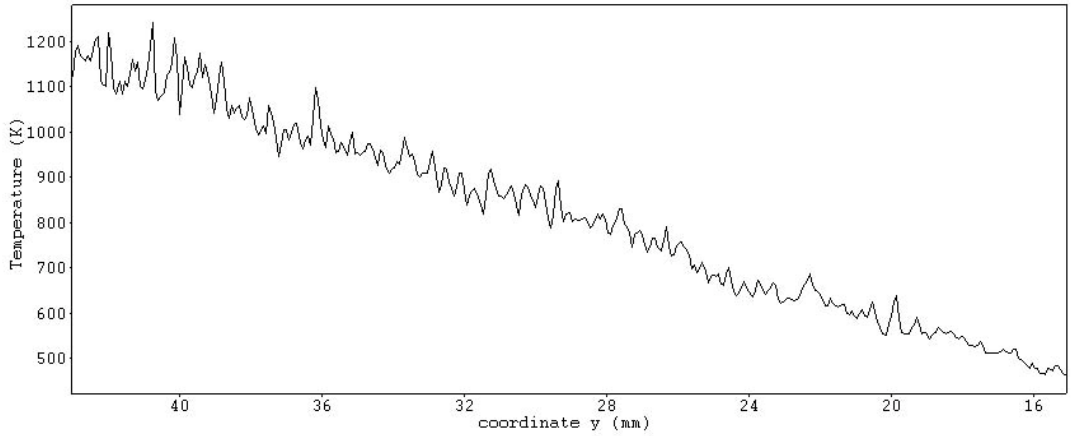

Figure 6.22. It is shown the plot of the temperature profile along the y axis of the temperature field in Figure 6.21.

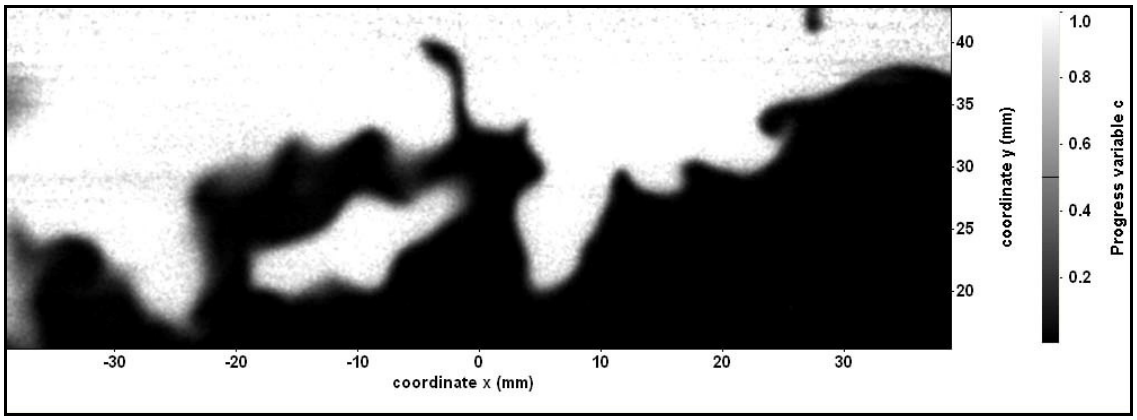

Figure 6.23. Instantaneous progress variable field for the experimental conditions defined by the following characteristics: Collar 1, Bulk Flow 1, Flame B, Image sequence number 15. These conditions are the same of the temperature field shown in Figure 6.19.

The temperature fields can be easily converted in progress variable fields using Equation (6.18) and an example is shown in Figure 6.23, which is obtained from the temperature field of Figure 6.19. The progress variable fields will be used to calculate the flame thermal thickness and curvature because they define clearly where there is the separation between the unburnt gases ($c = 0$) and the burnt gases ($c = 1$).

6.3 Flame Curvature

The flame front appears to oscillate and to assume different shapes even if consecutive images are considered. This apparent random behaviour needs to be analysed through a statistical approach. For this purpose the flame curvature values have been extrapolated from the progress variable fields along the flame front.

The flame curvature is defined as:

$$\kappa = \frac{d\theta}{ds_a} \qquad (6.19)$$

where θ is the tangential angle and s_a is the arc length. The flame curvature is positive if the flame is convex with respect to the unburnt mixture (Peters, 2000). In order to calculate the flame curvature the flame front has been identified first. The following section explains the procedure.

The starting point is the instantaneous progress variable field, an example is shown in Figure 6.24. It has been mentioned before that there is a steep temperature increase at

the flame front and consequently a steep increase of the progress variable c that changes quickly from 0 to 1. Pixels with a progress variable value equal to 0.3 are at the starting stage of the combustion process because the gas temperature increase is 30% of the total temperature raise due to combustion. These pixels can be used to define the flame front position. Following this assumption, the first step has been to produce a mask frame that associates the value 0 to the pixels with progress variable $c \geq 0.3$, while those pixels with $c < 0.3$ are assigned the value 1. This operation produced the masks of the unburnt gases and the mask obtained from the flame in Figure 6.24, is shown in Figure 6.25. It is then possible to separate those pixels that border the cold gases mask in order to define the flame front. For each pixel the sum of the eight pixels around it is considered and if the sum is less than 7, it is considered that the pixel is on the flame front. In Figure 6.26 it is displayed the flame front related to the flame of Figure 6.24.

Every flame front frame has been divided in interrogation windows of 8x8 pixels (0.5x0.5 mm). Only the interrogation windows intersected by the flame front have been considered for the curvature calculation. The flame front tangent line has been approximated with the linear interpolation of the pixels that define the flame front in the interrogation window considered. The variation of the tangential angle θ has been approximated with the difference between the angles of the interpolation lines related to two adjacent interrogation windows. The equations of the interpolation lines have been expressed based on the reference system where the x axis is in the horizontal direction proceeding from left to right, the y axis is in the vertical direction proceeding upwards and the origin is coincident with the top left corner of the frame. The arc length along the flame front curve has been approximated with the distance between the centres of the two adjacent interrogation windows.

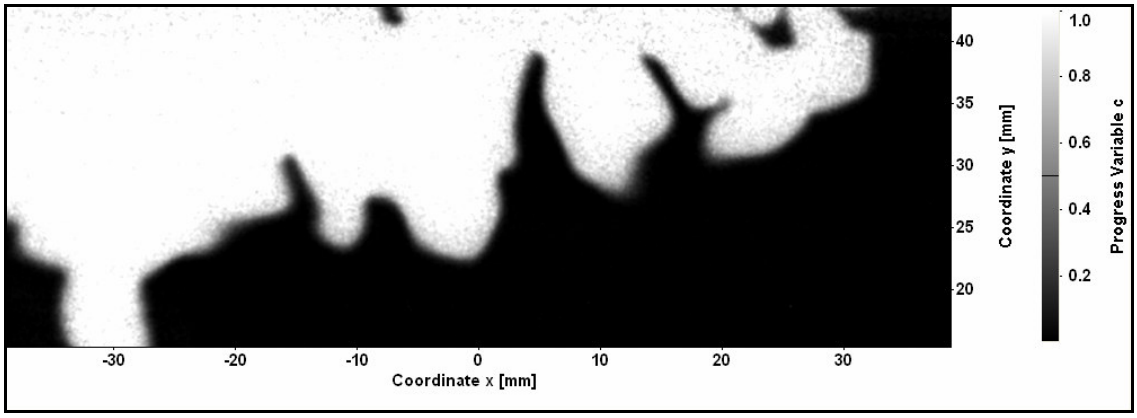

Figure 6.24. Instantaneous progress variable field.

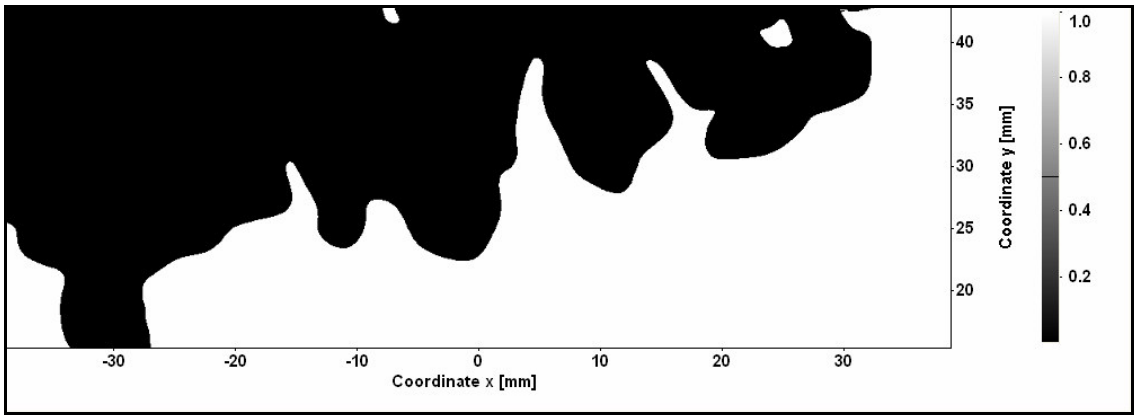

Figure 6.25. Unburnt gases mask of the instantaneous progress variable field shown in Figure 6.24.

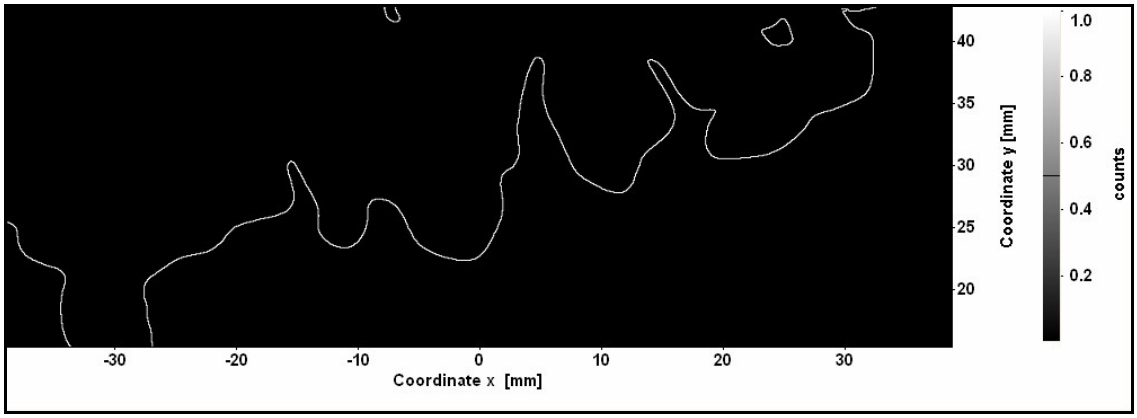

Figure 6.26. Flame front obtained from the unburnt gases mask shown in Figure 6.25.

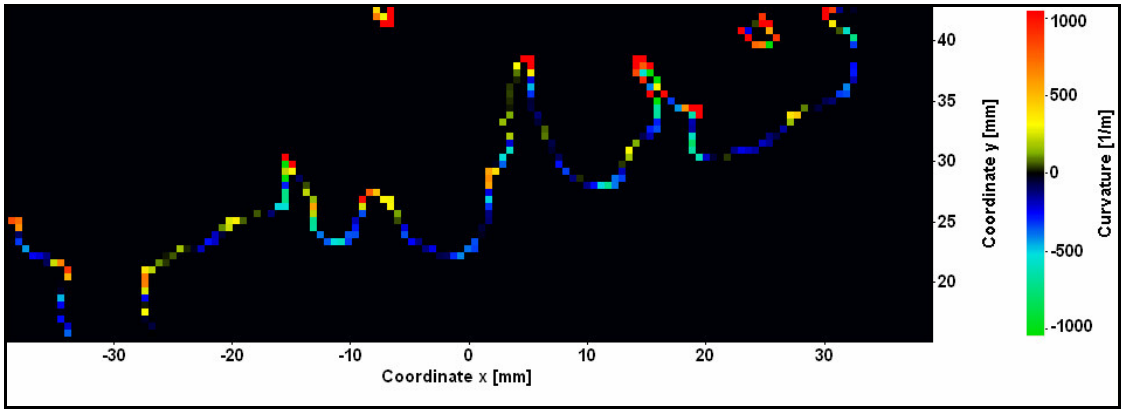

Figure 6.27. Flame curvature along the flame front shown in Figure 6.26.

An example of the curvature calculation result is shown in Figure 6.27, which has been obtained from the progress variable field in Figure 6.24. All the curvature values have been then collected for each flame condition considered in order to produce the respective PDF distribution and to allow a statistical analysis that will be presented in Section 9.2.

When the curvature is known, the radius of curvature (r_c) can be obtained using the following equation:

$$r_c = \frac{1}{\kappa} \qquad (6.20)$$

The radius of curvature is then the reciprocal of the curvature.

In the calculation procedure of curvature and radius of curvature it has been imposed a minimum limit for the length of the radius detectable. This is given by the distance between the centres of the interrogation regions previously defined. It follows that radius of curvature smaller than 0.5mm and curvature higher than $2000\,m^{-1}$ have not been detected. This determines also the limits of the variation of the tangential angle, $\Delta\theta: [-\pi/4;\pi/4]$.

The error introduced in the calculation of the radius of curvature due to the approximation of the arc length, Δs_a , with the chord , Δs_c , is given by the difference between the real radius of curvature and the calculated one, $r_c - [r_c]_C$. According to trigonometric rules the following equations define the arc length and a chord for a given tangential angle variation:

$$\Delta s_a = r_c\ 2\Delta\theta \qquad (6.21)$$

$$\Delta s_c = r_c\ 2\sin(\Delta\theta) \qquad (6.22)$$

The error introduced in the radius of curvature results is:

$$e_c = r_c - [r_c]_C = \frac{\Delta s_a}{\Delta\theta} - \frac{\Delta s_c}{\Delta\theta} = 2\ r_c - 2\ r_c\ \frac{\sin(\Delta\theta)}{\Delta\theta} = r_c\left(2 - 2\frac{\sin(\Delta\theta)}{\Delta\theta}\right) \qquad (6.23)$$

The relative error is:

$$e_c^R = \frac{e_c}{r_c} = 2 - 2\frac{\sin(\Delta\theta)}{\Delta\theta} \qquad (6.24)$$

Figure 6.28 shows the values of the relative error as a function of the tangential angle variation, $\Delta\theta$. The maximum relative error (20%) is encountered for the limit case ($\Delta\theta = \pi/4$). The relative error decreases when the radius of curvature increases.

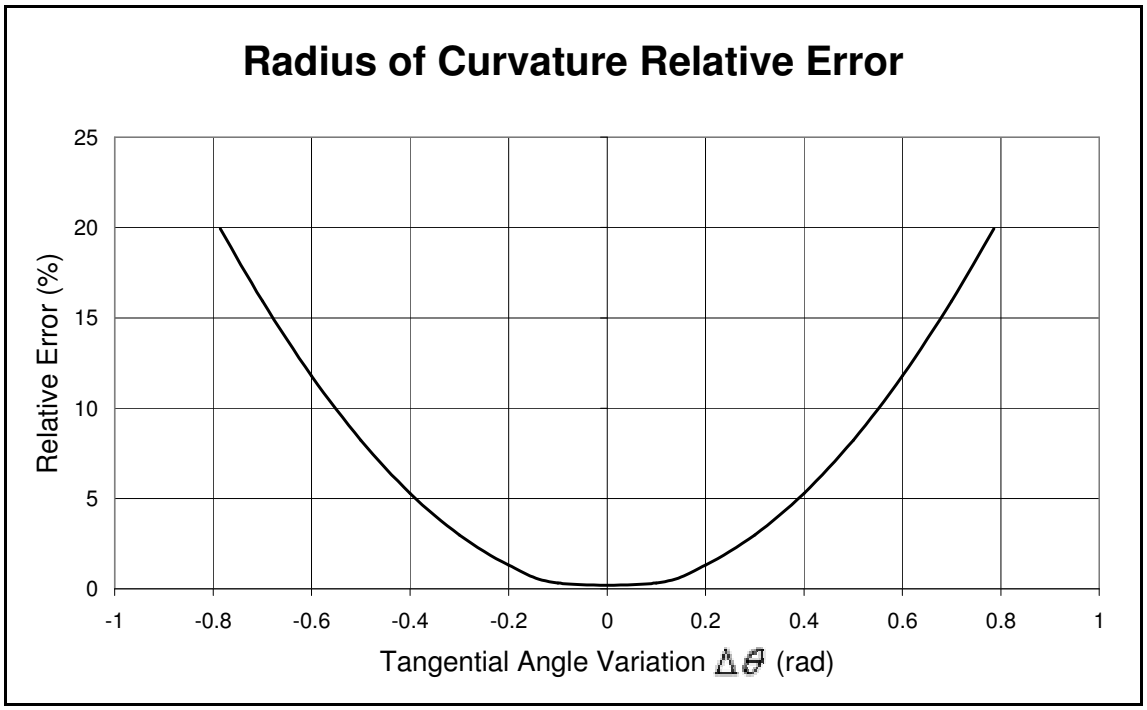

Figure 6.28. Relative error as a function of the tangential angle variation, $\Delta\theta$.

6.4 Flame Thermal Thickness

The flame thermal thickness is a flame front characteristic that is strongly related with the chemical properties of the fuel mixture and the turbulence level of the oncoming flow. Section 2.2.2 has been used to differentiate turbulent combustion regimes considering the thickening effect of the turbulence on the flame front. The following paragraph describes the procedure to extrapolate this parameter from the instantaneous progress variable fields.

The flame thermal thickness is defined using the reduced temperature profile along a line orthogonal to the flame front. The representative profile of the reduced temperature or the progress variable in the flame front of a premixed methane-air flame is shown in Figure 6.29. The progress variable plot is characterized by a change in concavity in P for values of c close to 0.5. The tangential line of the reduced temperature profile in P is used to obtain the flame thermal thickness. It is defined by the x coordinates of the intersections between the tangent in P and the horizontal lines at $c = 0$ and $c = 1$ (Poinsot and Veynante, 2001).

The flame thermal thickness has been calculated from the instantaneous progress variable fields approximating the tangent line in P with the line that passes through the points of the reduced temperature profile at $c = 0.6$ and $c = 0.4$. Following the approach shown in Figure 6.29 the thickness $\delta_{0.2}$ has been calculated between the points at $c = 0.4$ and $c = 0.6$, and then the flame thermal thickness using the relation

$\delta_{Th} \approx 5\delta_{0.2}$ has been obtained. The flame thickness $\delta_{0.2}$ has been calculated as the ratio of the area associated with the pixels at $0.4 \le c \le 0.6$ and the respective flame front length in the instantaneous progress variable fields.

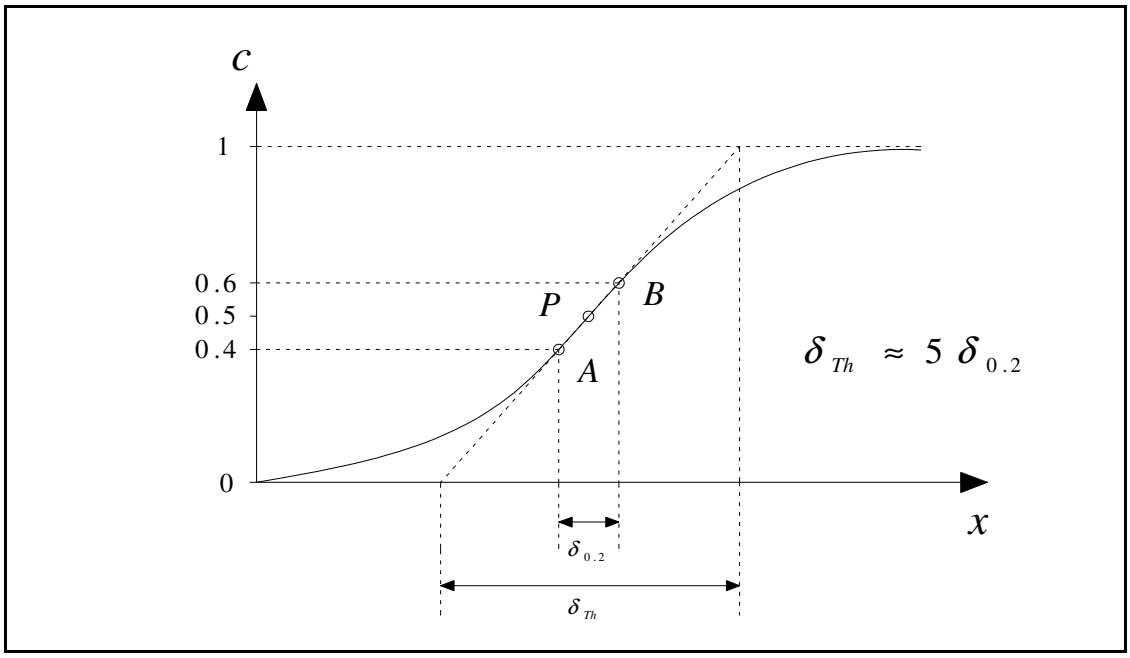

Figure 6.29. Schematic illustration of the progress variable profile for a premixed methane-air flame, with x the coordinate along a line orthogonal to the flame front. The progress variable (or reduced temperature) increases from 0 for the unburnt gases to 1 for the completely burnt gases. The reduced temperature profile is characterized by a change in concavity in P and the tangential line in this point is used to define the flame thermal thickness. The tangent's intersections with the horizontal lines for $c = 0$ and $c = 1$ determine on the x axis the value of the thermal thickness.

The operative procedure in order to obtain the flame thermal thickness begins with the division of the frame area in thirty regions associated to vertical and adjacent stripes of width 38 pixels (~3mm). In order to do these thirty mask frames have been defined, Ms_i with $i = 0,...,29$. For each progress variable field it has been possible to deduce up to thirty values for the flame thermal thickness, all related to different flame front segments.

The instantaneous progress variable fields have been converted in frames called Pv_R with pixels' value equal to 1 for $0.4 \le c \le 0.6$ and pixels' value equal to 0 for $c < 0.4$ and $c > 0.6$. Using the instantaneous progress variable fields the flame front frames, Pv_{FF} , has been obtained using the pixels with $c = 0.5$, following a similar procedure already used to define the flame front for the calculation of the flame curvature in Section 6.3. The flame thermal thickness relating to the $i-th$ vertical mask has been calculated according to the following equation:

$$\delta_{Th-i} = \frac{\int Ms_i \, Pv_R}{\int Ms_i \, Pv_{FF}} \qquad (6.25)$$

The integral operation is considered as a sum of the pixels' values for all the pixels of the frame that is the argument of the integral. The Equation (6.25) has been applied only for the vertical masks with: $\int Ms_i \, Pv_{FF} > 38$. This condition guarantees that the flame front length of the segment considered for the integration is at least 3mm. The values of the flame thermal thickness have been used to define the probability distributions that will be analyzed in Section 9.3.

For the flame thermal thickness calculation the absolute error is introduced by the larger of the two limits imposed by image resolution ($\approx 75\mu m$) and average laser sheet thickness ($\approx 160\mu m$). It follows that the absolute error can be assumed as $\approx 160\mu m$.

7 ACETONE PLIF EXPERIMENTS AND ANALYSIS

Experiments using PLIF signal from acetone have been performed in order to obtain data on fuel concentration. In this chapter the fuel tracer selection will be analyzed, considering the various fuel tracers available. The experimental apparatus is described with its optic tools used to manipulate the laser beam and to collect the fluorescence signal from the sample volumes selected. The images collected needed accurate processing in order to extract the fluorescence signal. From the knowledge of the relation between the fluorescence signal and the fuel concentration, the equivalence ratio distribution has been obtained. The information about the equivalence ratio distribution is important to analyze the fuel stratification effects on flame front propagation.

7.1 Fuel Tracer Selection

Laser induced fluorescence is emitted by atoms and molecules pumped at higher energy levels through the absorption of photons that are usually in the ultraviolet and visible spectral region. The wavelengths absorbed are directly proportional to the dimension of the molecule chromophore that is the active part of the excited molecule. The majority of combustion fuels are aliphatic hydrocarbons and consequently they are transparent within the spectral range mentioned. Many unsaturated and aromatic components are contained in commercial fuels and they are capable of a strong absorption that leads to an intense fluorescence. It has to be considered that the light emitted is characterized by various wavelengths because of the different sources involved. It is preferred to use signal coming from a single species when undertaking quantitative analysis. For this reason the flow analyzed is usually seeded with a well characterized fluorescing tracer. There is not a tracer that is suitable for all the experimental conditions. The tracer signal depends on temperature, pressure and other properties of the environment at which the experiments take place. It is important to know these interdependencies, in order to interpret correctly the data collected and to choose the most suitable tracer for the experiments objectives. The ideal tracer should have the same properties of the fuel considered in terms of diffusion, convection, reactivity, and reaction rate. It is difficult to find a tracer that is capable of matching exactly the fuel characteristics but the differences must be kept to a minimum.

7.1.1 Acetone Characteristics as Fuel Tracer

"Acetone ($CH_3 - CO - CH_3$) satisfies most of the requirements of a PLIF tracer for gaseous flows. It has a fairly high vapour pressure, 180 Torr at room temperature (20°C), which allows a maximum seeding density of ~30% mole fraction. It absorbs over a broad band of Wavelength (225-320nm) with a maximum between 270 and 280nm. The fluorescence emission is broadband in the blue (350-450nm) with an efficiency of 0.2% and a short lifetime of less than 4ns. The fluorescence is relatively independent of temperature and local gas composition. Acetone is not highly toxic, and its cost is economical" (Lozano, 1992).

Acetone is a ketone of molecular weight 58.08. Under normal conditions it is a transparent liquid with specific weight 0.79. It is highly flammable with melting point -95°C, boiling point at 56°C and autoignition temperature 465°C. The vapour pressure of acetone determines its maximum possible seeding density when used as fluorescent molecular marker. The vapour density at 20°C is double the density of the air. Acetone toxicity is very mild although prolonged exposure to its vapour or mist can irritate the eyes, mucous membranes and upper respiratory tract and cause nausea, headaches, vomiting and dizziness. Acetone is not considered to be carcinogen.

There are three electronic states involved in the photoemission processes: the ground state singlet (often referred as S_0), the first excited singlet (or S_1) and the first excited triplet (or T_3). Each electronic state has a manifold of vibrational levels. The absorption spectrum suggests several possible excitation sources for pumping acetone in a LIF experiment. These include a $XeCl$ excimer laser (λ=308nm, $\sigma = 1.6 \times 10^{-20} cm^2$), a KrF excimer laser (λ=248nm, $\sigma = 2.3 \times 10^{-20} cm^2$), a frequency quadrupled Nd:YAG laser (λ=266 nm, $\sigma = 4.4 \times 10^{-20} cm^2$). Most of the excited acetone molecules in the singlet state are transferred to the triplet state (intersystem crossing) with nearly 100% efficiency. Almost all of the remaining excited singlet molecules fluoresce. The emission spectrum of acetone is shown in Figure 7.1 upon excitation at 266nm at 20°C with 13mbar tracer in 1bar N_2.

Excited molecular levels can be depopulated through non-radiative relaxation processes which include predissociation, internal conversion, intersystem crossing and collisional quenching. Collisional quenching rates vary with temperature and local gas composition, thus complicating the interpretation of PLIF signals when such quenching is significant. The dominant de-excitation path for acetone singlets is the intra-molecular intersystem crossing to triplet levels: collisional quenching is negligible, and therefore the quantum yield is independent of molecular collisions, hence independent of temperature and local gas composition. For concentration measurements, acetone fluorescence signals are particularly easy to interpret.

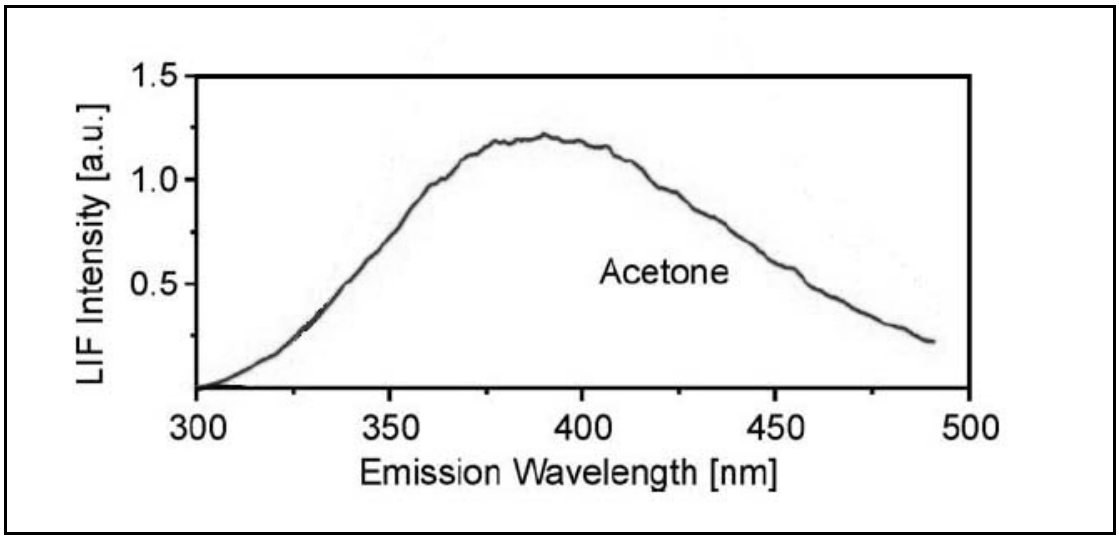

Figure 7.1. Emission spectrum of acetone upon excitation at 266nm at 20°C with 13mbar tracer in 1 bar of N_2 (Schulz and Sick, 2005).

7.1.2 Comparison with other Tracers

Several simple fluorescent tracer molecules have been used for concentration measurements in gas flows, including I_2, NO and NO_2 (Hiller and Hanson, 1990). These molecules have well characterized spectral properties. Specific rotational-vibrational states can be excited, and temperature, concentration, and velocity information can be obtained from the fluorescence signal. However, all these substances are highly toxic and I_2 in particular is highly corrosive. Furthermore, their fluorescence is strongly quenched by collisions with oxygen molecules. For these reasons, these tracers are better suited to low pressure, low flow rate applications.

For concentration measurements, the tracer molecule does need not to have a simple discrete absorption spectrum. The fluorescence need simply be related to concentration with a known dependence (preferably linear). A number of organic polyatomic molecules have been used, including biacetyl, acetaldehyde and acetone (Lozano et al., 1992). These have the advantages of lower toxicity and lower reactivity, and suffer less fluorescence quenching than the species cited above. These products have fairly low fluorescence efficiencies. Unfortunately most chemicals with high emission efficiencies are solids with extremely low vapour pressures (anthracene, naphthalene, fluorine, laser dyes). Though acetone, acetaldehyde, and biacetyl are liquids, their vapour pressures are high, and seeding is relatively easy, either by bubbling or injecting the carrier gas into the liquid container, or by spraying the liquid to a mixing tank. The more volatile a fluorescent marker, the higher the concentration that can be seeded in the flow, consequently increasing the emission signal.

Acetaldehyde ($CH_3 - CHO$) absorption (250-340nm) peaks at 290nm, with an absorption cross-section $\sigma = 4.6 \times 10^{-20} cm^2$. Acetaldehyde has a high vapour pressure (boiling point 21°C), which enables extremely high concentrations, although at some point the fluid will become an optically thick medium. The fluorescence spectrum is very close to that of acetone. Acetaldehyde has properties rather similar to those of acetone, but with the significant drawback that it is toxic and carcinogenic.

Biacetyl ($CH_3 - (CO)_2 - CH_3$) has been widely used as a PLIF tracer, and its photo-physical behaviour has been studied extensively (Liu et al., 1988). Biacetyl toxicity is very mild and its boiling point is 88°C (vapour pressure ~40Torr at 20°C). The absorption is broadband (340-470nm) with a peak at 417nm ($\sigma = 8 \times 10^{-20} cm^2$). The fluorescence emission is broadband in the blue with a lifetime of ~15ns and a peak at 485nm. The phosphorescence is long lived (lifetime of 1.5ms), and presents a strong peak at 512nm, a secondary peak at 610nm. Phosphorescence is 60 times stronger, but its long lifetime prevents its use in fast flow experiments, unless a gated camera system is used.

Another complex molecule, hexafluoroacetone ($CF_3 - CO - CF_3$), should be mentioned. It is a gas at room temperature (boiling point -26°C). The absorption cross section is $\sigma = 3.1 \times 10^{-20} cm^2$ at 303nm, with the absorption band extending from 245 to 355nm. Its fluorescence emission extends from 347 to 600nm with a maximum at about 430nm, and a lifetime of 84ns. Hexafluoroacetone would seem to be an ideal tracer for gaseous PLIF imaging. Unfortunately it is extremely toxic and potentially lethal if inhaled.

It can be concluded that acetone and acetaldehyde fluorescence signals are quite similar, so that acetone's lower toxicity makes it a preferable choice as a tracer molecule. Only hexafluoroacetone performs better than acetone, but its extreme toxicity makes it impractical.

7.2 Experimental Apparatus

The experimental apparatus used for Acetone-PLIF measurements is shown in Figure 7.2. It used an Nd:YAG Laser (Quanta Ray) as laser source, with around an 8ns pulse width and 600 mJ of energy. The output end of the Nd:YAG laser is coupled with a harmonic generator set for producing a third harmonic wavelength of 266nm (ultraviolet). The final output beam has a diameter approximately 8 mm and 120 mJ per pulse, with most of the light at 266 nm in addition to some residual infra-red and 532nm (green) light.

A front coated dichroic mirror (266nm) at 45° incident angle has been used to steer the output light from the second harmonic generator of the Nd:YAG laser. The 266 nm component of the beam has been reflected horizontally in the perpendicular direction. This beam has been reflected again perpendicularly by a second dichroic mirror of the same type mounted on an adjustable holder to steer the beam towards the burner at

some 1.5 meters away. A fused silica positive cylindrical lens (150mm focal length) and a fused silica positive spherical lens (1000mm focal length) have been used to produce a laser sheet ~30mm high with an average thickness of $160\mu m$. In order to measure the laser power output the laser beam component that passes through the second mirror has been reflected using a front coated dichroic mirror (266nm) to steer the beam towards a (266nm) mirror that then directs the laser beam on the camera lenses. The intensity of this laser beam component is further decreased using a neutral density filter of optical density 0.5, to avoid any damage on the collecting system (intensifier-camera CCD). This component of the laser beam has been focused by a fused silica positive spherical lens (500mm focal length) in order to be imaged on a corner of the camera CCD.

The images have been recorded using a La Vision Flow Master camera connected to a La Vision Intensifier with UV-Nikkor 105mm focal length lenses. The lenses aperture used for all the experiments has been f/1.8 and the intensifier gain has been set to 7.5, this combination was characterized by the higher signal to noise ratio (~18). Between the camera system and the burner a BG4 filter has been placed in order to guarantee that only the acetone fluorescence signal is collected. The BG4 filter optical transmission spectrum is shown in Figure 7.3. The software used for controlling the hardware while collecting the images was DaVis 7.1 from La Vision. The same software has been used for processing the collected images in order to gain the fuel concentration fields.

The acetone combustion process develops with a different chemistry and energy release when compared to methane. In the experiments here, the effect of small differences in methane concentration on the flame front propagation is studied, and the introduction of acetone in the combustible mixture would have hindered that analysis. For this reason Acetone-PLIF experiments have been performed only on cold flow conditions. The objective of the application of this experimental technique is to determine the average equivalence ratio distribution in the gas mixture upstream the flame.

The flow seeded with acetone has been used to substitute the methane flow in the burner's gas support system. The experiments have been performed for each "Bulk Flow" using both "Collars". In each condition the inner and annular combustible mixture flows have not been seeded at the same time, because it has been possible to seed only one line at a time. The experiments have been performed in two stages, one for the inner flow and another one for the annular flow. The average concentrations of the two flows in the imaged region have been correlated in order to determine the average equivalence ratio distribution.

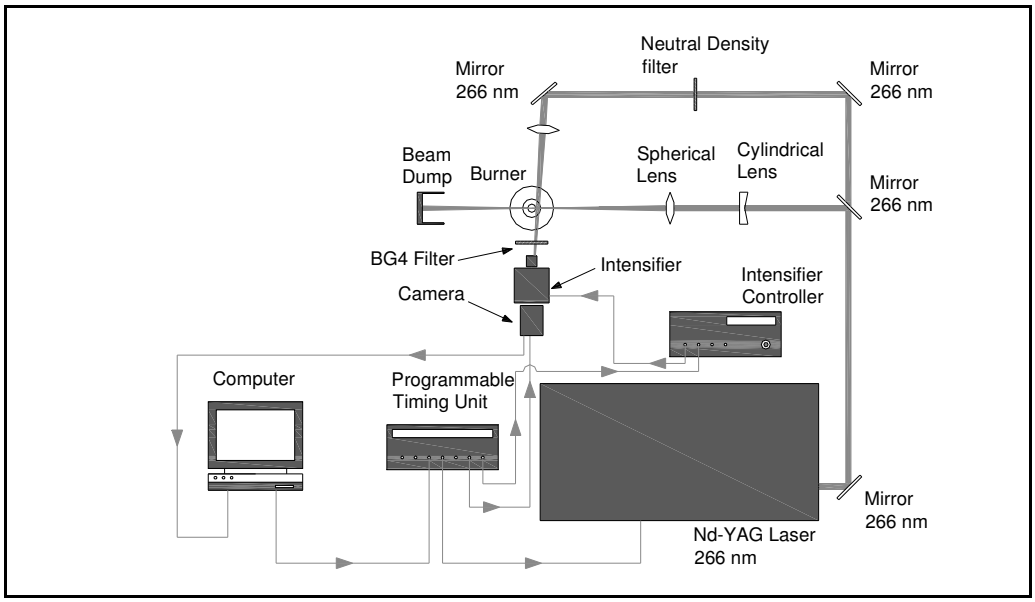

Figure 7.2. Experimental apparatus used for Acetone PLIF experiments. The laser source and the laser sheet forming optics are displayed. The electronic tools used for collecting the measurements and their connections are shown.

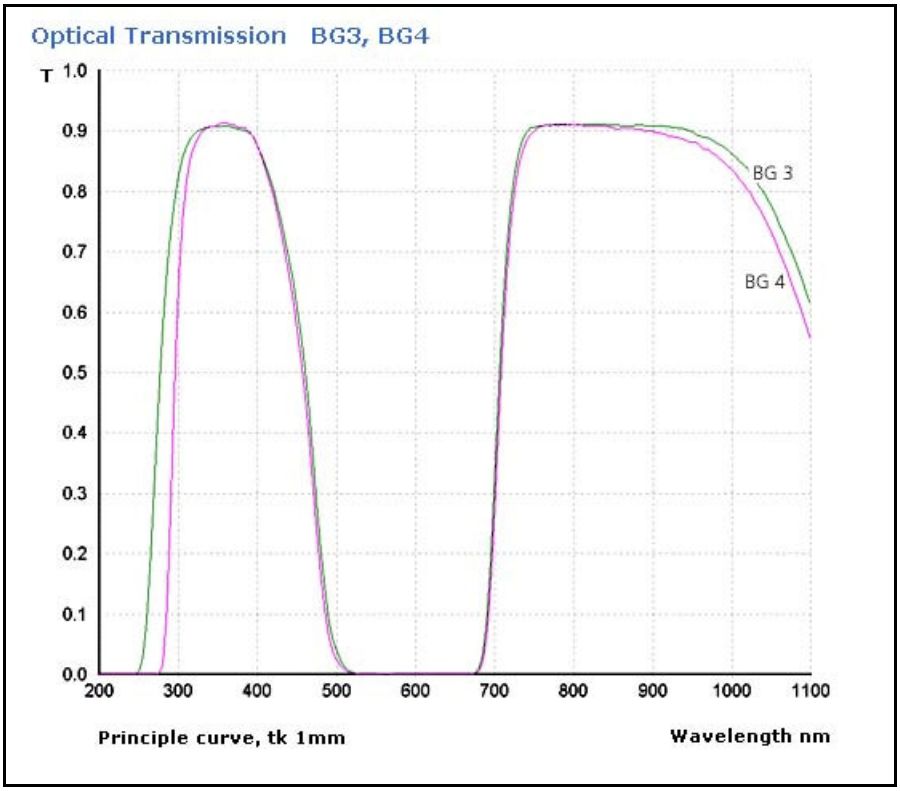

Figure 7.3. Optical transmission curve for BG4 and BG3 filters (Praezisions Glas & Optik GmbH, 2007).

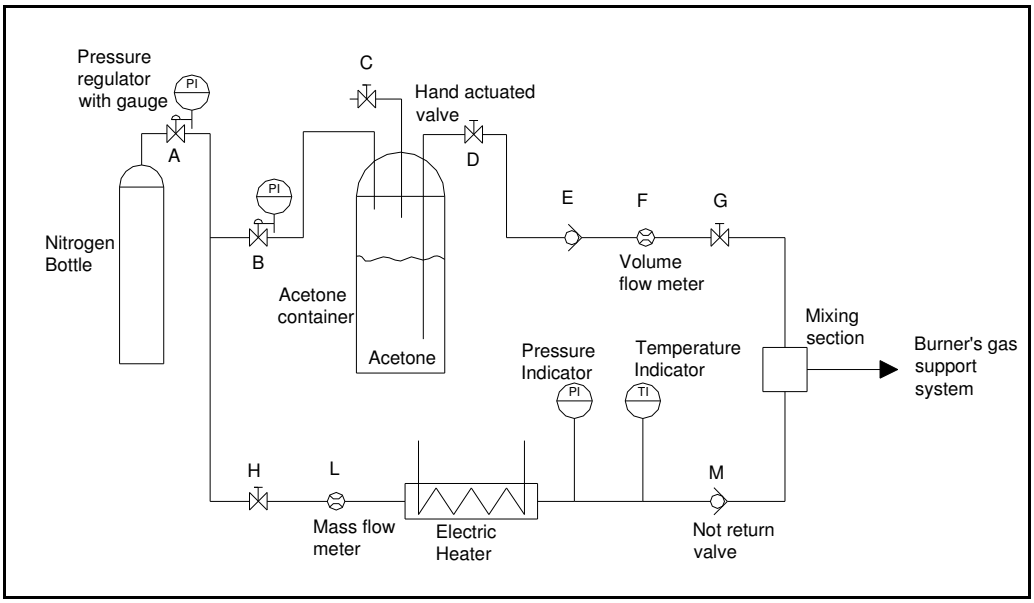

Figure 7.4. Acetone seeding system. The liquid acetone is injected in the heated flow of nitrogen (250°C) that controls the vaporization of acetone. The mixture of nitrogen and acetone is then used to replace the methane source line of the burner's gas support system.

The acetone used as fuel tracer has been seeded in nitrogen using the system shown in Figure 7.4. The acetone container is pressurized at 7 bar using nitrogen. After opening valve "D" the acetone flow rate is controlled by operating on valve "G" and measured by a volume flow meter. On a second line nitrogen is heated at 250°C using an electric heater. The nitrogen flow rate is measured by a mass flow meter. The liquid acetone is injected in the mixing section and it evaporates once in contact with nitrogen at 250°C. Nitrogen has been used to avoid any risk of igniting the acetone. The mixture of nitrogen seeded with acetone vapour is then sent to the burner gas support system to substitute the methane line. The system has been used with the following flow rate values:

- Nitrogen: 3g/s
- Acetone: 0.4g/s

The position and the dimensions of the imaged area for Collar 1 are displayed in Figure 7.5 while for the two cases of Collar 2 are presented in Figure 7.6 and Figure 7.7. The selection of the imaged area has been driven by the necessity of matching as close as possible the imaged areas used for PIV and Rayleigh measurements in order to correlate data collected using different techniques. The resolution for the images was $\approx 75 \mu m / pixel$ for all the experiments.

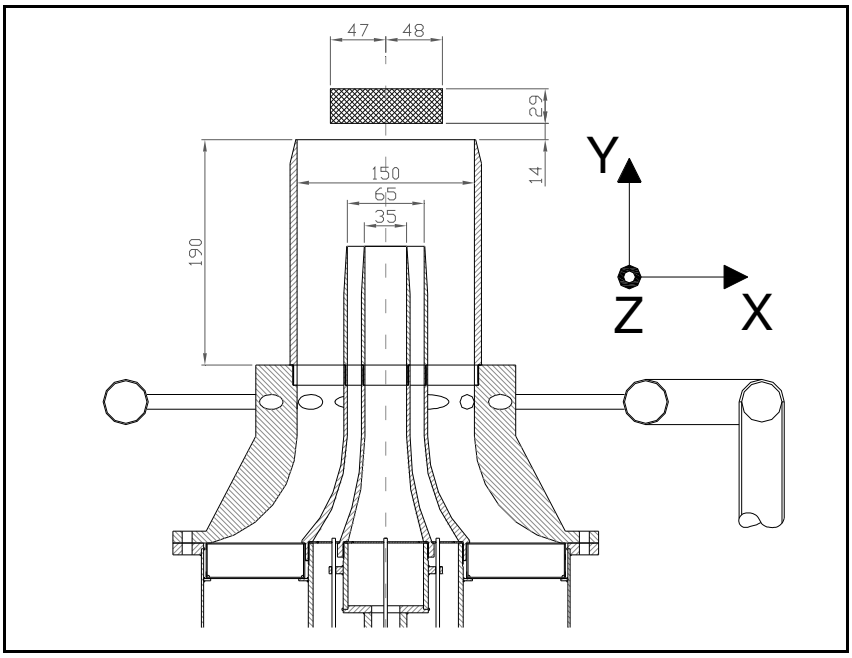

Figure 7.5. Dimensions and position of the area imaged using Acetone-PLIF on burner outlet configuration Collar 1 (all measures are in mm). The reference system is shown and its origin must be considered coincident with the centre of the burner outlet circular rim (150mm ID).

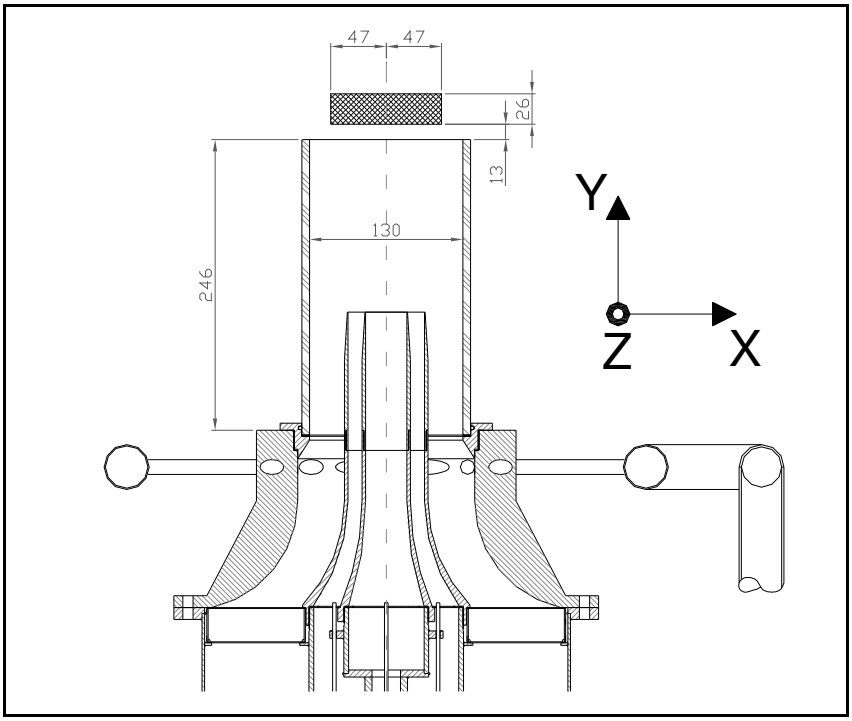

Figure 7.6. Dimensions and position of the area imaged using Acetone-PLIF on burner outlet configuration Collar 2 (all measures are in mm). The reference system is shown and its origin must be considered coincident with the centre of the burner outlet circular rim (130mm ID).

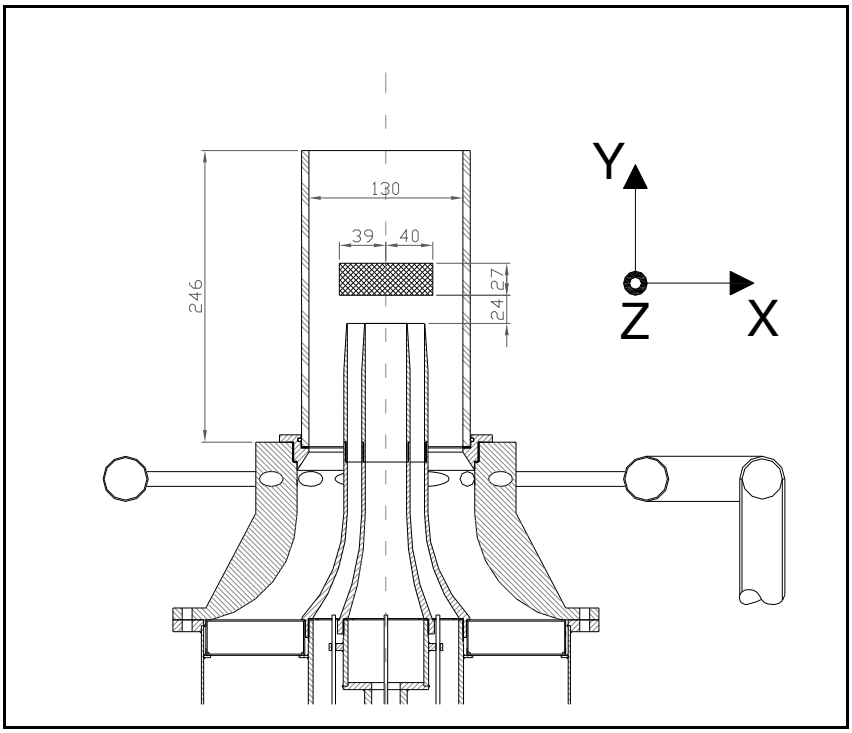

Figure 7.7. Dimensions and position of the area imaged using Acetone-PLIF on burner outlet configuration Collar 2 inside the glass tube (all measures are in mm). The reference system is shown and its origin must be considered coincident with the centre of the annular collar circular rim (65mm ID).

7.3 Image Processing

The raw images need to be corrected for inherent system characteristics in a similar manner to what has been done for the Rayleigh experiments irrespective of the type of light scattering processed involved.

Note that only for the image processing procedure the conventions are such that the laser sheets are parallel to the x-y plane, the x coordinate is parallel to the direction of beam travel, and the origin of the coordinates is placed at the top-left of the images. The units for the coordinate values of x and y are pixels.

Each untreated image is considered as a discrete light intensity function, $F_L(x, y)$, expressed algebraically as:

$$F_L(x, y) = k_L \; R_{op}(x, y) \left[S_{st}(y) \; I_{LIF}(x, y) + B_G(x, y) \right] + E_B(x, y) \qquad (7.1)$$

That is the LIF equivalent expression to that stated in Equation (6.1). The symbol $I_{LIF}(x,y)$ indicates the light intensity of the acetone fluorescence that we wish to obtain. The correction process involves in dealing with the following six aspects: electronic bias $E_B(x,y)$, laser energy fluctuation k_L, laser-induced background $B_G(x,y)$, optical response $R_{op}(x,y)$, and laser beam stripes $S_{st}(x,y)$.

For the experiments considered the wavelength of the acetone fluorescence light (350-450nm) is different from the laser beam light (266nm), therefore by using a BG4 filter in front of the camera lenses it has been possible to avoid the collection of any reflection from the laser beam light. The light collected by the camera system is constituted only by the acetone fluorescence signal and then the laser-induced background can be considered negligible. Applying the last consideration on Equation (7.1), it becomes:

$$F_L(x,y) = k_L\, R_{op}(x,y)\, S_{st}(y)\, I_{LIF}(x,y) + E_B(x,y) \qquad (7.2)$$

Rearranging Equation (7.2) it is possible to obtain the light intensity of the acetone fluorescence as:

$$I_{LIF}(x,y) = \frac{F_L(x,y) - E_B(x,y)}{k_L\, R_{op}(x,y)\, S_{st}(y)} \qquad (7.3)$$

Subtraction of electronic bias is done before any manipulation is performed on the images. A bias frame, $E_B(x,y)$, taken with an imaging system in the absence of light, represents the system DC level plus any small structure exhibited by the CCD and image intensifier. With the lasers inoperative, twenty frames were taken by the detection system to be averaged to form the bias frame for the system.

It has been mentioned before that the laser used is inherently unstable in its pulse to pulse energy and this is reflected in the images. For this reason a component of the laser beam has been redirected on a corner of the camera chip to monitor the beam profile of each pulse. The pulse energy is then measured using a scalar q that is obtained by averaging the whole beam profile imaged. Correcting for energy fluctuation is done simply by normalising each PLIF image by the value:

$$k_L = \frac{q}{q_{ref}} \qquad (7.4)$$

where the parameter q_{ref} is the maximum of all the values of q.

The variations introduced by the optical system responsivity are quantified using a correction frame, $R_{op}(x,y)$, or “flat field”. This is usually determined by imaging a uniform source of light. For the experimental setup considered here it is possible to use the monochromatic LIF signal emitted by a gas mixture at uniform concentration of acetone.

A probed volume at uniform concentration of acetone was created by mounting a cubic plexiglass box with 400mm side on the burner outlet. The box was provided with two vertical slots on opposite faces to allow the laser to enter and leave the volume. On the box face that was in front of the camera a rectangular hole allowed uninterrupted access of the probed volume by the camera. A continuous flow seeded with acetone was introduced in the box using the burner nozzle in order to set a uniform concentration of acetone in the box. The image collected in these conditions can be expressed by the following equation:

$$F_{Fl}(x,y) = k_{Fl}\, R_{op}(x,y)\, S_{st}(y)\, I_{Fl}(x,y) + E_B(x,y) \qquad (7.5)$$

Laser beam stripes are seen as non-uniform spatial distribution of laser energy across the height of the beam, and the distribution can be expressed by a function, $S_{st}(y)$. Although imaging the beam in a fluid at uniform concentration of acetone gives the appearance of the stripes, the exact nature of $S_{st}(y)$ is not easy to obtain since the optical response $R_{op}(x,y)$ of the imaging system is also a function of y.

Fortunately the product $R_{op}(x,y)S_{st}(y)$ is a term not difficult to correct for the LIF images. With the bias removed and energy fluctuation corrected, the grabbed image of Equation (7.2) is reduced to $R_{op}(x,y)S_{st}(y)I_{LIF}(x,y)$. Similarly the flat field image $F_{Fl}(x,y)$ of Equation (7.5) is reduced to $R_{op}(x,y)S_{st}(y)I_{Fl}(x,y)$. Dividing $R_{op}(x,y)S_{st}(y)I_{LIF}(x,y)$ by $R_{op}(x,y)S_{st}(y)I_{Fl}(x,y)$ simply removes the optical response and beam stripes problem and yields a corrected image, $\hat{I}_{LIF}(x,y)$:

$$\hat{I}_{LIF}(x,y) = \frac{c\, I_{LIF}(x,y)}{I_{Fl}(x,y)} \qquad (7.6)$$

Where c is just an arbitrary multiplying constant included for scaling the intensities.

7.4 Acquiring Equivalence Ratio

The flow has been seeded with acetone vapour as fuel tracer. From the fluorescence signal intensity it has been possible to calculate the acetone concentration and consequently the fuel concentration. It has been assumed that the acetone follows closely the methane molecules behaviour in terms of diffusion (gas-phase diffusion coefficient in air at 1 bar, 100°C: methane $0.344\,cm^2s^{-1}$, acetone $0.166\,cm^2s^{-1}$) and convection (gas-phase viscosity at 100°C: methane $13.4\,\mu Pa\,s$, acetone $9.5\ \mu Pa\,s$). It has been assumed that the high turbulence intensity in the flows here, reduce the influence of the diffusion in the mixing process. It is then expected that the lower diffusion rates of acetone do not significantly affect the results.

It has been underlined in Section 7.1.1 that acetone fluorescence is independent of temperature and local gas composition. Furthermore the experiments performed

involved the study of cold flow conditions that are characterized by constant and uniform temperature. The correlation between the fluorescence signal and acetone concentration is therefore linear.

The acetone concentration in the flow analyzed has been always set at the maximum capabilities of the acetone seeding system, in order to guarantee the maximum intensity of the fluorescence signal and a signal to noise ratio of ~18.

The experiments are performed for every Bulk Flow using each Collar. It has been possible to seed with acetone only one methane line each experimental session. Therefore the distributions of the inner and annular components of the oncoming flow have been analyzed separately seeding the two flow components in two separate stages. This means that the instantaneous image is not sufficient to calculate the equivalence ratio distribution in the flow, because it only allows calculation of the fuel concentration in one combustible flow at a time. Therefore the average frame, $\overline{\hat{I}_{LIF}}(x,y)$, has been considered for each set of images collected, calculated from 200 instantaneous corrected frames ($\hat{I}_{LIF-i}(x,y)$).

Four sets of 200 images are collected for each Bulk Flow considered, two sets for the annular flow and two sets for the inner flow. For both flow components, one set of images was collected at the conditions at which the flames are operated, then a metal extension was applied on the internal collars to deliver the mixture seeded with acetone to the imaged region without contamination by the other components of the oncoming flow. The second set of images, called reference set, has the aim to normalize the fluorescence signal, therefore it has been possible to determine the mass concentration of the flow component considered in the burner flow.

The normalization procedure is explained through an example that considers the case of Bulk Flow 1, Collar 2 and swirl number $S = 0.09$ when the imaged area is above the burner outlet (Figure 7.6). The average fluorescence signal frame, $\overline{\hat{I}_{LIF-inn}}(x,y)$, when the inner flow is seeded at the operative flame conditions is shown in Figure 7.8, while the average signal frame for the reference configuration, $\overline{\hat{I}_{LIF-inn-ref}}(x,y)$, is displayed in Figure 7.9. The average signal is calculated in the rectangle displayed in Figure 7.9 and its value, $\overline{I_{R-inn}}$, is considered as the reference signal for a sample volume where the mass percentage of inner flow is 100%. The average fluorescence signal frame is then normalized using the following operation:

$$I_{N-inn}(x,y) = \frac{\overline{\hat{I}_{LIF-inn}}(x,y)}{\overline{I_{R-inn}}} \times 100 \qquad (7.7)$$

The result, $I_{N-inn}(x,y)$, is displayed in Figure 7.10, and it represents the mass fraction of the inner flow, expressed as a percentage, in the region imaged taking into account that the oncoming flow of the burner outlet is composed of three components: inner flow, annular flow and swirl flow. The conversion from the normalized fluorescence signal to mass fraction of the seeded flow is allowed by the linear correlation between acetone fluorescence and its concentration in mass.

A similar normalization procedure is followed when the annular flow is seeded with acetone. The average fluorescence signal frame, $\overline{\hat{I}_{LIF-ann}(x,y)}$, for the operating conditions is shown in Figure 7.11, while the average signal frame for the reference configuration, $\overline{\hat{I}_{LIF-ann-ref}(x,y)}$, is displayed in Figure 7.12. The average signal, $\overline{I_{R-ann}}$, for the uncontaminated annular flow is now calculated considering the pixels' values in the two rectangles shown in Figure 7.12. The following equation is used for the signal normalization and conversion to annular flow mass fraction expressed in percentage:

$$I_{N-ann}(x,y) = \frac{\overline{\hat{I}_{LIF-ann}(x,y)}}{\overline{I_{R-ann}}} \times 100 \qquad (7.8)$$

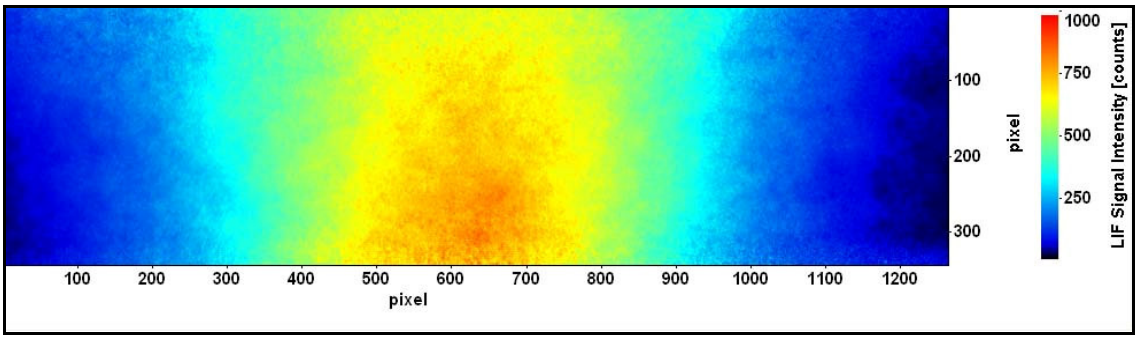

Figure 7.8. Average fluorescence signal from acetone seeded in the inner flow while running the burner in the operational conditions defined as: Bulk Flow 1, Collar 2, swirl number $S = 0.09$. The imaged area is the one above the burner outlet and it is shown in Figure 7.6.

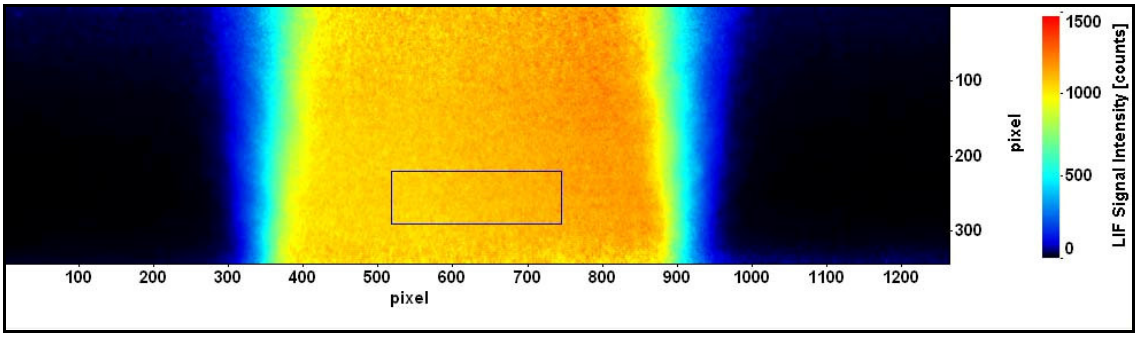

Figure 7.9. Average fluorescence signal from acetone seeded in the inner flow while running the burner in the same flow operational conditions as Figure 7.8. However on the internal collar an extension tube is installed that allows the seeded flow to reach the imaged area without mixing with the other two flow components (annular flow and swirl flow). The imaged area is the one above the burner outlet and it is shown in Figure 7.6. The average signal is calculated in the rectangle displayed and its value is considered as the reference signal for a sample volume where the mass percentage of inner flow is 100%.

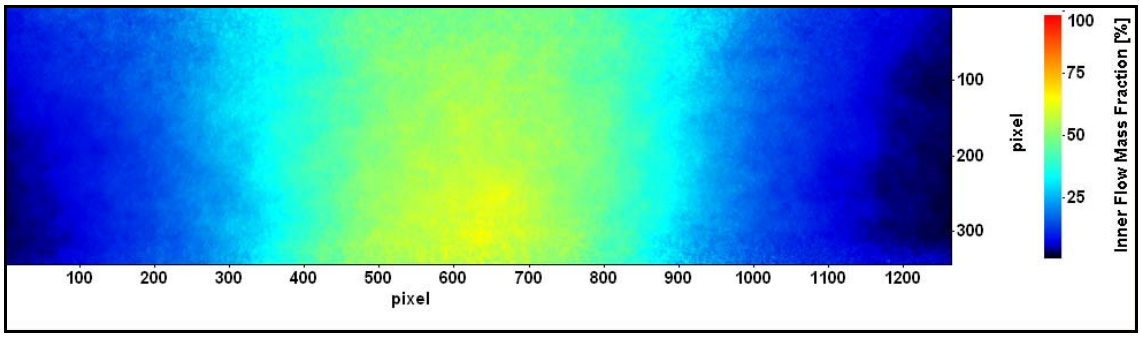

Figure 7.10. The flow where the flames propagate is composed of three components: inner flow, annular flow and swirl flow. In the figure is displayed the inner flow mass fraction express in % while running the burner in the operational conditions defined as: Bulk Flow 1, Collar 2, swirl number $S = 0.09$. The imaged area is the one above the burner outlet and it is shown in Figure 7.6.

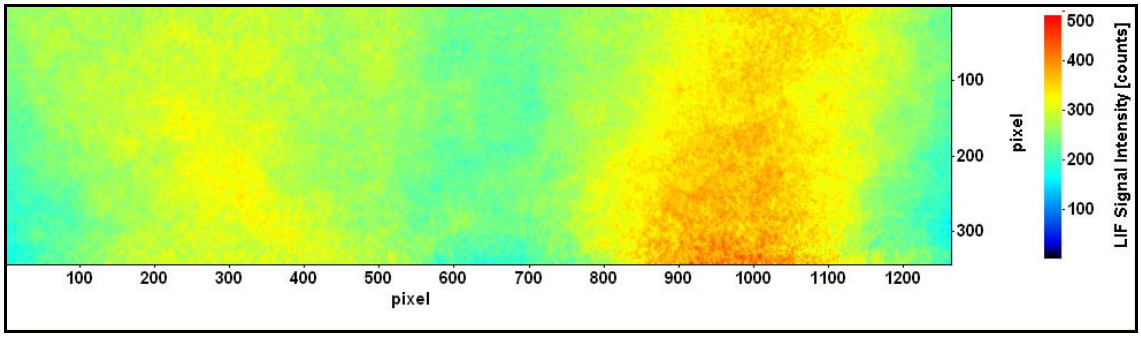

Figure 7.11. Average fluorescence signal from acetone seeded in the annular flow while running the burner in the operational conditions defined as: Bulk Flow 1, Collar 2, swirl number $S = 0.09$. The imaged area is the one above the burner outlet and it is shown in Figure 7.6.

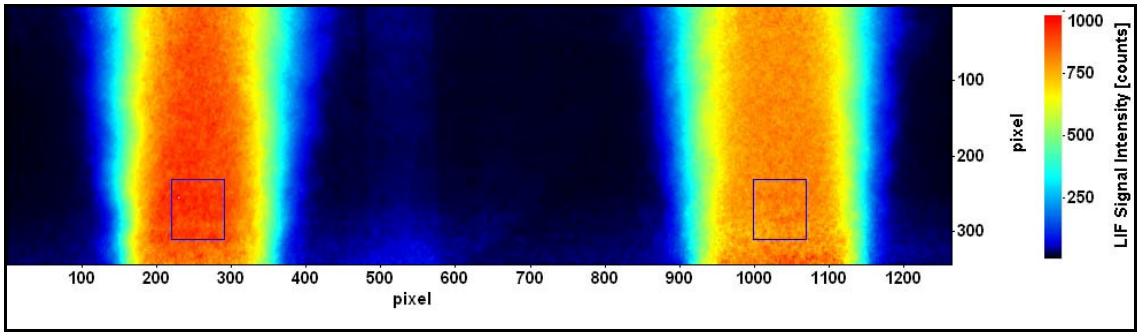

Figure 7.12. Average fluorescence signal from acetone seeded in the annular flow while running the burner in the same flow operational conditions as Figure 7.11. However on the internal collars are installed extension tubes that allow the seeded flow to reach the imaged area without mixing with the other two flow components (inner flow and swirl flow). The imaged area is the one above the burner outlet and it is shown in Figure 7.6. The average signal is calculated in the rectangles displayed and its value is considered as the reference signal for a sample volume where the mass percentage of annular flow is 100%.

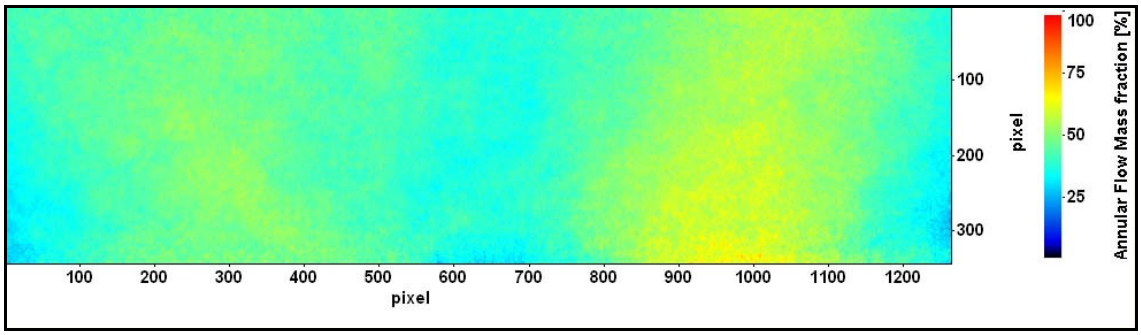

Figure 7.13. The flow where the flames propagate is composed of three components: inner flow, annular flow and swirl flow. In the figure is displayed the annular flow mass fraction express in % while running the burner in the operational conditions defined as: Bulk Flow 1, Collar 2, swirl number $S = 0.09$. The imaged area is the one above the burner outlet and it is shown in Figure 7.6.

The objective of the acetone PLIF experiments is to calculate the average equivalence ratio distribution for the flames' operating conditions, $\Phi(x, y)$. This function associates each pixel of the frame the value of the equivalence ratio ϕ. The equivalence ratio is defined as the actual fuel/air mass ratio, f, divided by the stoichiometric fuel/air mass ratio f_s:

$$\phi = \frac{f}{f_s} \qquad (7.9)$$

The ratio of the stoichiometric fuel and air mass used for the combustion is defined as:

$$f_s = \frac{M_f \times n_f}{M_a \times n_{as}} \qquad (7.10)$$

While the ratio of the actual fuel and air mass used for the combustion is defined as:

$$f = \frac{M_f \times n_f}{M_a \times n_a} \qquad (7.11)$$

The symbols used have the following meanings:

$M_f = 16$ = fuel molecular weight (methane)

$M_a = 28.96$ = air molecular weight

n_f = number of fuel moles that take part in the combustion reaction

n_a = number of air moles that take part in the actual combustion reaction

n_{as} = number of air moles that take part in the stoichiometric combustion reaction

The combustion of methane and air is defined by the following chemical reaction:

$$CH_4 + 2(O_2 + 3.76N_2) \rightarrow CO_2 + 2H_2O + 7.52N_2 \qquad (7.12)$$

From the reactants coefficients it follows that for the stoichiometric conditions:

$$n_{as} = 9.52 \times n_f \qquad (7.13)$$

If Equation (7.13) is substituted in Equation (7.10) it is possible to calculate the stoichiometric fuel/air mass ratio, $f_s = 0.05803$.

The number of fuel moles/number of air moles ratio can be also expressed as:

$$\frac{n_f}{n_a} = \frac{mc_f}{mc_a} \qquad (7.14)$$

where mc_f is the molar fraction of fuel and mc_a the actual molar fraction of air, which are related as follows:

$$mc_f + mc_a = 1 \qquad (7.15)$$

Rearranging Equation (7.9), and substituting Equation (7.11), (7.14)and (7.15), it is possible to obtain the molar fraction of fuel as function of the equivalence ratio.

$$mc_f = \frac{\phi\, f_s\, M_a}{M_f + \phi\, f_s\, M_a} = \frac{1.68 \times \phi}{16 + 1.68 \times \phi} \qquad (7.16)$$

Equation (7.16) can be used also to calculate the equivalence ratio, ϕ, from the fuel molar fraction, mc_f.

$$\phi = \frac{16 \times mc_f}{1.68 \times (1 - mc_f)} \qquad (7.17)$$

The function $Mc_f(x, y)$ defines the molar fraction of methane in the imaged area for the operative conditions and it can be calculated using the following equation:

$$Mc_f(x, y) = mc_{f-inn} \times I_{N-inn}(x, y) + mc_{f-ann} \times I_{N-ann}(x, y) \qquad (7.18)$$

All the necessary data to calculate $Mc_f(x, y)$ are available now using Equation (7.16). It is possible to obtain the fuel molar fraction for the inner flow (mc_{f-inn}) and the

annular flow (mc_{f-ann}) knowing of the respective equivalence ratio values defined in Section 4.5 for the various flames' operating conditions.

Once the molar fraction of methane is known, the equivalence ratio can be obtained applying Equation (7.17) to the function $Mc_f(x, y)$:

$$\Phi(x, y) = \frac{16 \times Mc_f(x, y)}{1.68 \times (1 - Mc_f(x, y))} \qquad (7.19)$$

Equations (7.18) and (7.19) have been applied to the experimental condition referred to Figure 7.10 and Figure 7.13 for Flame C, and the resulting equivalence ratio distribution is shown in Figure 7.14. Figure 7.15 displays the equivalence ratio profile along the horizontal line at $y = 200\,pixel$ extracted from Figure 7.14. This procedure, calculating the average equivalence ratio distribution, has been used for all the experimental conditions defined in Section 4.5.

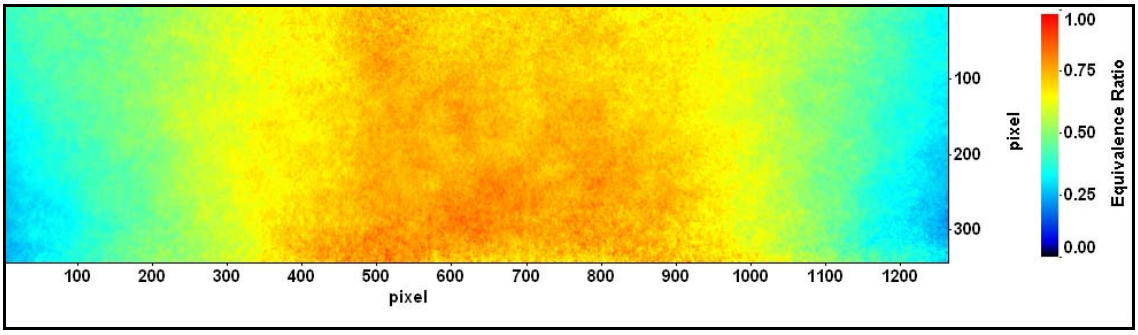

Figure 7.14. The average equivalence ratio distribution, $Mc_f(x, y)$, is displayed, when the following burner operational conditions are considered: Bulk Flow 1, Collar 2, Flame C, swirl number $S = 0.09$. The imaged area is the one above the burner outlet and it is shown in Figure 7.6.

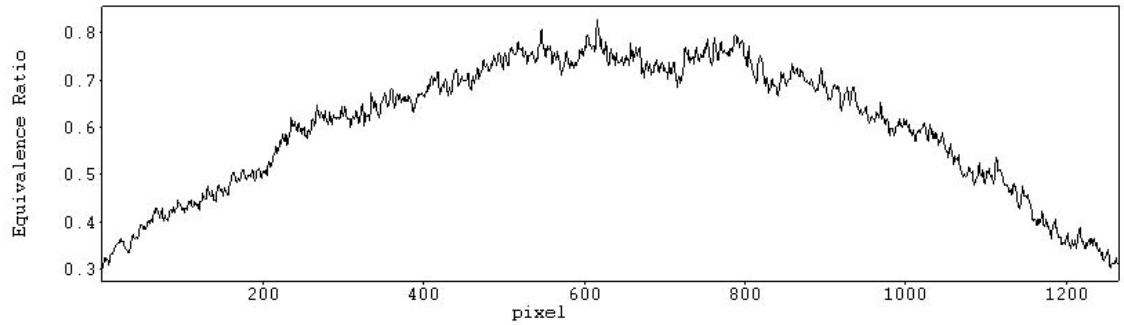

Figure 7.15. Equivalence ratio profile along the horizontal line at $y = 200\,pixel$ extracted from Figure 7.14.

8 FLAME CHARACTERISATION

Before analyzing the effect of fuel stratification on flame front propagation it is important to study the characteristics of the oncoming flow, into which the flame is propagating. At first the velocities and turbulence characteristics are studied, then the average equivalence ratio distribution will be considered. An important characteristic of the experimental data is that the boundary conditions are well defined and this allows an easy and straight forward comparison with the theoretical data that can be gained using computer modelling. The oncoming flow is well described by the velocity and concentration fields obtained in the burner outlet region and especially inside the collar mixing section. The properties of the oncoming flow play a fundamental role in determining the combustion regime that characterizes the flame propagation. In the last section of this chapter all the parameters necessary to obtain the Borghi diagram coordinates that identify the turbulent combustion regime will be calculated.

8.1 Velocity Fields analysis

PIV experiments have been performed for the all burner operational conditions defined in Section 4.5. Table 8.1 and Table 8.2 specify the flow conditions, the experimental technique used and the number of images collected for each case considered. Table 8.1 refers to burner outlet configuration Collar 1 and Table 8.2 to Collar 2. In the following analysis attention will be directed to the configuration Collar 2 because for this case Stereoscopic PIV experiments have been performed. The knowledge of all three components of the velocity allows a more complete study of the oncoming flow characteristics to be undertaken.

It has been specified in Section 5.2 that the vectors have been calculated only in the unburnt gases regions applying a dedicated mask procedure. A consequence the average quantities are conditioned averages. In the following part of the thesis, conditioned average values are considered when the analysis is related to velocity fields' data for the flames. It has been specified previously that the lack of information about the velocity fields in the hot gases region is not a major problem. The most important velocity related quantity is the burning velocity and its value is defined as the flow velocity just upstream of the flame front, this means at the edges of the cold gases area. In Section 5.3 the procedure to determine the burning velocity is analyzed accurately. In this section the velocity and turbulence characteristics of the burner outlet oncoming flow are analyzed.

Burner Outlet Configuration: Collar 1				
Bulk Flow Conditions	**Type of Flames or Flow**	**Flow Region Imaged Area**	**Experimental Technique**	**Number of Images**
Bulk Flow 1	Flame A	Burner Outlet (Figure 5.3)	2D-PIV	200
Bulk Flow 1	Flame B	Burner Outlet (Figure 5.3)	2D-PIV	200
Bulk Flow 1	Flame C	Burner Outlet (Figure 5.3)	2D-PIV	200
Bulk Flow 1	Flame D	Burner Outlet (Figure 5.3)	2D-PIV	200
Bulk Flow 1	Flame E	Burner Outlet (Figure 5.3)	2D-PIV	200
Bulk Flow 1	Flame F	Burner Outlet (Figure 5.3)	2D-PIV	200
Bulk Flow 1	Cold Flow	Burner Outlet (Figure 5.3)	2D-PIV	200
Bulk Flow 2	Flame A	Burner Outlet (Figure 5.3)	2D-PIV	200
Bulk Flow 2	Flame B	Burner Outlet (Figure 5.3)	2D-PIV	200
Bulk Flow 2	Flame C	Burner Outlet (Figure 5.3)	2D-PIV	200
Bulk Flow 2	Flame D	Burner Outlet (Figure 5.3)	2D-PIV	200
Bulk Flow 2	Flame E	Burner Outlet (Figure 5.3)	2D-PIV	200
Bulk Flow 2	Flame F	Burner Outlet (Figure 5.3)	2D-PIV	200
Bulk Flow 2	Cold Flow	Burner Outlet (Figure 5.3)	2D-PIV	200
Bulk Flow 3	Flame A	Burner Outlet (Figure 5.3)	2D-PIV	200
Bulk Flow 3	Flame B	Burner Outlet (Figure 5.3)	2D-PIV	200
Bulk Flow 3	Flame C	Burner Outlet (Figure 5.3)	2D-PIV	200
Bulk Flow 3	Flame D	Burner Outlet (Figure 5.3)	2D-PIV	200
Bulk Flow 3	Flame E	Burner Outlet (Figure 5.3)	2D-PIV	200
Bulk Flow 3	Flame F	Burner Outlet (Figure 5.3)	2D-PIV	200
Bulk Flow 3	Cold Flow	Burner Outlet (Figure 5.3)	2D-PIV	200

Table 8.1. Summary table of PIV experiments performed on Collar 1. For each set of images collected the flow conditions, the technique used and the number of images collected are specified.

A set of 150 images of cold flow conditions have been collected for Bulk Flow 1, 2 and 3, in order to analyze the flow fields when the flame was not present. The average velocity fields are shown in Figure 8.1, Figure 8.2 and Figure 8.3. The area imaged is the 91 x 37mm rectangle defined in Figure 5.4, in which the reference coordinate system is indicated. The coloured scale of the vectors is associated with the absolute value of the velocity, while the black and white scale of the background indicates the value of the z (out of plane) component of the velocity. The length and direction of the arrows are the result of the x and y component sum. In all three different conditions of oncoming flow rate (Bulk Flow 1, 2 and 3) there is a central region where the average velocity is low. This characteristic of the flow confirms the presence of the axial and radial pressure gradients produced by the weak swirl action. The axial pressure gradients are insufficiently large to cause internal recirculation but they have the effect of increasing the rate of velocity decay on the burner outlet section. At the same time the radial pressure gradients determine the divergent direction of the velocity vectors.

Burner Outlet Configuration: Collar 2				
Bulk Flow Conditions	**Type of Flames or Flow**	**Flow Region Imaged Area**	**Experimental Technique**	**Number of Images**
Bulk Flow 1	Flame A	Burner Outlet (Figure 5.4)	3D-PIV	200
Bulk Flow 1	Flame B	Burner Outlet (Figure 5.4)	3D-PIV	200
Bulk Flow 1	Flame C	Burner Outlet (Figure 5.4)	3D-PIV	200
Bulk Flow 1	Flame D	Burner Outlet (Figure 5.4)	3D-PIV	200
Bulk Flow 1	Flame E	Burner Outlet (Figure 5.4)	3D-PIV	200
Bulk Flow 1	Flame F	Burner Outlet (Figure 5.4)	3D-PIV	200
Bulk Flow 1	Cold Flow	Burner Outlet (Figure 5.4)	3D-PIV	150
Bulk Flow 2	Flame A	Burner Outlet (Figure 5.4)	3D-PIV	200
Bulk Flow 2	Flame B	Burner Outlet (Figure 5.4)	3D-PIV	200
Bulk Flow 2	Flame C	Burner Outlet (Figure 5.4)	3D-PIV	200
Bulk Flow 2	Flame D	Burner Outlet (Figure 5.4)	3D-PIV	200
Bulk Flow 2	Flame E	Burner Outlet (Figure 5.4)	3D-PIV	200
Bulk Flow 2	Flame F	Burner Outlet (Figure 5.4)	3D-PIV	200
Bulk Flow 2	Cold Flow	Burner Outlet (Figure 5.4)	3D-PIV	150
Bulk Flow 3	Flame A	Burner Outlet (Figure 5.4)	3D-PIV	200
Bulk Flow 3	Flame B	Burner Outlet (Figure 5.4)	3D-PIV	200
Bulk Flow 3	Flame C	Burner Outlet (Figure 5.4)	3D-PIV	200
Bulk Flow 3	Flame D	Burner Outlet (Figure 5.4)	3D-PIV	200
Bulk Flow 3	Flame E	Burner Outlet (Figure 5.4)	3D-PIV	200
Bulk Flow 3	Flame F	Burner Outlet (Figure 5.4)	3D-PIV	200
Bulk Flow 3	Cold Flow	Burner Outlet (Figure 5.4)	3D-PIV	150
Bulk Flow 1	Cold Flow	Inside Collar (Figure 5.5)	3D-PIV	100
Bulk Flow 2	Cold Flow	Inside Collar (Figure 5.5)	3D-PIV	100
Bulk Flow 3	Cold Flow	Inside Collar (Figure 5.5)	3D-PIV	100

Table 8.2. Summary table of PIV experiments performed on Collar 2. For each set of images collected the flow conditions, the technique used and the number of images collected are specified.

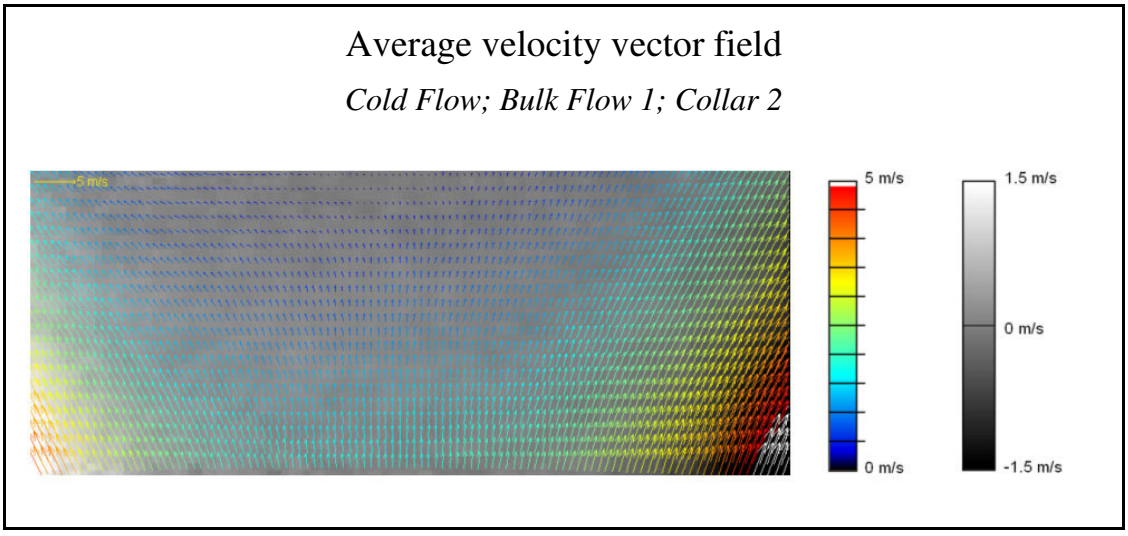

Figure 8.1. The average velocity vector field is calculated for the cold flow conditions. The experimental configuration considered is Collar 2 and Bulk Flow 1. The area imaged is the 91 x 37mm rectangle defined in Figure 5.4. The coloured scale of the vectors is associated with the absolute value of the velocity, while the black and white scale of the background indicates the value of the z (out of plane) component of the

velocity. The length and direction of the arrows in the image are the result of the x and y component sum.

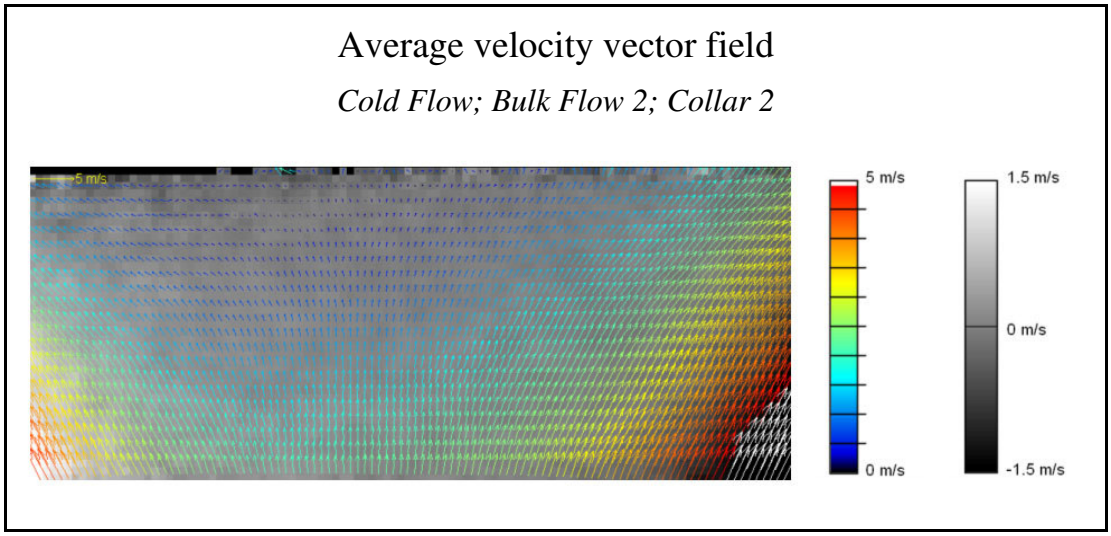

Figure 8.2. The average velocity vector field is calculated for the cold flow conditions. The experimental configuration considered is Collar 2 and Bulk Flow 2. The area imaged is the 91 x 37mm rectangle defined in Figure 5.4. The coloured scale of the vectors is associated with the absolute value of the velocity, while the black and white scale of the background indicates the value of the z (out of plane) component of the velocity. The length and direction of the arrows in the image are the result of the x and y component sum.

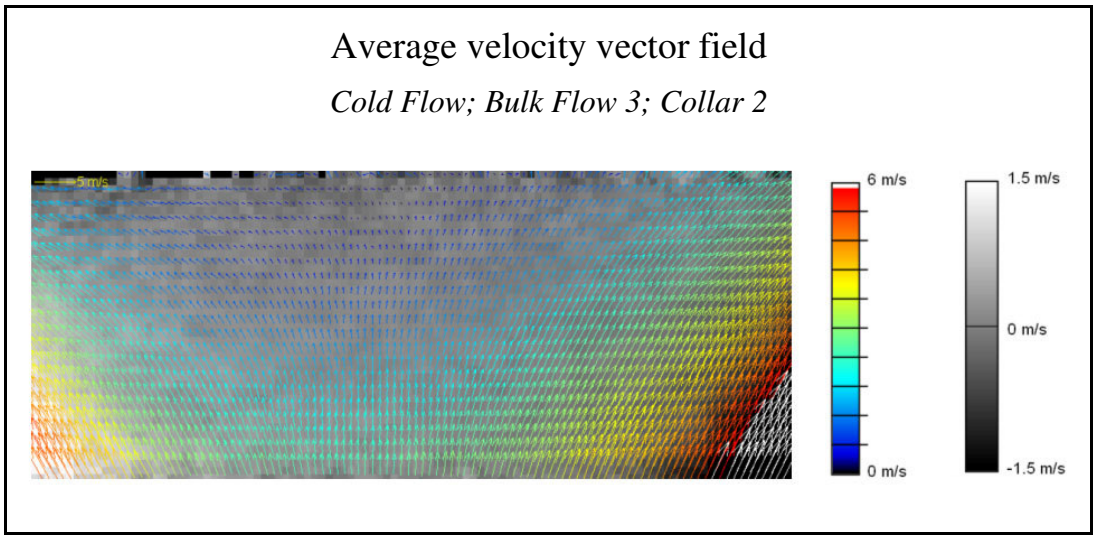

Figure 8.3. The average velocity vector field is calculated for the cold flow conditions. The experimental configuration considered is Collar 2 and Bulk Flow 3. The area imaged is the 91 x 37mm rectangle defined in Figure 5.4. The coloured scale of the vectors is associated with the absolute value of the velocity, while the black and white scale of the background indicates the value of the z (out of plane) component of the velocity. The length and direction of the arrows in the image are the result of the x and y component sum.

8.1.1 Comparison of the Velocity Vector Fields for Flames and Cold Flow Conditions

In order to compare the structure of the oncoming flow in cold flow conditions and flame conditions, Figure 8.4, Figure 8.5 and Figure 8.6 show the average velocity fields when the flame is propagating in the flow. The Flame F conditions are considered representative for the all set of flames because the conditioned average velocity fields do not change remarkably for the various flames associated with the same outlet flow rate. The average velocity field for flame conditions preserve the same structure as the cold flow case. A central region is still visible where the absolute velocity is lower in value, while on the sides it is higher. The velocity vectors maintain the divergent direction observed previously for the cold flow case.

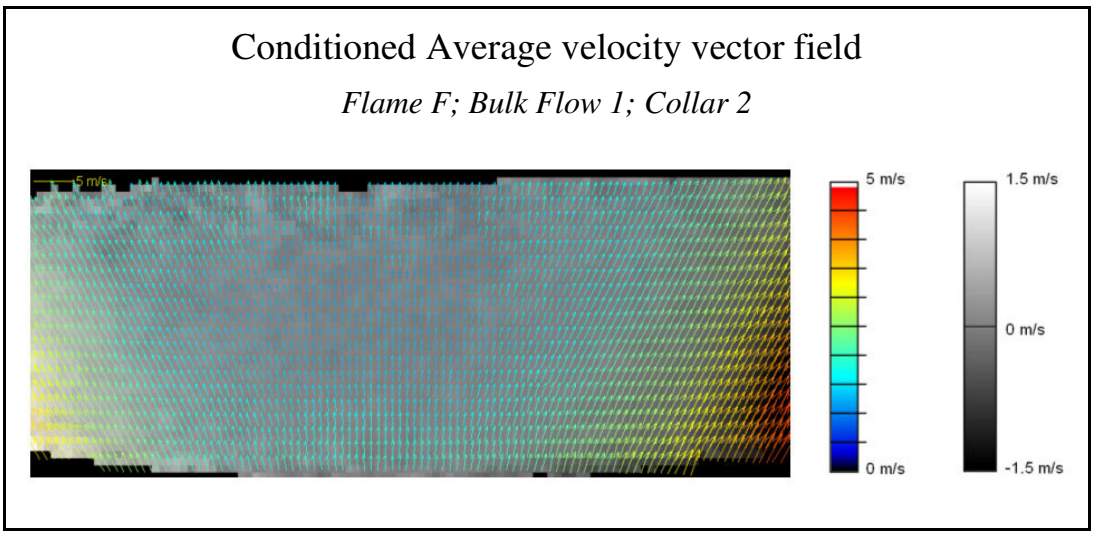

Figure 8.4. The average velocity vector field is calculated for Flame F conditions. The experimental configuration considered is Collar 2 and Bulk Flow 1. The area imaged is the 91 x 37mm rectangle defined in Figure 5.4. The coloured scale of the vectors is associated with the absolute value of the velocity, while the black and white scale of the background indicates the value of the z (out of plane) component of the velocity. The length and direction of the arrows in the image are the result of the x and y component sum.

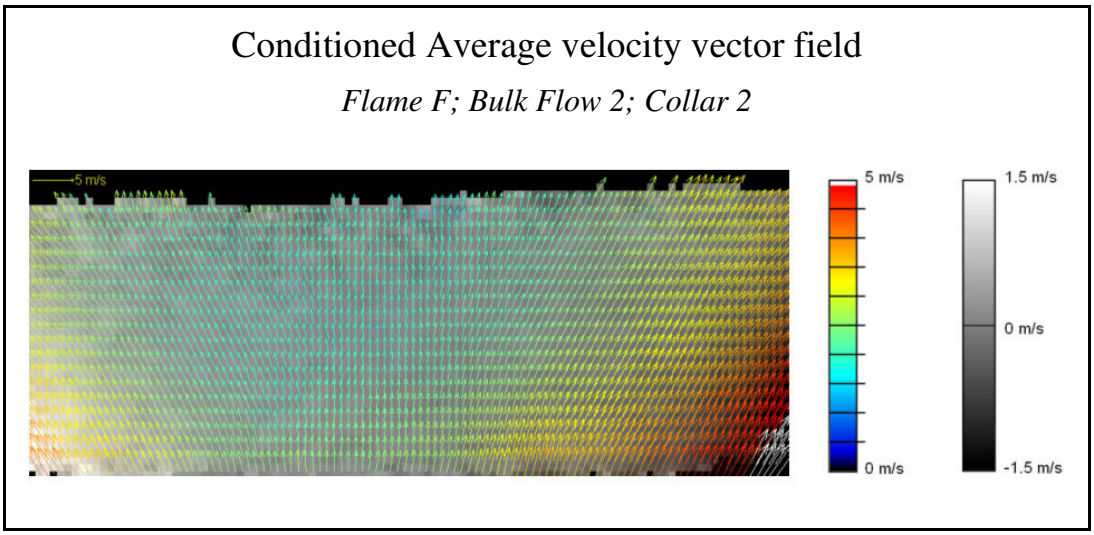

Figure 8.5. The average velocity vector field is calculated for Flame F conditions. The experimental configuration considered is Collar 2 and Bulk Flow 2. The area imaged is the 91 x 37mm rectangle defined in Figure 5.4. The coloured scale of the vectors is associated with the absolute value of the velocity, while the black and white scale of the background indicates the value of the z (out of plane) component of the velocity. The length and direction of the arrows in the image are the result of the x and y component sum.

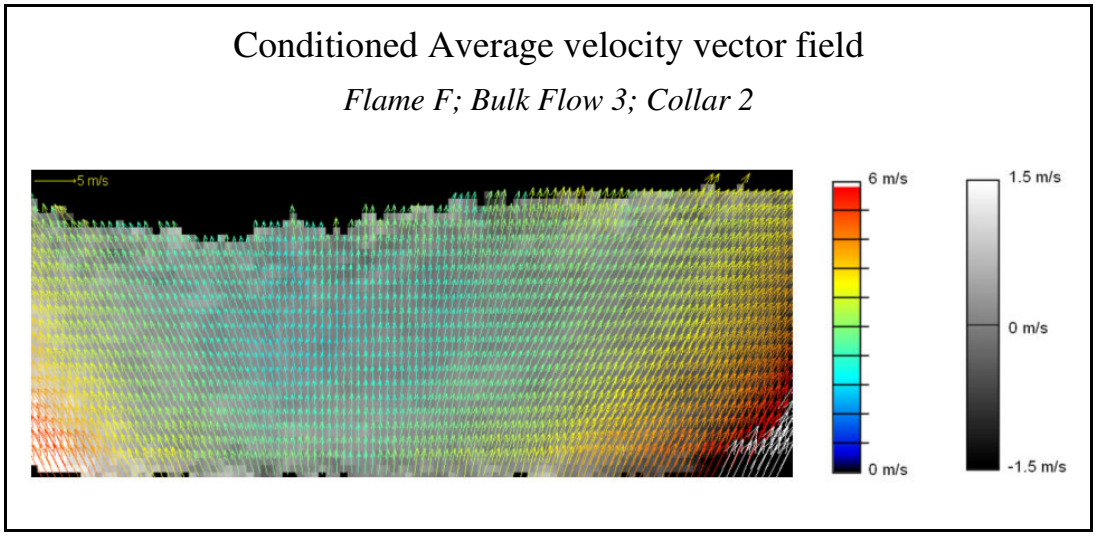

Figure 8.6. The average velocity vector field is calculated for Flame F conditions. The experimental configuration considered is Collar 2 and Bulk Flow 3. The area imaged is the 91 x 37mm rectangle defined in Figure 5.4. The coloured scale of the vectors is associated with the absolute value of the velocity, while the black and white scale of the background indicates the value of the z (out of plane) component of the velocity. The length and direction of the arrows in the image are the result of the x and y component sum.

A more detailed analysis is undertaken of the average absolute velocity values in Figure 8.7, Figure 8.8 and Figure 8.9 along a horizontal line 30mm above system origin. For Bulk Flow 1 the cold flow profile is nearly coincident with the flames profile. While for Bulk Flow 2 and Bulk Flow 3 the average absolute velocity is higher for flames conditions. When making this comparison it must be remembered that the conditioned average is calculated in the flames' case. Only the velocity vectors in the unburnt gases regions are calculated, the interrogation windows behind the flame front are not computed. When considering the instantaneous event, it can be assumed that the flame propagates along the flame front line with velocities that are equal to the oncoming unburnt flow velocities in those points. Considering that the burning velocity has a finite non-zero value, those regions where the local velocity is lower than the burning velocity are more likely to be in the burnt gases area. The related velocity vectors are not computed and their contribution is not recorded in the conditioned average velocity. The difference between the profiles for cold flow and flames is increased if higher flow rates are analyzed because the increased turbulence determines a higher burning velocity and then an increased threshold value for the unburnt gases velocities.

The threshold effect imposed by the burning velocity also reduces the variance of the absolute velocities associated with the unburnt gases. For this reason lower values of the absolute velocities RMS (root mean square) are observed for flame conditions when compared with cold flow situations as it is shown in Figure 8.10, Figure 8.11 and Figure 8.12. Except for this discrepancy related to the burning velocity threshold effect, the velocity fields in cold flow and flame conditions can be considered equivalent. Because the data collected in flame conditions are contaminated by the burning velocity threshold effect, the analysis of the oncoming flow turbulence characteristics is performed on the data collected using the cold flow case for each Bulk Flow condition.

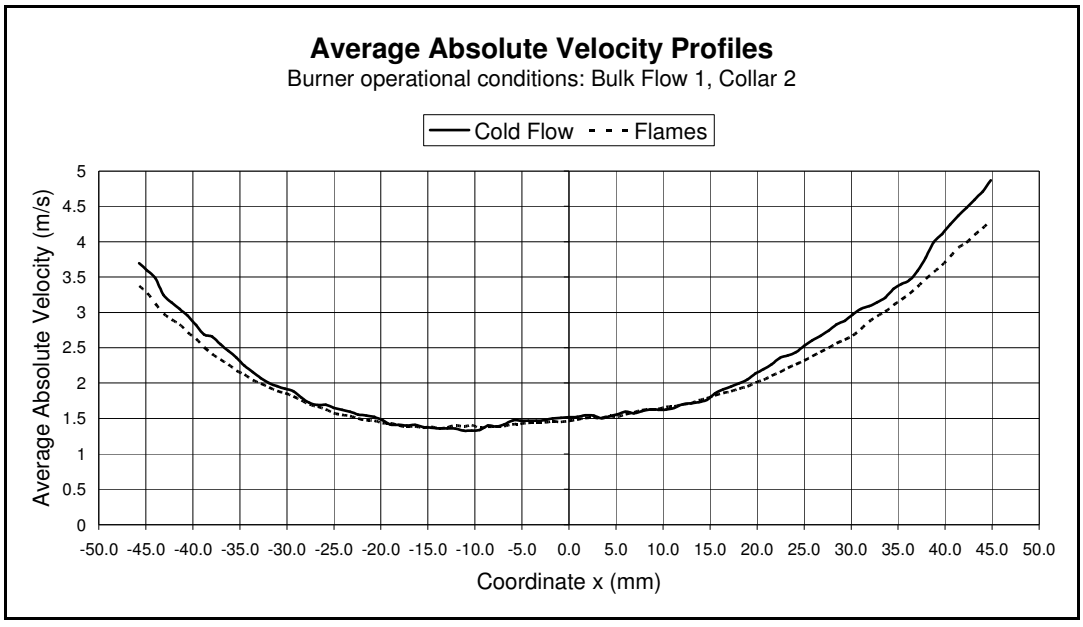

Figure 8.7. Average absolute velocity profiles along a horizontal line that intersects the burner axis 30 mm above the coordinate system origin. The profiles for the cold flow and flames conditions are plotted. The profile related to the flames conditions has been obtained using the set of velocity fields of all the flames (from A to F) for Bulk Flow 1.

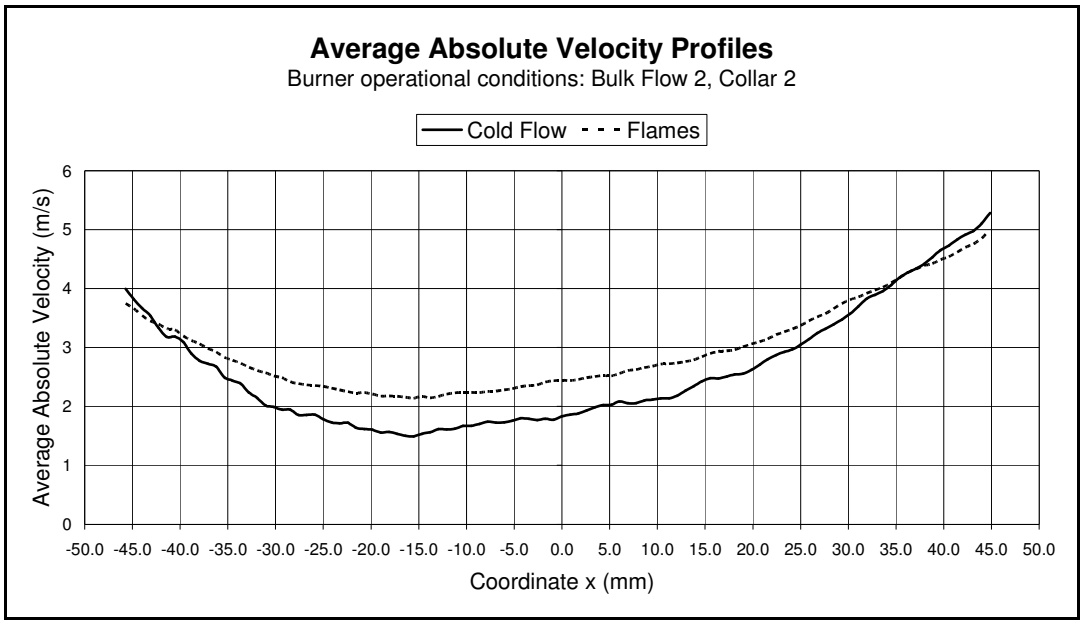

Figure 8.8. Average absolute velocity profiles along a horizontal line that intersects the burner axis 30 mm above the coordinate system origin. The profiles for the cold flow and flames conditions are plotted. The profile related to the flames conditions has been obtained using the set of velocity fields of all the flames (from A to F) for Bulk Flow 2.

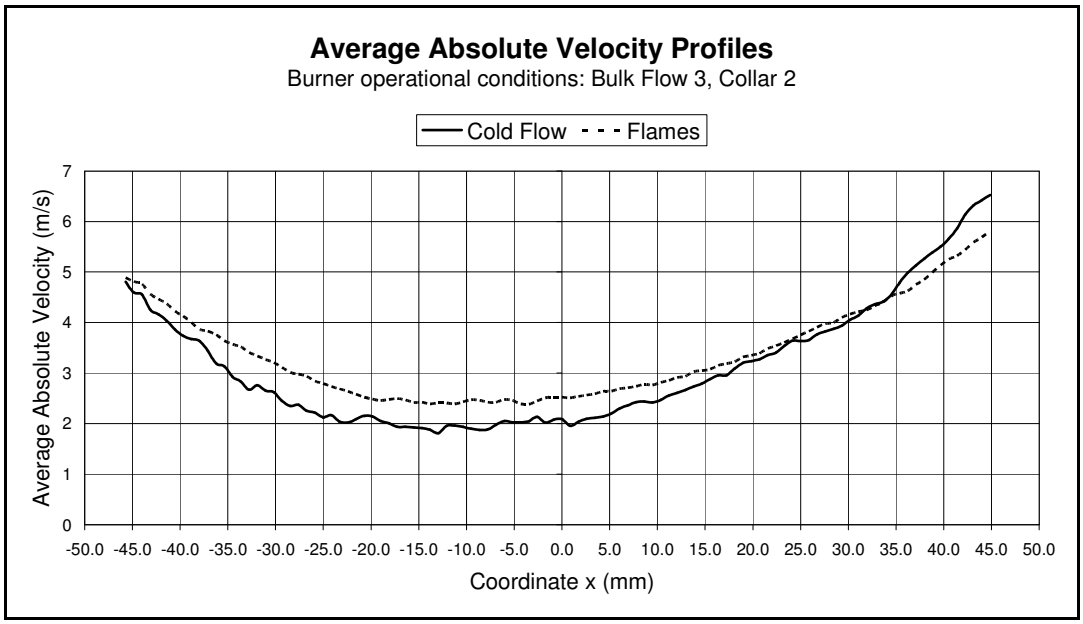

Figure 8.9. Average absolute velocity profiles along a horizontal line that intersects the burner axis 30 mm above the coordinate system origin. The profiles for the cold flow and flames conditions are plotted. The profile related to the flames conditions has been obtained using the set of velocity fields of all the flames (from A to F) for Bulk Flow 3.

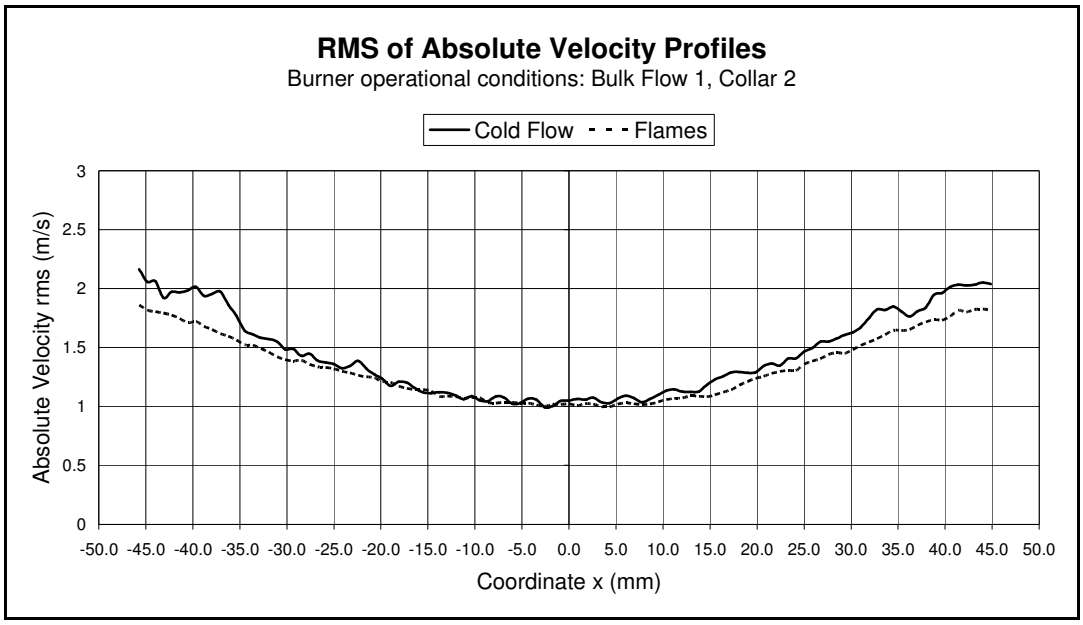

Figure 8.10. Absolute velocity profiles along a horizontal line that intersects the burner axis 30 mm above the coordinate system origin. The profiles for the cold flow and flames conditions are plotted. The profile related to the flames conditions has been obtained using the set of velocity fields of all the flames (from A to F) for Bulk Flow 1.

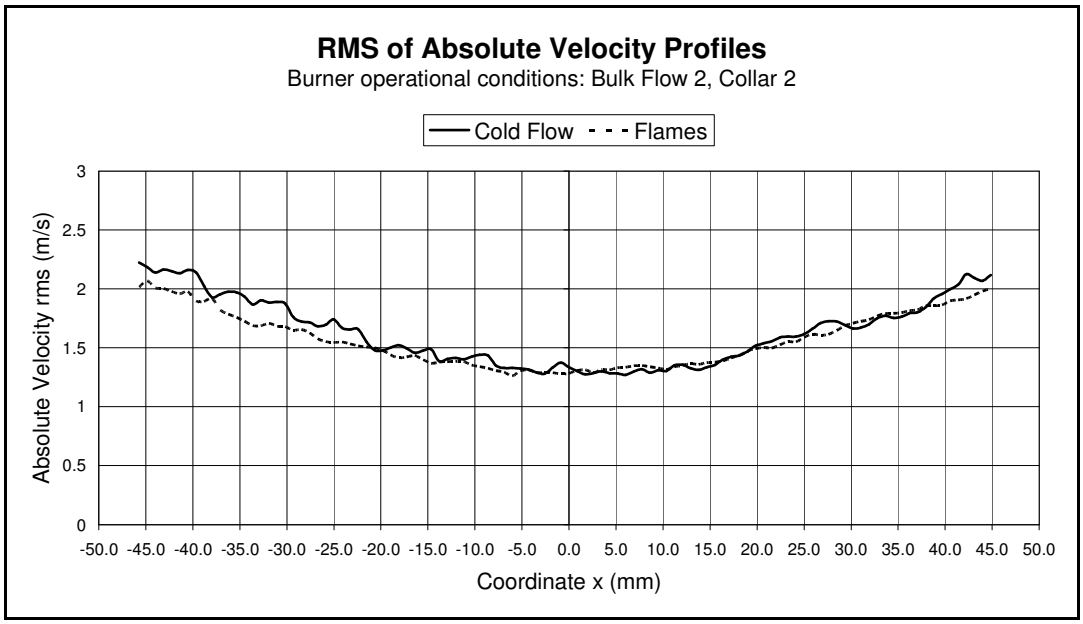

Figure 8.11. Absolute velocity profiles along a horizontal line that intersects the burner axis 30 mm above the coordinate system origin. The profiles for the cold flow and flames conditions are plotted. The profile related to the flames conditions has been obtained using the set of velocity fields of all the flames (from A to F) for Bulk Flow 2.

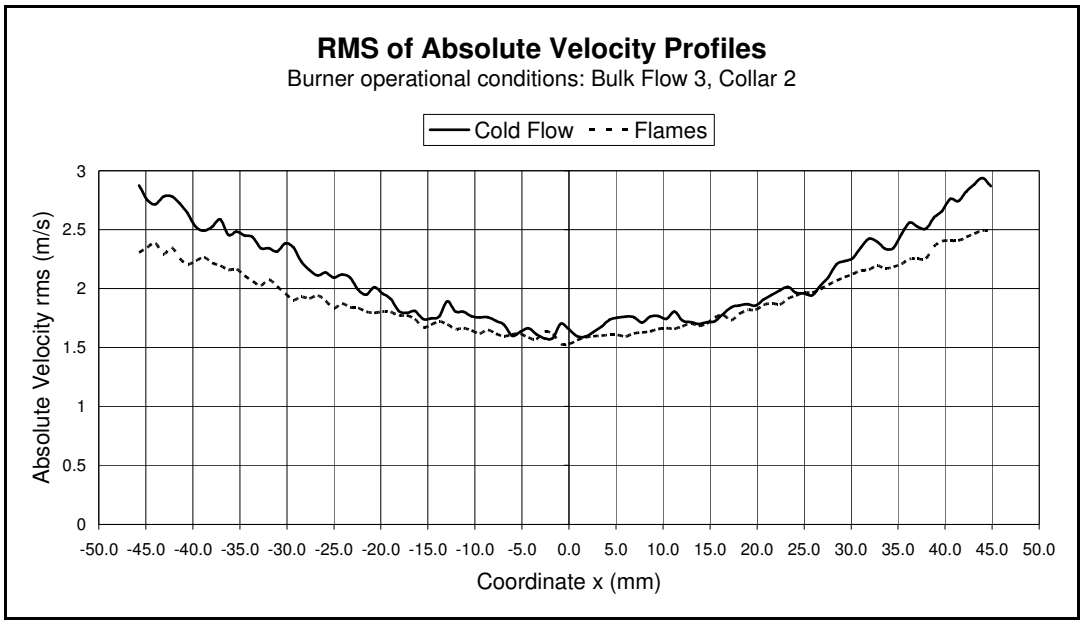

Figure 8.12. Absolute velocity profiles along a horizontal line that intersects the burner axis 30 mm above the coordinate system origin. The profiles for the cold flow and flames conditions are plotted. The profile related to the flames conditions has been obtained using the set of velocity fields of all the flames (from A to F) for Bulk Flow 3.

8.1.2 Characterization of the Velocity Components and the Turbulence in the Area above the Burner Outlet

A detailed description of the oncoming flow velocity distribution is given by the average velocity component profiles along a horizontal line that intersects the burner axis 30 mm above the coordinate system origin (the same horizontal line considered previously). The respective plots for Bulk Flow 1, 2 and 3 are shown in Figure 8.13, Figure 8.14, and Figure 8.15. In all three flow rate conditions the main component remains the component in the axial direction u_y. The divergent direction of the flow coming out of the burner outlet is linked with the radial component u_x profile that is positive on the right side of the coordinate system origin (same direction as the x axis), while is negative on the left side (opposite direction of the x axis). The out of plane component u_z is directly related to the swirl flow. The fact that it is negative on the right side of the system origin and it is positive on the left side, is a consequence of the anticlockwise rotation imposed by the tangential jets flow if the observer is watching from above the burner head.

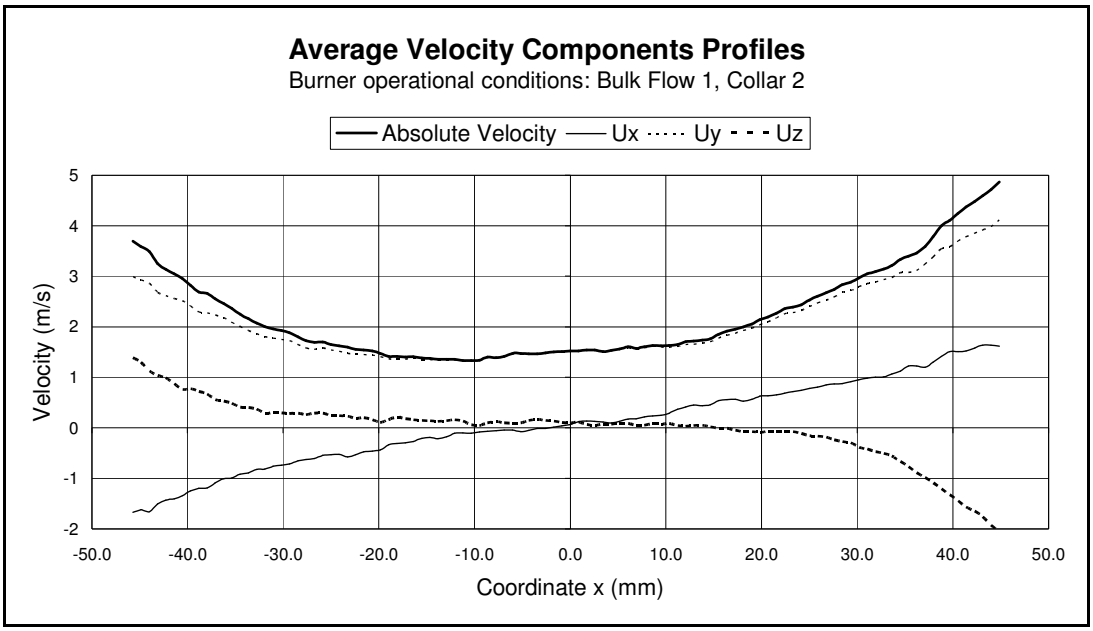

Figure 8.13. Average profiles of the velocity components (u_x, u_y, u_z) and its absolute value along a horizontal line that intersects the burner axis 30 mm above the coordinate system origin. The profiles are related to the cold flow conditions for Bulk Flow 1.

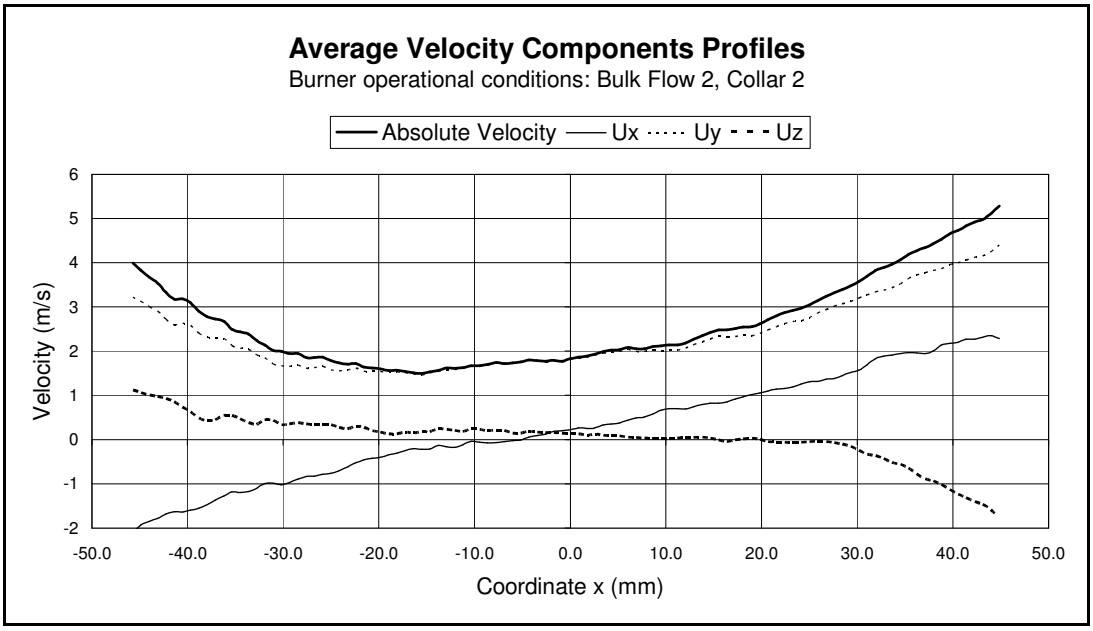

Figure 8.14. Average profiles of the velocity components (u_x, u_y, u_z) and its absolute value along a horizontal line that intersects the burner axis 30 mm above the coordinate system origin. The profiles are related to the cold flow conditions for Bulk Flow 2.

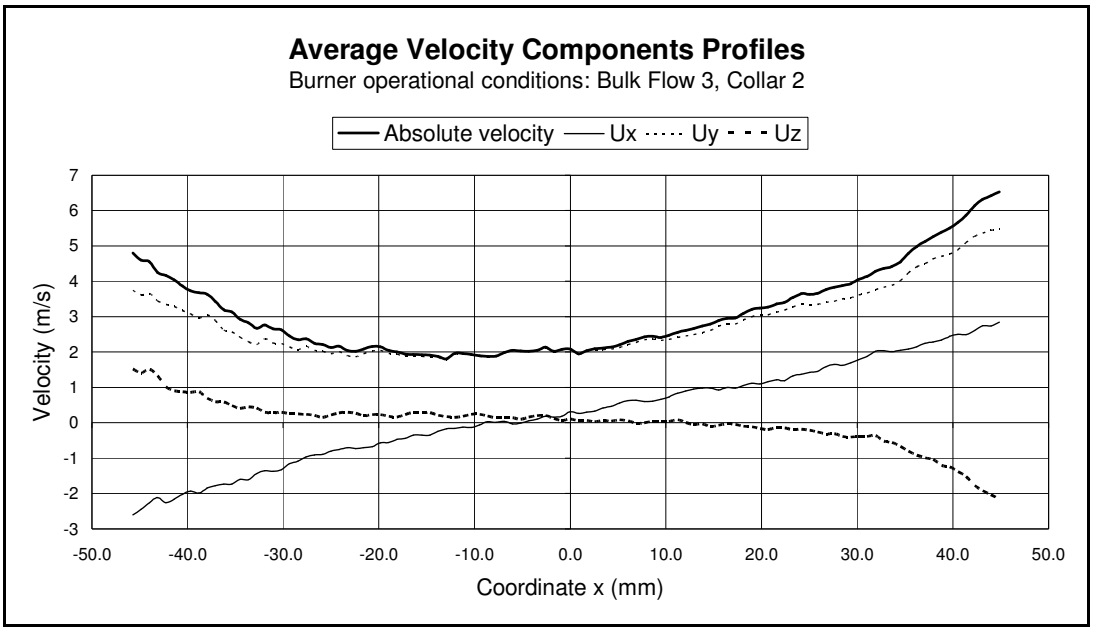

Figure 8.15. Average profiles of the velocity components (u_x, u_y, u_z) and its absolute value along a horizontal line that intersects the burner axis 30 mm above the coordinate system origin. The profiles are related to the cold flow conditions for Bulk Flow 3.

8.1.2.1 Turbulence Uniformity and Isotropy

The turbulence of the oncoming flow is described by the RMS of the velocities. In Figure 8.16, Figure 8.17 and Figure 8.18 are shown the RMS profiles of the velocity components and its absolute value along a horizontal line that intersects the burner axis 30 mm above the coordinate system origin. The profiles are related to the cold flow conditions for each Bulk Flow considered. The RMS profiles of the velocity components are very close, if the radial component, u_x, and the out of plane component, u_z, are considered. The axial component is around 0.4m/s higher than the other two components for every Bulk Flow considered. All the profiles are reasonably flat and this means that the ensemble average is close to the spatial average. This confirms that the turbulence generated can be considered homogeneous.

The turbulence uniformity allows the analysis of its interaction with the flame front propagation to be independent of the position selected within the imaged area. Furthermore this is an important characteristic because the objective of this research is the analysis of the effects of equivalence ratio stratification on lean flames, and the fuel stratification it is not a local point characteristic but it involves a region of the flow. The ability to keep as uniform as possible all the other variables of the system allows the study of the fuel stratification correlation with flame front propagation to be undertaken with minimum interference from additional parameters.

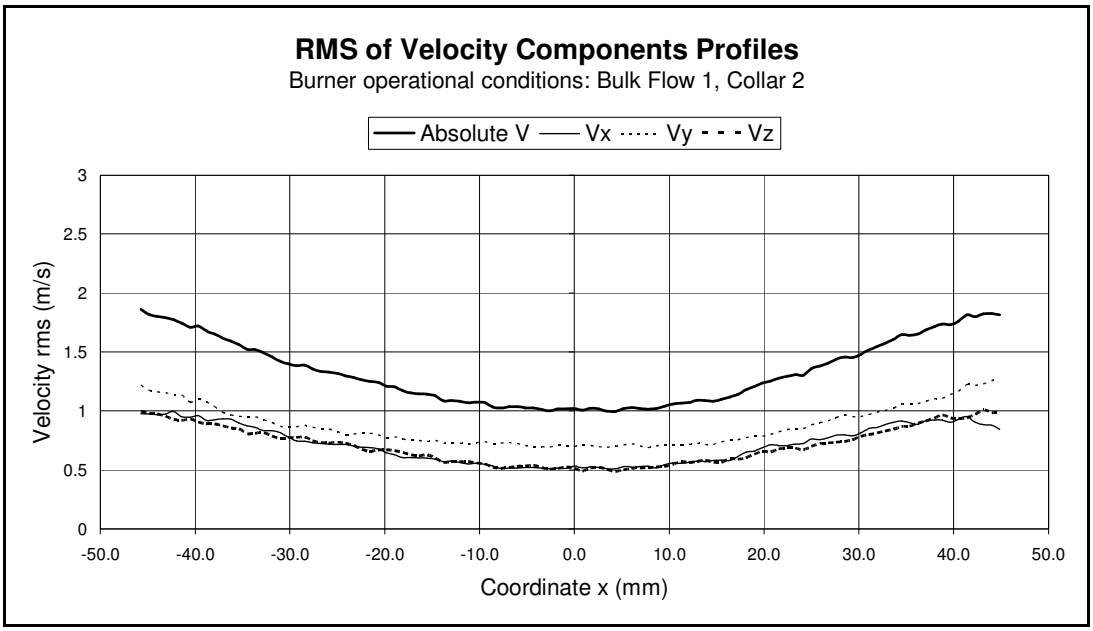

Figure 8.16. RMS profiles of the velocity components (u_x, u_y, u_z) and its absolute value along a horizontal line that intersects the burner axis 30 mm above the coordinate system origin. The profiles are related to the cold flow conditions for Bulk Flow 1.

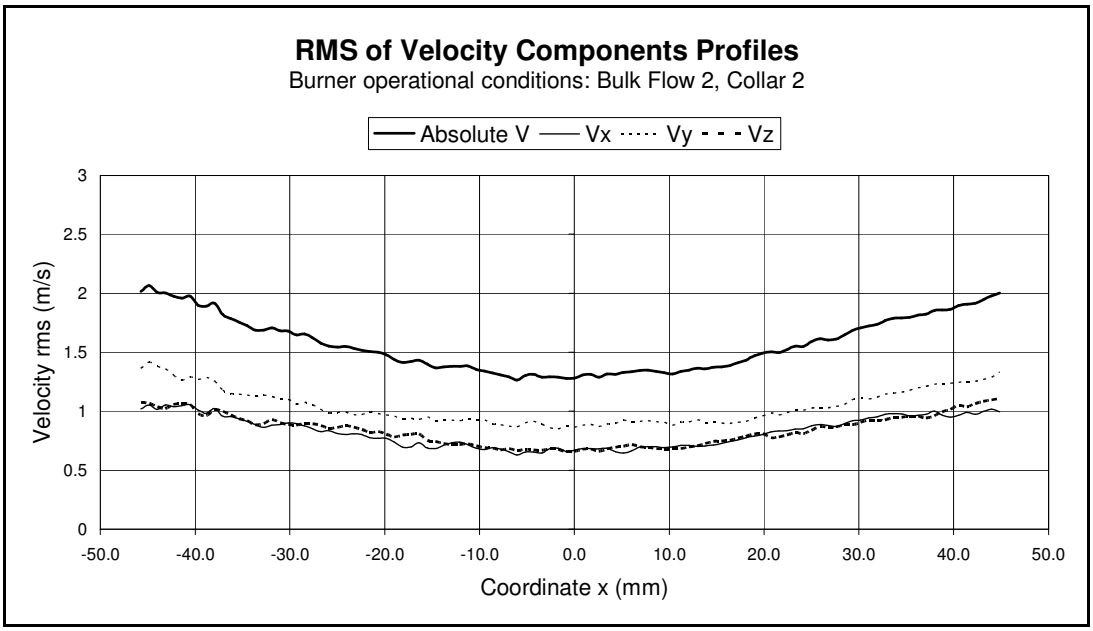

Figure 8.17. RMS profiles of the velocity components (u_x, u_y, u_z) and its absolute value along a horizontal line that intersects the burner axis 30 mm above the coordinate system origin. The profiles are related to the cold flow conditions for Bulk Flow 2.

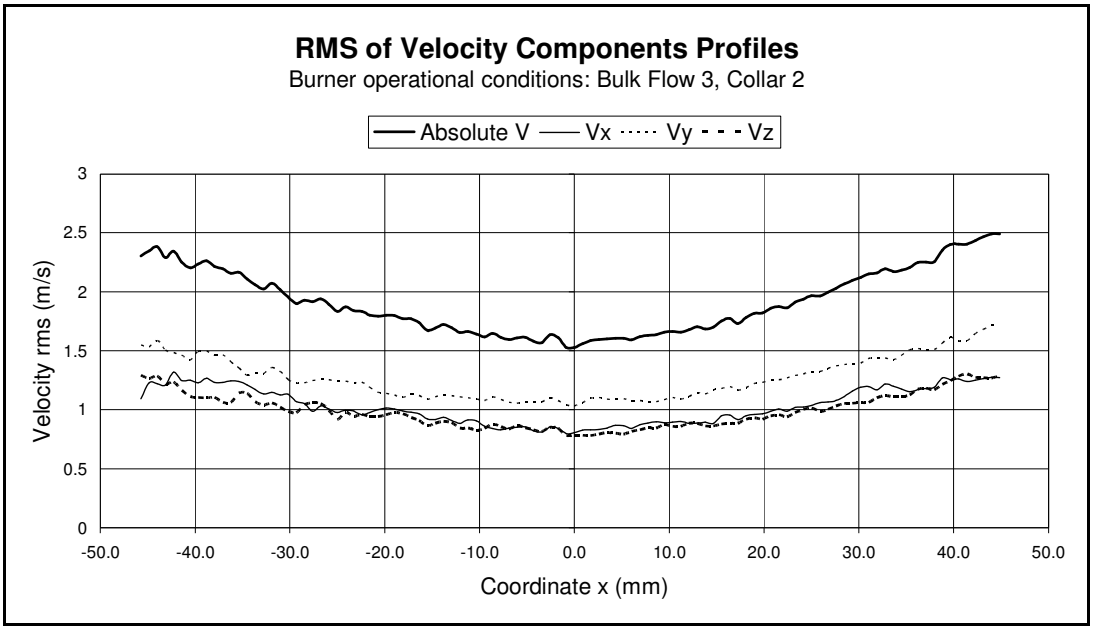

Figure 8.18. RMS profiles of the velocity components (u_x, u_y, u_z) and its absolute value along a horizontal line that intersects the burner axis 30 mm above the coordinate system origin. The profiles are related to the cold flow conditions for Bulk Flow 3.

The turbulent fluctuations are completely isotropic if they do not have any directional preference and as a consequence on that the off-diagonal components of the Reynolds stress tensor have to vanish ($\rho\,\overline{u_x u_y}$, $\rho\,\overline{u_x u_z}$, $\rho\,\overline{u_z u_y}$). The profiles of $\overline{u_x u_y}$, $\overline{u_x u_z}$ and $\overline{u_z u_y}$ are plotted in Figure 8.19, Figure 8.20 and Figure 8.21 for the various Bulk Flow conditions. As in other cases the profiles are considered along a horizontal line that intersects the burner axis 30 mm above the coordinate system origin. For all the conditions considered the profiles of $\overline{u_x u_y}$, $\overline{u_x u_z}$ and $\overline{u_z u_y}$ are very close to zero and confirms that the turbulence is near isotropic.

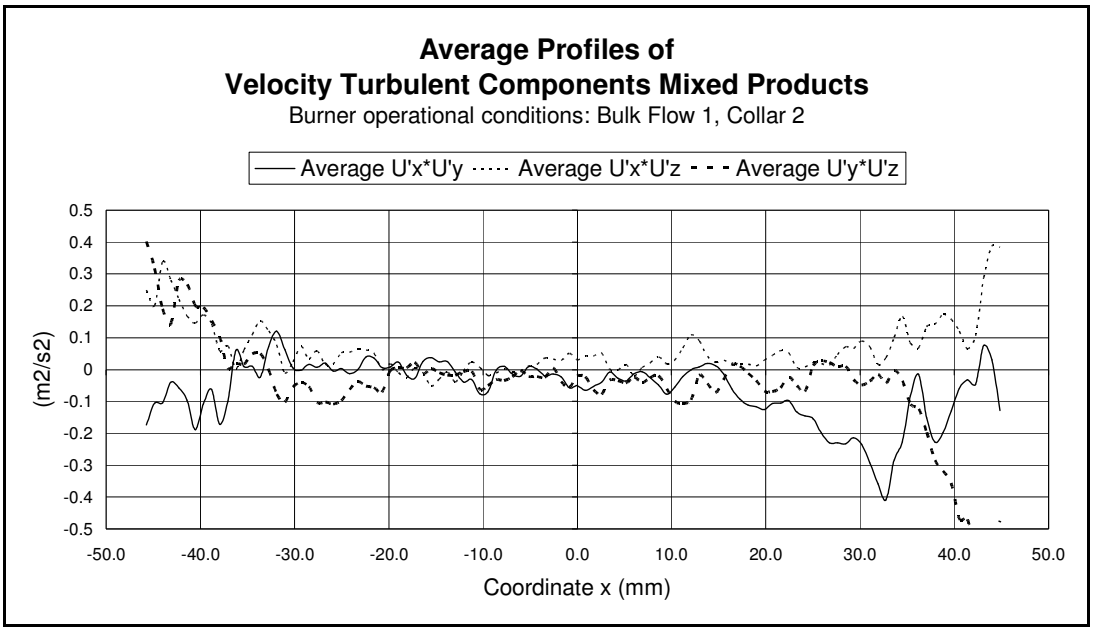

Figure 8.19. The profiles of $\overline{u_x u_y}$, $\overline{u_x u_z}$ and $\overline{u_z u_y}$ along a horizontal line that intersects the burner axis 30 mm above the coordinate system origin. The profiles are related to the cold flow conditions for Bulk Flow 1.

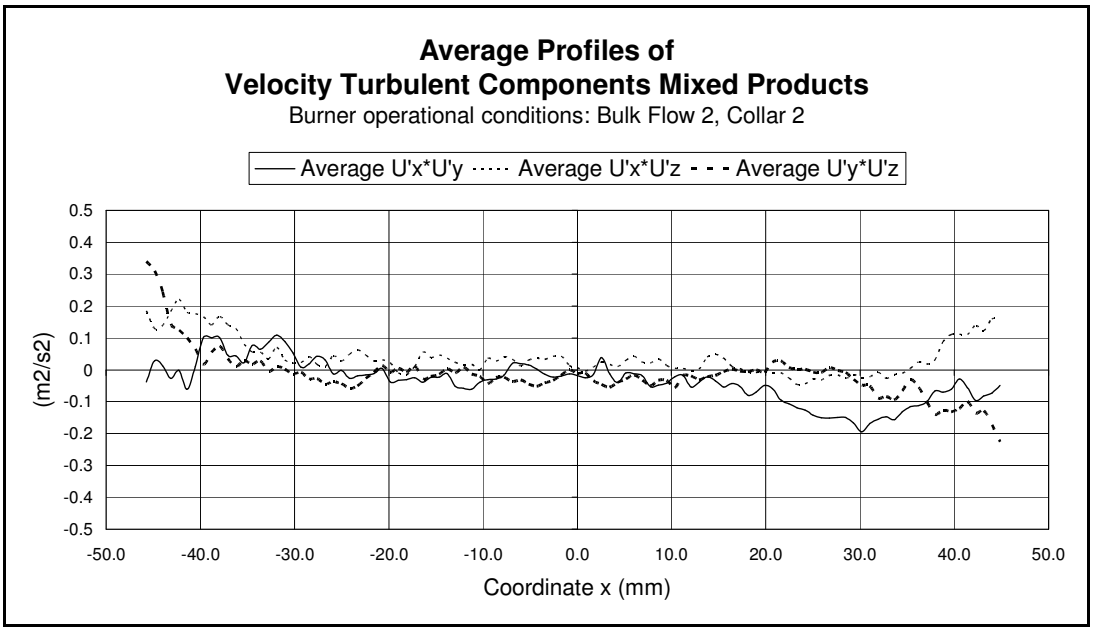

Figure 8.20. The profiles of $\overline{u_x u_y}$, $\overline{u_x u_z}$ and $\overline{u_z u_y}$ along a horizontal line that intersects the burner axis 30 mm above the coordinate system origin. The profiles are related to the cold flow conditions for Bulk Flow 2.

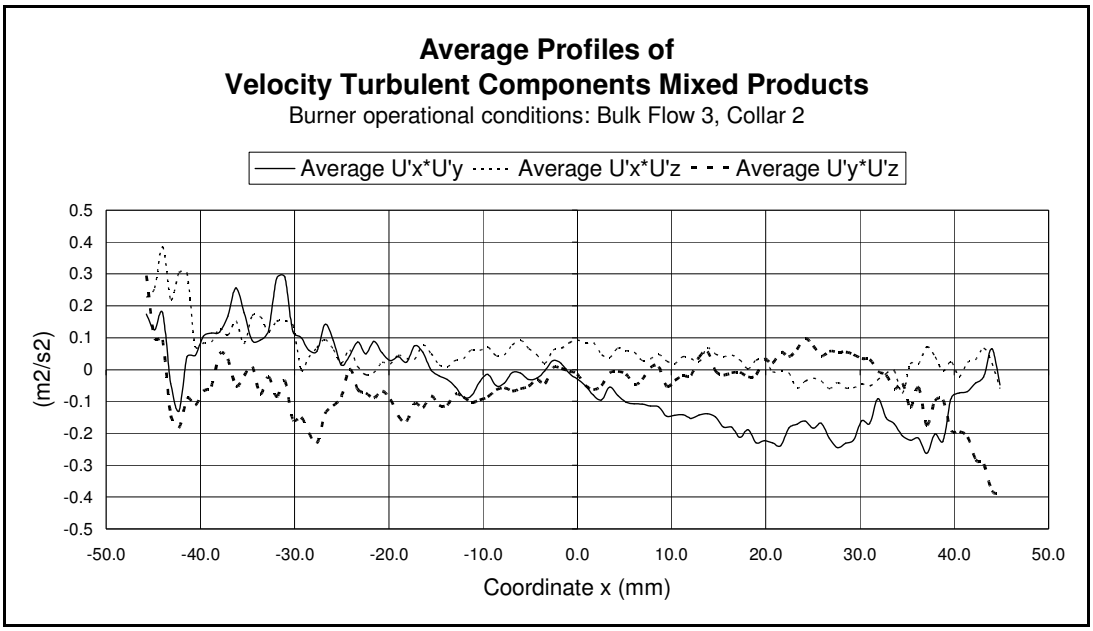

Figure 8.21. The profiles of $\overline{u_x u_y}$, $\overline{u_x u_z}$ and $\overline{u_z u_y}$ along a horizontal line that intersects the burner axis 30 mm above the coordinate system origin. The profiles are related to the cold flow conditions for Bulk Flow 3.

From the comparison of the absolute velocity RMS values for the three different flow rates considered, it is possible to demonstrate that the turbulence level in the oncoming flow can be controlled. In Figure 8.22 the absolute velocity RMS profiles are presented along a horizontal line that intersects the burner axis 30 mm above the coordinate system origin. The profiles have been defined considering the cold flow conditions for each of the three Bulk Flows. The RMS values of the absolute velocity increase with higher flow rates (progressing from Bulk Flow 1 to Bulk Flow 3). The possibility to change the level of turbulence in the oncoming flow was another capability requested for the burner designed, that has been fulfilled.

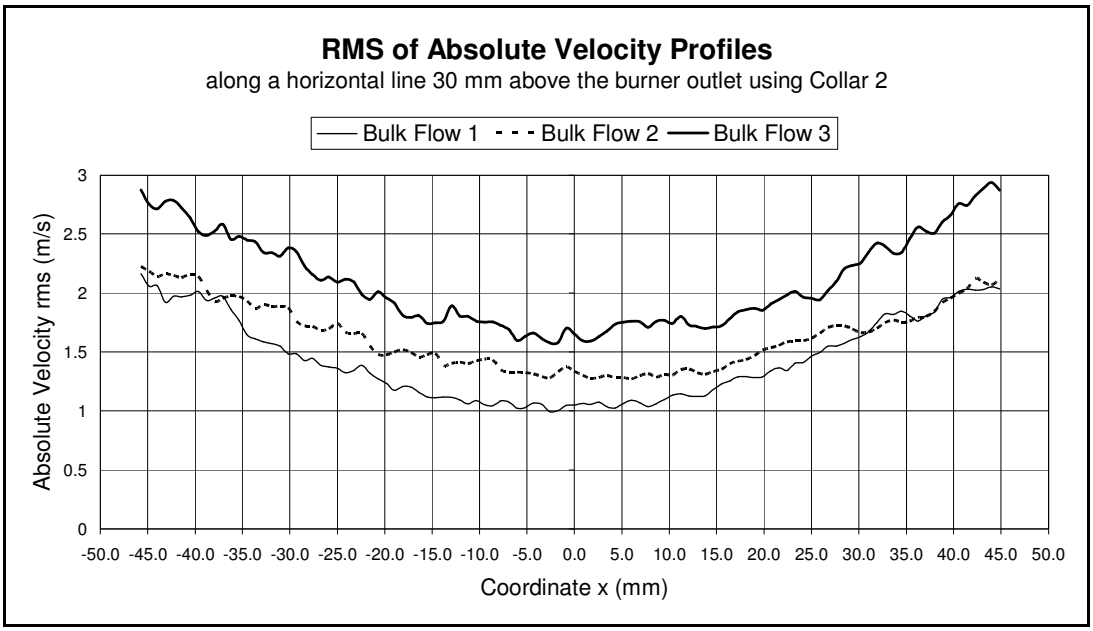

Figure 8.22. Absolute velocity RMS profiles along a horizontal line that intersects the burner axis 30 mm above the coordinate system origin. The profiles are considered in the cold flow conditions for each of the three Bulk Flows.

8.1.2.2 Turbulence Uniformity along the Flow Path

The profiles of several quantities have been considered along a horizontal line, but an important feature of the oncoming flow is the way it maintains the characteristics just described along its path. Therefore profiles along a vertical line coincident with the y axis are also considered. The first quantity to be analyzed is the average absolute velocity, whose profile is shown in Figure 8.23. The action of the swirl flow determines linear velocity decay and at a y coordinate of 45mm the three profiles are nearly undistinguished. It is the reduction of the flow velocity that stabilises the propagation of the flame front, avoiding flame blow off. If the oncoming flow in a particular point is characterized by a velocity higher than the burning velocity, the flame is pushed in the y direction towards areas where the oncoming flow velocity is lower.

While the velocity decays along a line coincident with the y axis, the turbulence remains constant. The profiles in Figure 8.24 show that the RMS of the absolute velocity is uniform along the y axis. This demonstrates that the turbulence produced by the burner is homogeneous along a vertical axis too. Additionally, the turbulent fluctuations are completely isotropic as demonstrated by the off-diagonal components of the Reynolds stress tensor being close to zero ($\rho\,\overline{u_x u_y}$, $\rho\,\overline{u_x u_z}$, $\rho\,\overline{u_z u_y}$) along the y axis.

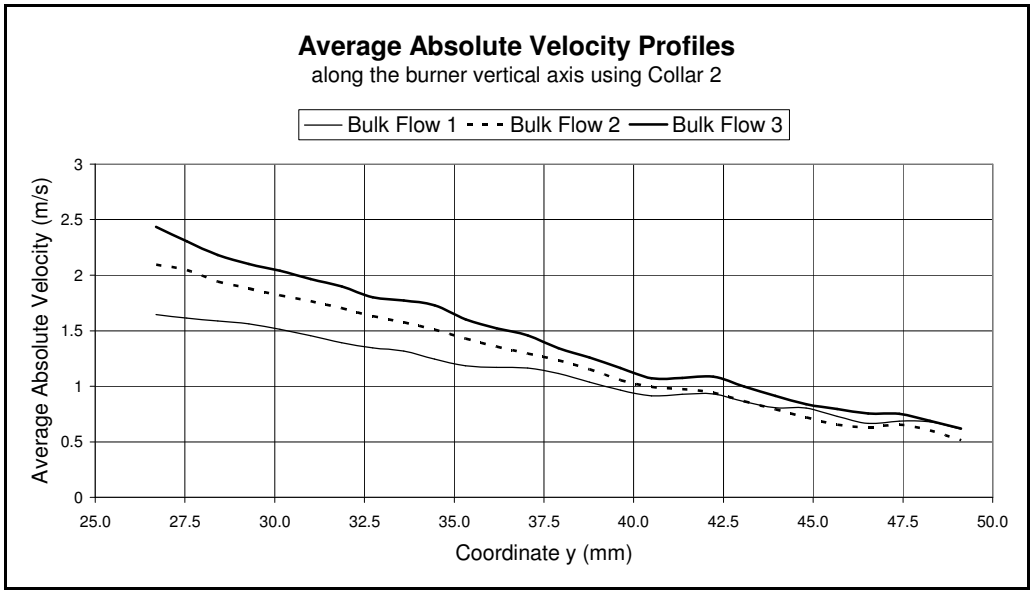

Figure 8.23. Absolute velocity average profiles along a line coincident with the y axis. The profiles are considered in the cold flow conditions for each of the three Bulk Flows.

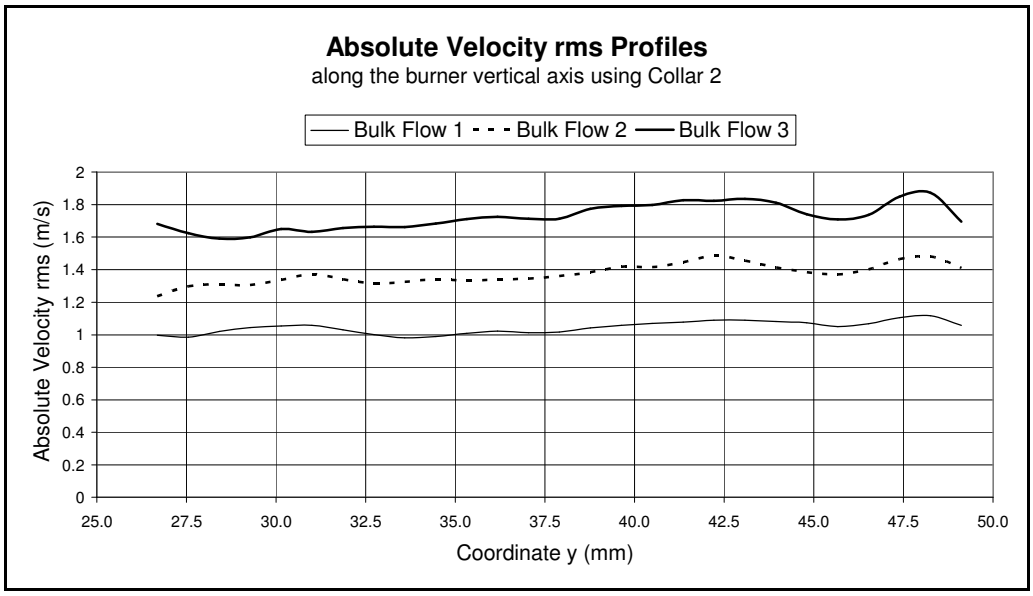

Figure 8.24. Absolute velocity RMS profiles along a line coincident with the y axis. The profiles are considered in the cold flow conditions for each of the three Bulk Flows.

8.1.3 Velocity Field Analysis inside the Burner Outlet Mixing Section

Stereoscopic PIV experiments have been executed in the area inside the burner outlet shown in Figure 5.5, in order to collect further information about the oncoming flow. These data can be used for the validation of the theoretical models because they can infer important information for defining the boundary conditions. It is of utmost importance to define the characteristics of the flow where the flames are propagating in order to compare the experimental data with the results of theoretical modelling. The imaged area considered allows the analysis of the velocity field just above the inner collars outlet. It gives information about the velocity of the flow and the turbulence generated by the turbulence generator before the interaction with the swirl flow. It has been mentioned before that the area imaged is reduced to the inner and annular flow because the seed particles have been injected only in those two flows. At that stage of the flow path the mixing process with the swirl flow is not strong enough to gain velocity vectors in interrogation windows placed at a distance from the burner axis greater than 32mm.

The velocity distribution along a horizontal line passing through the burner axis and placed 40mm above the inner collars rims is presented in Figure 8.25. For each Bulk Flow condition the values of the average absolute velocity and the average y velocity component (u_y) are displayed. From the plots at all conditions it is clear that the major component of the velocity is u_y, for this reason instead of a vector field image with all vertical vectors overlapping each other, it has been chosen to show the average absolute velocity field in Figure 8.26. The profiles in the figure confirm that the three Bulk Flow conditions are associated with three different average absolute velocities of the flow as specified in Section 4.5:

- Bulk Flow 1: flow average absolute velocity 6m/s.
- Bulk Flow 2: flow average absolute velocity 7m/s.
- Bulk Flow 3: flow average absolute velocity 9m/s.

From the profiles shown in Figure 8.25 it emerges that the average velocity is not uniform along the cross section area of the flow. In the regions with $15 < |x| < 22$ and $28 < |x| < 33$ there is a reduction, compensated by a velocity increase for $22 < |x| < 28$. Not uniform turbulence is produced by the collars rims and the region of the flow affected by this phenomenon is characterized by a decrease in absolute velocity. This flow region is associated with the blue areas in Figure 8.26. In the figures it is shown only the case of Bulk Flow 1 as representative of all flow conditions (Bulk Flow 2 and Bulk Flow 3).

The flow rate values have been imposed in order to have a uniform average y velocity component (u_y) along the cross sections of the annular flow and the inner flow, therefore the decrease in absolute velocity is compensated by an increase in the surrounding regions. From the analysis of the velocity profiles in the burner outlet

region it emerged that the effect of the vortices disappears when the flow reaches that area. This is an important feature of the mixing section because without it these irregularities of the velocity distribution would have interfered with the study of the fuel stratification effects.

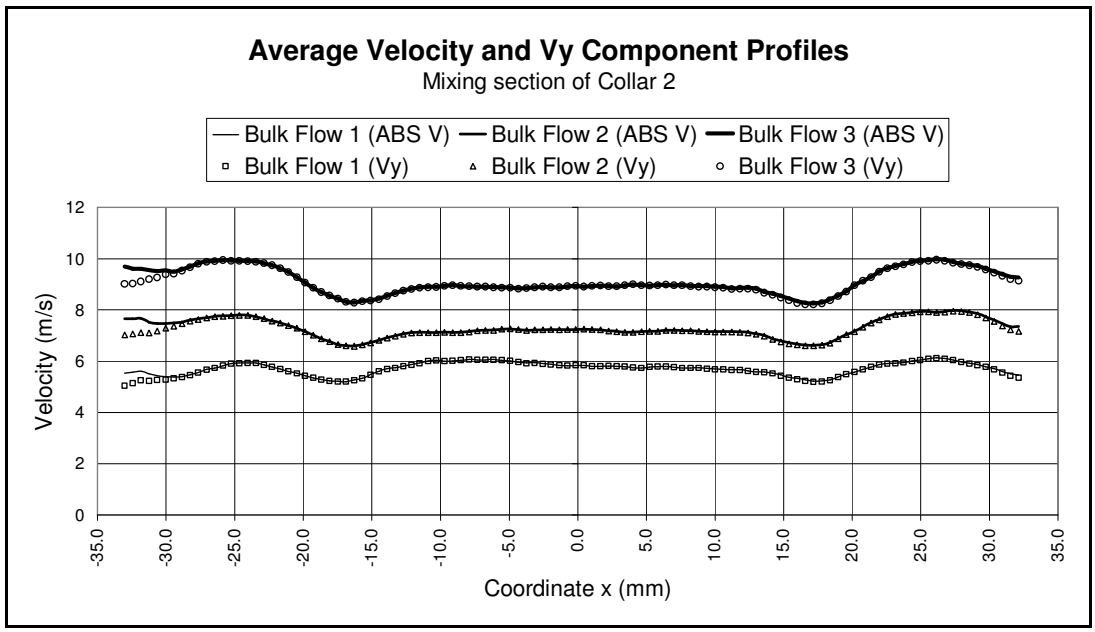

Figure 8.25. Absolute velocity average profiles along a horizontal line that intersects the burner axis 40 mm above the inside collars rim. The profiles for all Bulk Flows conditions are plotted.

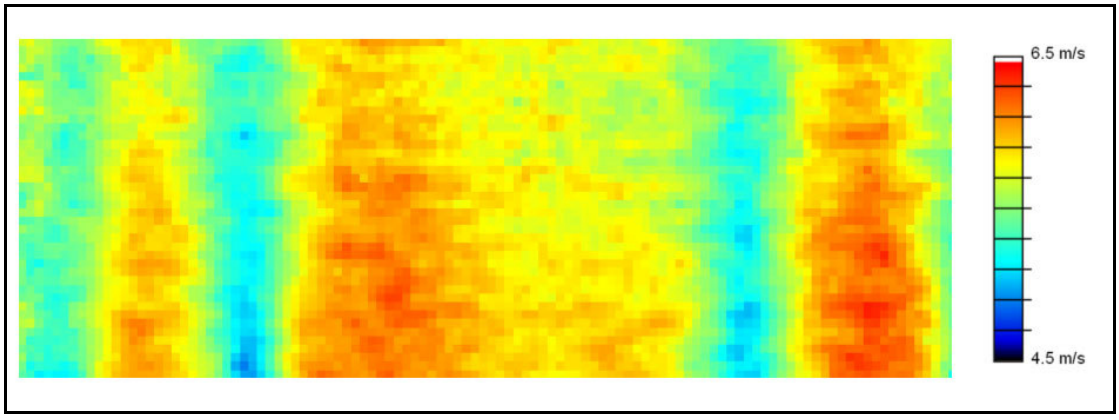

Figure 8.26. Average absolute velocity field inside Collar 2 with Bulk Flow 1. The area imaged is the 67x24mm rectangle defined in Figure 5.5. The coloured scale is associated with the absolute value of the velocity.

The turbulence produced by the collar rims is interesting as well. It can be observed in the profiles of the absolute velocity RMS presented in Figure 8.27 for all three Bulk Flows. For the inner flow the RMS profiles are uniform ($-17 < x < 17$), while in the

external region ($17 < |x|$) the RMS is increased by the presence of the vortices. Once the flow has reached the burner outlet the effect of the vortices on the velocity RMS is reduced and the profiles are characterized by a distributed uniformity as observed previously in the analysis. The mixing section favours the uniform generation of turbulence distribution avoiding the effects of vortices interrupting the flame propagation especially in those regions where the equivalence ratios gradients are present. Further confirmation given by Figure 8.27 is that by changing the Bulk Flow, it is possible to control the turbulence level. This is an important feature of the burner because it allows the analysis of different levels of turbulence on flame propagation.

Considering the same horizontal line as before passing through the burner axis and placed 40mm above the origin, the profiles of the velocity components RMS are reported for Bulk Flow1 in Figure 8.28. The plots of the three components of velocity are very close and this confirms that the turbulence produced by the turbulence generators is isotropic. It is during the mixing process with the swirl flow that the values of the velocity components (u_x and u_z) RMS on the horizontal plane are reduced by a greater amount when compared with the RMS of u_y as shown in Figure 8.16 for the burner outlet region.

The effect of the vortices produced by the collar rims is less intense if the velocity components RMS values are considered instead of the absolute velocity as shown in Figure 8.28. This confirms that the uniformity of the turbulence is well preserved even under the negative effect produced by the collar rims.

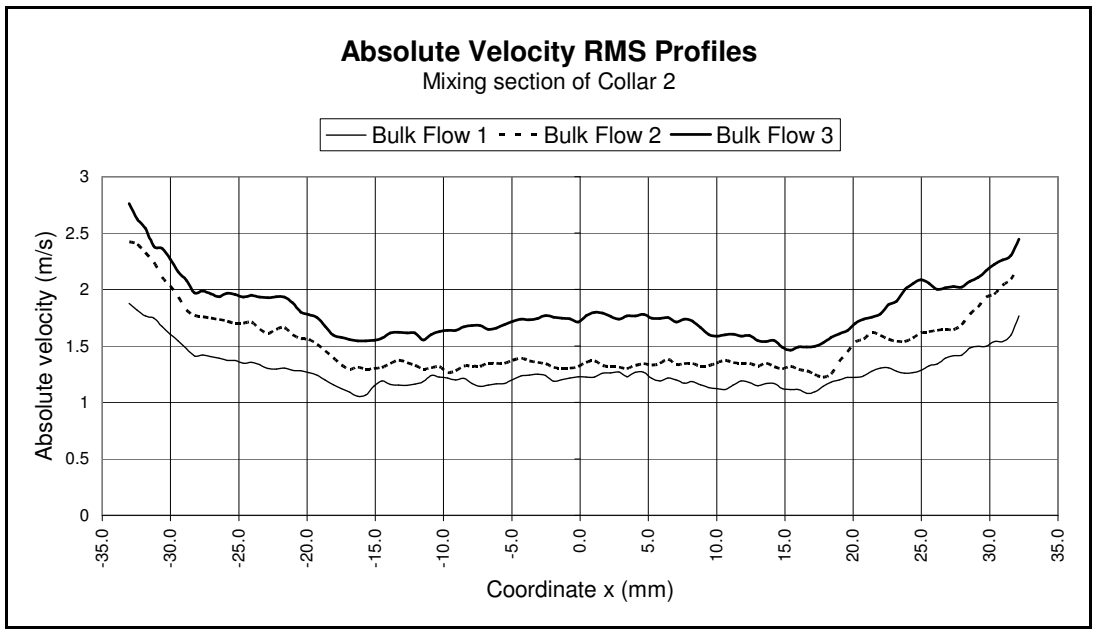

Figure 8.27. Absolute velocity RMS profiles along a horizontal line that intersects the burner axis 40 mm above the inside collars rim. The profiles for all Bulk Flows conditions are plotted.

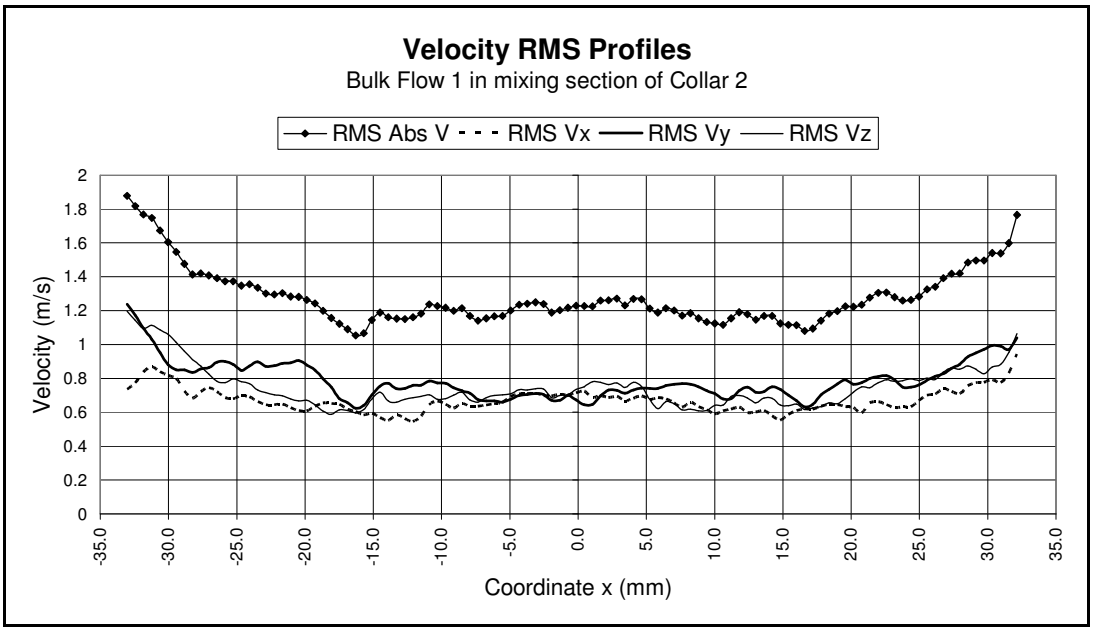

Figure 8.28. The profiles of the absolute velocity and the three velocity components are plotted along a horizontal line that intersects the burner axis 40 mm above the inside collars rim. Bulk Flow1 conditions are considered.

8.1.4 Comparison between the two Burner Outlet Configurations

In the previous analysis the attention has been focused on the velocity fields obtained using the burner outlet configuration Collar 2 because 3D-PIV data are available for it. The only differences between Collar 1 and Collar 2 are the diameters of the burner outlet (150mm for Collar1 and 130mm for Collar2) and their lengths (220mm for Collar1 and 280mm for Collar 2). The different diameter implies an increased flow rate associated to the air swirl flow only, while the increased length determines a longer mixing section. The inner flow (Flow 1) and the annular flow (Flow 2) are unchanged in their flow rates values and consequently the turbulence generators operates at the same conditions of Collar 2 for the three Bulk Flows.

The profiles of the absolute velocity and the velocity component shown in Figure 8.29, Figure 8.30 and Figure 8.31 have been extrapolated along a horizontal line that intersects the y axis 30mm above the burner outlet. They are related respectively to Bulk Flow 1, Bulk Flow 2 and Bulk Flow 3. If compared with the respective profiles obtained for Collar 2 and shown in Figure 8.13, Figure 8.14 and Figure 8.15 it appears that the average absolute velocity for Collar 1 is more uniform. The increased diameter allows a bigger volume in which the pressure gradients generated by the swirl flow are capable of reducing the local flow velocity. It has been observed in the Collar 2 vector fields that the external parts of the oncoming flow are characterized by higher local absolute velocities. Because of the bigger diameter of Collar 1, the region of higher

absolute velocities is further to the sides and consequently most of it is outside the imaged area.

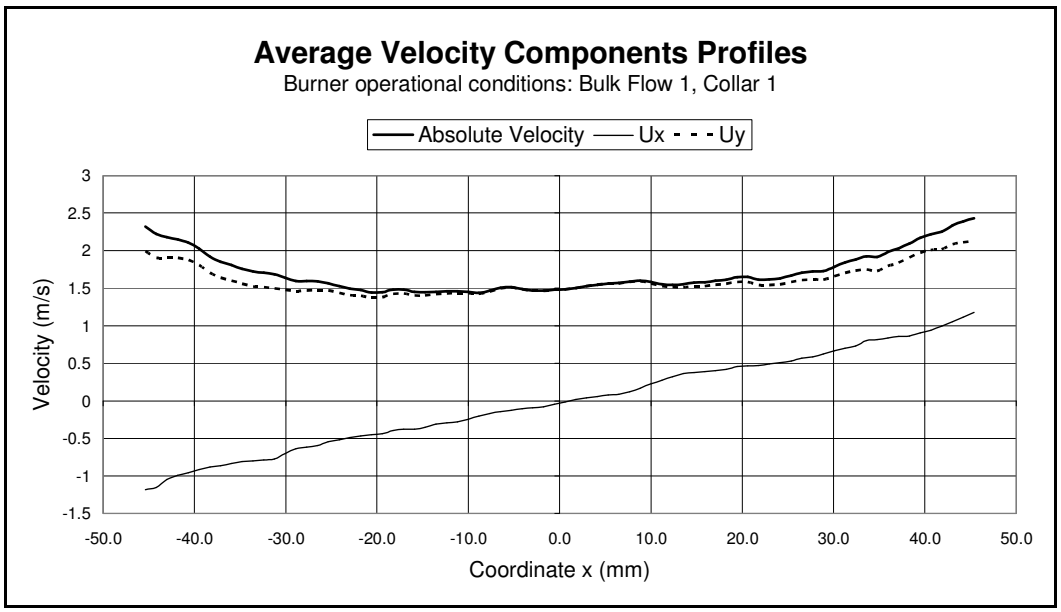

Figure 8.29. The average profiles of the velocity components (u_x, u_y, u_z) and its absolute value along a horizontal line that intersects the burner axis 30 mm above the coordinate system origin. The profiles are related to the cold flow conditions for Bulk Flow 1.

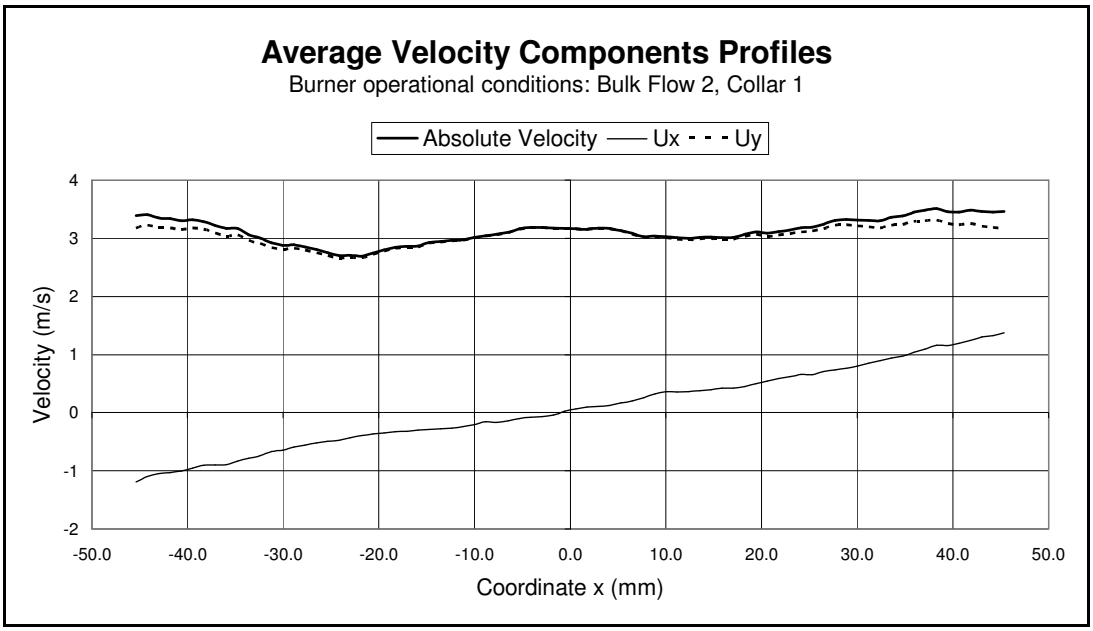

Figure 8.30. The average profiles of the velocity components (u_x, u_y, u_z) and its absolute value along a horizontal line that intersects the burner axis 30 mm above the coordinate system origin. The profiles are related to the cold flow conditions for Bulk Flow 2.

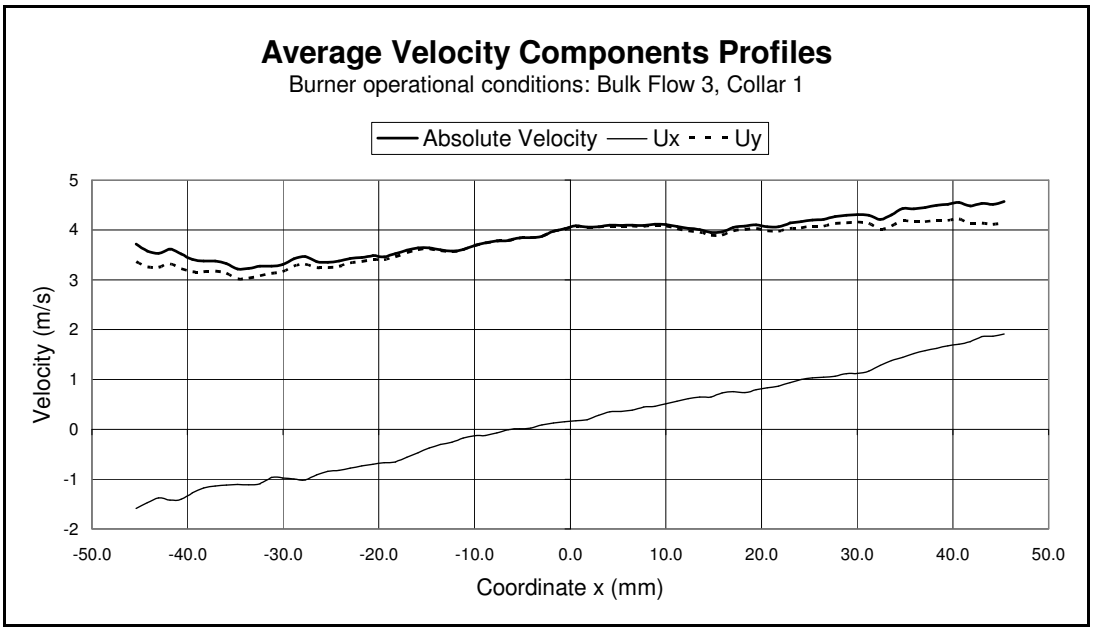

Figure 8.31. The average profiles of the velocity components (u_x, u_y, u_z) and its absolute value along a horizontal line that intersects the burner axis 30 mm above the coordinate system origin. The profiles are related to the cold flow conditions for Bulk Flow 3.

In the graphs related to Collar 1 the profile of the out-of-plane component (u_z) is missing because only 2D-PIV experiments have been performed. The axial velocity component (u_y) and the radial component (u_x) are associated with similar profiles already analyzed for Collar 2, especially when compared with the same Bulk Flow conditions.

The velocity RMS distributions are considered in order to analyze the characteristics of the turbulence. The absolute velocity RMS profiles are uniform along the same horizontal line considered previously as shown in Figure 8.32 and along the y axis as shown in Figure 8.33. This is an important characteristic because it allows an analysis of the flame front propagation without variation in turbulence across the region of interest. This characteristic has been underlined for the configuration using Collar 2 but it appears to be further confirmed in the case of Collar 1.

Also confirmed in this case is the possibility of controlling the turbulence level by increasing the flow rates passing through the burner nozzle. Progressing from Bulk Flow 1 to Bulk Flow 3, the values of velocity RMS are gradually increased. This is an important feature in order to analyze the conjunct effect of turbulence and fuel stratification on flame propagation.

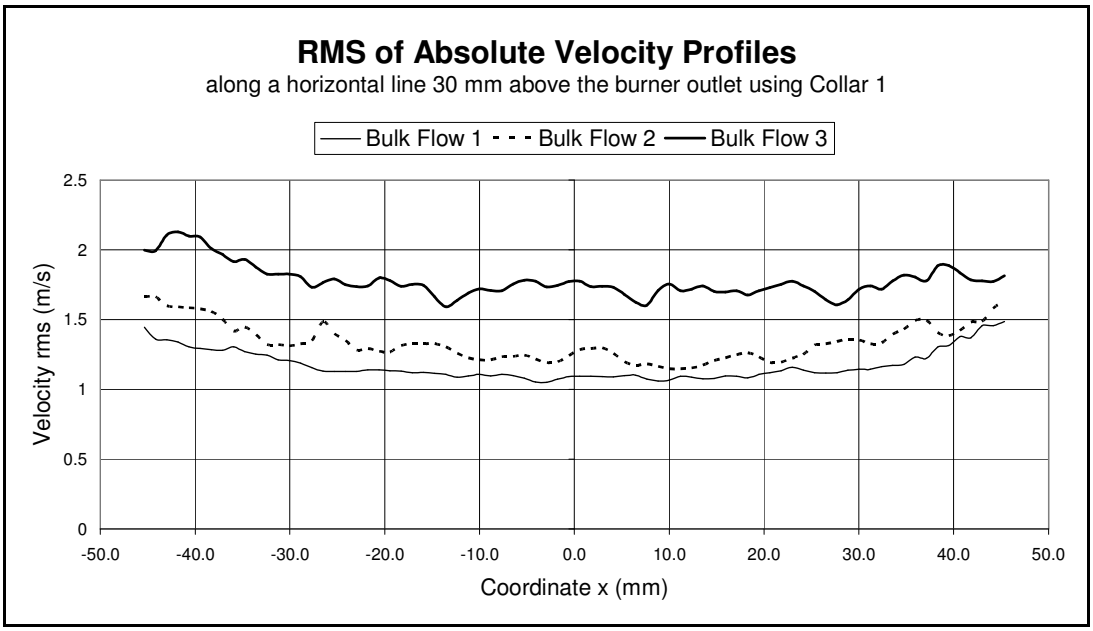

Figure 8.32. Absolute velocity RMS profiles along a horizontal line that intersects the burner axis 30 mm above the coordinate system origin. The profiles are considered in the cold flow conditions for each of the three Bulk Flows.

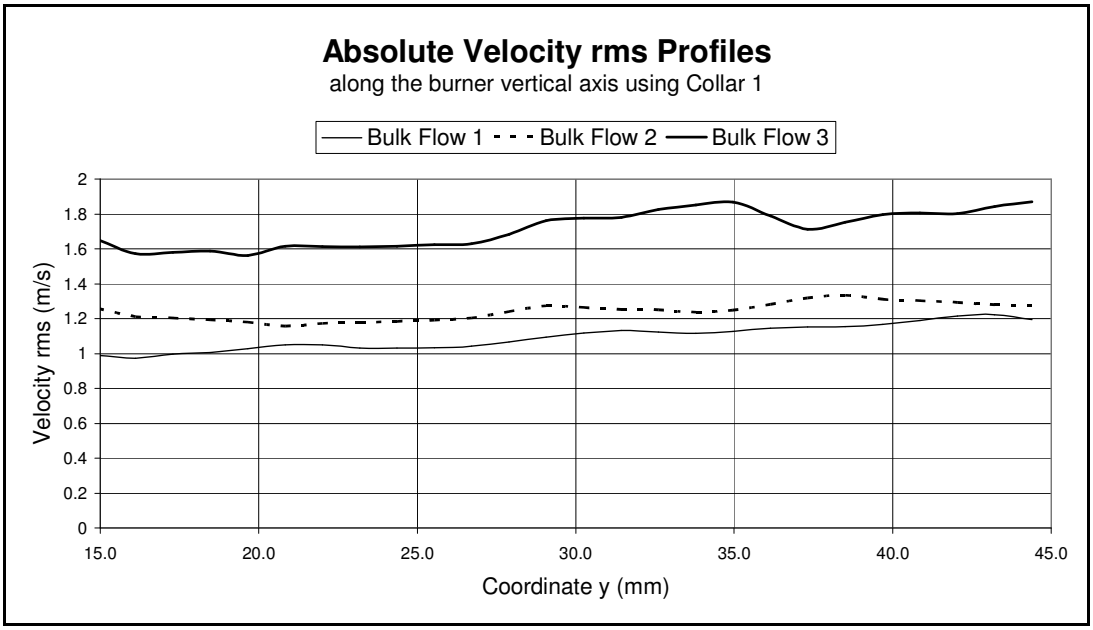

Figure 8.33. Absolute velocity RMS profiles along a line coincident with the y axis. The profiles are considered in the cold flow conditions for each of the three Bulk Flows.

8.2 Equivalence Ratio Stratification

The average equivalence ratio distribution has been obtained using Acetone-PLIF for all burner operational conditions defined in Section 4.5. They have been calculated in all the imaged areas shown in Figure 7.5 (Collar 1 outlet), Figure 7.6 (Collar 2 outlet) and Figure 7.7 (Collar 2 inside the burner outlet's mixing section). The data have been collected for the cold flow conditions, without igniting the flames. The major interest was to determine the average equivalence ratio distribution for the burner outlet flow, upstream of the flame area. It has been confirmed by the analysis in Section 8.1 that the velocity flow field does not remarkably change with the presence of the flames, and especially in the area upstream the flame front. Therefore the average equivalence ratio fields are going to be analyzed using the values along a horizontal line 30 mm above the burner outlet (for Collar 1 and Collar 2).

In Section 8.1 focus was on the configuration Collar 2 because 3D-PIV data were available both in the outlet region and inside the outlet's mixing section. The analysis of the equivalence ratio distribution will use the data of the configuration using Collar 2 because images have been collected, both in the outlet region and inside the mixing section of the burner outlet.

In Figure 8.34, Figure 8.35 and Figure 8.36 the average equivalence ratio values along a horizontal line 30 mm above the burner outlet using configuration Collar 2 are displayed. The figures are referred to Bulk Flow 1, Bulk Flow 2 and Bulk Flow 3 respectively. In all the figures the equivalence ratio profiles associated with Flame A and Flame F are shown, because they are limiting conditions and all the other flames are between their curves. Flame A is characterized by having the annular flow (Flow 2) at higher equivalence ratio, while Flame F has higher fuel concentration in the inner flow (Flow 1). A direct consequence is that the profiles for Flame F are associated with higher values of equivalence ratio in the inner region ($-15 < x < 15$).

The burner operational conditions defined in Section 4.5 are such that Flames A, B and C are characterized by an annular flow (Flow 2) at higher equivalence ratio when compared to the inner flow (Flow 1). This is not maintained in the average equivalence ratio profile upstream the flame front.

The air swirl flow, after mixing with Flow 2 and Flow 1 in the mixing section of the burner outlet, produces a leaning effect on the overall flow, and especially on the region of Flow 2. This is confirmed if the mass fraction profiles of the three flows are considered as it is shown in Figure 8.37. Only the case of Bulk Flow 1 is presented, but the profiles are similar for the other conditions. The air swirl flow mass fraction decreases while moving towards the inner part of the flow without going to zero. In the annular flow region $20 < |x| < 30$ it maintain its values at around 25%, with a detectable effect on the overall equivalence ratio if compared with the inner region when the percentage oscillate around 10%.

The difference between the profiles associated with the average equivalence ratio values for Flame A and F are not remarkably different because the inner and annular flows are mixed together. This is underlined by their average mass fraction profiles. The maximum value of mass fraction for the inner flow (Flow 1) is $\approx 55\%$, this means that

the inner flow influence on the average equivalence ratio is $\approx 55\%$ in the region of interest. The same consideration can be given to the annular flow (Flow 2). The intersection between the two profiles indicates the region where the effect of fuel stratification is statistically higher.

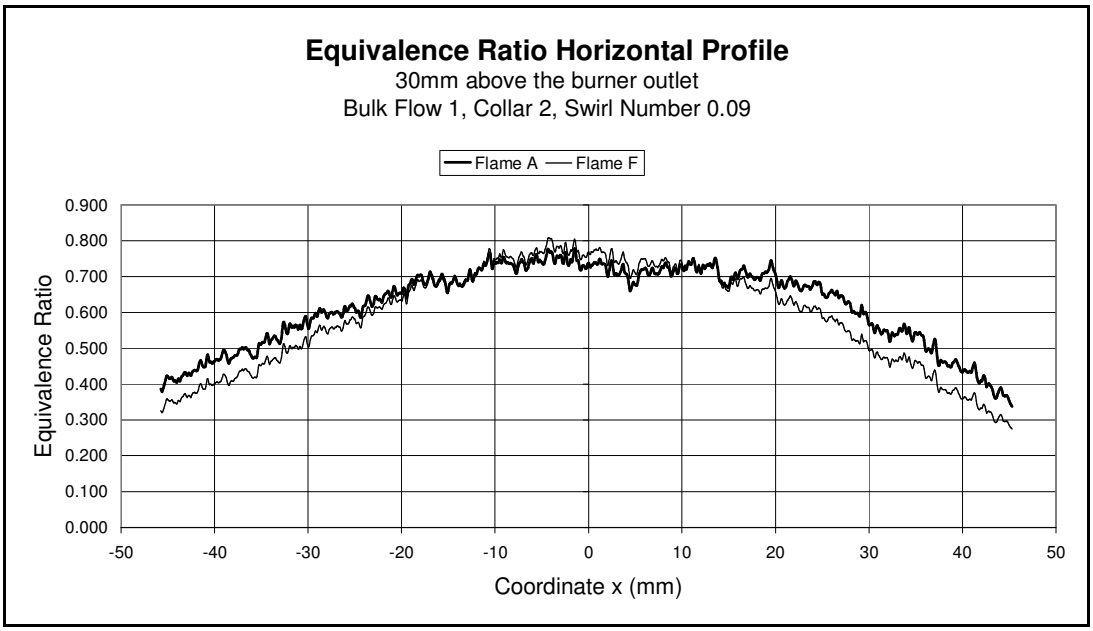

Figure 8.34. Average equivalence ratio profiles along a horizontal line 30mm above the burner outlet. The burner operational conditions considered are: Bulk Flow 1, Collar 2 and Swirl Number $S = 0.09$. The profiles associated to Flame A and F are displayed as representative for all the flames analyzed because they are the extreme cases.

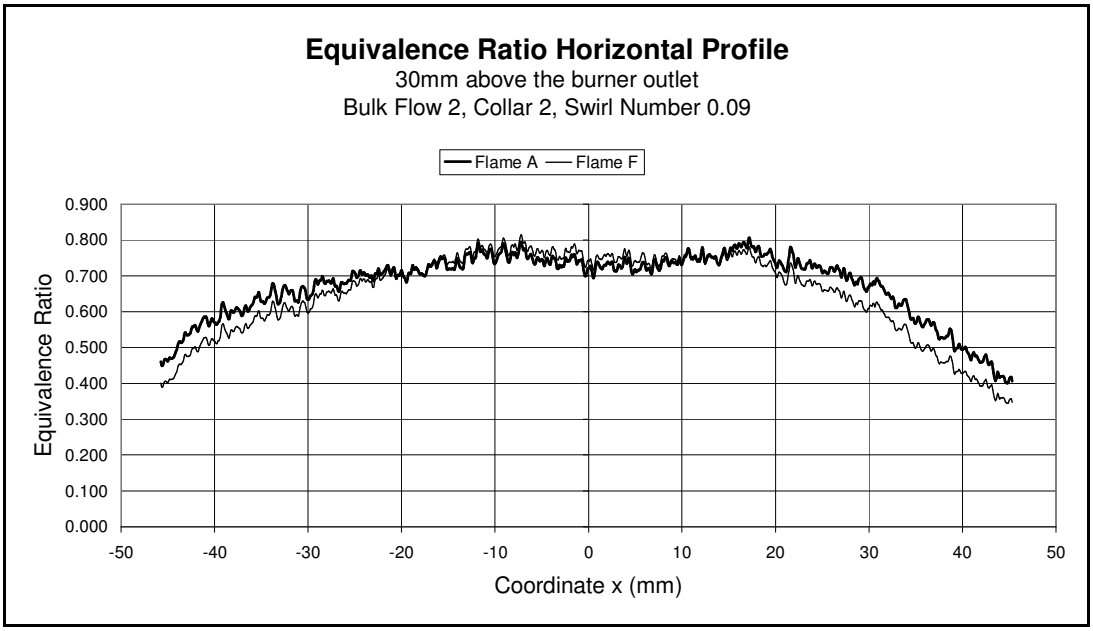

Figure 8.35. Average equivalence ratio profiles along a horizontal line 30mm above the burner outlet. The burner operational conditions considered are: Bulk Flow 2, Collar 2 and Swirl Number $S = 0.09$. The profiles associated to Flame A

and F are displayed as representative for all the flames analyzed because they are the extreme cases.

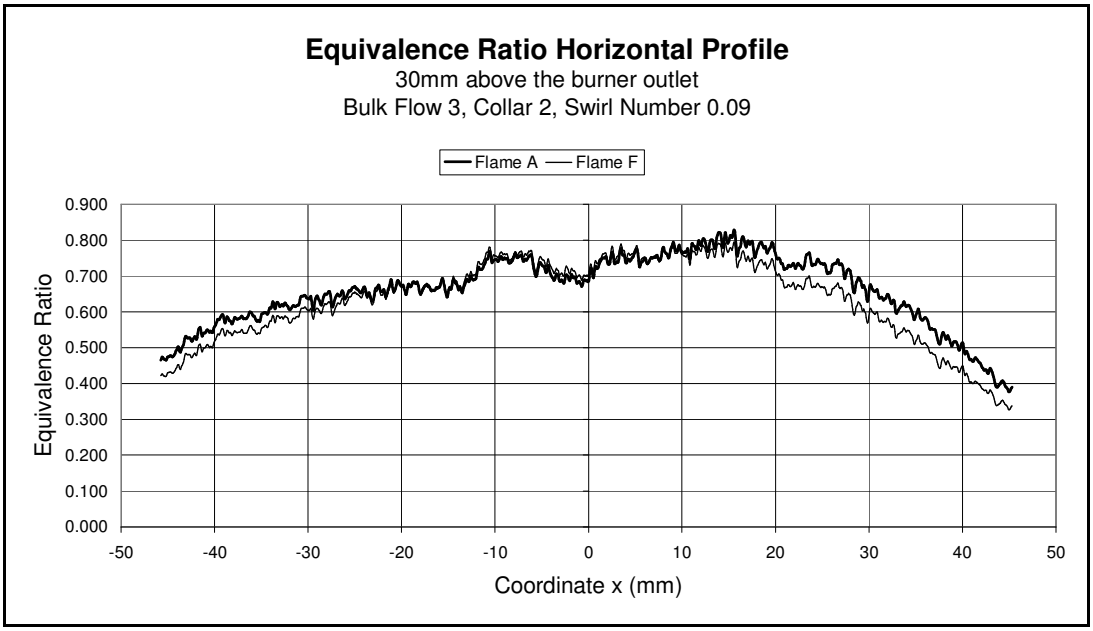

Figure 8.36. Average equivalence ratio profiles along a horizontal line 30mm above the burner outlet. The burner operational conditions considered are: Bulk Flow 3, Collar 2 and Swirl Number $S = 0.09$. The profiles associated to Flame A and F are displayed as representative for all the flames analyzed because they are the limiting cases.

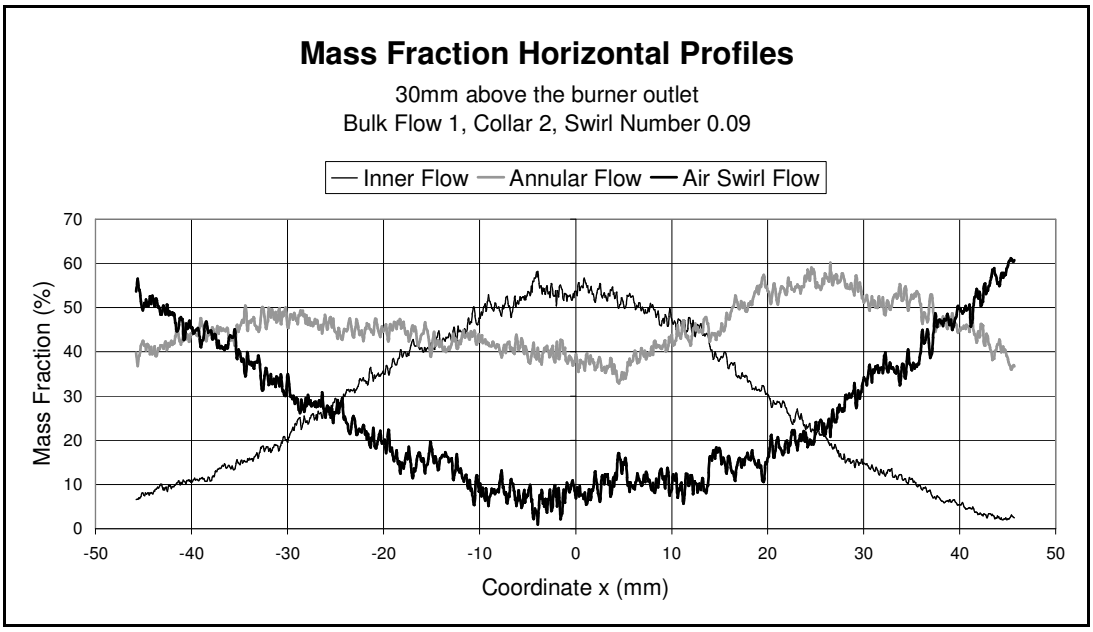

Figure 8.37. Average mass fraction profiles along a horizontal line 30mm above the burner outlet. The burner operational conditions considered are: Bulk Flow 1, Collar 2 and Swirl Number $S = 0.09$. The profiles displayed are associated to the three flow components (Flow 1, Flow 2 and Air Swirl Flow).

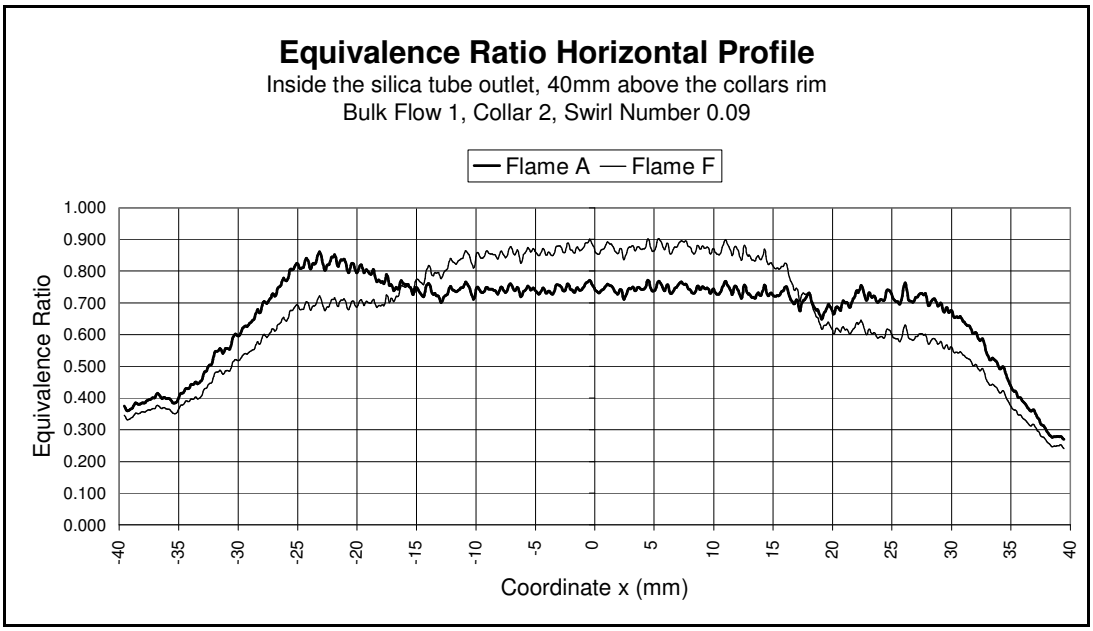

Figure 8.38. Average equivalence ratio profiles along a horizontal line 40mm above the inside collars rims in the burner outlet mixing section. The burner operational conditions considered are: Bulk Flow 1, Collar 2 and Swirl Number $S = 0.09$. The profiles associated to Flame A and F are displayed as representative for all the flames analyzed because they are the extreme cases.

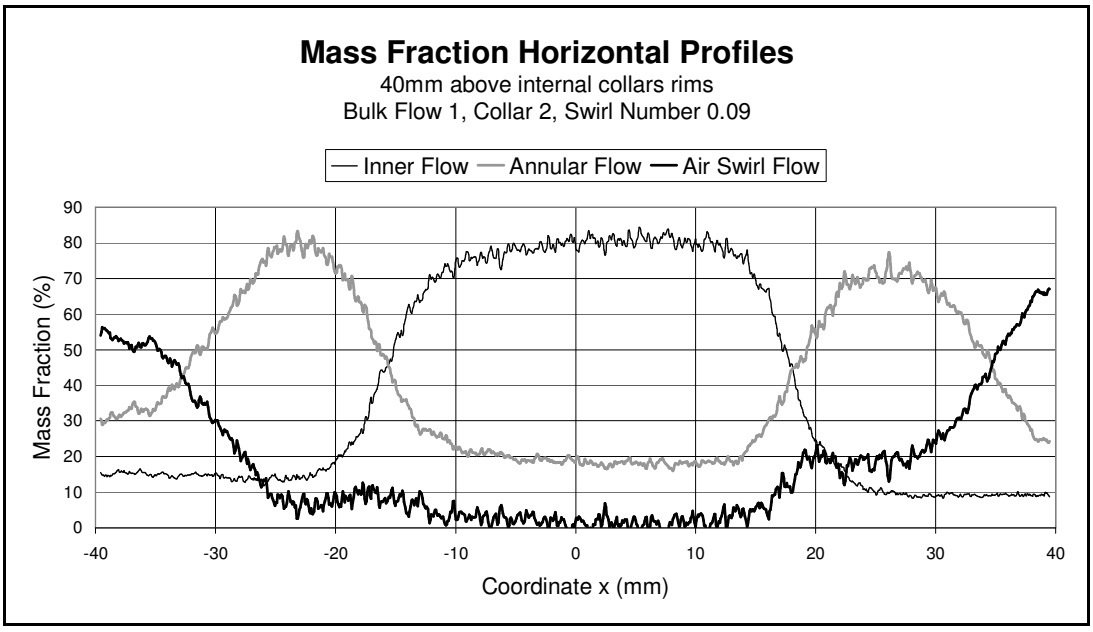

Figure 8.39. Average mass fraction profiles along a horizontal line 40mm above the inside collars rims in the burner outlet mixing section. The burner operational conditions considered are: Bulk Flow 1, Collar 2 and Swirl Number $S = 0.09$. The profiles displayed are associated to the three flow components (Flow 1, Flow 2 and Air Swirl Flow).

The average equivalence ratio distributions for Flame A and F are characterized by a stronger difference when considered inside Collar 2 outlet, because the mixing process is at its initial stages. The profiles of the average equivalence ratio inside Collar 2 associated to Flame A and F are shown in Figure 8.38, they are obtained along a horizontal line 40mm above the collars rims. Observing the profile for Flame A, the inner region is leaner than the annular area but not as much as the equivalence ratios associated to the inner flow and annular flow separately for this flame conditions. This suggests that the mixing process even at the initial stages already has affected the average equivalence ratio distribution.

Figure 8.39 shows the mixing of the three flows at the same experimental conditions considered for the profiles in Figure 8.38. The mass fraction percentage of Flow 1, Flow 2 and Swirl Flow are displayed as profiles along a horizontal line 40mm above the inside collars rims. The swirl flow has a detectable influence on the annular flow with a consequent leaning effect. The mixing of Flow 2 and Flow1 is already developed thanks to the turbulence produced by the collars rims even though the position is only 40mm into the mixing section. These two observations explain why the equivalence ratio values in the annular region of Flame A are less than the value associated to the unmixed annular flow.

The average equivalence ratio distribution along a horizontal line 30mm above the burner outlet for Collar 1 is shown in Figure 8.40. The experimental conditions for Bulk Flow 1, swirl number $S = 0.09$, and the profiles of Flame A and F are displayed. These plots can be compared with the ones shown in Figure 8.34 for Collar 2. The differences in average equivalence ratio for the two profiles are smaller than the case of Collar 2. This is due to the fact that Collar 1 internal diameter is bigger than Collar 2 (150mm instead of 130mm) and consequently the flow rate associated with the air swirl flow is larger. It has been shown for Collar 2 that the air swirl flow has a strong leaning effect especially on the annular flow. This is shown again in Figure 8.41 for Collar 1. The mass fraction profile for the air swirl flow is characterized by higher values when compared to the profile in Figure 8.37 for Collar 2.

It has to be underlined that the analysis has been performed using data about the average equivalence ratio, which indicates a statistical measure. In instantaneous cases, stronger gradients in equivalence ratio distribution are expected to appear.

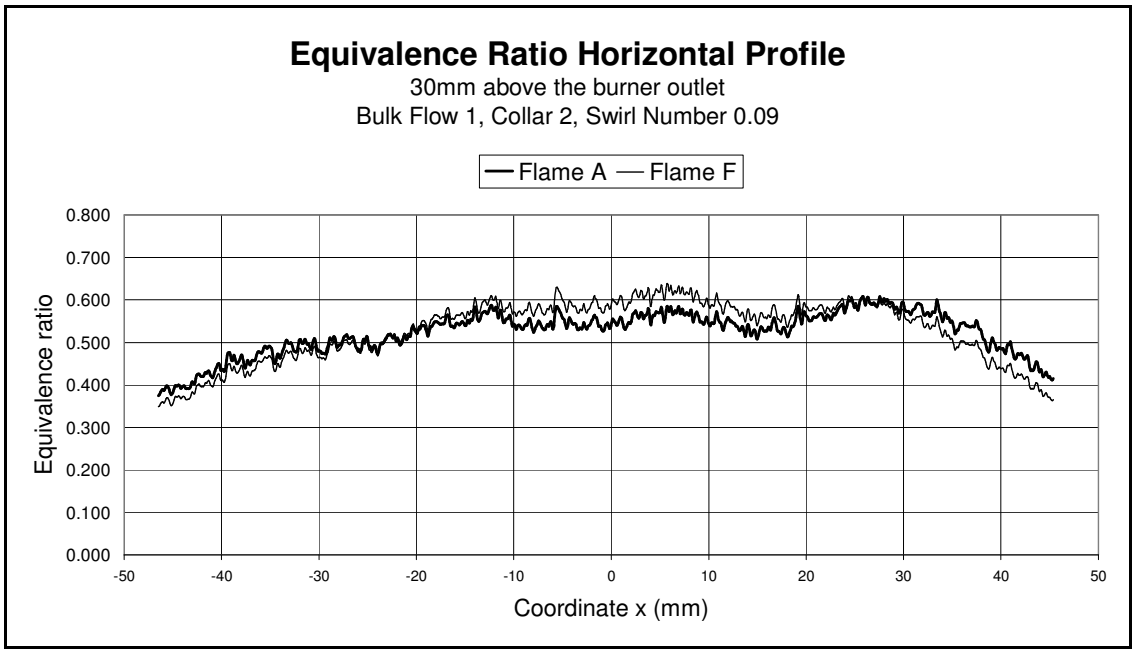

Figure 8.40. Average equivalence ratio profiles along a horizontal line 30mm above the burner outlet. The burner operational conditions considered are: Bulk Flow 1, Collar 1 and Swirl Number $S = 0.09$. The profiles associated to Flame A and F are displayed as representative for all the flames analyzed because they are the limiting cases.

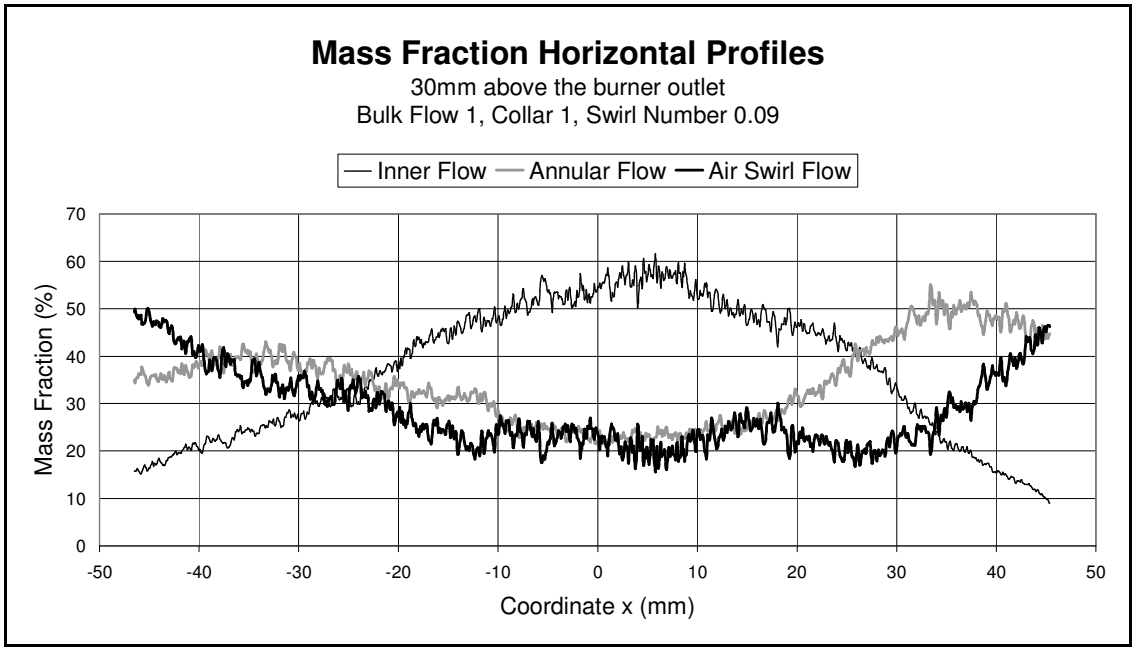

Figure 8.41. Average mass fraction profiles along a horizontal line 30mm above the burner outlet. The burner operational conditions considered are: Bulk Flow 1, Collar 2 and Swirl Number $S = 0.09$. The profiles displayed are associated to the three flow components (Flow 1, Flow 2 and Air Swirl Flow).

8.2.1 Masks Definition for Stratification Analysis

The equivalence ratio distribution is obviously not uniform, especially if the whole imaged area is considered. The analysis of the fuel concentration effects on flame propagation requires individual regions in which the average equivalence ratio can be assumed uniform. Therefore the flame front parameters can be compared across different regions. The imaged areas for Collar 1 and Collar 2 have been divided into ten regions that are equivalent to ten vertical stripes of constant width.

The equivalence ratio profiles analyzed have shown symmetry with respect to the y axis, therefore a further simplification has been applied, each of the ten regions has been paired with the symmetrical one. Consequently, 5 masks have been defined. They have been numbered from 1 to 5 when going from the external region to the centre of the area imaged. The masks have been defined for each one of the burner outlet configurations used (Collar 1 and Collar 2). In Figure 8.42 the masks defined for Collar 2 are shown. The geometrical dimensions of the masks have been kept constant when the experimental data collected using PIV, Rayleigh and Acetone-PLIF have been analysed for the fuel stratification effects on flame propagation.

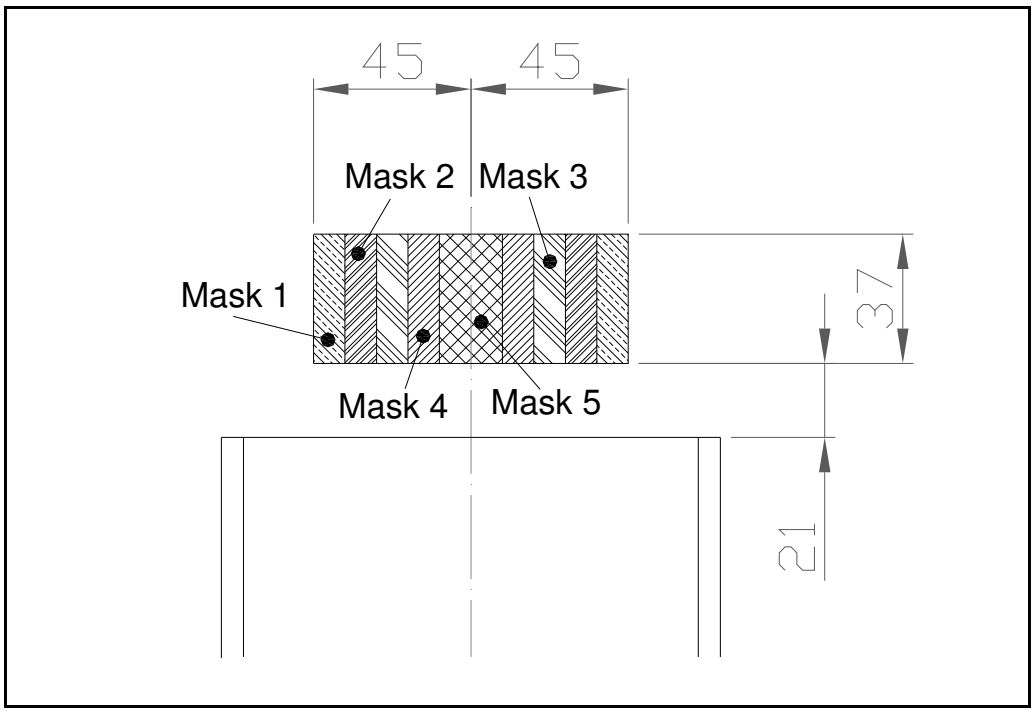

Figure 8.42. Masks defined for the burner outlet configuration Collar 2, in order to differentiate the analysis of the flame front propagation parameters. The five masks are indicated using five different geometric patterns.

8.3 Characterization of the Turbulent Combustion Regime

The flames are going to be characterized through the determination of several parameters that are important to define the turbulent combustion regime associated to the each flow condition. The configuration using Collar 2 will be considered in first place because 3D-PIV data are available. The results are shown in Table 8.3, and the same parameters are shown in Table 8.4 for the experimental conditions with Collar 1. The following section describes the procedures used to obtain the parameters reported in the two tables.

The average flow velocity without swirl has been obtained from the vector fields computed inside the burner outlet mixing section when the tangential jets flow was switched off. While the average velocity under the effect of the swirl flow has been calculated considering a point on the burner axis 30mm above the outlet rim. For each Bulk Flow 200 images of the cold flow conditions have been used to obtain the average value.

The average equivalence ratio has been obtained from the values along the horizontal line 30mm above the outlet rim within a diameter of 65mm. For each Bulk Flow condition all six flames that are associated with it have contributed to the average equivalence ratio calculation.

The laminar flame speed has been obtained for the experimental data presented by Gu (Gu et al., 2000). An interpolation has been used to define s_L for the equivalence ratio values previously computed. The reaction zone thickness δ_R is then calculated using the original Klimov criterion (Libby and Williams, 1980):

$$s_L \, \delta_R = \nu \qquad (8.1)$$

With ν the flow kinematic viscosity obtained from the tables in (Lide, 2003) at the temperature and pressure of the experimental conditions considered ($\nu = 1.79 \cdot 10^{-5} \, m^2/s$).

The flame thickness δ has been calculated averaging the flame thickness values extrapolated from the progress variable fields as explained in Section 6.4. All the values collected for each bulk flow rate have been averaged and the final results are reported in Table 8.3.

The average turbulent flame speed has been gained from the values extracted from the velocity fields through the procedure explained in Section 5.3. The average values for each Bulk flow have been considered. The flame speeds ratio s_T / s_L increases with the Bulk Flow and this is a straight consequence of the fact that higher turbulence determines higher burning velocities.

Parameter Description for COLLAR 2	Bulk Flow			Unit
	1	2	3	
Average flow velocity without swirl	6	7	9	m/s
Average flow velocity with swirl $\bar{u}$	1.51	1.88	2.11	m/s
Average combustible mixture mass flow rate	23.64	27.58	35.46	g/s
Swirl number S	0.09	0.09	0.09	-
Average equivalence ratio ϕ	0.60	0.66	0.65	-
Laminar flame speed s_L	0.12	0.17	0.16	m/s
Reaction zone thickness δ_R	151	105	111	μm
Flame thickness δ	1140	1124	1122	μm
Measured average turbulent flame speed s_T	2.13	2.82	3.47	m/s
Flame speeds ratio s_T/s_L	17.94	16.57	21.47	-
Turbulent radial velocity component u_x'	0.54	0.72	0.88	m/s
Turbulent axial velocity component u_y'	0.73	0.88	1.12	m/s
Turbulent tangential velocity component u_z'	0.54	0.67	0.89	m/s
Absolute velocity RMS u'	1.03	1.34	1.67	m/s
Turbulence intensity I_t	0.7	0.7	0.8	
Integral length scale l_t	15	15	15	mm
Turbulent Reynolds number Re_t	880	1106	1408	-
Taylor length scale λ_t	506	451	400	μm
Kolmogorov length scale η_K	93	78	65	μm
Borghi diagram x coordinate l_t/δ_R	13.16	13.33	13.37	-
Borghi diagram y coordinate u'/s_L	8.84	7.76	10.40	-
Damköhler number Da	1.49	1.72	1.29	-
Karlovitz number Ka	2.64	1.81	2.88	-

Table 8.3. Experimental parameters of the flow conditions considered for Collar 2.

The average turbulent components (u_x', u_y', u_z') of the velocity are a measure of the turbulent level and its isotropy. They have been obtained from the velocity vector fields in cold flow conditions for each Bulk Flow. The average values have been calculated on a point of the burner axis 30mm above the burner rim. The RMS value of the absolute velocity, u', has been determined using the same point and conditions indicated for the velocity components.

The turbulence intensity has been defined by the Equation (2.6) and it is a measure of the turbulence strength. It is calculated as the ratio of the absolute velocity RMS and the average absolute velocity ($u'/\bar{u}$).

The integral length scale has been calculated applying Taylor's hypothesis to the length scales deduced from the integration of the spatial correlation function for the radial component of the velocity (Kundu and Cohen, 2004):

$$r_{ac}(x) = \frac{\overline{u_x(x_0,t)\, u_x(x_0+x,t)}}{\overline{u_x^2}} \qquad (8.2)$$

The integral length scale can be defined as:

$$l_t = \int_0^\infty r_{ac}(x)dx \qquad (8.3)$$

The integral operation has been applied on a horizontal line 30mm above the burner outlet for each velocity vector field obtained in the cold flow conditions. The overall average value is reported in Table 8.3 and Table 8.4. The same value has been obtained by Bedat and Cheng for a burner using a turbulence generator with similar geometrical characteristics (Bedat and Cheng, 1995). Once the integral length scale is known it is possible to calculate the turbulent Reynolds number according to Equation (2.8).

The Taylor length scale, λ_t, and the Kolmogorov length scale, η_k, can be defined with the following equations when the integral length scale and the turbulent Reynolds number is known (Libby and Williams, 1980):

$$\lambda_t = \frac{l_t}{\mathrm{Re}_t^{1/2}} \qquad (8.4)$$

$$\eta_k = \frac{l_t}{\mathrm{Re}_t^{3/4}} \qquad (8.5)$$

The Damköhler number, Da, can be calculated according to Equation (2.17), while for Karlovitz number, Ka, the Equation (2.18) can be modified in (Peters, 2000):

$$Ka = \frac{\tau_c}{\tau_k} = \frac{\delta_R^2}{\eta_k^2} \qquad (8.6)$$

It in now possible to define for the flames considered with Collar 2 their positions in the modified Borghi diagram shown in Figure 8.43 and previously described in Section 2.2.2. According to the modified Borghi diagram the flames considered are above the Klimov Williams limit and below the line at $Da = 1$. It means that the combustion regime is the thickened-wrinkled flames. The smallest scales of turbulence are capable to enter and thicken the flame preheat zone but they are not small enough to enter the reaction zone.

The same parameters have been obtained for the experimental configuration using Collar 1. The results are reported in Table 8.4 and the positions in the modified Borghi diagram are shown in Figure 8.44. Also in this case the combustion is in the thickened-wrinkled flame regime, above the Klimov Williams limit and below the line at $Da = 1$. It is reasonable that the two configurations are related to the same area in the Borghi diagram. The combustible mixtures flow rates are the same and the equivalence ratios values are very close. The turbulence generator does not change in the two configurations and consequently the turbulence characteristics for Collar 1 and Collar 2 are equivalent.

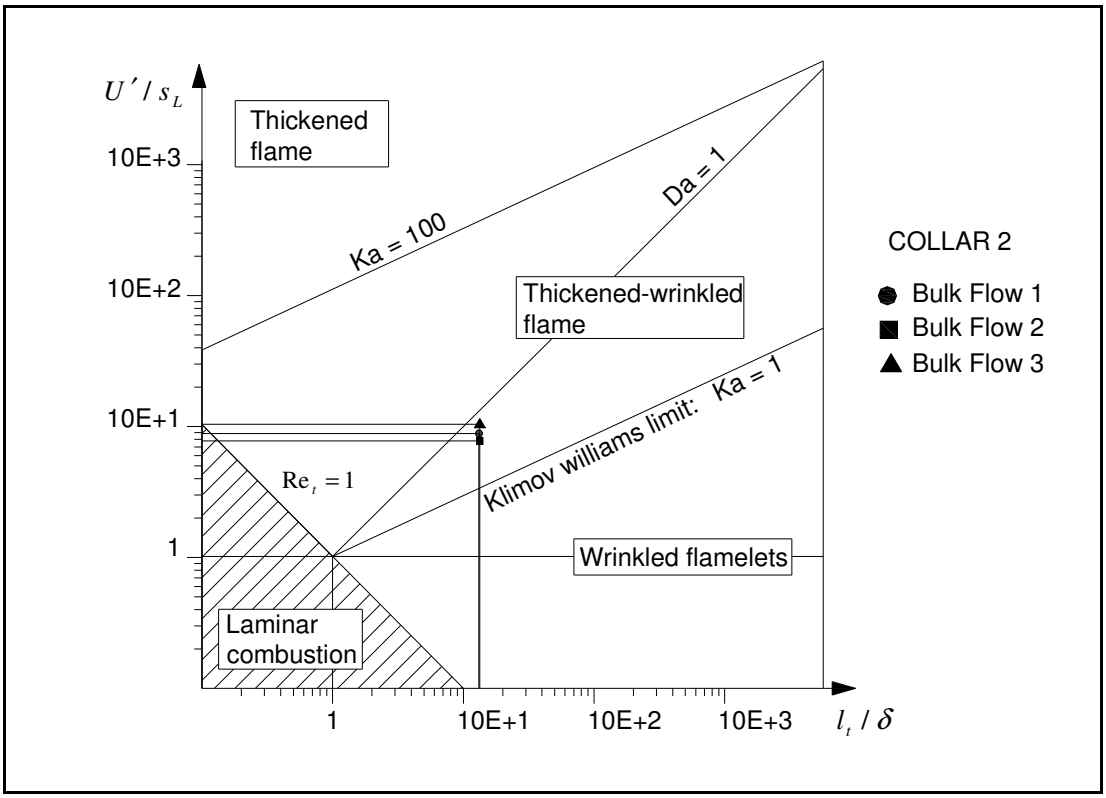

Figure 8.43. Classification on the modified Borghi diagram of the cases considered for the burner outlet configuration Collar 2.

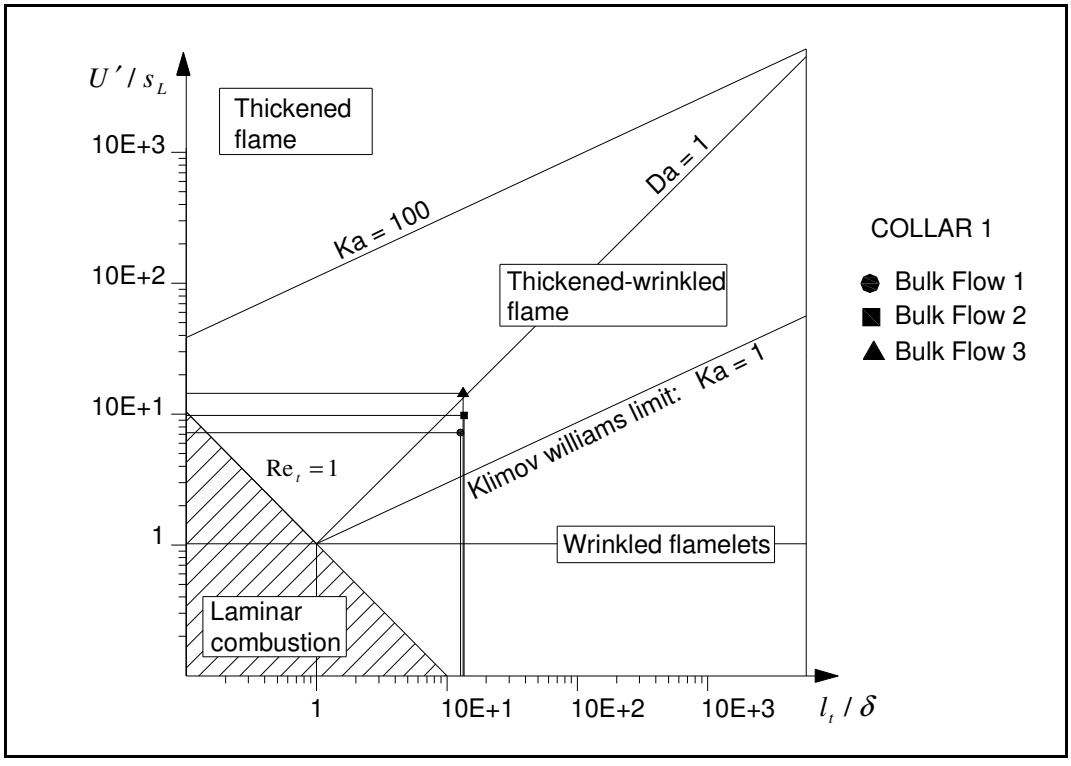

Figure 8.44. Classification on the modified Borghi diagram of the cases considered for the burner outlet configuration Collar 1.

Parameter Description for COLLAR 1	Bulk Flow			Unit
	1	2	3	
Average flow velocity without swirl	6	7	9	m/s
Average flow velocity with swirl $\bar{u}$	1.24	1.64	2.17	m/s
Average combustible mixture mass flow rate	23.64	27.58	35.46	g/s
Swirl number S	0.09	0.09	0.09	-
Average equivalence ratio ϕ	0.60	0.60	0.59	-
Laminar flame speed s_L	0.12	0.12	0.11	m/s
Reaction zone thickness δ_R	151	151	162	μm
Flame thickness δ	1183	1114	1127	μm
Measured average turbulent flame speed s_T	2.12	2.86	3.55	m/s
Flame speeds ratio s_T/s_L	17.85	24.08	32.22	-
Absolute velocity RMS u'	0.85	1.18	1.57	m/s
Turbulence intensity I_t	0.69	0.71	0.73	-
Integral length scale l_t	15	15	15	mm
Turbulent Reynolds number Re_t	721	972	1332	-
Taylor length scale λ_t	559	481	411	μm
Kolmogorov length scale η_K	108	86	68	μm
Borghi diagram x coordinate l_t/δ_R	12.7	13.5	13.3	-
Borghi diagram y coordinate u'/s_L	7.24	9.77	14.43	-
Damköhler number Da	1.75	1.38	0.92	-
Karlovitz number Ka	1.95	3.06	5.7	-

Table 8.4. Experimental parameters of the flow conditions considered for Collar 1.

9 EQUIVALENCE RATIO STRATIFICATION EFFECTS ON FLAME PROPAGATION

In the previous chapters, parameters like burning velocity, flame curvature and flame thermal thickness have been extracted from the experimental data collected through PIV and Rayleigh measurements. These are important characteristics of the flame front and their interaction with the equivalence ratio stratification is a key factor for the understanding of the flame front propagation in stratified mixtures.

It has been underlined previously that the analysis of the flame front propagation needs a statistical approach. For this reason the data about burning velocity, flame curvature and flame thermal thickness have been organized as PDF distributions for each of the different experimental conditions considered. For every flame defined in the operating conditions in Section 4.5 a PDF distribution of the above parameters has been created. At this stage the objective is to show the relation between equivalence ratio stratification and flame front propagation, therefore the PDF distribution of each flame has been further divided into PDF distributions associated with each of the five masks that divide the imaged area as defined in Section 8.2.1.

In the following analysis the PDF distribution characteristics and their respective changes are going to be considered. It is consequently important to introduce the statistical tools used to study the probability distributions of burning velocity, flame curvature and flame thermal thickness.

When a set of data tends to group around a particular value, it could help to associate few scalars that describe the characteristics of the set of data. These numbers are defined as moments. The most commonly used is the mean of the values $w_1,...,w_N$.

$$\overline{w} = \frac{1}{N}\sum_{j=1}^{N} w_j \qquad (9.1)$$

The mean is not the only quantity capable to estimate the central clustering of the set of data, and it is not always the best one. When the probability distribution has very broad "tails", the mean may be the wrong estimator to use. Other useful quantities are the median and the mode. The median is the value w_{med} for which the probability associated to the occurrence of higher and lower values of w is equal. If the values $w_j \;\; j = 1,...,N$ are arranged into ascending or descending order, the median can be determined using the following formula:

$$w_{med} = w_{(N+1)/2} \quad with\ N\ odd; \quad w_{med} = \frac{1}{2}\left(w_{N/2} + w_{(N/2)+1}\right) \quad with\ N\ even \qquad (9.2)$$

When the area of the tails is large the median it is not a good measure of the central tendency. When the probability distribution is characterized by a sharp maximum for a

determined value w, this is called mode and it can be used as an estimator of the central tendency.

After the determination of the central value of the set of data considered, it is necessary to define the variability around that value. There are several quantities that measure the width of the probability distribution and the most commonly used is the variance:

$$Var(w) = \frac{1}{N-1}\sum_{j=1}^{N}\left(w_j - \overline{w}\right)^2 \qquad (9.3)$$

Or its square root, the standard deviation:

$$\sigma_P(w) = \sqrt{Var(w)} \qquad (9.4)$$

The comparison between two probability distributions involves considering the difference between their central values, and normally it is the mean used as an estimator. The reference unit to analyze this difference it is not the standard deviation but the standard deviation of the mean. The standard deviation of the mean measures the accuracy of the sample mean and it is correlated to the standard deviation of a known distribution from previous measurements (σ_{PK}).

$$Er_{st}(w) = \frac{\sigma_{PK}(w)}{\sqrt{N}} \qquad (9.5)$$

Collar	Bulk Flow	Standard Deviation σ_{PK} (m/s)
1	1	0.86
1	2	1.16
1	3	1.59
2	1	1.05
2	2	1.32
2	3	1.68

Table 9.1. Standard deviation values of the experimental data for all the experimental conditions considered when running the burner in cold flow. The values reported in the table are associated to a point of the burner axis 30 mm above outlet rim.

The measurement system used for collecting the data that will be analyzed in this section is Stereoscopic PIV and the known distributions are the measurements collected when running the burner without igniting the flame. These conditions have been previously defined as cold flow conditions. For both burner outlet configurations and all three bulk flows conditions have been collected experimental data when running cold flow. The standard deviation associated to a point on the burner axis 30 mm above the outlet rim for all the experimental conditions considered are reported in Table 9.1. These values are going to be used as σ_{PK} for the respective experimental conditions while calculating the standard deviation of the mean.

9.1 Burning Velocity Dependence on Fuel Stratification and Turbulence

The procedure used to extrapolate the sets of data for the burning velocity is described in Section 5.3. For each flame condition 200 images have been collected and for each Bulk Flow conditions six flames have been considered. The burning velocity selection procedure described in Section 5.3 allows the determination of an average of ~230 samples from each processed image.

The burning velocity is a flame characteristic strongly related to the turbulence and the equivalence ratio. The influence of these parameters will be studied by varying them independently while keeping the other constant. This procedure allows isolating the effects of one variable in particular to undertake a targeted analysis.

The influence of the turbulence on the burning velocity is shown when considering the burning velocity PDF distributions associated with the three different bulk flows used for the experiments (Bulk Flow 1, 2, 3). The plots are shown in Figure 9.1 for Collar 1 and Figure 9.2 for Collar 2. The turbulence increases with the overall flow rate, as a consequence of this, Bulk Flow 3 produces the highest level of turbulence. The probability distributions in Figure 9.1 and Figure 9.2, show that the increase in turbulence produces a shifting in the probability distribution towards higher values of burning velocity and at the same time the width of the distribution peak is increased. These results are reflected in the values of the mean and the standard deviation reported in Table 9.2, they increase with higher turbulence. The number of samples is very high and this allows a more precise comparison between the pdf distributions considered.

The standard deviations of the means are very low when compared with the variations between the mean values of the three pdf distributions, this underlines the significance of those differences. It can be concluded that the effect of the turbulence on the burning velocity probability distribution is strong.

Collar	**Bulk Flow**	**Standard Deviation** (m/s)	**Mean** (m/s)	**Standard Deviation of the Mean** $(10^{-3} m/s)$	**Number of Samples**
1	1	0.75	2.372	1.8	236,578
1	2	1.23	3.110	2.1	304,483
1	3	1.87	3.797	3.0	285,479
2	1	1.15	2.131	2.4	193,945
2	2	1.24	2.818	2.8	215,355
2	3	1.79	3.470	3.7	200,967

Table 9.2. Standard deviation, mean, standard deviation of the mean and number of samples for burning velocity probability distributions associated to different Bulk Flow conditions.

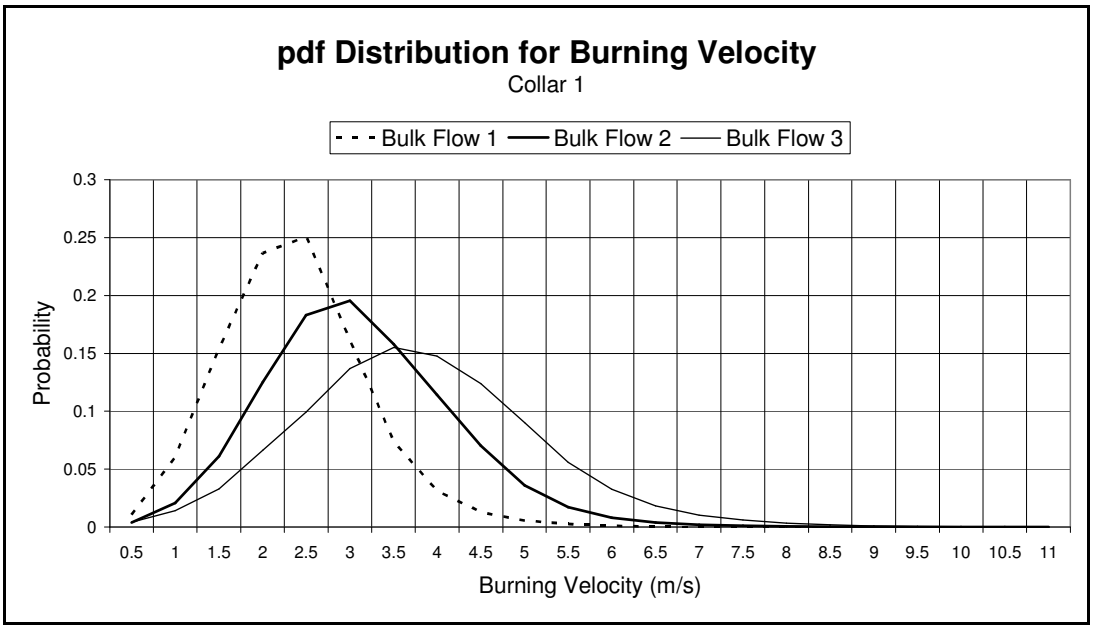

Figure 9.1. Burning velocity PDF distributions associated to the three different bulk flows considered for each set of six flames. The data are referred to the burner outlet configuration defined as Collar 1.

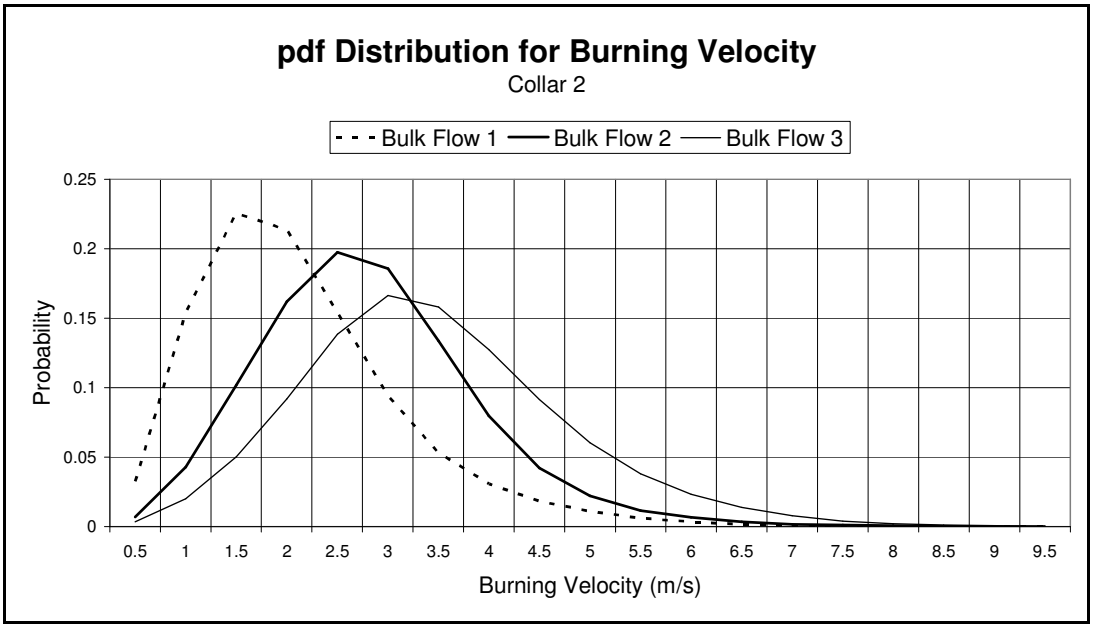

Figure 9.2. Burning velocity PDF distributions associated to the three different bulk flows considered for each set of six flames. The data are referred to the burner outlet configuration defined as Collar 2.

The equivalence ratio acts on the burning velocity in two ways, at first through its absolute value and secondly through its level of stratification. It is difficult to distinguish the two effects because they are linked to the same variable. For this reason sets of six flames (called A, B, C, D , E, F) at different equivalence ratio stratification for each bulk flow have been selected. In Section 4.5 the values of the equivalence ratio for inner flow and annular flow of every flame can be found. Going from Flame A to Flame F the inner flow is associated with an increased concentration in fuel while the annular flow becomes leaner at each step. The change in fuel concentration is associated to variations of equivalence ratio ± 0.025. Flame A is produced by an annular flow (Flow 2) that is characterized by a higher equivalence ratio than the inner flow (Flow 1). Flame D is the first to be associated with an inner flow having higher equivalence ratio than the annular flow.

From the analysis of the equivalence ratio distribution in the previous chapter, the leaning effect of the air swirl flow has been observed, especially on the external region associated to the annular flow (Flow 2). This means that the flames A, B, C are not associated with strong gradients in fuel concentration. Flames D, E, F in which the inner flow (Flow 1) has an increased concentration of fuel and is not affected in the same manner by the leaning effect of the air swirl flow, then the stratification is preserved. In the following analysis flames D, E, F will be considered as increasingly stratified while flames A, B, C are assumed to have an increased fuel concentration in the external regions of the imaged areas, but their equivalence ratio stratification is moderated.

The correlation between burning velocity and equivalence ratio stratification will be analyzed considering three flames in particular: Flame F , Flame C and Flame A. The first is the case associated with the stronger stratification, the second is used as the reference condition because is a flame with nearly uniform equivalence ratio. The third is a flame characterized by a moderate stratification but still with a higher fuel concentration in the annular region.

Table 9.3 gives the values of the mean, the standard deviation and the standard deviation of the mean for the three flames above, when operated in experimental conditions defined by three combinations of two burner outlet configurations and two bulk flow rates. For each one of these combinations, the burning velocity probability distributions are displayed in Figure 9.3, Figure 9.4 and Figure 9.5.

When Bulk Flow 1 is considered, the probability distribution of Flame F is always shifted towards higher values of burning velocity for both burner outlet configurations (Figure 9.3 and Figure 9.4). This is also underlined by the higher values of the mean for Flame F when compared with Flame A and Flame C. The differences in this case are less strong than the case when the turbulence effect has been studied, but considering that they are ≈ 10 times the values of the standard deviation of the mean, they are still of good significance.

The air swirl flow rate when using Collar 1 is greater than the case when using Collar 2 because of the two different dimensions of the internal diameters of the two burner outlet configurations. It has been observed when analyzing the equivalence ratio distribution in Section 8.2 that this determines a reduced leaning effect on the annular flow (Flow 2) when Collar 2 is used. Flame A, when operated using Collar 2, has to be assumed to have a stronger stratification than the case with Collar 1. This determines an increase in the difference of the mean burning velocities for Flame A and Flame C when

comparing the two cases of Collar 1 and Collar 2 at Bulk Flow 1. The mean burning velocity for Flame A remains always less than the value associated with Flame F, because Flame F still represents the condition at higher gradients in fuel stratification.

The differences of the mean burning velocities are smaller if compared with the differences observed when analyzing the effect of turbulence. This is related to the fact that when the equivalence ratio stratification is considered, it is necessary to compare flames at the same level of turbulence and consequently at the same Bulk Flow. The differences between the mean burning velocities of the various flames are consequently very close. The velocity flow fields for the same Bulk Flow are characterized by nearly uniform horizontal velocity distributions while in the vertical direction, the velocity decreases at increased distances from the outlet rim. A flame associated with a higher burning velocity can propagate closer to the outlet rim, but the differences are still rather inferior to the case when the velocity fields of two Bulk Flows are compared.

When operational conditions at higher levels of turbulence are considered, it is impossible to observe the effect of fuel stratification on the burning velocity. It has been underlined that an increase in turbulence determines a greater peak width (standard deviation). This makes the observation of the fuel stratification effect difficult because the differences between the mean values are too close to the standard deviations of the means. Furthermore, the increased turbulence creates a better mixing between the three flow components and consequently a reduction of the gradients in fuel stratification. In Figure 9.5 the probability distributions of the burning velocity for Collar 2 and Bulk Flow 2 are shown for Flames A, C and F. The curves associated to the three flames are nearly undistinguishable.

Collar	**Bulk Flow**	**Flame**	**Standard Deviation** (m/s)	**Mean** (m/s)	**Standard Deviation of the Mean** ($10^{-3} m/s$)	**Number of Samples**
1	1	A	0.868	2.340	4.7	33,424
1	1	C	0.783	2.345	4.2	41,197
1	1	F	0.774	2.415	4.1	43,969
2	1	A	1.203	2.133	5.6	35,400
2	1	C	1.162	2.063	5.9	31,179
2	1	F	1.126	2.184	6.1	29,671
2	2	A	1.253	2.842	6.3	43,906
2	2	C	1.276	2.825	7.3	32,850
2	2	F	1.269	2.849	7.5	31,200

Table 9.3. Standard deviation, mean, standard deviation of the mean and number of samples for burning velocity probability distributions in relation to selected flames.

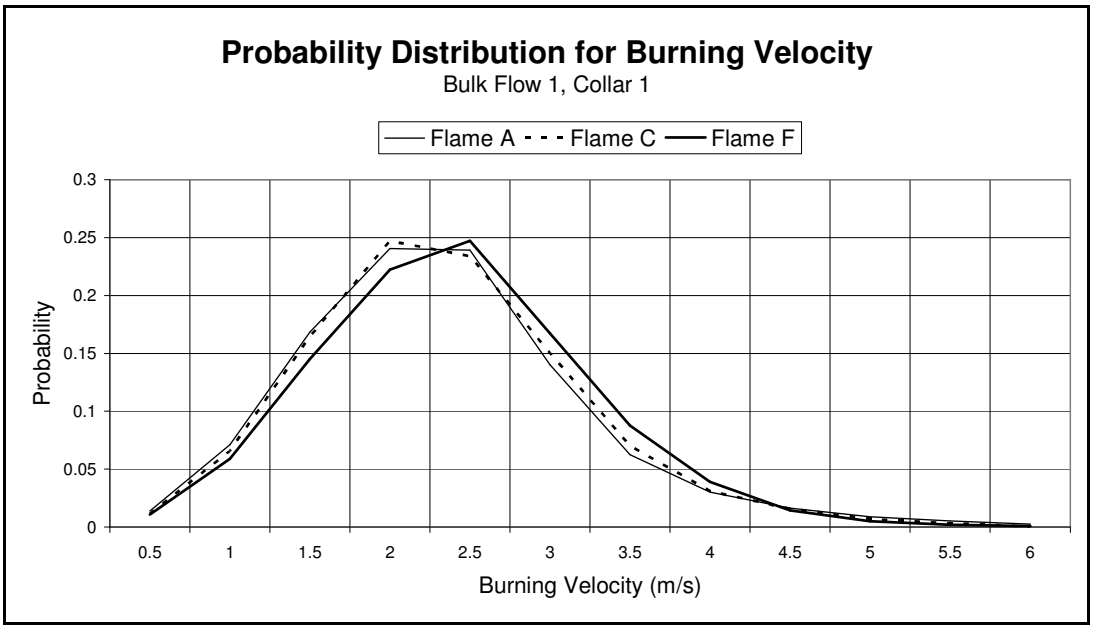

Figure 9.3. Burning velocity PDF distributions associated to three flames (A, C, F) for Bulk Flow 1. The data refers to the burner outlet configuration defined as Collar 1.

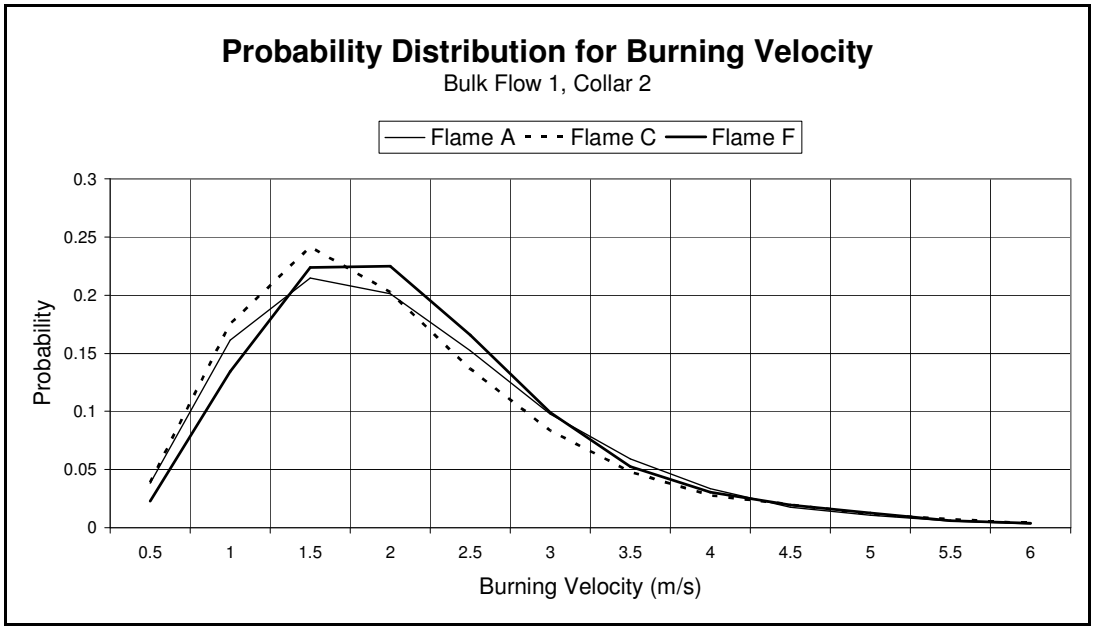

Figure 9.4. Burning velocity PDF distributions associated to three flames (A, C, F) for Bulk Flow 1. The data refers to the burner outlet configuration Collar 2.

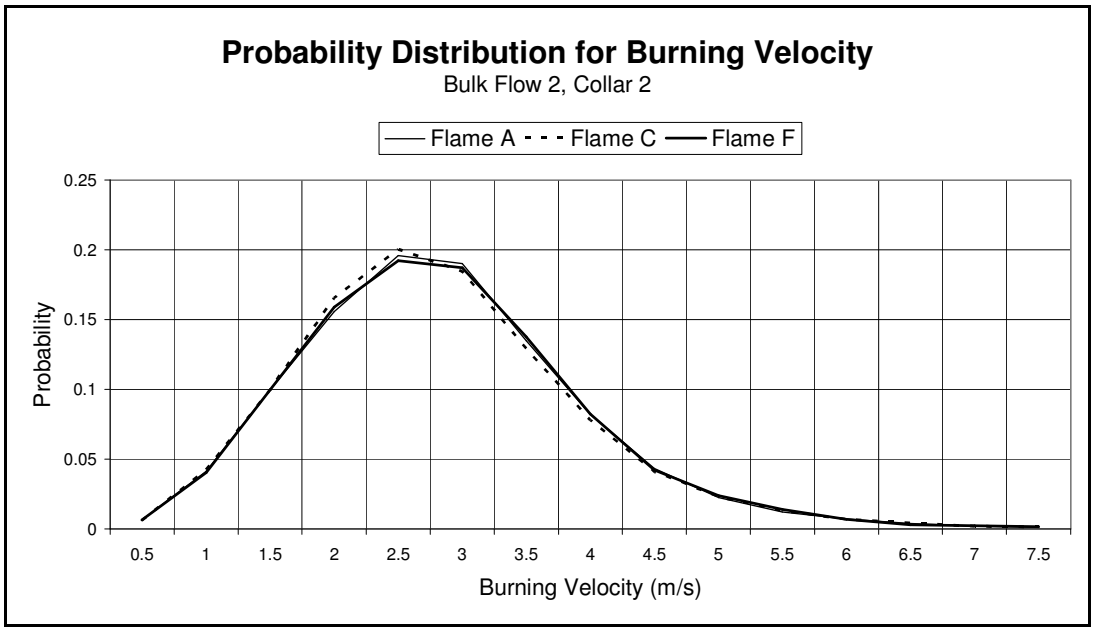

Figure 9.5. Burning velocity PDF distributions associated to three flames (A, C, F) for Bulk Flow 2. The data refers to the burner outlet configuration Collar 2.

9.1.1 Normalized Burning Velocity

The burning velocity is related to the turbulence and the fuel concentration. In order to restrict the analysis to the equivalence ratio distribution effects only, it is necessary to remove the influence of the turbulence. A mathematical expression for the correlation between turbulence and burning velocity has been derived by Cheng (Cheng et al., 2002):

$$\frac{s_T}{s_L} = 2.12\left(\frac{u'}{s_L}\right)+1 \qquad (9.6)$$

It can be applied to the flames considered in this thesis because the experimental analysis of Cheng used a burner with similar geometrical properties and the flames produced are in the same region of the Borghi diagram (same turbulent combustion regime).

The values of the turbulent burning velocity, s_T, have been obtained through the procedure explained in Section 5.3, the absolute velocity RMS values, u', are extrapolated from the velocity fields computed using PIV experiments, and the laminar flame speed, s_L, can be calculated interpolating the experimental results obtained by Gu (Gu et al., 2000). It is then possible to use one of the laminar flame speed variables

present in Equation (9.6) to obtain the normalized burning velocity, s_N, as function of s_T, u' and s_L, whose values are known.

$$s_N = \frac{s_T}{\left(2.12\left(\frac{u'}{s_L}\right)+1\right)} \qquad (9.7)$$

This equation has been used to obtain the normalized burning velocities from all the values of the turbulent burning velocities extrapolated in Section 5.3. Equation (9.7) has been applied to the respective values of the mean equivalence ratio and the absolute velocity RMS for the five regions defined in Section 8.2.1.

The normalized burning velocity is a dimensional quantity and it is analyzed using the probability distributions of the individual regions in the imaged area. These regions are associated with the previously determined average equivalence ratios, obtained from the Acetone-PLIF experiments. In Figure 9.6 the probability distributions of the normalized burning velocities are shown when conditioned on Mask 5 (central region of the area imaged) for Bulk Flow 1 considering the three flames selected previously, Flame A, C and F. In the inner region of the flow, Flame F is characterized by the maximum value for the average equivalence ratio, while Flame A is associated with the minimum. The normalized burning velocity PDF distribution for Flame F is shifted towards larger velocity values as a consequence of the bigger equivalence ratio value. The opposite occurs for Flame A, which is characterized by the smaller values for fuel concentration in this region. The behaviour of the three flames is reversed when Mask 1 (external region of the flow) is considered in Figure 9.7. This time Flame A has the greater fuel concentration, while Flame F is the leanest. The probability distribution of Flame A is shifted towards the higher values of normalized burning velocity.

This is confirmed by the mean values of the normalized burning velocity for the probability distributions studied. Means, standard deviations and standard deviations of the means are reported in Table 9.4. The differences between the mean values confirm the assumptions extracted from the plots of the PDF distributions. These differences can be considered of significance because they are reasonably larger than the related standard deviations of the means.

Figure 9.8 and Figure 9.9 display the probability distributions of the normalized burning velocity for Flames A, C, F in the same experimental conditions considered respectively in Figure 9.6 and Figure 9.7, with Collar 2. These cases also confirm that the flames characterized by higher equivalence ratio in the region considered are associated with normalized burning velocities with larger values. Table 9.4 summarises means, standard deviations and standard errors for the PDF distributions shown in Figure 9.8 and Figure 9.9.

The normalization procedure has been applied to the turbulent burning velocity in order to remove the effect of the turbulence and highlight the analysis of the equivalence ratio correlation with the burning velocity. In the previous section the difficulty in highlighting the consequences of the stratified equivalence ratio when flames at higher level of turbulence are considered has been underlined. It has been shown in Figure 9.5 that for the case of Bulk Flow 2 for Collar 2, the differences between the mean burning

velocities of Flame A, C and F are negligible. After the application of the normalization procedure it is possible to isolate the effect of the equivalence ratio in those experimental conditions.

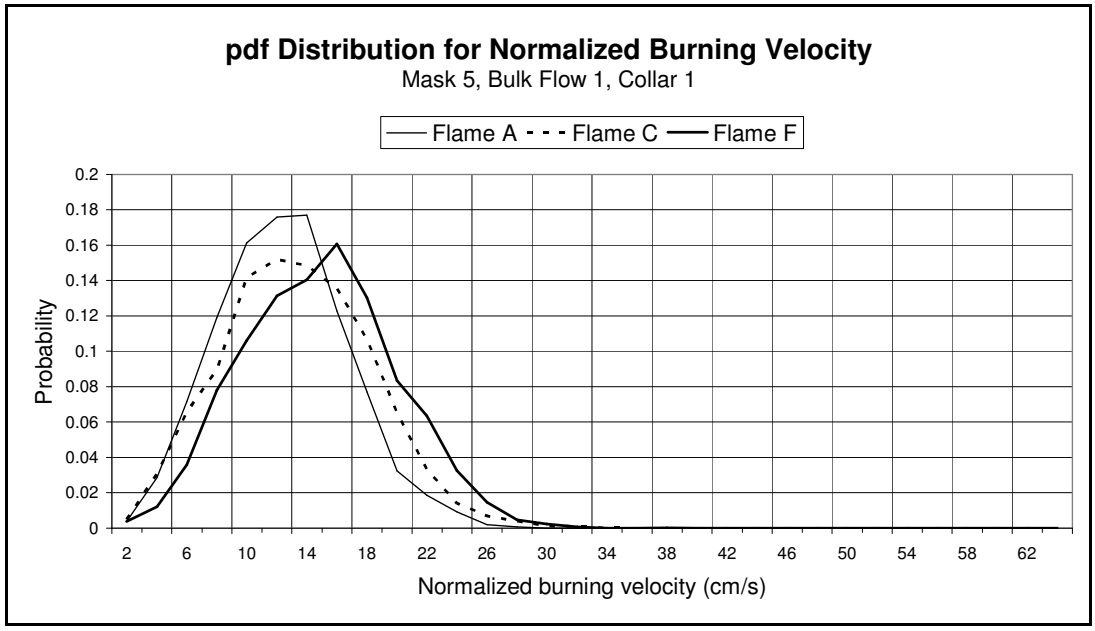

Figure 9.6. Normalized burning velocity PDF distributions associated to the region of Mask 5 for three flames (A, C, F) at Bulk Flow 1. The data refers to the burner outlet configuration defined as Collar 1.

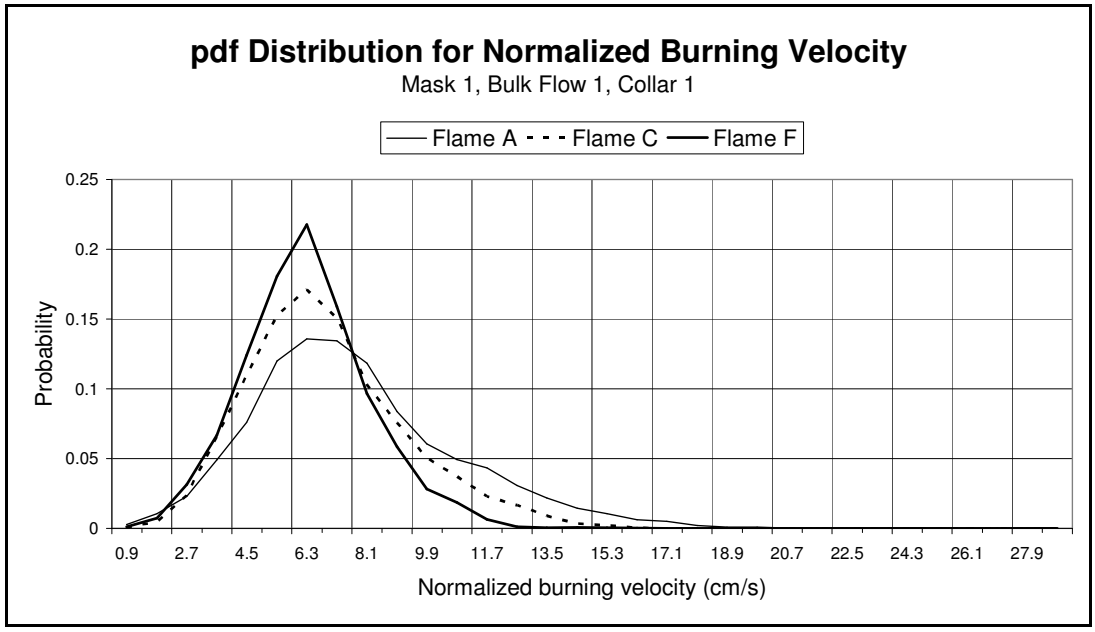

Figure 9.7. Normalized burning velocity PDF distributions associated to the region of Mask 1 for three flames (A, C, F) at Bulk Flow 1. The data refers to the burner outlet configuration defined as Collar 1.

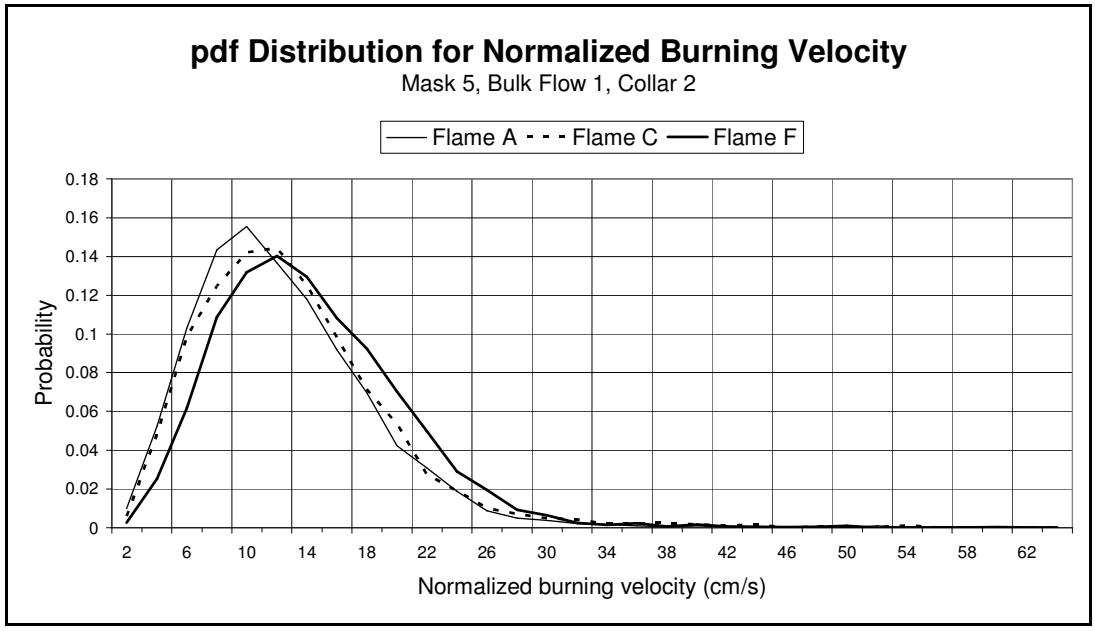

Figure 9.8. Normalized burning velocity PDF distributions associated to the region of Mask 5 for three flames (A, C, F) at Bulk Flow 1. The data refers to the burner outlet configuration defined as Collar 2.

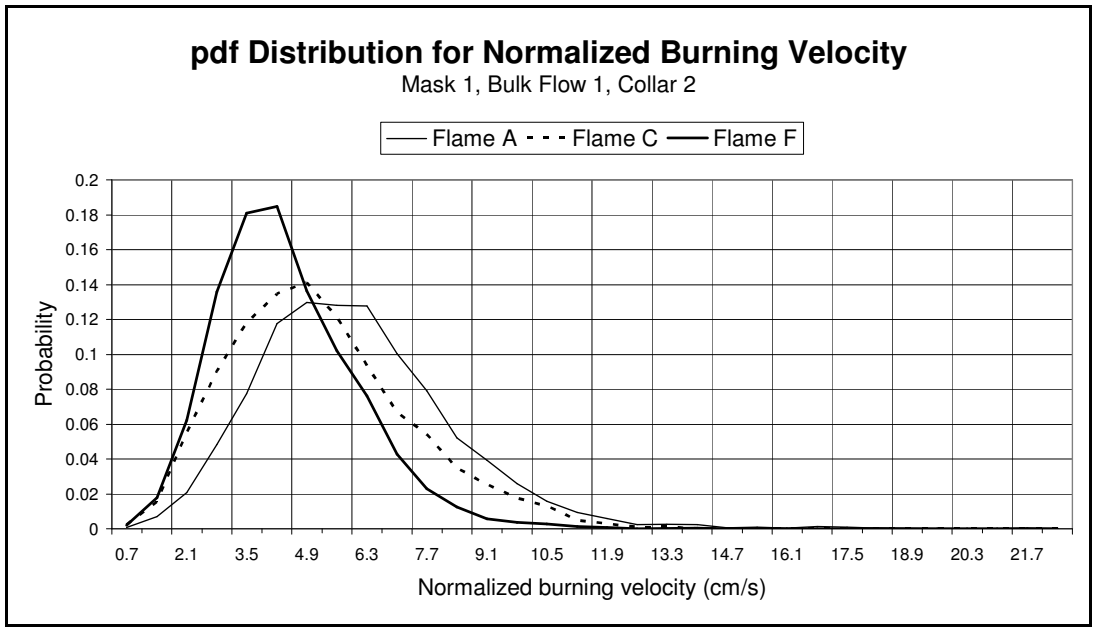

Figure 9.9. Normalized burning velocity PDF distributions associated to the region of Mask 1 for three flames (A, C, F) at Bulk Flow 1. The data refers to the burner outlet configuration defined as Collar 2.

Collar	Mask	Bulk Flow	Flame	Standard Deviation (cm/s)	Mean (m/s)	Standard Deviation of the Mean ($10^{-3} m/s$)	Number of Samples
1	1	1	A	3.12	0.731	9.6	7,960
1	1	1	C	2.39	0.644	8.8	9,595
1	1	1	F	2.03	0.583	8.5	10,121
1	5	1	A	4.30	1.141	10.9	6,254
1	5	1	C	4.93	1.238	9.8	7,755
1	5	1	F	5.63	1.384	9.6	8,099
2	1	1	A	2.76	0.573	11.5	8,336
2	1	1	C	3.59	0.508	12.1	7,557
2	1	1	F	3.80	0.440	12.6	6,983
2	5	1	A	6.25	1.146	13.5	6,073
2	5	1	C	7.02	1.212	14.0	5,614
2	5	1	F	6.79	1.337	14.5	5,270
2	1	2	A	3.92	0.889	13.8	9,180
2	1	2	C	5.25	0.828	14.9	7,839
2	1	2	F	8.37	0.826	15.3	7,409
2	5	2	A	11.68	1.687	14.2	8,646
2	5	2	C	14.10	1.740	17.2	5,878
2	5	2	F	19.53	2.006	17.4	5,738

Table 9.4 . Standard deviation, mean, standard deviation of the mean and number of samples for normalized burning velocity probability distributions.

Figure 9.10 and Figure 9.11 display the PDF distributions of the normalized burning velocity respectively for Mask 5 and Mask 1 when Flame A, C and F are operated in the experimental condition defined by Bulk Flow 2 and Collar 2. In Figure 9.10 Flame F is characterized by the maximum equivalence ratio and this determines that the PDF distribution of the normalized burning velocity is consequently shifted towards higher values. In Figure 9.11 Flame A has the highest fuel concentration and its PDF distribution is shifted towards increased values of normalized burning velocity. These observations are further confirmed by the mean values reported in Table 9.4, in these cases the differences between the mean values are higher than the standard errors.

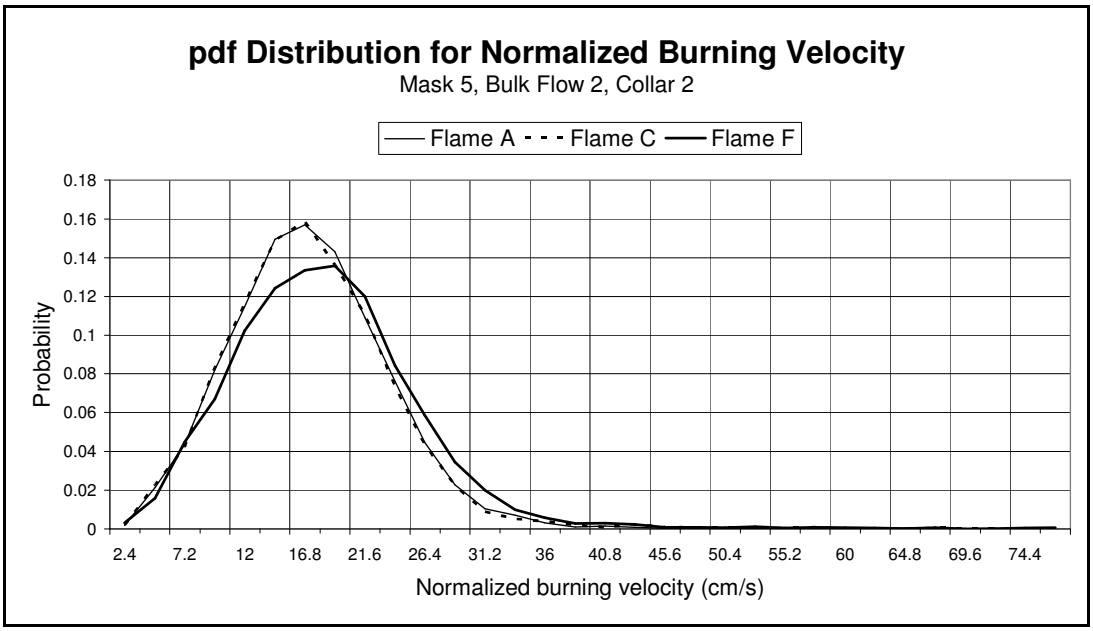

Figure 9.10. Normalized burning velocity PDF distributions associated to the region of Mask 5 for three flames (A, C, F) at Bulk Flow 2. The data refers to the burner outlet configuration defined as Collar 2.

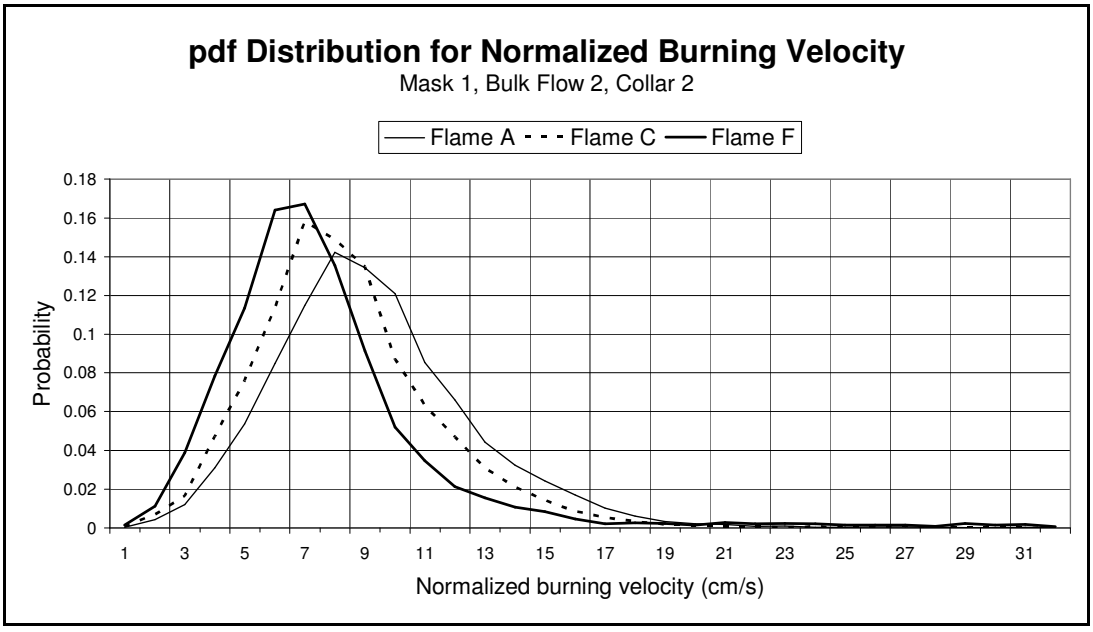

Figure 9.11. Normalized burning velocity PDF distributions associated to the region of Mask 1 for three flames (A, C, F) at Bulk Flow 2. The data refers to the burner outlet configuration defined as Collar 2.

9.2 Flame Curvature Variations under the Effect of Fuel Stratification and Turbulence

The procedure applied to extract the flame curvature data from the temperature fields is explained in Section 6.3. All the values of flame curvature are presented in probability distributions associated with each flame condition. This allows a comparison between different flames at the same Bulk Flow in order to analyze the effect of fuel stratification on flame curvature maintaining the same turbulence levels. The evaluation of the relationship between curvature and turbulence can be undertaken analyzing the probability distribution associated to the three Bulk Flows.

Figure 9.12 shows the probability distributions of flame front curvature for Bulk Flow 1, Bulk Flow 2 and Bulk Flow 3 using Collar 1. The plots show a unique peak centered on curvature zero and two symmetrical tails for positive and negative values. The turbulence increases from Bulk Flow 1 to Bulk Flow 3, and the peaks of the PDF curves are associated with decreasing probability when considering higher level of turbulence. As the probability of larger absolute values of curvature increases, flame front shapes with small radius of curvature are more likely to be observed. The same effect is observed in Figure 9.13 where the probability distributions are referred to the experimental configuration using Collar 2. This means that for higher levels of turbulence the oncoming flow is more capable of wrinkling the flame front.

The influence of turbulence on flame front wrinkling can be underlined using the probability distributions associated to the radius of curvature as well. In Figure 9.14 the PDF curves are displayed for Bulk Flow 1, Bulk Flow 2 and Bulk Flow 3 when Collar 1 is used. The plots show two peaks, one for the positive and one for the negative radius of curvature values. The mode of the negative peak is -1mm while the mode of the positive peak is 1 mm, these are quite small absolute values for the radius of curvature. The modes always remain the same for all the experimental conditions considered. Even if the mode values are symmetrical, the positive and negative sides of the probability density function curves are not. Both positive and negative peaks are associated with increased probability when higher levels of turbulence are applied. This is shown also from the probability distributions displayed in Figure 9.15 for the case of Collar 2 when Bulk Flow 1, Bulk Flow 2 and Bulk Flow 3 are considered. Both figures confirm the turbulence capability of increasing the flame front wrinkling. This phenomenon determines an enlargement of the flame front surface and consequently a higher flame speed.

The analysis of the probability distributions has been done considering the probability associated with the peaks and observing the modes values. The mean values have not been used because they are not significant for the PDF curves considered. For the case of the curvature the mean value is zero, while for the radius of curvature the probability distribution is bimodal.

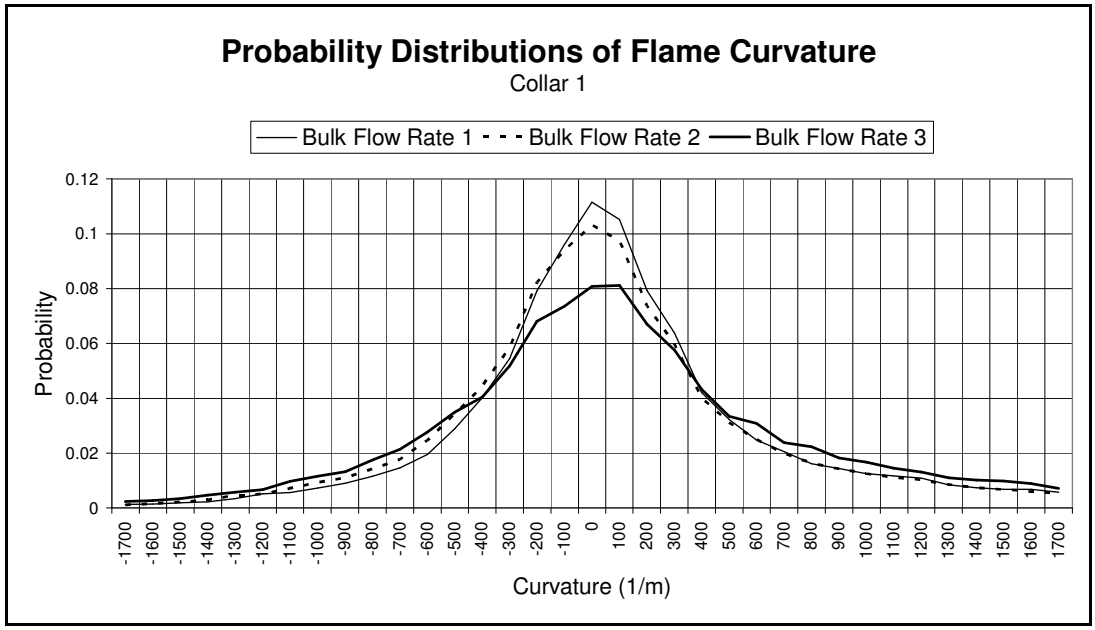

Figure 9.12. Probability distributions of curvature for Bulk Flow 1, Bulk Flow 2 and Bulk Flow 3 when using Collar 1.

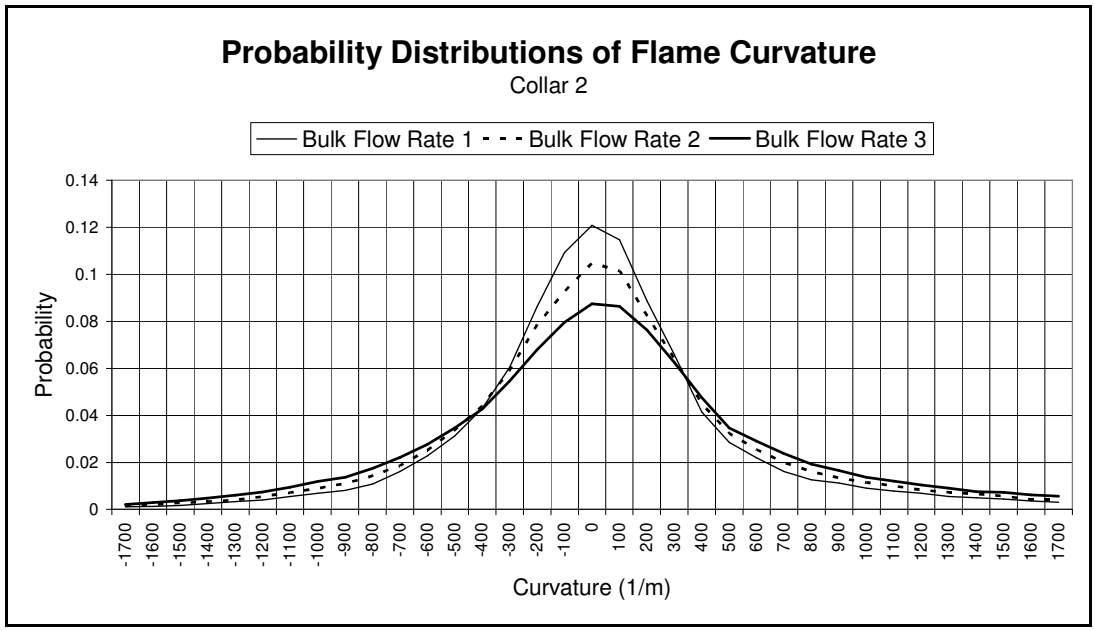

Figure 9.13. Probability distributions of curvature for Bulk Flow 1, Bulk Flow 2 and Bulk Flow 3 when using Collar 2.

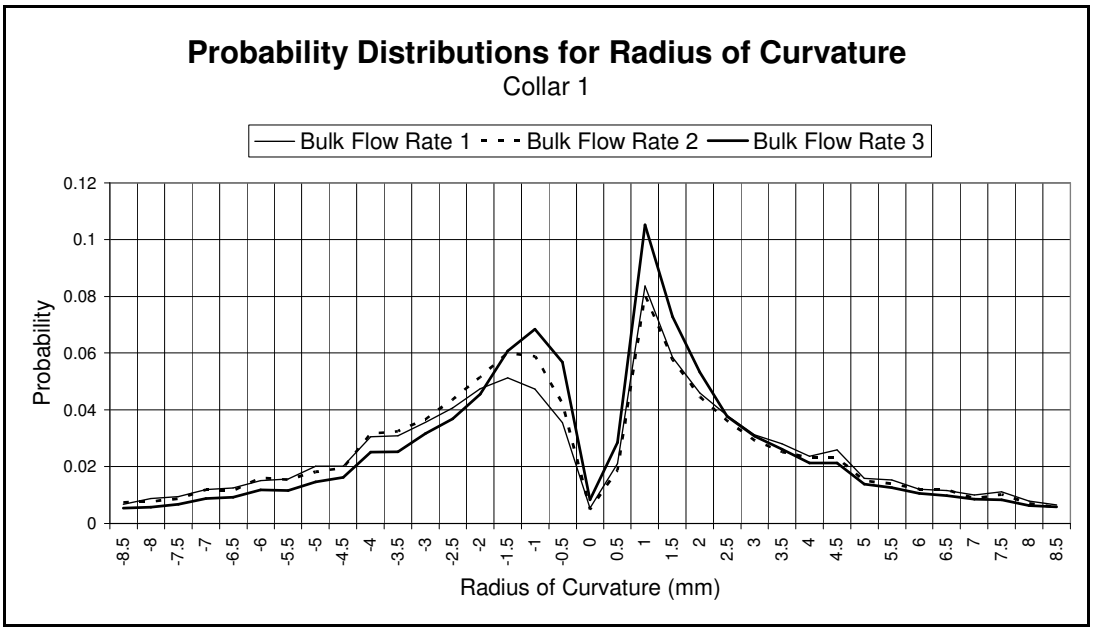

Figure 9.14. Probability distributions of the radius of curvature for Bulk Flow 1, Bulk Flow 2 and Bulk Flow 3 when using Collar 1.

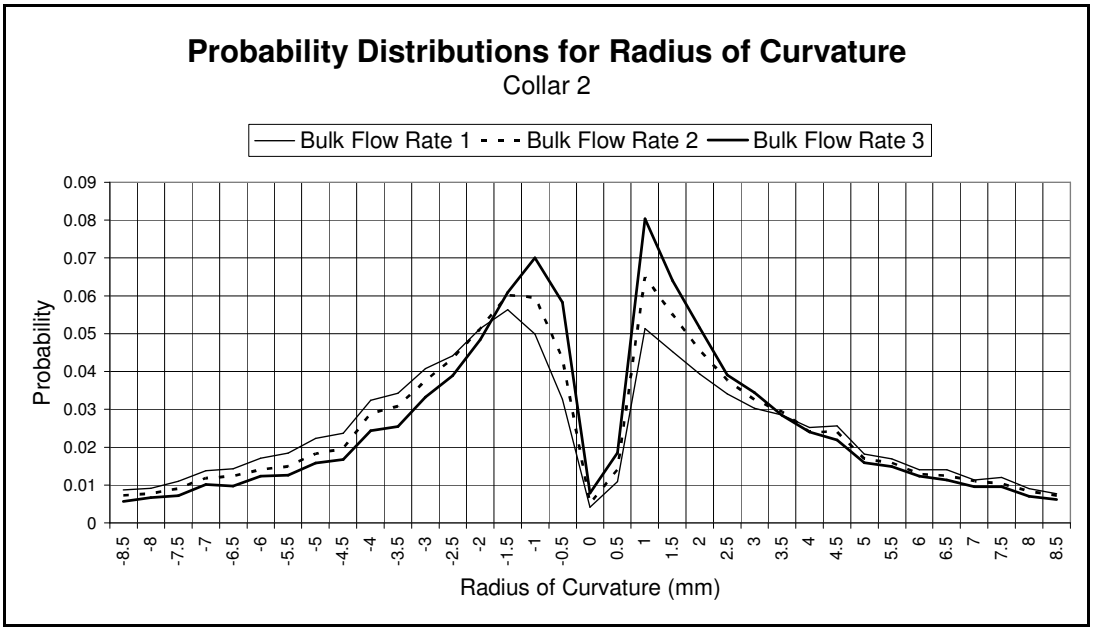

Figure 9.15. Probability distributions of the radius of curvature for Bulk Flow 1, Bulk Flow 2 and Bulk Flow 3 when using Collar 2.

The influence of fuel stratification on flame front curvature is studied by comparing the probability distributions associated with Flame A, Flame C and Flame F at the same Bulk Flow conditions. Using this approach the turbulence level is maintained at a constant level for the three flames while the only variations are introduced by the

gradients associated to the fuel stratification. It has been explained previously that Flame F is a stratified flame, Flame C is at uniform fuel concentration. Flame A is characterized by a very lean inner region and an annular region that should have been at higher equivalence ratio but the leaning effect of the swirl flow reduces its value and consequently the expected fuel stratification.

In Figure 9.16, the probability distributions for the radius of curvature values are shown for Bulk Flow 1 using Collar 1. While Figure 9.17 shows the PDF curves for the same conditions but using Collar 2. From the plots in the two figures it can be observed that the increased stratification of Flame F determines a higher probability associated to the peak on the positive side of the radius of curvature. On the negative side of the radius of curvature there is not a sensible variation in the peak probability. The physical consequence of this is that when flames of higher fuel stratification are considered, it is more probable that the flame front presents wrinkling features with small positive radius of curvature. The moderate stratification of Flame A does not introduce any difference when compared to Flame C.

Higher levels of turbulence make it more difficult to distinguish the influence of fuel stratification on flame front propagation, this has been mentioned when considering the burning velocity, and it is also valid for the flame curvature. One of the negative implications correlated with the use of Bulk Flow 2 and Bulk Flow 3 is that the increased turbulence favours the mixing between the three flow components and consequently it reduces the fuel stratification of the flames considered. This is more intense when Collar 1 is used because it is associated with a larger air swirl flow rate. For this reason Figure 9.18 shows only the case of Collar 2 for Flame A, Flame C and Flame F when using Bulk Flow 2. The probability of small positive values of radius of curvature is higher when Flame F is considered. This confirms the influence of the fuel stratification on flame wrinkling. The fuel stratification associated with Flame A is further decreased by the leaning effect of the air swirl flow if compared with Bulk Flow 1, this determines that the probability of small positive radius of curvature values is definitely less to Flame C. The case of Collar 1 at Bulk Flow 2 is not reported because the differences between the three flames are not significant. Similar considerations are valid for Bulk Flow 3 using both Collar configurations.

The effect of fuel stratification on flame curvature is similar to that of turbulence, but the difference is that, the first influences only the positive radius of curvature, while the second applies the same wrinkling effect on positive and negative curvature. This means that the flame front modifies its shape favouring the formation of features with small positive radius of curvature when it propagates into a flow characterized by an orthogonal gradient of fuel concentration with respect to the direction of propagation.

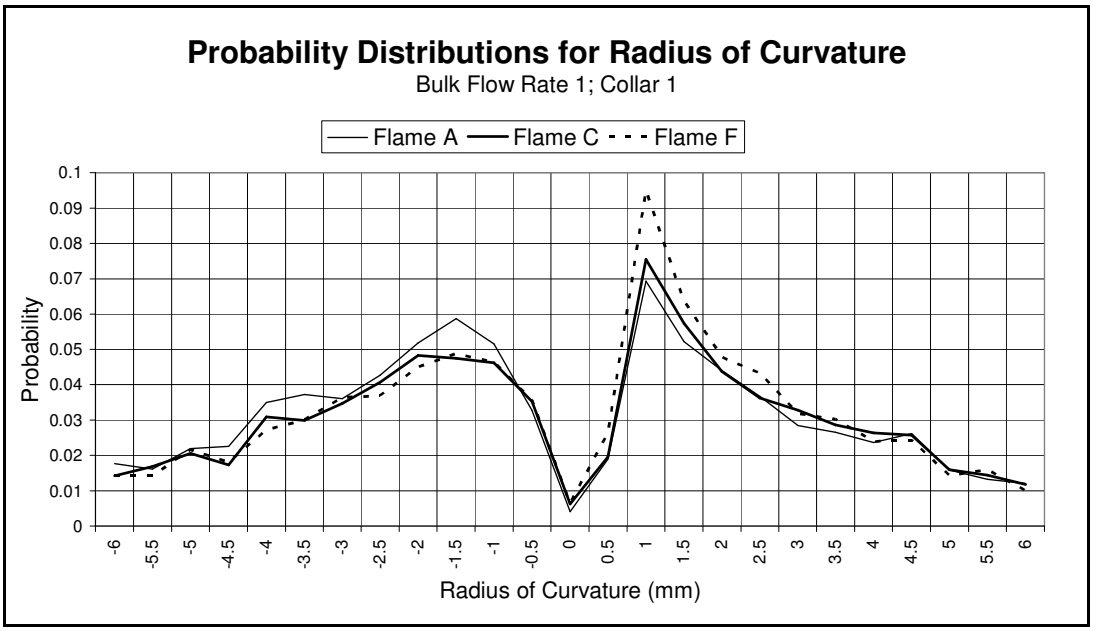

Figure 9.16. Probability distributions of the radius of curvature for Flame A, Flame C and Flame F when using Collar 1 with Bulk Flow 1.

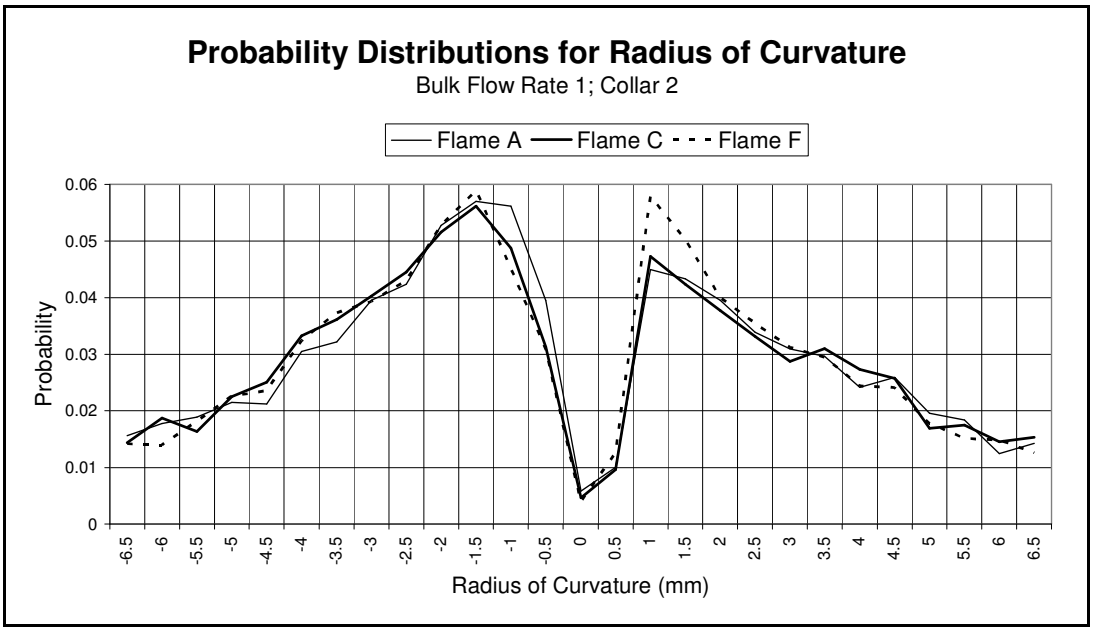

Figure 9.17. Probability distributions of the radius of curvature for Flame A, Flame C and Flame F when using Collar 2 with Bulk Flow 1.

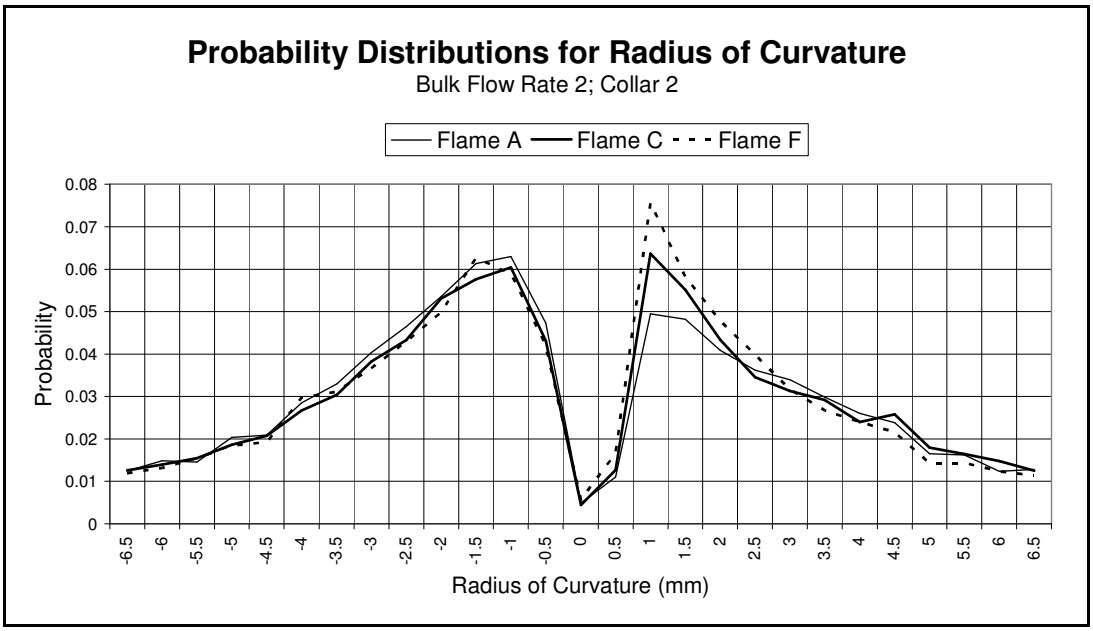

Figure 9.18. Probability distributions of the radius of curvature for Flame A, Flame C and Flame F when using Collar 2 with Bulk Flow 2.

9.3 Flame Thermal Thickness Correlation with Equivalence Ratio and Turbulence

The flame thermal thickness data has been obtained from the reduced temperature fields using the procedure shown in Section 6.4. The flame thickness is a flame front characteristic that is used to distinguish the turbulent combustion regimes. The data about the flame thermal thickness have been organized in probability distributions associated to each mask of every flame. The masks here mentioned are those defined in Section 8.2.1 as a result of the analysis of the equivalence ratio distribution. In the area imaged five masks have been defined in order to distinguish regions at different equivalence ratios. The inner region of the imaged area is covered by Mask 5 while the two external parts on the two sides (left and right) are associated to Mask 1. All the other masks (Mask 2, Mask 3 and Mask 4) are in the middle of the two just described.

Figure 9.19 displays the probability distributions of the flame thermal thickness for all the masks of Flame F when Collar 1 is used with Bulk Flow 1. It has been decided to show one flame only in order to highlight that the probability distributions associated to the external parts of the imaged area (Mask 2 and Mask 3) do not have a defined peak value. It appears that higher values of flame thickness have an increased probability.

This is explained by the fact that the external part of the flow has a strong leaning effect from the air swirl flow, and consequently the very low equivalence ratio induces phenomena of flame extinction, and that increases flame thickening. The objective is to study the effect of fuel stratification on flame front thickness, not the influence of flame front extinction in lean mixtures. For this reason it has been decided to exclude the effect of flame extinction from the probability distributions associated to the flame thermal thickness by considering only Mask 4 and Mask 5 when the flames have been produced using Collar 1.

The same phenomenon is noticed when the flames obtained using Collar 2 are considered. Figure 9.20 shows the probability distributions of flame thermal thickness for all the masks of Flame F when Collar 2 is used with Bulk Flow 1. In this case Mask 3 can also be considered without the presence of flame extinction. This is related to the fact that Collar 2 is associated with a smaller flow rate for the air swirl flow and consequently a reduced leaning effect, when compared with Collar 1. For the flames obtained using Collar 2, the PDF distributions are obtained from Mask 3, Mask 4 and Mask 5 only.

The influence of turbulence on flame thermal thickness is analyzed considering the probability distributions shown in Figure 9.21 for Bulk Flow 1, Bulk Flow 2 and Bulk Flow 3 when Collar 1 is used. The probability distributions have one peak only but the "tails" of the curve are not symmetric. Furthermore the tails on the right hand side are associated with a slow decrease in probability. This determines a high first moment and consequently a strong interference on the mean values of the probability distribution. For the same reason the median value too is strongly influenced by the tail on the right hand side. Only the mode is not affected by the asymmetry of the PDF curve. The left hand side tail is characterized by a sharp rise that goes quickly up to the probability of the mode value. It follows that the left hand side of the PDF curves can be used for a comparison between them.

For the case of Figure 9.21 there is not a remarkable difference between the three probability distributions associated to Bulk Flow 1, Bulk Flow 2 and Bulk Flow 3. The same is observed in Figure 9.22 when Collar 2 is used. The change in turbulence intensity from Bulk Flow 1 to Bulk Flow 3 is not large enough to modify the thickness of the flame. This subject has been already studied experimentally and the conclusions have been that the premixed laminar flamelet is much more robust than the scaling arguments of the Klimov Williams criterion would indicate (Shepherd et al., 2002). This is the reason why the modified Borghi diagram suggested by Peters has been used (Figure 2.4). The results are consistent with an interpretation of combustion/turbulence interactions which sees the reaction zone thickness as the significant scalar length scale.

The analysis of the influence of equivalence ratio on flame thermal thickness uses the three flames selected in the previous sections: Flame A, Flame C and Flame F. The flame thermal thickness probability distributions are obtained from the data collected only on the central part of the flow and consequently they are strongly related to the equivalence ratio value of the inner component of the flow. The three flames considered are characterized by an increased fuel concentration in the inner flow when going from Flame A to Flame F. Figure 9.23 displays the probability distributions of the flame thermal thickness for Flame A, Flame C and Flame F when Collar 1 is used with Bulk Flow 1. The PDF curve of Flame F is shifted towards smaller values of flame thermal

thickness with a mode of $800\mu m$. Flame A is characterized by larger probabilities for bigger values of flame thermal thickness and its mode is $900\mu m$. The curve of Flame C is in between the PDF distributions of Flame A and Flame F. This confirms that flamelets propagating in mixtures at higher concentration of fuel are characterized by a smaller thickness.

The influence of turbulence on flame thermal thickness is not strong enough to provoke any sensible change when considering the three Bulk Flows. This allows the thickening effect induced by leaner fuel mixtures to be observed even when Bulk Flow 2 and Bulk Flow 3 are considered. Figure 9.24, Figure 9.25 and Figure 9.26 show the probability distributions of Flame A, Flame C and Flame F for the three cases of Bulk Flow 1, Bulk Flow 2 and Bulk Flow 3 when using Collar 2. In these figures the PDF curve of Flame F is always characterized by smaller values of flame thermal thickness. The differences between the PDF distributions of Flame A and Flame F are reduced if the case of Bulk Flow 1 and Bulk Flow 3 are compared, because at higher flow rates, the mixing of the three flow components is increased and the differences between the equivalence ratio distributions for the three flames are reduced.

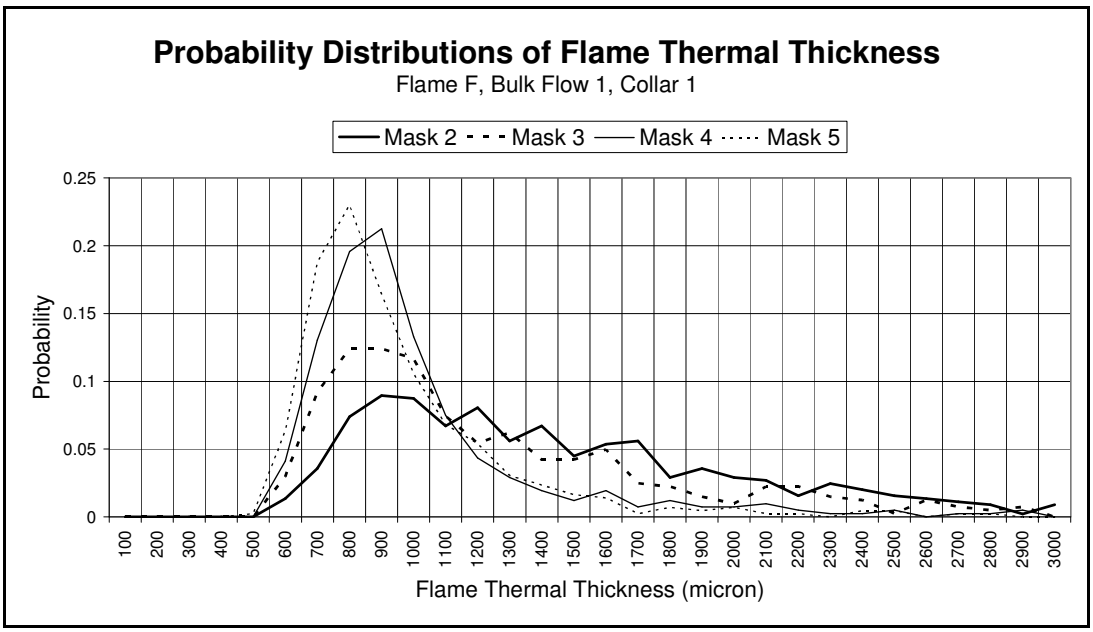

Figure 9.19. Probability distributions of the flame thermal thickness for the masks applied to Flame F using Collar 1 with Bulk Flow 1.

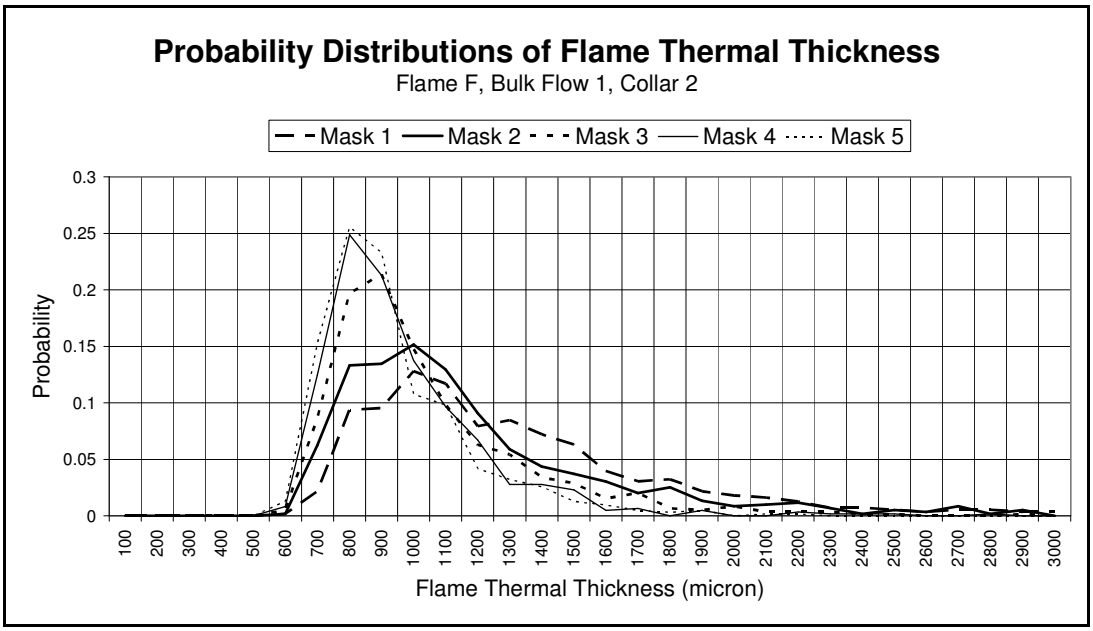

Figure 9.20. Probability distributions of the flame thermal thickness for the masks applied to Flame F using Collar 2 with Bulk Flow 1.

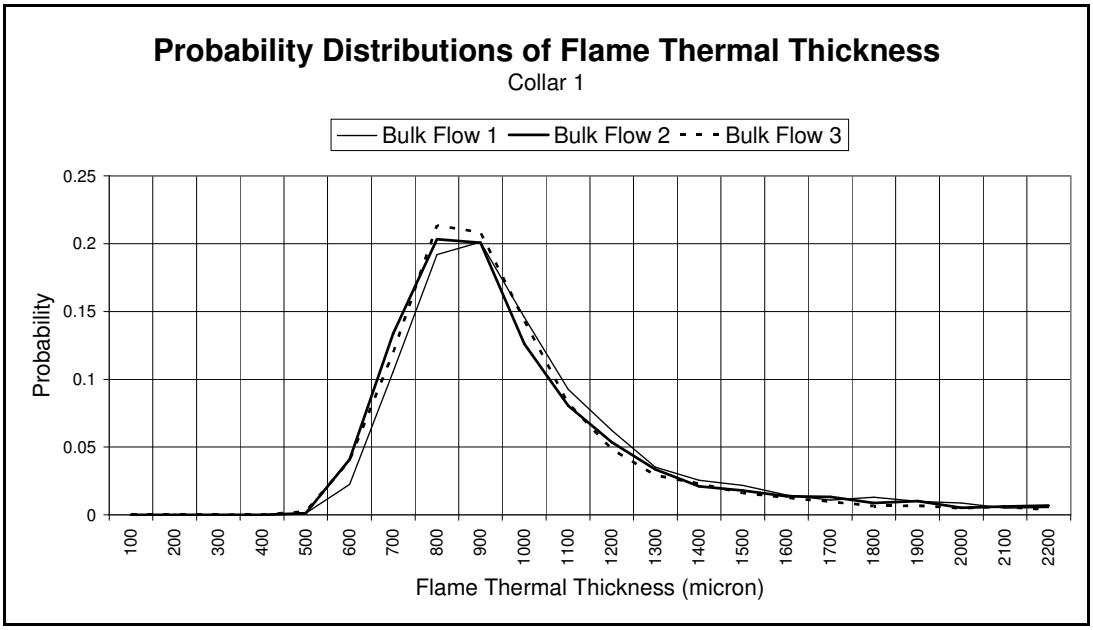

Figure 9.21. Probability distributions of the flame thermal thickness for Bulk Flow 1, Bulk Flow 2 and Bulk Flow 3 when using Collar 1.

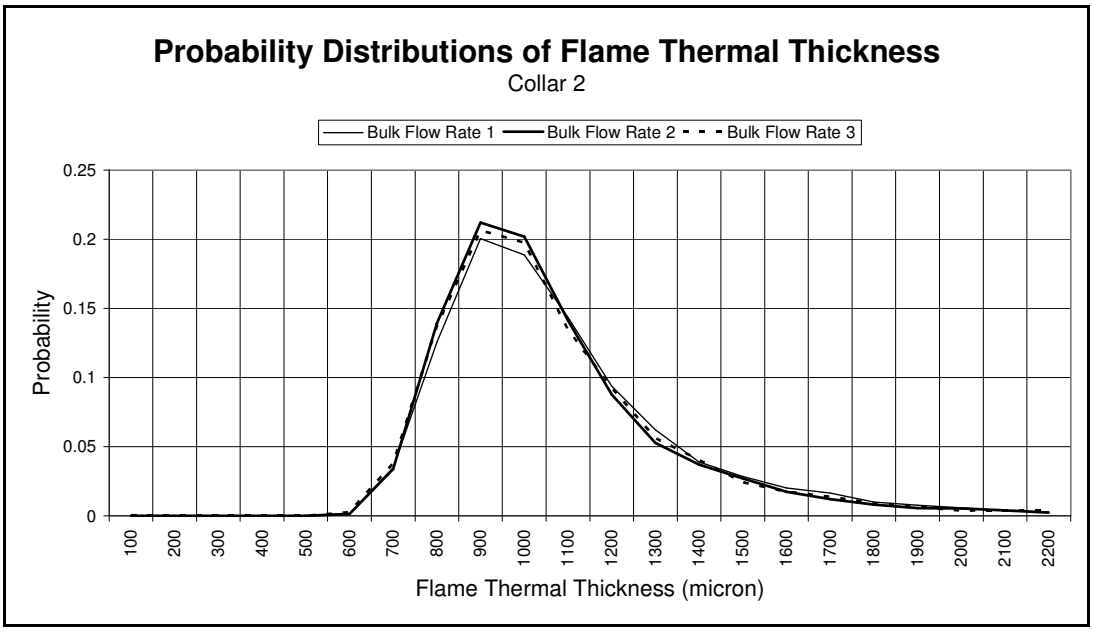

Figure 9.22. Probability distributions of the flame thermal thickness for Bulk Flow 1, Bulk Flow 2 and Bulk Flow 3 when using Collar 2.

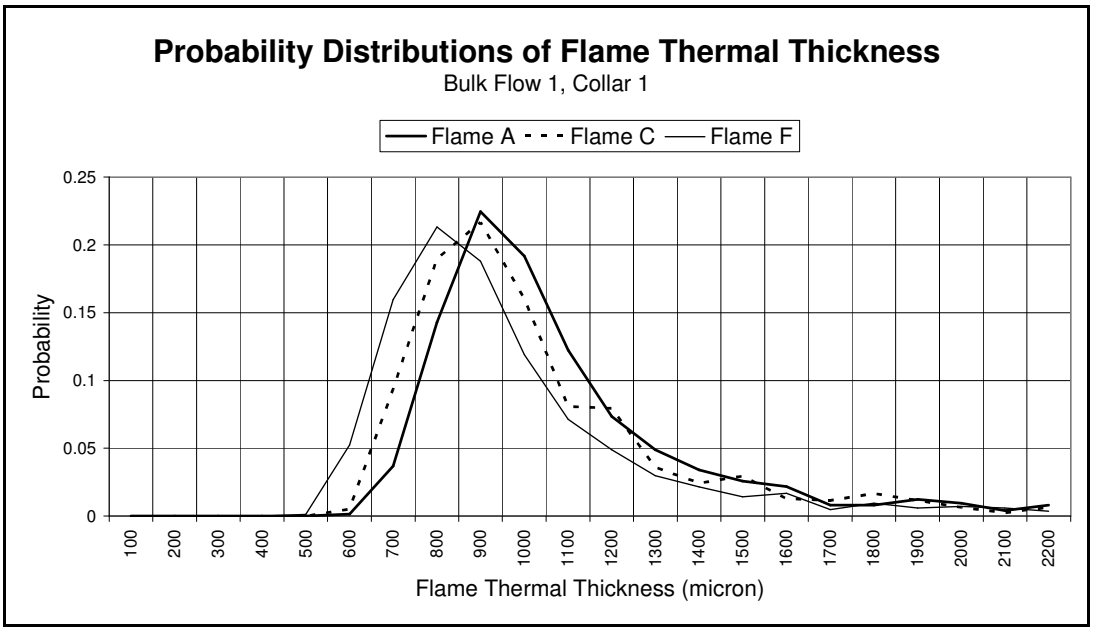

Figure 9.23. Probability distributions of the flame thermal thickness for Flame A, Flame C and Flame F when using Collar 1 with Bulk Flow 1.

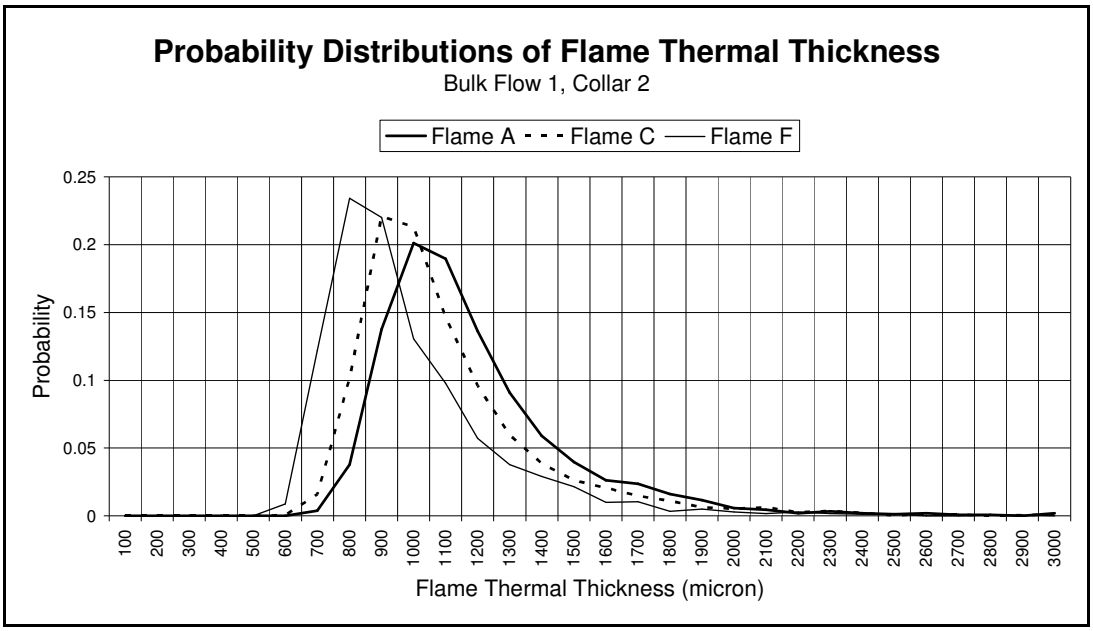

Figure 9.24. Probability distributions of the flame thermal thickness for Flame A, Flame C and Flame F when using Collar 2 with Bulk Flow 1.

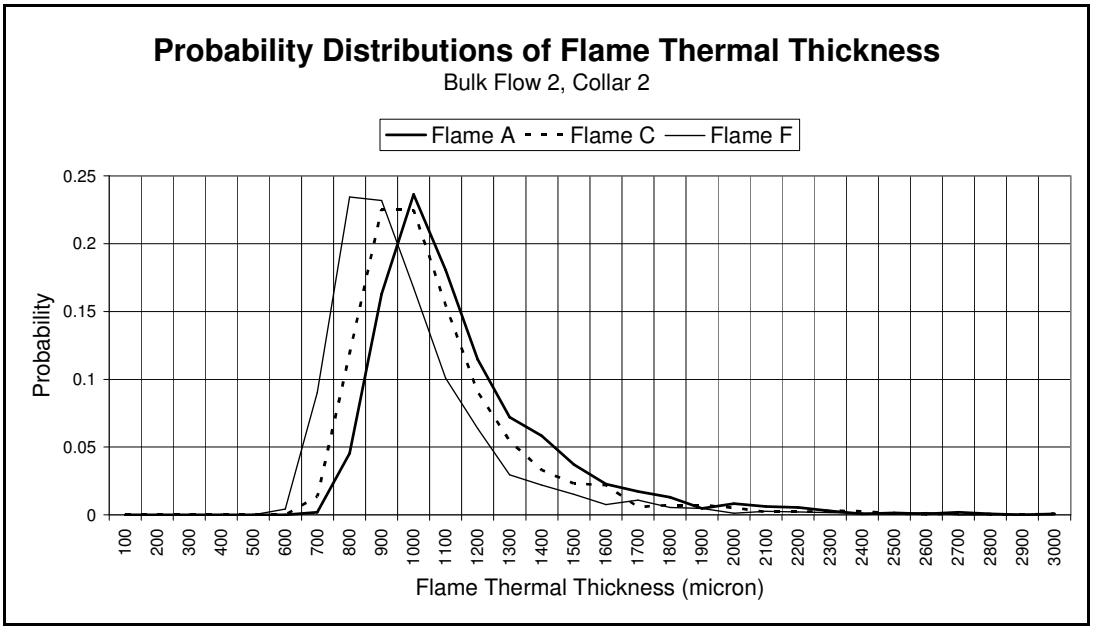

Figure 9.25. Probability distributions of the flame thermal thickness for Flame A, Flame C and Flame F when using Collar 2 with Bulk Flow 2.

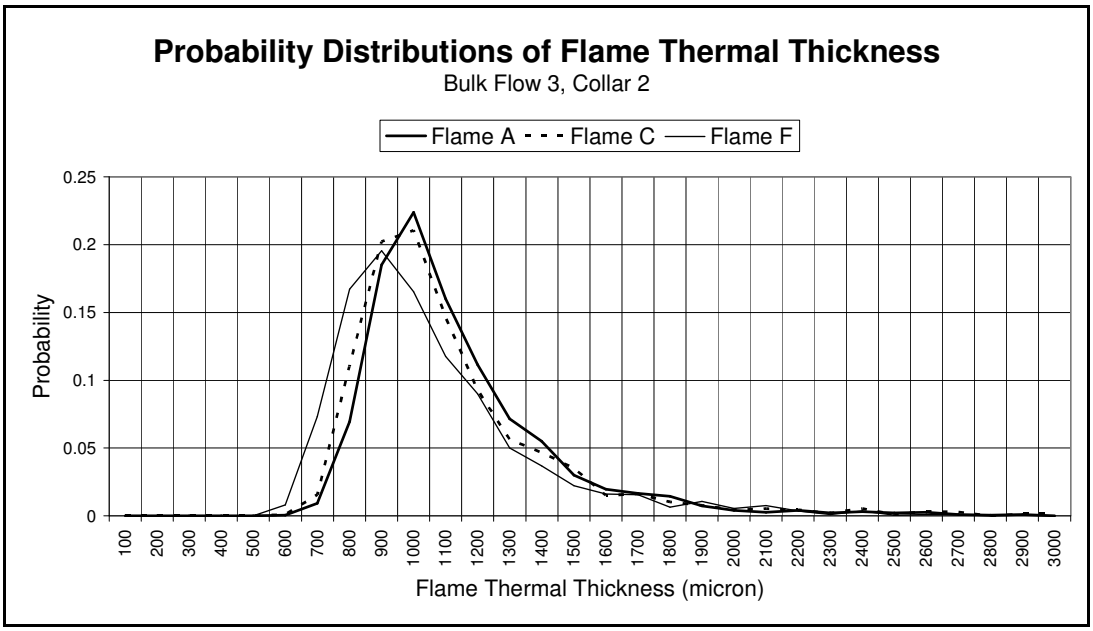

Figure 9.26. Probability distributions of the flame thermal thickness for Flame A, Flame C and Flame F when using Collar 2 with Bulk Flow 3.

10 CONCLUSIONS

The burner that has been presented here to produce stratified turbulent methane flames stabilized using weak swirl has shown new and interesting effects of stratified flame propagation. The objective was to obtain a better insight into the flame structures at high turbulence and under the effect of various level of fuel stratification. The flame front region has been studied using three laser diagnostics techniques: Stereo-PIV, Rayleigh scattering, and Acetone-PLIF. Velocity fields, temperature fields and average equivalence ratio distribution fields have been obtained. The values of turbulent burning velocity, flame curvature and flame thermal thickness have been extracted and the related probability distributions defined. The influences of turbulence and fuel stratification on these parameters have been studied.

The turbulent burning velocity data confirmed its relation with the turbulence of the oncoming flow in agreement with previous researchers. An increase in turbulence is associated with a higher mean value of the turbulent burning velocity and an increase of its probability distribution variance. The statistical analysis of flames characterized by larger gradients in fuel concentration showed their capability of propagating at an increased turbulent burning velocity.

The flame thermal thickness is not influenced by the increasing turbulence. This confirms that the premixed laminar flamelet is much more robust than the scaling arguments of the Klimov Williams criterion would indicate. The results are consistent with Peters' interpretation of combustion/turbulence interactions which sees the reaction zone thickness as the significant scalar length scale.

The flame front curvature probability distributions appear symmetric with mean value zero. When higher turbulence levels are considered, the variance of the distribution increases and consequently the probability associated with higher values of absolute curvature increases. The PDFs of the radius of curvature are bimodal with one peak on the positive side and one on the negative side. When higher turbulence levels are applied, the probabilities of the two mode values (+1mm, -1mm) are increased. This confirms the capacity of the turbulence to wrinkle the flame front. Fuel stratification instead influences the probability of only the positive values of radius of curvature. The formation of flame front shapes with small positive radius of curvature is more probable with stratified flames.

Higher fuel concentrations correspond to increased burning velocities. Consequently in those regions affected by equivalence ratio gradients, the flame front propagates with different burning velocity at each point, this determines a deformation in the flame front shape, which has to find an irregular equilibrium with the oncoming flow velocities. The consequent deformation on a statistical basis appears to favour the formation of shapes with small positive radius of curvature.

It follows that the fuel stratification is a cause of increased wrinkling of the flame front. Turbulent premixed flame propagation strongly depends on the degree of wrinkling of the flame surface and its effect on the total surface area available for reaction. It follows that the increment in the turbulent burning velocity introduced by the effect of fuel

stratification can be correlated with the increased wrinkling produced by the equivalence ratio gradients.

The increments in flame surface appear to be linked to those flow regions where the mixing layer between inner flow and annular flow is present. It would be an important improvement to use simultaneous laser diagnostics techniques in order to identify those regions instantaneously while collecting information on velocities and flame front properties. A solution could be the simultaneous use of PIV, OH-LIF and NO-LIF (with NO seeded only in the inner flow). PIV would be used to obtain the velocity fields, the fluorescence signal from OH radicals would identify the flame front while the fluorescence of the NO seeded in the inner flow would indicate the region of interest by marking the mixing layer between the inner and the annular flow. Turbulent burning velocities and flame curvature values would be selected in those regions where the fuel concentration gradients are present and consequently the related probability distributions would not be contaminated by data from regions where fuel stratification is not present. Acetone as fuel tracer would influence the combustion in the stratification region because of its different chemistry characteristics to methane. The use of NO as fuel tracer would avoid this problem at low concentrations.

APPENDIX A

Results of the sonic nozzle calibration

In the following figures are reported the values of the discharge coefficient calculated according to Equation (4.5):

$$C = \left(\frac{R T_{up}}{M_{air}} \right)^{\frac{1}{2}} \dot{m} / \left(P_{up} \, A_{th} \, C' \right)$$

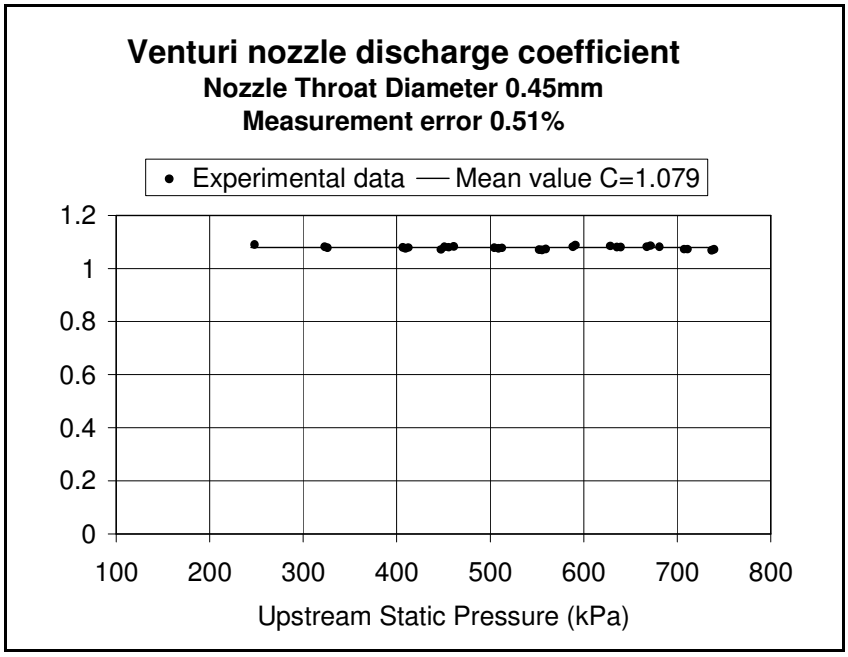

Figure A.1. Sonic nozzle discharge coefficient calibration diagram for 0.45mm nozzle throat diameter.

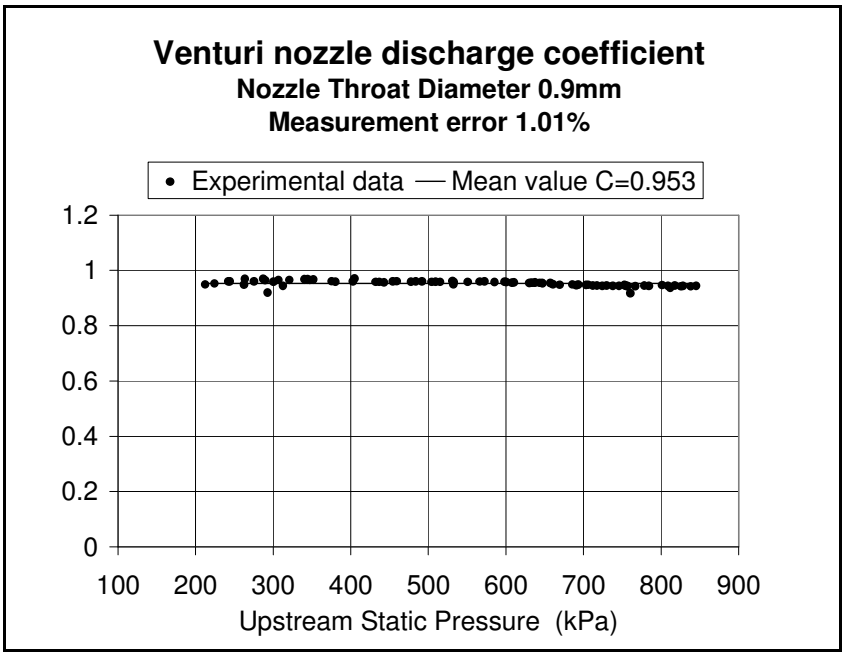

Figure A.2. Sonic nozzle discharge coefficient calibration diagram for 0.9mm nozzle throat diameter.

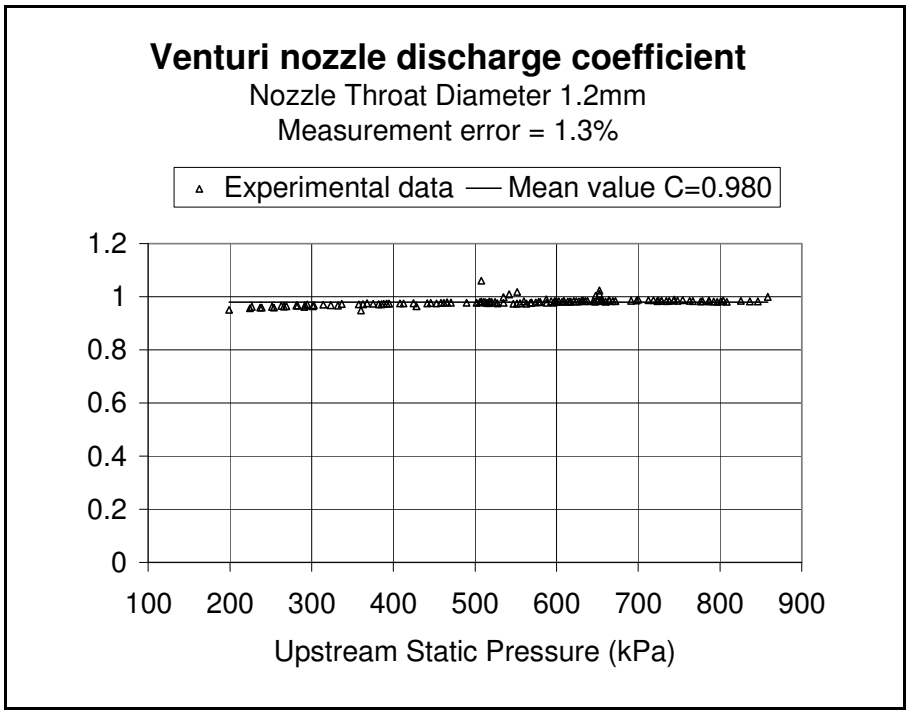

Figure A.3. Sonic nozzle discharge coefficient calibration diagram for 1.2mm nozzle throat diameter.

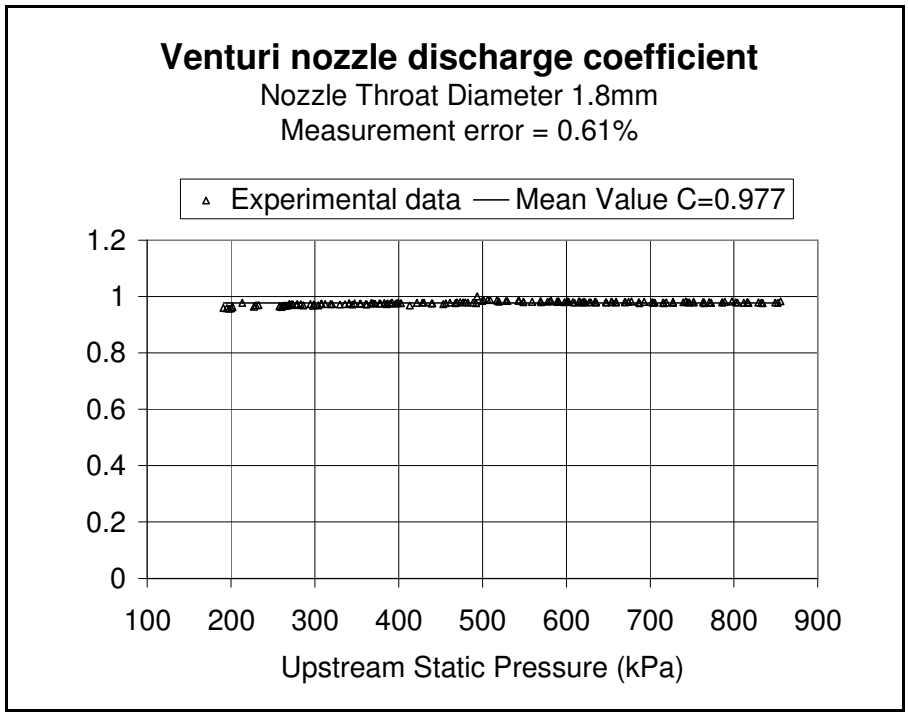

Figure A.4. Sonic nozzle discharge coefficient calibration diagram for 1.8mm nozzle throat diameter.

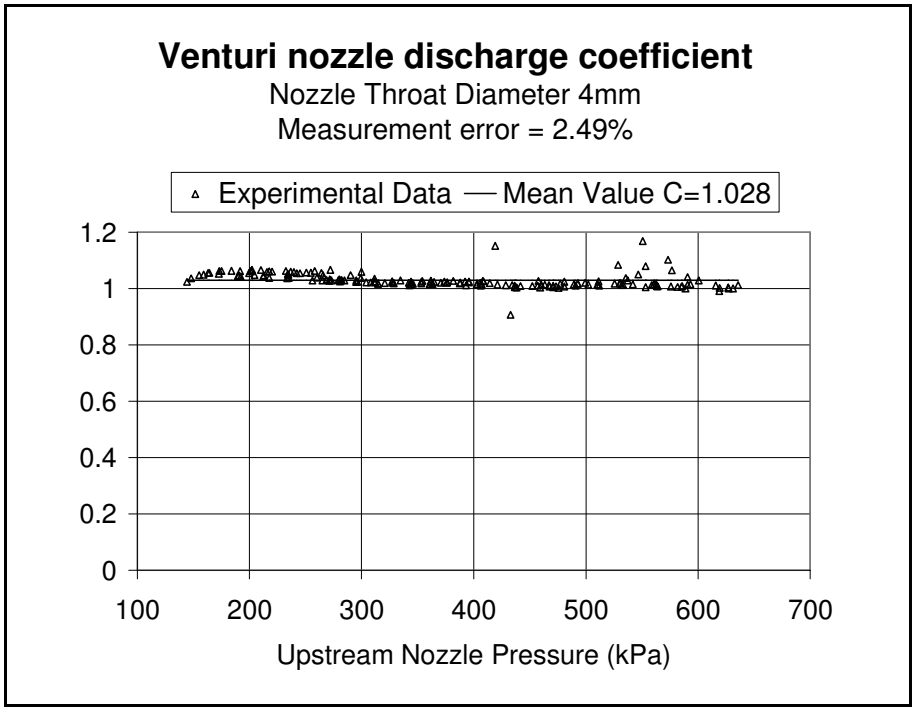

Figure A.5. Sonic nozzle discharge coefficient calibration diagram for 4mm nozzle throat diameter.

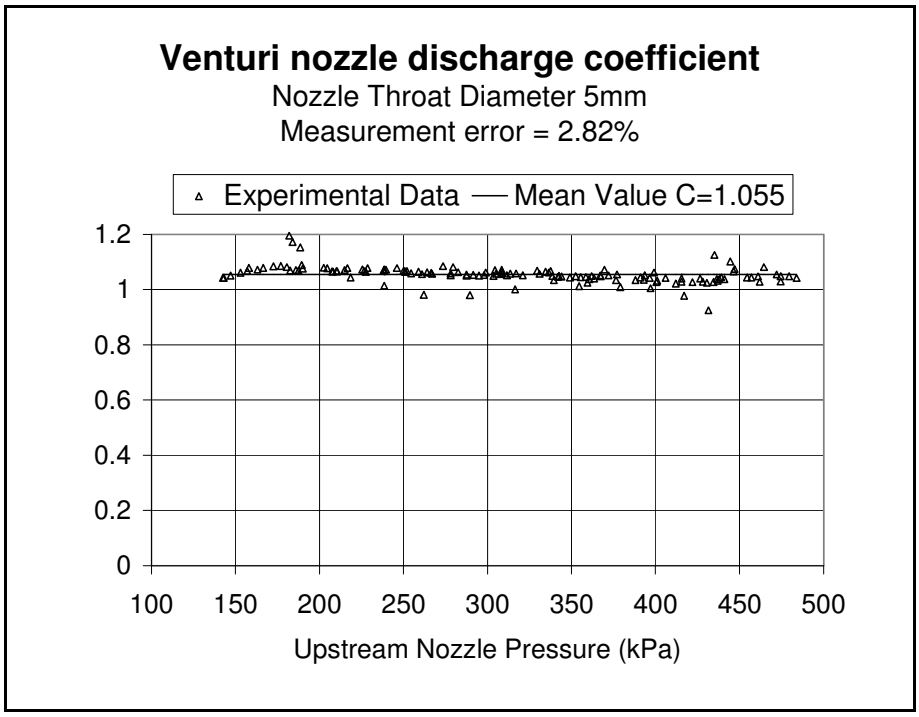

Figure A.6. Sonic nozzle discharge coefficient calibration diagram for 5mm nozzle throat diameter.

APPENDIX B

One dimensional laminar code data using CHEMKIN

The results of the calculations using the premixed laminar flame model are reported in the following tables. Several equivalence ratios values have been considered for the combustible mixtures of methane and air in order to cover the all range of equivalence ratio values used in the experiments.

x cm	T K	X_i H_2	X_i O_2	X_i H_2O	X_i CH_4	X_i CO	X_i CO_2	X_i N_2	X_i Ar	σ_R	I_R
0.00E+00	300	1.95E-03	1.90E-01	8.67E-03	6.44E-02	1.03E-03	6.97E-04	7.23E-01	9.28E-03	6.286	500.0
1.02E-02	350	2.32E-03	1.87E-01	1.43E-02	6.18E-02	1.77E-03	1.36E-03	7.22E-01	9.26E-03	6.265	427.0
1.53E-02	384	2.51E-03	1.84E-01	1.81E-02	6.00E-02	2.30E-03	1.87E-03	7.21E-01	9.25E-03	6.253	388.2
2.04E-02	426	2.71E-03	1.81E-01	2.25E-02	5.80E-02	2.95E-03	2.55E-03	7.21E-01	9.24E-03	6.238	349.7
2.55E-02	474	2.90E-03	1.77E-01	2.76E-02	5.55E-02	3.74E-03	3.42E-03	7.20E-01	9.23E-03	6.222	313.0
3.06E-02	531	3.10E-03	1.73E-01	3.34E-02	5.27E-02	4.67E-03	4.51E-03	7.19E-01	9.22E-03	6.205	279.1
3.32E-02	562	3.20E-03	1.70E-01	3.65E-02	5.11E-02	5.20E-03	5.16E-03	7.19E-01	9.21E-03	6.196	263.3
3.57E-02	595	3.30E-03	1.68E-01	3.98E-02	4.94E-02	5.77E-03	5.87E-03	7.18E-01	9.21E-03	6.187	248.3
3.83E-02	629	3.39E-03	1.65E-01	4.32E-02	4.76E-02	6.39E-03	6.65E-03	7.18E-01	9.21E-03	6.177	234.2
4.08E-02	666	3.49E-03	1.62E-01	4.68E-02	4.58E-02	7.05E-03	7.52E-03	7.18E-01	9.20E-03	6.167	220.9
4.34E-02	705	3.58E-03	1.58E-01	5.05E-02	4.38E-02	7.75E-03	8.46E-03	7.17E-01	9.20E-03	6.158	208.5
4.59E-02	745	3.68E-03	1.55E-01	5.43E-02	4.17E-02	8.49E-03	9.49E-03	7.17E-01	9.19E-03	6.148	196.9
5.10E-02	831	3.87E-03	1.47E-01	6.23E-02	3.73E-02	1.01E-02	1.18E-02	7.17E-01	9.19E-03	6.129	176.1
5.36E-02	876	3.96E-03	1.43E-01	6.65E-02	3.50E-02	1.10E-02	1.31E-02	7.17E-01	9.19E-03	6.119	166.8
5.61E-02	922	4.05E-03	1.39E-01	7.08E-02	3.26E-02	1.19E-02	1.45E-02	7.17E-01	9.18E-03	6.110	158.1
5.87E-02	970	4.13E-03	1.35E-01	7.51E-02	3.00E-02	1.28E-02	1.59E-02	7.16E-01	9.18E-03	6.101	150.1
6.12E-02	1019	4.22E-03	1.30E-01	7.95E-02	2.75E-02	1.38E-02	1.75E-02	7.16E-01	9.18E-03	6.092	142.7
6.38E-02	1069	4.29E-03	1.25E-01	8.40E-02	2.48E-02	1.48E-02	1.92E-02	7.16E-01	9.18E-03	6.084	135.8
6.63E-02	1119	4.36E-03	1.21E-01	8.86E-02	2.21E-02	1.58E-02	2.10E-02	7.16E-01	9.18E-03	6.076	129.5

x cm	T K	X_i H_2	X_i O_2	X_i H_2O	X_i CH_4	X_i CO	X_i CO_2	X_i N_2	X_i Ar	σ_R	I_R
6.89E-02	1170	4.42E-03	1.16E-01	9.31E-02	1.94E-02	1.68E-02	2.28E-02	7.17E-01	9.18E-03	6.069	123.8
7.14E-02	1221	4.47E-03	1.11E-01	9.75E-02	1.68E-02	1.78E-02	2.48E-02	7.17E-01	9.18E-03	6.064	118.5
7.40E-02	1271	4.49E-03	1.06E-01	1.02E-01	1.41E-02	1.87E-02	2.69E-02	7.17E-01	9.19E-03	6.059	113.8
7.65E-02	1319	4.48E-03	1.01E-01	1.06E-01	1.16E-02	1.95E-02	2.90E-02	7.17E-01	9.19E-03	6.057	109.6
7.78E-02	1342	4.46E-03	9.82E-02	1.08E-01	1.04E-02	1.99E-02	3.01E-02	7.17E-01	9.19E-03	6.056	107.7
7.91E-02	1365	4.43E-03	9.58E-02	1.10E-01	9.29E-03	2.02E-02	3.12E-02	7.17E-01	9.19E-03	6.056	105.9
8.04E-02	1386	4.39E-03	9.35E-02	1.12E-01	8.21E-03	2.05E-02	3.23E-02	7.17E-01	9.19E-03	6.056	104.2
8.16E-02	1407	4.34E-03	9.12E-02	1.14E-01	7.20E-03	2.06E-02	3.35E-02	7.17E-01	9.19E-03	6.057	102.7
8.29E-02	1427	4.28E-03	8.90E-02	1.15E-01	6.25E-03	2.08E-02	3.46E-02	7.18E-01	9.20E-03	6.058	101.3
8.42E-02	1445	4.20E-03	8.69E-02	1.17E-01	5.39E-03	2.08E-02	3.57E-02	7.18E-01	9.20E-03	6.060	100.0
8.55E-02	1463	4.12E-03	8.49E-02	1.19E-01	4.60E-03	2.08E-02	3.69E-02	7.18E-01	9.20E-03	6.062	98.9
8.67E-02	1479	4.02E-03	8.31E-02	1.20E-01	3.89E-03	2.07E-02	3.80E-02	7.18E-01	9.20E-03	6.065	97.8
8.93E-02	1508	3.80E-03	7.97E-02	1.22E-01	2.71E-03	2.03E-02	4.02E-02	7.18E-01	9.21E-03	6.072	96.1
9.18E-02	1533	3.55E-03	7.67E-02	1.24E-01	1.83E-03	1.96E-02	4.23E-02	7.19E-01	9.21E-03	6.080	94.7
9.31E-02	1543	3.42E-03	7.54E-02	1.25E-01	1.48E-03	1.92E-02	4.33E-02	7.19E-01	9.21E-03	6.084	94.1
9.44E-02	1553	3.29E-03	7.42E-02	1.26E-01	1.19E-03	1.87E-02	4.43E-02	7.19E-01	9.22E-03	6.089	93.6
9.69E-02	1570	3.04E-03	7.21E-02	1.27E-01	7.54E-04	1.76E-02	4.63E-02	7.20E-01	9.22E-03	6.098	92.7
9.95E-02	1584	2.81E-03	7.04E-02	1.28E-01	4.68E-04	1.65E-02	4.80E-02	7.20E-01	9.23E-03	6.107	92.0
1.02E-01	1596	2.61E-03	6.90E-02	1.28E-01	2.85E-04	1.53E-02	4.97E-02	7.20E-01	9.23E-03	6.116	91.5
1.05E-01	1607	2.43E-03	6.78E-02	1.29E-01	1.70E-04	1.42E-02	5.12E-02	7.21E-01	9.24E-03	6.125	91.0
1.07E-01	1616	2.27E-03	6.69E-02	1.29E-01	9.91E-05	1.31E-02	5.26E-02	7.21E-01	9.24E-03	6.134	90.6
1.12E-01	1633	2.04E-03	6.54E-02	1.30E-01	3.61E-05	1.12E-02	5.50E-02	7.22E-01	9.25E-03	6.149	89.9
1.17E-01	1647	1.87E-03	6.43E-02	1.30E-01	1.29E-05	9.52E-03	5.69E-02	7.22E-01	9.25E-03	6.163	89.3
1.22E-01	1659	1.74E-03	6.34E-02	1.31E-01	4.19E-06	8.17E-03	5.85E-02	7.22E-01	9.26E-03	6.174	88.8
1.33E-01	1680	1.54E-03	6.23E-02	1.31E-01	7.09E-07	6.19E-03	6.08E-02	7.23E-01	9.27E-03	6.192	88.0
1.43E-01	1696	1.38E-03	6.15E-02	1.32E-01	1.25E-07	4.83E-03	6.24E-02	7.24E-01	9.28E-03	6.205	87.3
1.63E-01	1720	1.10E-03	6.05E-02	1.33E-01	3.69E-09	3.17E-03	6.43E-02	7.24E-01	9.29E-03	6.214	86.8
2.04E-01	1747	7.01E-04	5.97E-02	1.34E-01	2.87E-11	1.75E-03	6.59E-02	7.25E-01	9.30E-03	6.222	86.3
2.45E-01	1761	4.62E-04	5.94E-02	1.35E-01	2.88E-13	1.10E-03	6.66E-02	7.26E-01	9.30E-03	6.233	85.7

x cm	T K	X_i H_2	X_i O_2	X_i H_2O	X_i CH_4	X_i CO	X_i CO_2	X_i N_2	X_i Ar	σ_R	I_R
2.86E-01	1768	3.24E-04	5.92E-02	1.35E-01	1.53E-14	7.68E-04	6.70E-02	7.26E-01	9.30E-03	6.240	85.3
3.27E-01	1773	2.36E-04	5.92E-02	1.36E-01	9.71E-16	5.59E-04	6.73E-02	7.26E-01	9.31E-03	6.246	84.9
3.67E-01	1776	1.78E-04	5.91E-02	1.36E-01	7.63E-17	4.21E-04	6.74E-02	7.26E-01	9.31E-03	6.250	84.7
4.08E-01	1778	1.39E-04	5.91E-02	1.36E-01	9.83E-18	3.27E-04	6.75E-02	7.26E-01	9.31E-03	6.255	84.4
4.49E-01	1780	1.12E-04	5.91E-02	1.36E-01	3.53E-18	2.61E-04	6.76E-02	7.26E-01	9.31E-03	6.259	84.2
4.90E-01	1781	9.18E-05	5.91E-02	1.36E-01	2.45E-18	2.13E-04	6.77E-02	7.26E-01	9.31E-03	6.261	84.1
5.31E-01	1782	7.74E-05	5.91E-02	1.36E-01	2.00E-18	1.78E-04	6.77E-02	7.26E-01	9.31E-03	6.263	84.0
5.71E-01	1783	6.66E-05	5.91E-02	1.36E-01	1.71E-18	1.51E-04	6.77E-02	7.26E-01	9.31E-03	6.264	84.0
6.12E-01	1783	5.84E-05	5.91E-02	1.37E-01	1.50E-18	1.31E-04	6.77E-02	7.26E-01	9.31E-03	6.265	83.9
6.53E-01	1784	5.21E-05	5.91E-02	1.37E-01	1.33E-18	1.15E-04	6.78E-02	7.26E-01	9.31E-03	6.266	83.9
6.94E-01	1784	4.71E-05	5.91E-02	1.37E-01	1.20E-18	1.02E-04	6.78E-02	7.26E-01	9.31E-03	6.267	83.9
7.35E-01	1784	4.32E-05	5.91E-02	1.37E-01	1.10E-18	9.26E-05	6.78E-02	7.26E-01	9.31E-03	6.267	83.9
7.76E-01	1784	4.01E-05	5.91E-02	1.37E-01	1.01E-18	8.47E-05	6.78E-02	7.26E-01	9.31E-03	6.268	83.9
8.16E-01	1785	3.77E-05	5.91E-02	1.37E-01	9.38E-19	7.84E-05	6.78E-02	7.26E-01	9.31E-03	6.268	83.8
8.57E-01	1785	3.56E-05	5.91E-02	1.37E-01	8.76E-19	7.32E-05	6.78E-02	7.26E-01	9.31E-03	6.268	83.8
8.98E-01	1785	3.40E-05	5.91E-02	1.37E-01	8.24E-19	6.91E-05	6.78E-02	7.26E-01	9.31E-03	6.268	83.8
9.39E-01	1785	3.27E-05	5.91E-02	1.37E-01	7.78E-19	6.57E-05	6.78E-02	7.26E-01	9.31E-03	6.269	83.8
9.80E-01	1785	3.16E-05	5.91E-02	1.37E-01	7.38E-19	6.29E-05	6.78E-02	7.26E-01	9.31E-03	6.269	83.8
1.02E+00	1785	3.07E-05	5.91E-02	1.37E-01	7.03E-19	6.05E-05	6.78E-02	7.26E-01	9.31E-03	6.269	83.8
1.06E+00	1785	3.00E-05	5.91E-02	1.37E-01	6.71E-19	5.86E-05	6.78E-02	7.26E-01	9.31E-03	6.269	83.8
1.10E+00	1785	2.94E-05	5.91E-02	1.37E-01	6.42E-19	5.71E-05	6.78E-02	7.26E-01	9.31E-03	6.269	83.8
1.14E+00	1785	2.89E-05	5.91E-02	1.37E-01	6.16E-19	5.58E-05	6.78E-02	7.26E-01	9.31E-03	6.269	83.8
1.18E+00	1785	2.85E-05	5.91E-02	1.37E-01	5.92E-19	5.47E-05	6.78E-02	7.26E-01	9.31E-03	6.269	83.8
1.22E+00	1785	2.81E-05	5.91E-02	1.37E-01	5.69E-19	5.38E-05	6.78E-02	7.26E-01	9.31E-03	6.269	83.8
1.27E+00	1785	2.78E-05	5.91E-02	1.37E-01	5.49E-19	5.30E-05	6.78E-02	7.26E-01	9.31E-03	6.269	83.8
1.31E+00	1785	2.76E-05	5.91E-02	1.37E-01	5.29E-19	5.24E-05	6.78E-02	7.26E-01	9.31E-03	6.269	83.8
1.35E+00	1785	2.74E-05	5.91E-02	1.37E-01	5.11E-19	5.19E-05	6.78E-02	7.26E-01	9.31E-03	6.269	83.8
1.39E+00	1785	2.73E-05	5.91E-02	1.37E-01	4.94E-19	5.15E-05	6.78E-02	7.26E-01	9.31E-03	6.269	83.8
1.43E+00	1785	2.71E-05	5.91E-02	1.37E-01	4.77E-19	5.12E-05	6.78E-02	7.26E-01	9.31E-03	6.269	83.8

x cm	T K	X_i H_2	X_i O_2	X_i H_2O	X_i CH_4	X_i CO	X_i CO_2	X_i N_2	X_i Ar	σ_R	I_R
1.47E+00	1785	2.71E-05	5.91E-02	1.37E-01	4.62E-19	5.09E-05	6.78E-02	7.26E-01	9.31E-03	6.269	83.8
1.51E+00	1785	2.70E-05	5.91E-02	1.37E-01	4.47E-19	5.08E-05	6.78E-02	7.26E-01	9.31E-03	6.269	83.8
1.55E+00	1785	2.71E-05	5.91E-02	1.37E-01	4.33E-19	5.07E-05	6.78E-02	7.26E-01	9.31E-03	6.269	83.8
1.59E+00	1785	2.72E-05	5.91E-02	1.37E-01	4.20E-19	5.09E-05	6.78E-02	7.26E-01	9.31E-03	6.269	83.8
1.63E+00	1785	2.75E-05	5.91E-02	1.37E-01	4.08E-19	5.13E-05	6.78E-02	7.26E-01	9.31E-03	6.269	83.8
1.67E+00	1786	2.81E-05	5.91E-02	1.37E-01	3.98E-19	5.22E-05	6.78E-02	7.26E-01	9.31E-03	6.269	83.8
1.71E+00	1786	2.93E-05	5.91E-02	1.37E-01	3.90E-19	5.39E-05	6.78E-02	7.26E-01	9.31E-03	6.269	83.8
1.76E+00	1786	3.16E-05	5.91E-02	1.37E-01	3.85E-19	5.70E-05	6.78E-02	7.26E-01	9.31E-03	6.269	83.8
1.80E+00	1786	3.62E-05	5.90E-02	1.37E-01	3.89E-19	6.23E-05	6.78E-02	7.26E-01	9.31E-03	6.269	83.8
1.84E+00	1786	4.67E-05	5.89E-02	1.37E-01	4.09E-19	7.07E-05	6.78E-02	7.26E-01	9.31E-03	6.269	83.8
1.88E+00	1786	7.54E-05	5.88E-02	1.37E-01	4.52E-19	8.11E-05	6.78E-02	7.26E-01	9.31E-03	6.269	83.8
1.92E+00	1786	1.76E-04	5.88E-02	1.37E-01	2.10E-19	8.12E-05	6.78E-02	7.26E-01	9.31E-03	6.269	83.8
1.94E+00	1787	3.27E-04	5.90E-02	1.37E-01	-1.96E-18	6.04E-05	6.78E-02	7.26E-01	9.31E-03	6.268	83.8
1.95E+00	1787	4.27E-04	5.93E-02	1.37E-01	-4.54E-18	4.37E-05	6.78E-02	7.26E-01	9.31E-03	6.268	83.7
1.96E+00	1787	5.23E-04	5.95E-02	1.37E-01	-7.76E-18	2.63E-05	6.79E-02	7.26E-01	9.31E-03	6.268	83.7
2.00E+00	1787	5.23E-04	5.95E-02	1.37E-01	-7.76E-18	2.63E-05	6.79E-02	7.26E-01	9.31E-03	6.270	83.7

Table B-1. Output for $\phi = 0.7$, CH_4/ air premixed flames. Only the species with relevant mole fractions are reported.

x cm	T K	X_i H_2	X_i O_2	X_i H_2O	X_i CH_4	X_i CO	X_i CO_2	X_i N_2	X_i Ar	σ_R	I_R
0.00E+00	300	2.50E-03	1.90E-01	7.22E-03	6.95E-02	9.43E-04	4.93E-04	7.20E-01	9.23E-03	6.322	500.0
5.10E-03	327	2.81E-03	1.88E-01	1.04E-02	6.80E-02	1.39E-03	8.01E-04	7.19E-01	9.22E-03	6.309	457.4
1.02E-02	364	3.14E-03	1.86E-01	1.45E-02	6.61E-02	2.01E-03	1.26E-03	7.18E-01	9.21E-03	6.294	410.7
1.53E-02	410	3.47E-03	1.82E-01	1.96E-02	6.36E-02	2.83E-03	1.93E-03	7.17E-01	9.19E-03	6.275	362.8
2.04E-02	468	3.82E-03	1.78E-01	2.58E-02	6.06E-02	3.88E-03	2.85E-03	7.16E-01	9.18E-03	6.254	316.8
2.30E-02	502	3.99E-03	1.75E-01	2.93E-02	5.89E-02	4.51E-03	3.43E-03	7.15E-01	9.17E-03	6.242	295.1
2.55E-02	539	4.16E-03	1.72E-01	3.31E-02	5.70E-02	5.21E-03	4.10E-03	7.15E-01	9.16E-03	6.230	274.4

x cm	T K	X_i H_2	X_i O_2	X_i H_2O	X_i CH_4	X_i CO	X_i CO_2	X_i N_2	X_i Ar	σ_R	I_R
2.81E-02	579	4.33E-03	1.69E-01	3.71E-02	5.49E-02	5.98E-03	4.86E-03	7.14E-01	9.16E-03	6.218	255.0
3.06E-02	621	4.50E-03	1.65E-01	4.14E-02	5.27E-02	6.83E-03	5.73E-03	7.14E-01	9.15E-03	6.204	236.9
3.32E-02	667	4.67E-03	1.61E-01	4.59E-02	5.03E-02	7.76E-03	6.71E-03	7.13E-01	9.14E-03	6.191	220.2
3.57E-02	716	4.83E-03	1.57E-01	5.06E-02	4.77E-02	8.77E-03	7.81E-03	7.13E-01	9.14E-03	6.177	204.7
3.83E-02	767	5.00E-03	1.53E-01	5.56E-02	4.50E-02	9.86E-03	9.03E-03	7.12E-01	9.13E-03	6.163	190.6
4.08E-02	822	5.16E-03	1.48E-01	6.07E-02	4.21E-02	1.10E-02	1.04E-02	7.12E-01	9.13E-03	6.149	177.6
4.34E-02	878	5.32E-03	1.43E-01	6.61E-02	3.91E-02	1.23E-02	1.19E-02	7.12E-01	9.12E-03	6.135	165.8
4.59E-02	937	5.47E-03	1.38E-01	7.16E-02	3.59E-02	1.36E-02	1.35E-02	7.11E-01	9.12E-03	6.122	155.1
4.85E-02	998	5.62E-03	1.32E-01	7.72E-02	3.26E-02	1.50E-02	1.52E-02	7.11E-01	9.12E-03	6.108	145.3
5.10E-02	1060	5.77E-03	1.26E-01	8.29E-02	2.92E-02	1.64E-02	1.71E-02	7.11E-01	9.11E-03	6.096	136.5
5.36E-02	1123	5.90E-03	1.20E-01	8.87E-02	2.57E-02	1.79E-02	1.92E-02	7.11E-01	9.11E-03	6.083	128.5
5.61E-02	1187	6.01E-03	1.14E-01	9.45E-02	2.22E-02	1.94E-02	2.14E-02	7.11E-01	9.11E-03	6.072	121.4
5.87E-02	1250	6.09E-03	1.08E-01	1.00E-01	1.87E-02	2.08E-02	2.38E-02	7.11E-01	9.11E-03	6.063	115.1
6.12E-02	1312	6.13E-03	1.01E-01	1.06E-01	1.53E-02	2.22E-02	2.62E-02	7.11E-01	9.12E-03	6.055	109.5
6.25E-02	1342	6.13E-03	9.80E-02	1.09E-01	1.36E-02	2.28E-02	2.75E-02	7.11E-01	9.12E-03	6.053	107.0
6.38E-02	1371	6.11E-03	9.48E-02	1.11E-01	1.21E-02	2.33E-02	2.88E-02	7.11E-01	9.12E-03	6.050	104.7
6.51E-02	1399	6.07E-03	9.18E-02	1.14E-01	1.06E-02	2.38E-02	3.01E-02	7.12E-01	9.12E-03	6.049	102.6
6.63E-02	1426	6.02E-03	8.88E-02	1.16E-01	9.18E-03	2.42E-02	3.15E-02	7.12E-01	9.12E-03	6.049	100.7
6.76E-02	1451	5.94E-03	8.60E-02	1.18E-01	7.87E-03	2.46E-02	3.28E-02	7.12E-01	9.12E-03	6.049	98.9
6.89E-02	1475	5.85E-03	8.32E-02	1.21E-01	6.68E-03	2.48E-02	3.42E-02	7.12E-01	9.12E-03	6.050	97.4
7.02E-02	1497	5.73E-03	8.06E-02	1.22E-01	5.60E-03	2.49E-02	3.56E-02	7.12E-01	9.13E-03	6.052	95.9
7.14E-02	1517	5.60E-03	7.82E-02	1.24E-01	4.64E-03	2.49E-02	3.69E-02	7.12E-01	9.13E-03	6.055	94.7
7.27E-02	1536	5.45E-03	7.59E-02	1.26E-01	3.80E-03	2.48E-02	3.83E-02	7.13E-01	9.13E-03	6.058	93.6
7.40E-02	1553	5.28E-03	7.37E-02	1.27E-01	3.08E-03	2.45E-02	3.96E-02	7.13E-01	9.14E-03	6.062	92.6
7.53E-02	1568	5.11E-03	7.18E-02	1.29E-01	2.47E-03	2.42E-02	4.09E-02	7.13E-01	9.14E-03	6.066	91.8
7.65E-02	1582	4.92E-03	7.00E-02	1.30E-01	1.96E-03	2.38E-02	4.22E-02	7.13E-01	9.14E-03	6.071	91.1
7.78E-02	1594	4.74E-03	6.83E-02	1.31E-01	1.53E-03	2.32E-02	4.35E-02	7.13E-01	9.14E-03	6.076	90.4
7.91E-02	1605	4.55E-03	6.69E-02	1.32E-01	1.19E-03	2.27E-02	4.47E-02	7.14E-01	9.15E-03	6.081	89.9
8.04E-02	1615	4.37E-03	6.55E-02	1.32E-01	9.16E-04	2.20E-02	4.59E-02	7.14E-01	9.15E-03	6.087	89.4

x cm	T K	X_i H_2	X_i O_2	X_i H_2O	X_i CH_4	X_i CO	X_i CO_2	X_i N_2	X_i Ar	σ_R	I_R
8.16E-02	1624	4.20E-03	6.43E-02	1.33E-01	6.99E-04	2.13E-02	4.70E-02	7.14E-01	9.15E-03	6.092	89.0
8.29E-02	1632	4.03E-03	6.32E-02	1.33E-01	5.28E-04	2.06E-02	4.81E-02	7.14E-01	9.16E-03	6.098	88.7
8.42E-02	1639	3.88E-03	6.23E-02	1.34E-01	3.95E-04	1.99E-02	4.91E-02	7.15E-01	9.16E-03	6.104	88.3
8.67E-02	1652	3.61E-03	6.06E-02	1.35E-01	2.17E-04	1.85E-02	5.11E-02	7.15E-01	9.16E-03	6.115	87.8
9.18E-02	1674	3.20E-03	5.83E-02	1.36E-01	7.07E-05	1.57E-02	5.45E-02	7.16E-01	9.18E-03	6.135	87.0
9.69E-02	1692	2.92E-03	5.66E-02	1.36E-01	2.25E-05	1.34E-02	5.72E-02	7.17E-01	9.18E-03	6.153	86.3
1.02E-01	1707	2.73E-03	5.54E-02	1.37E-01	7.10E-06	1.15E-02	5.94E-02	7.17E-01	9.19E-03	6.169	85.7
1.07E-01	1721	2.59E-03	5.45E-02	1.37E-01	2.22E-06	1.00E-02	6.12E-02	7.18E-01	9.20E-03	6.182	85.2
1.12E-01	1733	2.46E-03	5.38E-02	1.37E-01	6.25E-07	8.76E-03	6.27E-02	7.18E-01	9.20E-03	6.193	84.8
1.22E-01	1754	2.25E-03	5.27E-02	1.38E-01	8.95E-08	6.98E-03	6.47E-02	7.19E-01	9.21E-03	6.209	84.0
1.33E-01	1771	2.04E-03	5.20E-02	1.39E-01	1.34E-08	5.75E-03	6.61E-02	7.19E-01	9.22E-03	6.222	83.4
1.43E-01	1784	1.86E-03	5.15E-02	1.39E-01	2.10E-09	4.86E-03	6.71E-02	7.20E-01	9.23E-03	6.232	82.9
1.53E-01	1796	1.68E-03	5.10E-02	1.40E-01	3.44E-10	4.20E-03	6.79E-02	7.20E-01	9.23E-03	6.239	82.4
1.63E-01	1805	1.53E-03	5.07E-02	1.40E-01	4.93E-11	3.69E-03	6.85E-02	7.20E-01	9.23E-03	6.246	82.1
1.84E-01	1820	1.26E-03	5.03E-02	1.41E-01	3.58E-12	2.96E-03	6.93E-02	7.21E-01	9.24E-03	6.255	81.6
2.04E-01	1831	1.05E-03	4.99E-02	1.42E-01	2.89E-13	2.45E-03	6.99E-02	7.21E-01	9.25E-03	6.263	81.2
2.24E-01	1839	8.86E-04	4.97E-02	1.42E-01	2.57E-14	2.06E-03	7.03E-02	7.21E-01	9.25E-03	6.268	80.9
2.45E-01	1846	7.53E-04	4.95E-02	1.43E-01	2.08E-15	1.75E-03	7.07E-02	7.22E-01	9.25E-03	6.273	80.6
2.86E-01	1855	5.65E-04	4.93E-02	1.43E-01	9.22E-17	1.33E-03	7.12E-02	7.22E-01	9.26E-03	6.280	80.3
3.27E-01	1861	4.37E-04	4.92E-02	1.44E-01	5.81E-18	1.03E-03	7.15E-02	7.22E-01	9.26E-03	6.284	80.1
3.67E-01	1865	3.48E-04	4.91E-02	1.44E-01	1.01E-18	8.24E-04	7.17E-02	7.22E-01	9.26E-03	6.288	80.0
4.08E-01	1868	2.84E-04	4.91E-02	1.44E-01	4.96E-19	6.73E-04	7.19E-02	7.22E-01	9.26E-03	6.290	79.9
4.49E-01	1870	2.37E-04	4.90E-02	1.45E-01	3.32E-19	5.60E-04	7.20E-02	7.23E-01	9.26E-03	6.292	79.8
4.90E-01	1872	2.02E-04	4.90E-02	1.45E-01	2.42E-19	4.75E-04	7.21E-02	7.23E-01	9.26E-03	6.294	79.8
5.31E-01	1874	1.75E-04	4.90E-02	1.45E-01	1.85E-19	4.09E-04	7.22E-02	7.23E-01	9.26E-03	6.295	79.7
5.71E-01	1875	1.55E-04	4.90E-02	1.45E-01	1.47E-19	3.58E-04	7.22E-02	7.23E-01	9.27E-03	6.296	79.7
6.12E-01	1876	1.39E-04	4.90E-02	1.45E-01	1.20E-19	3.18E-04	7.23E-02	7.23E-01	9.27E-03	6.297	79.7
6.53E-01	1876	1.26E-04	4.90E-02	1.45E-01	9.98E-20	2.87E-04	7.23E-02	7.23E-01	9.27E-03	6.297	79.6
6.94E-01	1877	1.16E-04	4.90E-02	1.45E-01	8.47E-20	2.61E-04	7.23E-02	7.23E-01	9.27E-03	6.298	79.6

x cm	T K	X_i H_2	X_i O_2	X_i H_2O	X_i CH_4	X_i CO	X_i CO_2	X_i N_2	X_i Ar	σ_R	I_R
7.35E-01	1877	1.08E-04	4.90E-02	1.45E-01	7.30E-20	2.41E-04	7.24E-02	7.23E-01	9.27E-03	6.298	79.6
7.76E-01	1878	1.01E-04	4.90E-02	1.45E-01	6.37E-20	2.25E-04	7.24E-02	7.23E-01	9.27E-03	6.299	79.6
8.16E-01	1878	9.61E-05	4.90E-02	1.45E-01	5.61E-20	2.11E-04	7.24E-02	7.23E-01	9.27E-03	6.299	79.6
8.57E-01	1878	9.18E-05	4.90E-02	1.45E-01	4.99E-20	2.00E-04	7.24E-02	7.23E-01	9.27E-03	6.299	79.6
8.98E-01	1878	8.83E-05	4.90E-02	1.45E-01	4.46E-20	1.91E-04	7.24E-02	7.23E-01	9.27E-03	6.299	79.6
9.39E-01	1878	8.54E-05	4.90E-02	1.45E-01	4.02E-20	1.84E-04	7.24E-02	7.23E-01	9.27E-03	6.299	79.6
9.80E-01	1879	8.31E-05	4.90E-02	1.45E-01	3.64E-20	1.78E-04	7.24E-02	7.23E-01	9.27E-03	6.300	79.6
1.02E+00	1879	8.11E-05	4.90E-02	1.45E-01	3.30E-20	1.72E-04	7.24E-02	7.23E-01	9.27E-03	6.300	79.6
1.06E+00	1879	7.95E-05	4.90E-02	1.45E-01	3.01E-20	1.68E-04	7.25E-02	7.23E-01	9.27E-03	6.300	79.6
1.10E+00	1879	7.82E-05	4.90E-02	1.45E-01	2.76E-20	1.65E-04	7.25E-02	7.23E-01	9.27E-03	6.300	79.6
1.14E+00	1879	7.71E-05	4.90E-02	1.45E-01	2.53E-20	1.62E-04	7.25E-02	7.23E-01	9.27E-03	6.300	79.6
1.18E+00	1879	7.62E-05	4.90E-02	1.45E-01	2.32E-20	1.60E-04	7.25E-02	7.23E-01	9.27E-03	6.300	79.6
1.22E+00	1879	7.55E-05	4.90E-02	1.45E-01	2.14E-20	1.58E-04	7.25E-02	7.23E-01	9.27E-03	6.300	79.6
1.27E+00	1879	7.48E-05	4.90E-02	1.45E-01	1.97E-20	1.56E-04	7.25E-02	7.23E-01	9.27E-03	6.300	79.6
1.31E+00	1879	7.43E-05	4.90E-02	1.45E-01	1.82E-20	1.55E-04	7.25E-02	7.23E-01	9.27E-03	6.300	79.6
1.35E+00	1879	7.39E-05	4.90E-02	1.45E-01	1.68E-20	1.53E-04	7.25E-02	7.23E-01	9.27E-03	6.300	79.6
1.39E+00	1879	7.35E-05	4.90E-02	1.45E-01	1.55E-20	1.52E-04	7.25E-02	7.23E-01	9.27E-03	6.300	79.6
1.43E+00	1879	7.32E-05	4.90E-02	1.45E-01	1.44E-20	1.52E-04	7.25E-02	7.23E-01	9.27E-03	6.300	79.6
1.47E+00	1879	7.30E-05	4.90E-02	1.45E-01	1.33E-20	1.51E-04	7.25E-02	7.23E-01	9.27E-03	6.300	79.6
1.51E+00	1879	7.27E-05	4.90E-02	1.45E-01	1.23E-20	1.50E-04	7.25E-02	7.23E-01	9.27E-03	6.300	79.6
1.55E+00	1879	7.26E-05	4.90E-02	1.45E-01	1.14E-20	1.50E-04	7.25E-02	7.23E-01	9.27E-03	6.300	79.6
1.59E+00	1879	7.24E-05	4.90E-02	1.45E-01	1.06E-20	1.50E-04	7.25E-02	7.23E-01	9.27E-03	6.300	79.6
1.63E+00	1879	7.23E-05	4.90E-02	1.45E-01	9.80E-21	1.49E-04	7.25E-02	7.23E-01	9.27E-03	6.300	79.5
1.67E+00	1879	7.22E-05	4.90E-02	1.45E-01	9.09E-21	1.49E-04	7.25E-02	7.23E-01	9.27E-03	6.300	79.5
1.71E+00	1879	7.21E-05	4.90E-02	1.45E-01	8.44E-21	1.49E-04	7.25E-02	7.23E-01	9.27E-03	6.300	79.5
1.76E+00	1879	7.20E-05	4.90E-02	1.45E-01	7.83E-21	1.49E-04	7.25E-02	7.23E-01	9.27E-03	6.300	79.5
1.80E+00	1879	7.20E-05	4.90E-02	1.45E-01	7.27E-21	1.48E-04	7.25E-02	7.23E-01	9.27E-03	6.300	79.5
1.84E+00	1879	7.19E-05	4.90E-02	1.45E-01	6.76E-21	1.48E-04	7.25E-02	7.23E-01	9.27E-03	6.300	79.5
1.88E+00	1879	7.19E-05	4.90E-02	1.45E-01	6.30E-21	1.48E-04	7.25E-02	7.23E-01	9.27E-03	6.300	79.5

x cm	T K	X_i H_2	X_i O_2	X_i H_2O	X_i CH_4	X_i CO	X_i CO_2	X_i N_2	X_i Ar	σ_R	I_R
1.92E+00	1879	7.19E-05	4.90E-02	1.45E-01	5.91E-21	1.48E-04	7.25E-02	7.23E-01	9.27E-03	6.300	79.5
1.96E+00	1879	7.19E-05	4.90E-02	1.45E-01	5.65E-21	1.48E-04	7.25E-02	7.23E-01	9.27E-03	6.300	79.5
2.00E+00	1879	7.19E-05	4.90E-02	1.45E-01	5.65E-21	1.48E-04	7.25E-02	7.23E-01	9.27E-03	6.300	79.5

Table B-2. Output for $\phi = 0.75$, CH_4/ air premixed flames. Only the species with relevant mole fractions are reported.

x cm	T K	X_i H_2	X_i O_2	X_i H_2O	X_i CH_4	X_i CO	X_i CO_2	X_i N_2	X_i Ar	σ_R	I_R
0.00E+00	295	2.25E-03	1.92E-01	2.44E-03	7.62E-02	3.22E-04	1.02E-04	7.17E-01	9.20E-03	6.375	500.0
1.02E-02	319	2.99E-03	1.91E-01	5.28E-03	7.48E-02	7.30E-04	2.73E-04	7.16E-01	9.18E-03	6.360	462.0
1.53E-02	339	3.43E-03	1.89E-01	7.76E-03	7.36E-02	1.11E-03	4.54E-04	7.15E-01	9.17E-03	6.348	432.8
2.04E-02	370	3.92E-03	1.87E-01	1.13E-02	7.19E-02	1.68E-03	7.58E-04	7.14E-01	9.16E-03	6.333	396.1
2.55E-02	413	4.44E-03	1.84E-01	1.62E-02	6.96E-02	2.51E-03	1.25E-03	7.13E-01	9.14E-03	6.313	353.9
2.81E-02	440	4.71E-03	1.82E-01	1.92E-02	6.81E-02	3.06E-03	1.59E-03	7.12E-01	9.13E-03	6.301	331.3
3.06E-02	472	4.99E-03	1.79E-01	2.27E-02	6.64E-02	3.71E-03	2.02E-03	7.11E-01	9.12E-03	6.288	308.4
3.32E-02	508	5.27E-03	1.76E-01	2.66E-02	6.44E-02	4.47E-03	2.55E-03	7.11E-01	9.11E-03	6.273	285.7
3.57E-02	549	5.55E-03	1.73E-01	3.09E-02	6.22E-02	5.36E-03	3.19E-03	7.10E-01	9.10E-03	6.258	263.7
3.83E-02	595	5.83E-03	1.69E-01	3.56E-02	5.98E-02	6.37E-03	3.96E-03	7.09E-01	9.09E-03	6.241	242.7
4.08E-02	646	6.11E-03	1.65E-01	4.08E-02	5.70E-02	7.52E-03	4.87E-03	7.08E-01	9.08E-03	6.224	223.0
4.34E-02	701	6.39E-03	1.61E-01	4.64E-02	5.40E-02	8.82E-03	5.93E-03	7.08E-01	9.07E-03	6.205	204.8
4.59E-02	761	6.67E-03	1.55E-01	5.23E-02	5.08E-02	1.03E-02	7.16E-03	7.07E-01	9.06E-03	6.186	188.1
4.85E-02	825	6.94E-03	1.50E-01	5.86E-02	4.72E-02	1.18E-02	8.56E-03	7.06E-01	9.06E-03	6.166	172.9
5.10E-02	893	7.21E-03	1.44E-01	6.51E-02	4.34E-02	1.36E-02	1.01E-02	7.06E-01	9.05E-03	6.147	159.2
5.36E-02	965	7.47E-03	1.37E-01	7.20E-02	3.94E-02	1.54E-02	1.19E-02	7.05E-01	9.04E-03	6.127	146.9
5.61E-02	1040	7.73E-03	1.30E-01	7.91E-02	3.52E-02	1.74E-02	1.39E-02	7.05E-01	9.04E-03	6.107	135.9
5.87E-02	1117	7.96E-03	1.23E-01	8.63E-02	3.08E-02	1.95E-02	1.61E-02	7.05E-01	9.03E-03	6.088	126.1
5.99E-02	1156	8.07E-03	1.19E-01	9.00E-02	2.85E-02	2.06E-02	1.73E-02	7.05E-01	9.03E-03	6.079	121.7
6.12E-02	1195	8.16E-03	1.15E-01	9.37E-02	2.62E-02	2.16E-02	1.85E-02	7.05E-01	9.03E-03	6.070	117.5
6.38E-02	1273	8.32E-03	1.07E-01	1.01E-01	2.17E-02	2.38E-02	2.11E-02	7.05E-01	9.03E-03	6.054	110.1

x cm	T K	X_i H_2	X_i O_2	X_i H_2O	X_i CH_4	X_i CO	X_i CO_2	X_i N_2	X_i Ar	σ_R	I_R
6.51E-02	1311	8.37E-03	1.03E-01	1.05E-01	1.95E-02	2.48E-02	2.25E-02	7.05E-01	9.03E-03	6.047	106.7
6.63E-02	1349	8.41E-03	9.93E-02	1.08E-01	1.73E-02	2.58E-02	2.39E-02	7.05E-01	9.03E-03	6.041	103.7
6.76E-02	1385	8.41E-03	9.53E-02	1.12E-01	1.52E-02	2.67E-02	2.54E-02	7.05E-01	9.03E-03	6.036	100.8
6.89E-02	1420	8.39E-03	9.14E-02	1.15E-01	1.32E-02	2.75E-02	2.69E-02	7.05E-01	9.03E-03	6.032	98.3
7.02E-02	1453	8.33E-03	8.76E-02	1.18E-01	1.13E-02	2.83E-02	2.85E-02	7.05E-01	9.03E-03	6.029	96.0
7.14E-02	1485	8.25E-03	8.39E-02	1.21E-01	9.53E-03	2.89E-02	3.00E-02	7.05E-01	9.04E-03	6.028	93.9
7.27E-02	1514	8.12E-03	8.04E-02	1.24E-01	7.94E-03	2.93E-02	3.16E-02	7.05E-01	9.04E-03	6.027	92.1
7.40E-02	1542	7.97E-03	7.71E-02	1.26E-01	6.53E-03	2.97E-02	3.32E-02	7.05E-01	9.04E-03	6.028	90.5
7.53E-02	1566	7.78E-03	7.39E-02	1.29E-01	5.28E-03	2.98E-02	3.48E-02	7.06E-01	9.04E-03	6.031	89.1
7.65E-02	1588	7.56E-03	7.10E-02	1.31E-01	4.21E-03	2.98E-02	3.64E-02	7.06E-01	9.05E-03	6.034	87.9
7.78E-02	1608	7.32E-03	6.84E-02	1.33E-01	3.31E-03	2.95E-02	3.80E-02	7.06E-01	9.05E-03	6.038	86.9
7.91E-02	1626	7.06E-03	6.59E-02	1.34E-01	2.57E-03	2.92E-02	3.95E-02	7.06E-01	9.05E-03	6.043	86.0
8.04E-02	1641	6.80E-03	6.37E-02	1.35E-01	1.97E-03	2.87E-02	4.11E-02	7.06E-01	9.05E-03	6.048	85.3
8.16E-02	1655	6.53E-03	6.18E-02	1.37E-01	1.49E-03	2.80E-02	4.25E-02	7.07E-01	9.06E-03	6.054	84.6
8.29E-02	1667	6.27E-03	6.00E-02	1.38E-01	1.11E-03	2.73E-02	4.40E-02	7.07E-01	9.06E-03	6.060	84.1
8.42E-02	1677	6.01E-03	5.84E-02	1.38E-01	8.21E-04	2.65E-02	4.54E-02	7.07E-01	9.07E-03	6.067	83.7
8.55E-02	1687	5.77E-03	5.70E-02	1.39E-01	6.02E-04	2.57E-02	4.67E-02	7.08E-01	9.07E-03	6.073	83.3
8.67E-02	1695	5.55E-03	5.58E-02	1.40E-01	4.37E-04	2.48E-02	4.80E-02	7.08E-01	9.07E-03	6.080	83.0
8.80E-02	1703	5.35E-03	5.47E-02	1.40E-01	3.14E-04	2.39E-02	4.92E-02	7.08E-01	9.08E-03	6.087	82.7
8.93E-02	1710	5.17E-03	5.37E-02	1.41E-01	2.24E-04	2.30E-02	5.04E-02	7.08E-01	9.08E-03	6.093	82.5
9.18E-02	1722	4.86E-03	5.21E-02	1.41E-01	1.15E-04	2.13E-02	5.26E-02	7.09E-01	9.09E-03	6.106	82.0
9.44E-02	1733	4.61E-03	5.08E-02	1.42E-01	5.86E-05	1.97E-02	5.45E-02	7.09E-01	9.09E-03	6.118	81.7
9.69E-02	1743	4.43E-03	4.97E-02	1.42E-01	2.94E-05	1.82E-02	5.62E-02	7.10E-01	9.10E-03	6.129	81.4
9.95E-02	1753	4.28E-03	4.89E-02	1.42E-01	1.46E-05	1.69E-02	5.78E-02	7.10E-01	9.10E-03	6.139	81.1
1.02E-01	1761	4.16E-03	4.81E-02	1.43E-01	6.92E-06	1.57E-02	5.91E-02	7.11E-01	9.11E-03	6.149	80.8
1.07E-01	1777	3.98E-03	4.70E-02	1.43E-01	1.90E-06	1.38E-02	6.14E-02	7.11E-01	9.12E-03	6.165	80.3
1.12E-01	1791	3.83E-03	4.61E-02	1.43E-01	5.21E-07	1.22E-02	6.32E-02	7.12E-01	9.13E-03	6.178	79.8
1.17E-01	1804	3.70E-03	4.54E-02	1.44E-01	1.42E-07	1.09E-02	6.46E-02	7.12E-01	9.13E-03	6.190	79.4
1.22E-01	1815	3.57E-03	4.48E-02	1.44E-01	2.73E-08	9.90E-03	6.58E-02	7.13E-01	9.14E-03	6.199	79.0

x cm	T K	X_i H_2	X_i O_2	X_i H_2O	X_i CH_4	X_i CO	X_i CO_2	X_i N_2	X_i Ar	σ_R	I_R
1.43E-01	1850	3.08E-03	4.33E-02	1.46E-01	1.28E-09	7.54E-03	6.85E-02	7.14E-01	9.15E-03	6.224	77.9
1.63E-01	1875	2.64E-03	4.24E-02	1.47E-01	6.61E-11	6.14E-03	7.01E-02	7.15E-01	9.16E-03	6.241	77.0
1.84E-01	1893	2.26E-03	4.17E-02	1.48E-01	3.78E-12	5.20E-03	7.11E-02	7.15E-01	9.17E-03	6.254	76.4
2.04E-01	1908	1.95E-03	4.12E-02	1.49E-01	1.97E-13	4.49E-03	7.19E-02	7.16E-01	9.18E-03	6.263	76.0
2.45E-01	1927	1.51E-03	4.06E-02	1.50E-01	5.49E-15	3.51E-03	7.30E-02	7.17E-01	9.19E-03	6.277	75.4
2.86E-01	1941	1.19E-03	4.02E-02	1.51E-01	1.79E-16	2.82E-03	7.38E-02	7.17E-01	9.19E-03	6.287	75.0
3.27E-01	1950	9.68E-04	3.99E-02	1.52E-01	7.07E-18	2.31E-03	7.43E-02	7.18E-01	9.20E-03	6.295	74.7
3.67E-01	1957	8.03E-04	3.98E-02	1.52E-01	4.77E-19	1.93E-03	7.48E-02	7.18E-01	9.20E-03	6.300	74.5
4.08E-01	1962	6.78E-04	3.96E-02	1.52E-01	1.13E-19	1.63E-03	7.51E-02	7.18E-01	9.21E-03	6.304	74.3
4.49E-01	1966	5.83E-04	3.95E-02	1.53E-01	5.66E-20	1.41E-03	7.53E-02	7.18E-01	9.21E-03	6.308	74.2
4.90E-01	1969	5.09E-04	3.94E-02	1.53E-01	3.38E-20	1.23E-03	7.55E-02	7.18E-01	9.21E-03	6.310	74.1
5.31E-01	1972	4.51E-04	3.94E-02	1.53E-01	2.18E-20	1.09E-03	7.57E-02	7.18E-01	9.21E-03	6.313	74.1
5.71E-01	1974	4.05E-04	3.93E-02	1.53E-01	1.48E-20	9.72E-04	7.58E-02	7.19E-01	9.21E-03	6.314	74.0
6.12E-01	1975	3.68E-04	3.93E-02	1.53E-01	1.06E-20	8.80E-04	7.59E-02	7.19E-01	9.21E-03	6.316	74.0
6.53E-01	1977	3.38E-04	3.93E-02	1.53E-01	7.81E-21	8.05E-04	7.60E-02	7.19E-01	9.21E-03	6.317	73.9
6.94E-01	1978	3.14E-04	3.93E-02	1.54E-01	5.98E-21	7.44E-04	7.61E-02	7.19E-01	9.21E-03	6.318	73.9
7.35E-01	1979	2.94E-04	3.92E-02	1.54E-01	4.70E-21	6.94E-04	7.61E-02	7.19E-01	9.21E-03	6.319	73.9
7.76E-01	1979	2.78E-04	3.92E-02	1.54E-01	3.80E-21	6.52E-04	7.62E-02	7.19E-01	9.22E-03	6.319	73.9
8.16E-01	1980	2.65E-04	3.92E-02	1.54E-01	3.13E-21	6.18E-04	7.62E-02	7.19E-01	9.22E-03	6.320	73.9
8.57E-01	1980	2.54E-04	3.92E-02	1.54E-01	2.64E-21	5.90E-04	7.62E-02	7.19E-01	9.22E-03	6.320	73.8
8.98E-01	1981	2.44E-04	3.92E-02	1.54E-01	2.26E-21	5.66E-04	7.63E-02	7.19E-01	9.22E-03	6.321	73.8
9.39E-01	1981	2.37E-04	3.92E-02	1.54E-01	1.97E-21	5.46E-04	7.63E-02	7.19E-01	9.22E-03	6.321	73.8
9.80E-01	1981	2.30E-04	3.92E-02	1.54E-01	1.75E-21	5.29E-04	7.63E-02	7.19E-01	9.22E-03	6.321	73.8
1.02E+00	1982	2.25E-04	3.92E-02	1.54E-01	1.57E-21	5.16E-04	7.63E-02	7.19E-01	9.22E-03	6.322	73.8
1.06E+00	1982	2.21E-04	3.92E-02	1.54E-01	1.43E-21	5.04E-04	7.63E-02	7.19E-01	9.22E-03	6.322	73.8
1.10E+00	1982	2.17E-04	3.92E-02	1.54E-01	1.31E-21	4.94E-04	7.64E-02	7.19E-01	9.22E-03	6.322	73.8
1.14E+00	1982	2.14E-04	3.92E-02	1.54E-01	1.22E-21	4.86E-04	7.64E-02	7.19E-01	9.22E-03	6.322	73.8
1.18E+00	1982	2.11E-04	3.92E-02	1.54E-01	1.14E-21	4.79E-04	7.64E-02	7.19E-01	9.22E-03	6.322	73.8
1.22E+00	1982	2.09E-04	3.92E-02	1.54E-01	1.08E-21	4.73E-04	7.64E-02	7.19E-01	9.22E-03	6.322	73.8

x cm	T K	X_i H_2	X_i O_2	X_i H_2O	X_i CH_4	X_i CO	X_i CO_2	X_i N_2	X_i Ar	σ_R	I_R
1.27E+00	1983	2.07E-04	3.92E-02	1.54E-01	1.03E-21	4.68E-04	7.64E-02	7.19E-01	9.22E-03	6.322	73.8
1.31E+00	1983	2.06E-04	3.92E-02	1.54E-01	9.86E-22	4.64E-04	7.64E-02	7.19E-01	9.22E-03	6.322	73.8
1.35E+00	1983	2.04E-04	3.92E-02	1.54E-01	9.51E-22	4.61E-04	7.64E-02	7.19E-01	9.22E-03	6.322	73.8
1.39E+00	1983	2.03E-04	3.92E-02	1.54E-01	9.22E-22	4.58E-04	7.64E-02	7.19E-01	9.22E-03	6.323	73.8
1.43E+00	1983	2.02E-04	3.92E-02	1.54E-01	8.97E-22	4.55E-04	7.64E-02	7.19E-01	9.22E-03	6.323	73.8
1.47E+00	1983	2.01E-04	3.92E-02	1.54E-01	8.77E-22	4.53E-04	7.64E-02	7.19E-01	9.22E-03	6.323	73.8
1.51E+00	1983	2.01E-04	3.92E-02	1.54E-01	8.60E-22	4.51E-04	7.64E-02	7.19E-01	9.22E-03	6.323	73.8
1.55E+00	1983	2.00E-04	3.92E-02	1.54E-01	8.46E-22	4.50E-04	7.64E-02	7.19E-01	9.22E-03	6.323	73.8
1.59E+00	1983	2.00E-04	3.92E-02	1.54E-01	8.34E-22	4.49E-04	7.64E-02	7.19E-01	9.22E-03	6.323	73.8
1.63E+00	1983	1.99E-04	3.92E-02	1.54E-01	8.24E-22	4.48E-04	7.64E-02	7.19E-01	9.22E-03	6.323	73.8
1.67E+00	1983	1.99E-04	3.92E-02	1.54E-01	8.16E-22	4.47E-04	7.64E-02	7.19E-01	9.22E-03	6.323	73.8
1.71E+00	1983	1.99E-04	3.92E-02	1.54E-01	8.09E-22	4.46E-04	7.64E-02	7.19E-01	9.22E-03	6.323	73.8
1.76E+00	1983	1.98E-04	3.92E-02	1.54E-01	8.03E-22	4.45E-04	7.64E-02	7.19E-01	9.22E-03	6.323	73.8
1.80E+00	1983	1.98E-04	3.92E-02	1.54E-01	7.98E-22	4.45E-04	7.64E-02	7.19E-01	9.22E-03	6.323	73.8
1.84E+00	1983	1.98E-04	3.92E-02	1.54E-01	7.94E-22	4.44E-04	7.64E-02	7.19E-01	9.22E-03	6.323	73.8
1.88E+00	1983	1.98E-04	3.92E-02	1.54E-01	7.90E-22	4.44E-04	7.64E-02	7.19E-01	9.22E-03	6.323	73.8
1.92E+00	1983	1.98E-04	3.92E-02	1.54E-01	7.87E-22	4.44E-04	7.64E-02	7.19E-01	9.22E-03	6.323	73.8
1.96E+00	1983	1.98E-04	3.92E-02	1.54E-01	7.86E-22	4.44E-04	7.64E-02	7.19E-01	9.22E-03	6.323	73.8
2.00E+00	1983	1.98E-04	3.92E-02	1.54E-01	7.86E-22	4.44E-04	7.64E-02	7.19E-01	9.22E-03	6.323	73.8

Table B-3. Output for $\phi = 0.8$, CH_4/ air premixed flames. Only the species with relevant mole fractions are reported.

APPENDIX C

Error analysis for Stereo-PIV measurements

The errors introduced in the vector field computation are mainly related to two factors, the first is the accuracy of the particles shift (ds) detection by the cross correlation procedure and the second is the geometric error related to the stereoscopic configuration of the optical system used to record images.

The vector field computation procedures embedded in the software DaVis are associated with an error of 0.1 pixels for the individuation of the average particles shift in the image plane (e_{ds}). This error can be considered the same for all the coordinates' directions in the two image planes.

$$e_{ds} = \delta^r(\Delta X_1) = \delta^r(\Delta Y_1) = \delta^r(\Delta X_2) = \delta^r(\Delta Y_2) = 0.1\, pix = 0.67 \mu m \qquad (C.\ 1)$$

For the analysis of the geometric error, the model proposed by Lawson and Wu is applied in the following analysis (Lawson and Wu, 1997). In Figure C.1 the diagram of a stereoscopic camera system is shown, two cameras, $j = 1, 2$, are imaging a common object plane in a fluid with coordinates (x, y, z) and origin O and which have image planes (X_j, Y_j). In Figure C.1 the two cameras are separated by a distance h along the x axes with respect to the lens centres O_j. For the stereoscopic case the distance $h = 0$. The camera optical axes are rotated by an angle α with respect to the z axes. The experimental setup considered in Chapter 5 is characterized by the angle $\alpha = 45°$, object distances $d_{0j} = d_0 = 60mm$ and image distances $d_j = d = 500mm$. The corresponding coordinates in the image plane are:

$$X_j = -M_j x'_j \qquad (C.\ 2)$$

$$Y_j = -M_j y'_j \qquad (C.\ 3)$$

Where the magnification can be considered the same for both cameras due to the symmetry of the system and it can be assumed uniform in the object plane because Scheimpflug mounts have been applied ($M_j = M = 0.123$).

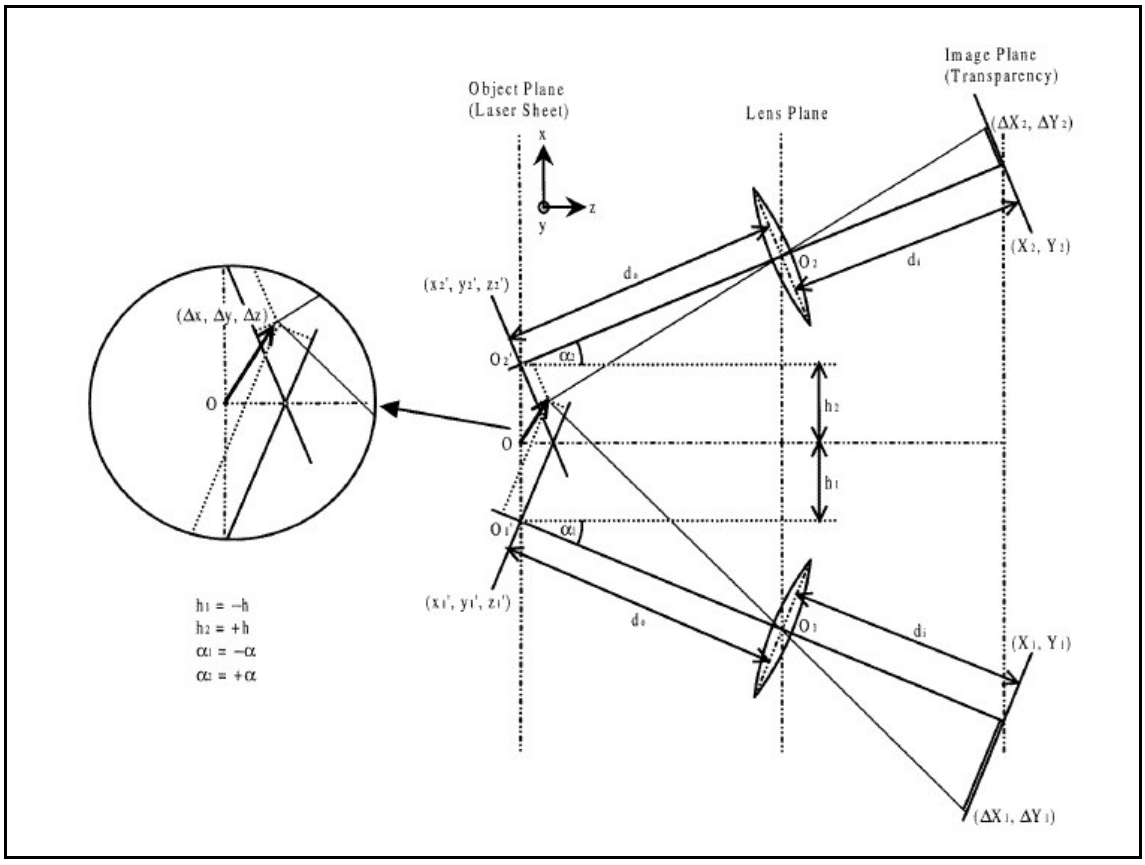

Figure C.1. Diagram of stereoscopic camera system (Lawson and Wu, 1997).

The error model proposed by Lawson and Wu defines the geometric error in the object plane coordinates as function of the error in the image plane previously expressed by Equation (C. 1). The uncertainties in the object planes, Δx, Δy and Δz can be written using the following equations where $\delta^r(\ )$ represents the error of a given variable (Lawson and Wu, 1997):

$$\delta^r(\Delta x) = \frac{\sqrt{b_1^2 + b_2^2}}{|a_1 b_2 - a_2 b_1|} e_{ds} \qquad (C.\ 4)$$

$$\delta^r(\Delta y) = \left(\sqrt{c_1^2 + c_2^2}\right) e_{ds} \qquad (C.\ 5)$$

$$\delta^r(\Delta z) = \frac{\sqrt{a_1^2 + a_2^2}}{|a_1 b_2 - a_2 b_1|} e_{ds} \qquad (C.\ 6)$$

With

$$a_1 = -M\cos\alpha + (M\sin\alpha / d_0)[z\sin\alpha - x\cos\alpha] \qquad (C.\ 7)$$

$$a_2 = -M\cos\alpha + (M\sin\alpha / d_0)\left[z\sin\alpha + x\cos\alpha\right] \quad (C.\ 8)$$

$$b_1 = -M\sin\alpha + (M\cos\alpha / d_0)\left[z\sin\alpha - x\cos\alpha\right] \quad (C.\ 9)$$

$$b_2 = -M\sin\alpha - (M\cos\alpha / d_0)\left[z\sin\alpha + x\cos\alpha\right] \quad (C.\ 10)$$

$$c_1 = -\frac{1}{M} \quad (C.\ 11)$$

$$c_2 = -\frac{y\cos\alpha}{2M}\left[\frac{2M\sqrt{a_1^2 + a_2^2}}{d_0\left(a_2 b_1 - a_1 b_2\right)}\right] \quad (C.\ 12)$$

Lawson and Wu observed that the ratio of the uncertainties in the object planes of Δx and Δz is equal to 1 for any given values of x, y and z, if it used a stereoscopic configuration with $\alpha = 45°$ like the experimental setup considered in Chapter 5. Applying the necessary substitutions in Equations (C. 4), (C. 5)and (C. 6), the uncertainties in the object planes, Δx, Δy and Δz can be written as:

$$\delta^r(\Delta x) = \delta^r(\Delta z) = \frac{\sqrt{1 + \frac{z^2 + x^2}{2\,d_0} + \frac{\sqrt{2}\,z}{d_0}}}{M\left|1 - \frac{z^2 - x^2}{2\,d_0}\right|}\, e_{ds} \quad (C.\ 13)$$

$$\delta^r(\Delta y) = \frac{1}{M}\sqrt{1 + \frac{y^2\left(1 + \frac{z^2 + x^2}{2\,d_0^2} - \frac{\sqrt{2}\,z}{d_0}\right)}{2\,d_0^2\left(1 - \frac{z^2 - x^2}{2\,d_0^2}\right)}}\, e_{ds} \quad (C.\ 14)$$

The ranges of values for x, y and z are: $-45mm \le x \le 45mm$, $-20mm \le y \le 20mm$ and $-0.5mm \le z \le 0.5mm$. It follows that:

$$\frac{z^2 + x^2}{2\,d_0^2} < \frac{1}{200} \quad (C.\ 15)$$

$$\frac{z^2 + x^2}{2\,d_0^2} < \frac{1}{200} \quad (C.\ 16)$$

$$\frac{\sqrt{2}\,z}{d_0} < \frac{1}{500} \quad (C.\ 17)$$

The expressions defined by Equations (C. 15), (C. 16) and (C. 17) can be assumed negligible when used in Equations (C. 13), (C. 14) that can be written as:

$$\delta^r(\Delta x) = \delta^r(\Delta y) = \delta^r(\Delta z) = \frac{1}{M} e_{ds} = 5.45 \mu m \qquad \text{(C. 18)}$$

Finally if the laser pulse separation is $dt = 50 \mu s$ the three dimensional velocity vector $\vec{V}$ is characterized by the following uncertainty for each of its components:

$$e_v = \frac{\delta^r(\Delta x)}{dt} = 0.1\, m/s \qquad \text{(C. 19)}$$

REFERENCES

Al-Abdeli, Y. M. and Masri, A. R. (2003a), "Recirculation and flowfield regimes of unconfined non-reacting swirling flows", *Experimental Thermal and Fluid Science,* vol. 27, no. 5, pp. 655-665.

Al-Abdeli, Y. M. and Masri, A. R. (2003b), "Stability characteristics and flowfields of turbulent non-premixed swirling flames", *Combustion Theory and Modelling,* vol. 7, no. 4, pp. 731-766.

Bedat, B. and Cheng, R. K. (1995), "Experimental study of premixed flames in intense isotropic turbulence", *Combustion and Flame,* vol. 100, no. 3, pp. 485-493.

Beer, J. M. and Chigier, N. A. (1972), *Combustion aerodynamics,* Aplied Science Pubblications, London, UK.

Bilger, R. W. (1993), "Basic considerations", in Taylor, A. M. K. P. (ed.) *Instrumentation for flows with combustion,* Academic Press, London UK, pp. 3-51.

Boger, M., Veynante, D., Boughanem, H. and Trouve, A. (1998), "Direct numerical simulation analysis of flame surface density concept for large eddy simulation of turbulent premixed combustion", *27th International Symposium on Combustion,* Vol. 1, Aug 2-Aug 7 1998, Combustion Inst, Pittsburg, PA, USA, Boulder, CO, USA, pp. 917.

Borman, G. L. and Ragland, K. W. (1998), *Combustion Engineering,* McGraw-Hill, Singapore.

Box, G. E. P., Hunter, J. S. and Hunter, W. G. (2005), *Statistics for experimenters : design, innovation and discovery,* Second ed. ed, Wiley-Interscience.

Brewster, B. S., Cannon, S. M., Farmer, J. R. and Meng, F. (1999), "Modeling of lean premixed combustion in stationary gas turbines", *Progress in Energy and Combustion Science,* vol. 25, no. 4, pp. 353-385.

British Standards Institution, (1991), *Measurement of fluid flow in closed conduits*, BS 1042: Section 1.3.

Butler, T. D. and O'Rourke, P. J. (1976), "Numerical method for two dimensional unsteady reacting flows", *16th Symposium International on Combustion,* Aug 15-20 1976, Cambridge, MA, USA, Combust Institute, Pittsburgh, Pa, pp. 1503.

Chan, C. K., Lau, K. S., Chin, W. K. and Cheng, R. K. (1992), "Freely propagating open premixed turbulent flames stabilized by swirl", *Proceedings of the 24th*

International Symposium On Combustion, Jul 5-10 1992, Publ by Combustion Inst, Pittsburgh, PA, USA, Sydney, Engl, pp. 511.

Cheng, R. K. (1995), "Velocity and scalar characteristics of premixed turbulent flames stabilized by weak swirl", *Combustion and Flame,* vol. 101, no. 1-2, pp. 1-14.

Cheng, R. K., Shepherd, I. G., Bedat, B. and Talbot, L. (2002), "Premixed turbulent flame structures in moderate and intense isotropic turbulence", *Combustion Science and Technology,* vol. 174, no. 1, pp. 29-59.

Claypole, T. C. and Syred, N. (1980), "Effect of swirl burner aerodynamics on NOx formation", *18th Symposium (International) on Combustion,* Waterloo, Ont, USA, Combust Institute, Pittsburgh, Pa, USA, pp. 81.

Degardin, O., Renou, B. and Boukhalfa, A. M. (2006), "Simultaneous measurement of temperature and fuel mole fraction using acetone planar induced fluorescence and Rayleigh scattering in stratified flames", *Experiments in Fluids,* vol. 40, no. 3, pp. 452-463.

Eckbreth, A. C. (1988), *Laser diagnostics for combustion temperature and species,* Abacus Press.

Edwards, J. B. (1974), *Combustion formation and emission of trace species,* Ann Arbor Science Publisher Inc., Michigan.

Galizzi, C. and Escudie, D. (2006), "Experimental analysis of an oblique laminar flame front propagating in a stratified flow", *Combustion and Flame,* vol. 145, no. 3, pp. 621-634.

Glassman, I. (1996), *Combustion,* Third edition, Academic Press, San Diego.

Golden, D. M. (2000), "Interaction of combustion with the atmosphere", *28th International Symposium on Combustion,* Vol. 28, Jul 30-Aug 4 2000, Combustion Institute, Edinburgh, United Kingdom, pp. 2383.

Gu, X. J., Haq, M. Z., Lawes, M. and Woolley, R. (2000), "Laminar burning velocity and markstein lengths of methane-air mixtures", *Combustion and Flame,* vol. 121, no. 1, pp. 41-58.

Hiller, B. and Hanson, R. K. (1990), "Properties of the iodine molecule relevant to laser-induced fluorescence experiments in gas flows", vol. 10, no. 1, pp. 1-11.

Hinsch, K. D. (1995), "Three-dimensional particle velocimetry", *Measurement Science & Technology,* vol. 6, no. 6, pp. 742-753.

Jimenez, C., Cuenot, B., Poinsot, T. and Haworth, D. (2002), "Numerical simulation and modeling for lean stratified propane-air flames", *Combustion and Flame, v 128, n 1-2, 2002, p 1-21,* vol. 128, no. 1-2, pp. 1-21.

Kalt, P. A., Al-Abdeli, Y. M., Masri, A. R. and Barlow, R. S. (2002), "Swirling turbulent non-premixed flames of methane: Flow field and compositional structure", *29th International Symposium on Combustion,* Vol. 29, Combustion Institute, Sapporo, Japan, pp. 1913.

Kang, T. and Kyritsis, D. C. (2005), "Methane flame propagation in compositionally stratified gases", *Combustion Science and Technology,* vol. 177, no. 11, pp. 2191-2210.

Kundu, P. K. and Cohen, I. M. (2004), *Fluid Mechanics,* Third ed, Elsevier, London.

Kuo, K. K. (1986), *Principles of Combustion,* John Wiley & Sons Inc., New York.

Landenfeld, T., Kremer, A., Hassel, E. P., Janicka, J., Schaefer, T., Kazenwadel, J., Schulz, C. and Wolfrum, J. (1998), "Laser-diagnostic and numerical study of strongly swirling natural gas flames", *27th International Symposium on Combustion,* Vol. 1, Aug 2-Aug 7 1998, Combustion Inst, Pittsburg, PA, USA, Boulder, CO, USA, pp. 1023.

Lawson, N. J., Wu, J. (1997), "Three-dimensional particle velocimetry: error analysis of stereoscopic techniques", *Measurement Science & Technology,* vol. 8, no. 8, pp. 894-900.

Libby, P. A. and Williams, F. A. (1980), "Fundamental aspects, in turbulent reacting flows", in Libby, P. A. and Williams, F. A. (eds.) *Topics in applied physics,* Springer-Verlag, Berlin, Heidelberg, New York, pp. 1-42.

Lide, D. R. (2003), *CRC handbook of chemistry and physics,* 84th ed, CRC Press.

Lieuwen, T., Neumeier, Y. and Zinn, B. T. (1998a), "Role of unmixedness and chemical kinetics in driving combustion instabilities in lean premixed combustors", *Combustion Science and Technology,* vol. 135, no. 1-6, pp. 193-211.

Lieuwen, T. and Zinn, B. T. (1998b), "Role of equivalence ratio oscillations in driving combustion instabilities in low NO_x gas turbines", *27th International Symposium on Combustion,* Vol. 2, Boulder, CO, USA, Combustion Institute, Pittsburg, PA, USA, pp. 1809.

Lieuwen, T., Zinn, B. T. and Johnson, C. (2001), "A mechanism of combustion instability in lean premixed gas turbine combustors", *Journal of Engineering for Gas Turbines and Power,* vol. 123, no. 1, pp. 182-189.

Liu, J. B., Pan, Q., Liu, C. S. and Shi, J. R. (1988), "Principles of flow field diagnostics by laser induced biacetyl phosphorescence", *Experiments in Fluids,* vol. 6, no. 8, pp. 505-513.

Long, M. B. (1993), "Multidimensional Imaging in Combustion Flows by Lorenz-Mie, Rayleigh, and Raman scattering", in Taylor, A. M. K. P. (ed.) *Instrumentation for flows with combustion,* Academic Press, , pp. 467-490.

Lozano, A., YIP, B. and HANSON, R. K. (1992), "Acetone - A tracer for concentration measurements in gaseous flows by planar laser-induced fluorescence", *Experiments in Fluids,* vol. 13, no. 6, pp. 369-376.

Masri, A. R., Kalt, P. A. and Barlow, R. S. (2004), "The compositional structure of swirl-stabilised turbulent nonpremixed flames", *Combustion and Flame,* vol. 137, no. 1-2, pp. 1-37.

Masri, A. R., Pope, S. B. and Dally, B. B. (2000), "Probability density function computations of a strongly swirling nonpremixed flame stabilized on a new burner", *28th International Symposium on Combustion,* Vol. 28, Combustion Institute, Edinburgh, United Kingdom, pp. 123.

O'Young, F. and Bilger, R. W. (1997), "Scalar gradient and related quantities in turbulent premixed flames", *Combustion and Flame,* vol. 109, no. 4, pp. 682-700.

Peters, N. (2000), *Turbulent combustion,* Cambridge University Press.

Peters, N. (1999), "Turbulent burning velocity for large-scale and small-scale turbulence", *Journal of Fluid Mechanics,* vol. 384, pp. 107-132.

Peters, N. (1986), "Laminar flamelet concepts in turbulent combustion", *21st Symposium (International) on Combustion, 3-8 Aug. 1986,* Munich, Federal Republic of Germany, Combustion Institute, Pittsburgh, pp. 1231.

Pires Da Cruz, A., Dean, A. M. and Grenda, J. M. (2000), "A numerical study of the laminar flame speed of stratified methane/air flames", *Proceedings of the Combustion Institute, Volume 28,* Vol. 28, pp. 1925-1932.

Plessing, T., Kortschik, C., Peters, N., Mansour, M. S. and Cheng, R. K. (2000), "Measurements of the turbulent burning velocity and the structure of premixed flames on a low-swirl burner", *28th International Symposium on Combustion, Jul 30-Aug 4 2000,* Vol. 28, Edinburgh, United Kingdom, Combustion Institute, Pittsburgh, pp. 359.

Poinsot, T. and Veynante, D. (2001), *Theoretical and numerical combustion,* Edwards Inc., Philadelphia, Pa, USA.

Poinsot, T., Veynante, D. and Candel, S. (1990) “Diagrams of premixed turbulent combustion based on direct simulation”, *23rd Symposium (International) on Combustion,* 22-27 July 1990, Orleans, France, Combustion Institute, Pittsburgh, PA, pp. 613.

Pope, S. B. (1990), "Computations of turbulent combustion - Progress and challenges", *23rd Symposium (International) on Combustion,* 22-27 July 1990, Orleans, France, Combustion Institute, Pittsburgh, PA, pp. 591.

Praezisions Glas & Optik GmbH (2007)*, Product specifications: Optical Transmission of BG3 and BG4 filters*, available at: http://www.pgo-

online.com/intl/katalog/curves/optical_glassfilters/BG3_BG4.html (accessed 15th of January).

Prasad, A. K. (2000), "Stereoscopic particle image velocimetry", *Experiments in Fluids,* vol. 29, no. 2, pp. 103-116.

Prasad, A. K. and Adrian, R. J. (1993), "Stereoscopic particle image velocimetry applied to liquid flows", *Experiments in Fluids,* vol. 15, no. 1, pp. 49-60.

Schmittel, P., Gunther, B., Lenze, B., Leuckel, W. and Bockhorn, H. (2000), "Turbulent swirling flames: Experimental investigation of the flow field and formation of nitrogen oxide", *28th International Symposium on Combustion,* Vol. 28, Combustion Institute, Edinburgh, United Kingdom, pp. 303.

Schulz, C. and Sick, V. (2005), "Tracer-LIF diagnostics: Quantitative measurement of fuel concentration, temperature and fuel/air ratio in practical combustion systems", *Progress in Energy and Combustion Science,* vol. 31, no. 1, pp. 75-121.

Seitzman, J. M. and Hanson, R. K. (1993), "Planar fluorescence imaging in gases", in Taylor, A. M. K. P. (ed.) *Instrumentation for flows with Combustion,* Academic Press, London, UK, pp. 405-459.

Seshadri, K. and Peters, N. (1990), "Inner structure of methane-air flames", *Combustion and Flame,* vol. 81, no. 2, pp. 96-118.

Shepherd, I. G., Cheng, R. K., Plessing, T., Kortschik, C. and Peters, N. (2002), "Premixed flame front structure in intense turbulence", *Twenty-Ninth International Symposium on Combustion Hokkaido University Sapporo Japan, Jul 21-25 2002,* Vol. 29, Sapporo, Japan, Combustion Institute, Pittsburgh, pp. 1833.

Starner, S. H. and Bilger, R. W. (1986), "Joint measurements of velocity and scalars in a turbulent diffusion flame with moderate swirl", *21st Symposium (International) on Combustion, 3-8 Aug. 1986,* Munich, Federal Republic of Germany, Combustion Institute, Pittsburgh, pp. 1569.

Sutton, G., Levick, A., Edwards, G. and Greenhalgh, D. (2006), "A combustion temperature and species standard for the calibration of laser diagnostic techniques", *Combustion and Flame,* vol. 147, no. 1, pp. 39-48.

Videto, B. D. and Santavicca, D. A. (1991), "Brief Communication: A turbulent flow system for studying turbulent combustion processes", *Combustion Science and Technology,* vol. 76, pp. 159-164.

Willert, C. (1997), "Stereoscopic digital particle image velocimetry for application in wind tunnel flows", *Measurement Science & Technology,* vol. 8, no. 12, pp. 1465-1479.

Williams, F. A. (1985), *Combustion theory, the fundamental theory of chemically reacting flow systems,* Second edition ed, Benjamin/Cummings Pub. Co., Menlo Park.

BIBLIOGRAPHY

Adrian, R. J. (2005), "Twenty years of particle image velocimetry", *Experiments in Fluids,* vol. 39, no. 2, pp. 159-169.

Adrian, R. J. and YAO, C. -. (1985), "Pulsed laser technique application to liquid and gaseous flows and the scattering power of seed materials", vol. 24, no. 1 Jan., pp. 44-52.

Arroyo, M. P. and Greated, C. A. (1991), "Stereoscopic particle image velocimetry", *Measurement Science & Technology,* vol. 2, no. 12, pp. 1181-1186.

Ayoola, B. O., Balachandran, R., Frank, J. H., Mastorakos, E. and Kaminski, C. F. (2006), "Spatially resolved heat release rate measurements in turbulent premixed flames", *Combustion and Flame,* vol. 144, no. 1-2, pp. 1-16.

Balachandran, R., Ayoola, B. O., Kaminski, C. F., Dowling, A. P. and Mastorakos, E. (2005), "Experimental investigation of the nonlinear response of turbulent premixed flames to imposed inlet velocity oscillations", *Combustion and Flame,* vol. 143, no. 1-2, pp. 37-55.

Beer, J. M., Toqan, M. A., Haynes, J. M. and Borio, R. W. (2004), "Development of the radially stratified flame core low NO_X burner: From fundamentals to industrial applications", *Journal of Engineering for Gas Turbines and Power,* vol. 126, no. 2, pp. 248-253.

Bolinder, J. (1999), On the accuracy of a digital particle image velocimetry system, , Department of Heat and Power Engineering, Division of Fluid Mechanics, Lund Institute of Technology, Lund, Sweden.

Bondi, S. and Jones, W. P. (2002), "A combustion model for premixed flames with varying stoichiometry", *29th International Symposium on Combustion,* Vol. 29, Hokkaido University Sapporo Japan, Combustion Institute, Sapporo, Japan, pp. 2123.

Bradley, D., Gaskell, P. H., Gu, X. J., Lawes, M. and Scott, M. J. (1998), "Premixed turbulent flame instability and NO formation in a lean-burn swirl burner", *Combustion and Flame,* vol. 115, no. 4, pp. 515-538.

Bradley, D., Gaskell, P. H., Sedaghat, A. and Gu, X. J. (2003), "Generation of PDFS for flame curvature and for flame stretch rate in premixed turbulent combustion", *Combustion and Flame,* vol. 135, no. 4, pp. 503-523.

Broda, J. C., Seo, S., Santoro, R. J., Shirhattikar, G. and Yang, V. (1998), "Experimental study of combustion dynamics of a premixed swirl injector", *27th*

International Symposium on Combustion, Vol. 2, Boulder, CO, USA, Combustion Institute, Pittsburg, PA, USA, pp. 1849.

Cabra, R., Myhrvold, T., Chen, J. Y., Dibble, R. W., Karpetis, A. N. and Barlow, R. S. (2002), "Simultaneous laser Raman-Rayleigh-LIF measurements and numerical modeling results of a lifted turbulent H_2/N_2 jet flame in a vitiated co-flow", *29th International Symposium on Combustion,* Vol. 29, Hokkaido University Sapporo Japan, Jul 21-25 2002, Combustion Institute, Sapporo, Japan, pp. 1881.

Chen, J. H. and Im, H. G. (1998), "Correlation of flame speed with stretch in turbulent premixed methane/air flames", *27th International Symposium on Combustion, Aug 2-Aug 7 1998,* Vol. 1, Combustion Inst, Pittsburg, PA, USA, Boulder, CO, USA, pp. 819.

Chen, J. Y., Cabra, R., Dibble, R. W., Karpetis, A. N. and Barlow, R. S. (2005), "Lifted methane-air jet flames in a vitiated co-flow", *Combustion and Flame,* vol. 143, no. 4, pp. 491-506.

Chen, Y. -. and Bilger, R. W. (2004), "Experimental investigation of three-dimensional flame-front structure in premixed turbulent combustion II. Lean hydrogen/air Bunsen flames", *Combustion and Flame,* vol. 138, no. 1-2, pp. 155-174.

Chen, Y. -. and Bilger, R. W. (2002), "Experimental investigation of three-dimensional flame-front structure in premixed turbulent combustion - I: Hydrocarbon/air Bunsen flames", *Combustion and Flame,* vol. 131, no. 4, pp. 400-435.

Cheng, R. K. and Shepherd, I. G. (1991), "The influence of burner geometry on premixed turbulent flame propagation", *Combustion and Flame,* vol. 85, no. May, pp. 7-26.

Choi, C. W. and Puri, I. K. (2001), "Contribution of curvature to flame-stretch effects on premixed flames", *Combustion and Flame,* vol. 126, no. 3, pp. 1640-1654.

Choi, C. W. and Puri, I. K. (2000), "Flame stretch effects on partially premixed flames", *Combustion and Flame,* vol. 123, no. 1, pp. 119-139.

Dally, B. B., Karpetis, A. N. and Barlow, R. S. (2002), "Structure of turbulent non-premixed jet flames in a diluted hot co-flow", *29th International Symposium on Combustion,* Vol. 29, Hokkaido University Sapporo Japan, Jul 21-25 2002, Combustion Institute, Sapporo, Japan, pp. 1147.

Di Benedetto, A., Marra, F. S. and Russo, G. (2002), "Spontaneous oscillations in lean premixed combustion", *Combustion Science and Technology,* vol. 174, no. 10, pp. 1-18.

Fournel, T., Coudert, S., Fournier, C. and Ducottet, C. (2003), "Stereoscopic particle image velocimetry using telecentric lenses", *Measurement Science and Technology,* vol. 14, no. 4, pp. 494-499.

Frank, J. H., Kalt, P. A. and Bilger, R. W. (1999), "Measurements of conditional velocities in turbulent premixed flames by simultaneous OH PLIF and PIV", *Combustion and Flame,* vol. 116, no. 1-2, pp. 220-232.

Frank, J. H., Lyons, K. M. and Long, M. B. (1996), "Simultaneous scalar/velocity field measurements in turbulent gas-phase flows", *Combustion and Flame,* vol. 107, no. 1-2, pp. 1-12.

Gashi, S., Hult, J., Jenkins, K. W., Chakraborty, N., Cant, S., Kaminski, C. F., Poinsot, T. and Kalt, P. A. (2005), "Curvature and wrinkling of premixed flame kernels-comparisons of OH PLIF and DNS data", *Proceedings of the Combustion Institute,* vol. 30, no. 1, pp. 809-817.

Grant, I. (1997), "Particle image velocimetry: A review", *Proceedings of the Institution of Mechanical Engineers, Part C: Journal of Mechanical Engineering Science,* vol. 211, no. 1, pp. 55-76.

Hill, D. F., Sharp, K. V. and Adrian, R. J. (2000), "Stereoscopic particle image velocimetry measurements of the flow around a Rushton turbine", *Experiments in Fluids,* vol. 29, no. 5, pp. 478-485.

Kalt, P. A., Frank, J. H. and Bilger, R. W. (1998), "Laser imaging of conditional velocities in premixed propane-air flames by simultaneous OH PLIF and PIV", *27th International Symposium on Combustion,* Vol. 1, Boulder, CO, USA, Combustion Inst, Pittsburg, PA, USA, pp. 751.

Keller, D. and Peters, N. (1994), "Transient pressure effects in the evolution equation for premixed flame fronts", *Theoretical and Computational Fluid Dynamics,* vol. 6, no. 2-3, pp. 141-159.

Kerstein, A. R. (2002), "Turbulence in combustion processes: Modeling challenges", *29th International Symposium on Combustion,* Vol. 29, Jul 21-25 2002, Hokkaido University Sapporo Japan, Combustion Institute, Sapporo, Japan, pp. 1763.

Kioni, P. N., Bray, K. N. C., Greenhalgh, D. A. and Rogg, B. (1999), "Experimental and numerical studies of a triple flame", *Combustion and Flame,* vol. 116, no. 1-2, pp. 192-206.

Kioni, P. N., Rogg, B., Bray, K. N. C. and Linan, A. (1993), "Flame spread in laminar mixing layers. The triple flame", *Combustion and Flame,* vol. 95, no. 3, pp. 276-290.

Knaus, D. A., Sattler, S. S. and Gouldin, F. C. (2005), "Three-dimensional temperature gradients in premixed turbulent flamelets via crossed-plane Rayleigh imaging", *Combustion and Flame,* vol. 141, no. 3, pp. 253-270.

Ko, Y. S. and Chung, S. H. (1999), "Propagation of unsteady tribrachial flames in laminar non-premixed jets", *Combustion and Flame,* vol. 118, no. 1-2, pp. 151-163.

Koch, J. D. and Hanson, R. K. (2001), Ketone photo-physics for quantitative PLIF imaging, AIAA-2001-413, AIAA, Reno, NV.

Konrath, R. and Schroder, W. (2002), "Telecentric lenses for imaging in particle image velocimetry: A new stereoscopic approach", *Experiments in Fluids,* vol. 33, no. 5, pp. 703-708.

Konrath, R. and Schroder, W. (2000), "Stereoscopic Particle-Image Velocimetry (PIV) a new approach using telecentric lenses", *10th International Symposium on Applications of Laser Techniques to Fluid Mechanics, July 10-13, 2000, Paper n. 6.3,* Lisbon, .

Kortschik, C., Plessing, T. and Peters, N. (2004), "Laser optical investigation of turbulent transport of temperature ahead of the preheat zone in a premixed flame", *Combustion and Flame,* vol. 136, no. 1-2, pp. 43-50.

Laverdant, A. and Thevenin, D. (2003), "Interaction of a Gaussian acoustic wave with a turbulent premixed flame", *Combustion and Flame,* vol. 134, no. 1-2, pp. 11-19.

Law, C. K. and Sung, C. J. (2000), "Structure, aerodynamics, and geometry of premixed flamelets", *Progress in Energy and Combustion Science,* vol. 26, no. 4, pp. 459-505.

Lee, B. J. and Chung, S. H. (1997), "Stabilization of lifted tribrachial flames in a laminar nonpremixed jet", *Combustion and Flame,* vol. 109, no. 1-2, pp. 163-172.

Lee, B. J., Won, S. H., Jin, S. H. and Chung, S. H. (2003), "Lifted flames in laminar jets of propane in co-flow air", *Combustion and Flame,* vol. 135, no. 4, pp. 449-462.

Lee, B. J., Won, S. H., Jin, S. H., Chung, S. H., Fujita, O. and Ito, K. (2003), "Propagation speed of tribrachial (triple) flame of propane in laminar jets under normal and micro gravity conditions", *Combustion and Flame,* vol. 134, no. 4, pp. 411-420.

Lee, S. -., Seo, S., Broda, J. C., Pal, S. and Santoro, R. J. (2000), "An experimental estimation of mean reaction rate and flame structure during combustion instability in a lean premixed gas turbine combustor", *28th International Symposium on Combustion,* Vol. 28, Jul 30-Aug 4 2000, Combustion Institute, Edinburgh, United Kingdom, pp. 775.

Lengrocht, J. and Schimmels, S. (2000), "Stereoscopic particle image velocimetry in the hydraulic engineering laboratory", *The Leipzig annual Civil Engineering Report,* Institut für Massivbau und Baustofftechnologie, Leipzig, Federal Republic of Germany, pp. 569.

Lockett, R. D., Boulanger, B., Harding, S. C. and Greenhalgh, D. A. (1999), "The structure and stability of the laminar counter-flow partially premixed methane/air triple flame", *Combustion and Flame,* vol. 119, no. 1-2, pp. 109-120.

Lourenco, L. (2001), "Basic techniques in PIV", in *Particle image velocimetry and asociated techniques,* von Karman Institute for Fluid Dynamics, , pp. 1-53.

Mandai, S., Uda, N. and Nishida, H. (2003), "Premixed combustion models for gas turbine with stratified fueling systems", *JSME International Journal, Series B: Fluids and Thermal Engineering,* vol. 46, no. 1, pp. 145-153.

Mansour, M. S. (2002), "A study of turbulent partially premixed flames based on simultaneous imaging of velocity field and OH radical", *Combustion Science and Technology,* vol. 174, no. 2, pp. 47-78.

Montgomery, D. C. (2001), *Design and analysis of experiments,* 5th edition, John Wiley& Sons Inc., New York.

Nooren, P. A., Versluis, M., Van Der Meer, T. H., Barlow, R. S. and Frank, J. H. (2000), "Raman-Rayleigh-LIF measurements of temperature and species concentrations in the Delft piloted turbulent jet diffusion flame", *Applied Physics B: Lasers and Optics,* vol. 71, no. 1, pp. 95-111.

Pasquier, N., Lecordier, B., Trinite´, M. and Cessou, A. (2006), "An experimental investigation of flame propagation through a turbulent stratified mixture", *Proceedings of the Combustion Institute (2006), doi:10.1016/j.proci.2006.07.118.* Published by Elsevier Inc. on behalf of The Combustion Institute, .

Peters, N. (1992), "A spectral closure for premixed turbulent combustion in the flamelet regime", *Journal of Fluid Mechanics,* vol. 242, no. Sept., pp. 611-629.

Peters, N. (1985), "Partially premixed diffusion flamelets in non-premixed turbulent combustion", *20th Symposium (International) on Combustion,* 12-17 Aug. 1984, Ann Arbor, MI; UNITED STATES, Combustion Institute, PA, Pittsburgh, .

Pfadler, S., Loffler, M., Dinkelacker, F. and Leipertz, A. (2005), "Measurement of the conditioned turbulence and temperature field of a premixed Bunsen burner by planar laser Rayleigh scattering and stereo particle image velocimetry", *Experiments in Fluids,* vol. 39, no. 2, pp. 375-384.

Plessing, T., Terhoeven, P., Peters, N. and Mansour, M. S. (1998), "An experimental and numerical study of laminar triple flame", *Combustion and Flame,* vol. 115, no. 3, pp. 335-353.

Prasad, A. K. and Jensen, K. (1995), "Scheimpflug stereo-camera for particle image velocimetry in liquid flows", *Applied Optics,* vol. 34, no. 30, pp. 7092.

Qin, X., Puri, I. K. and Aggarwal, S. K. (2002), "Characteristics of lifted triple flames stabilized in the near field of a partially premixed axisymmetric jet", *29th International Symposium on Combustion,* Vol. 29, Hokkaido University Sapporo Japan, Jul 21-25 2002, Combustion Institute, Sapporo, Japan, pp. 1565.

Rangel, L. P., Fletcher, L. M., Pourkashanian, M. and Williams, A. (2006), "Fundamental studies of a partial premixed counter-flow combustion system and its

effect on NO_x emissions", *Combustion Science and Technology,* vol. 178, no. 8, pp. 1457-1476.

Rendu, B., Samson, E. and Boukhalfa, A. M. (2004), "An experimental study of freely propagating turbulent propane/air flames in stratified inhomogeneous mixtures", *Combustion Science and Technology,* vol. 176, no. 11, pp. 1867-1890.

Schefer, R. W. and Goix, P. J. (1998), "Mechanism of flame stabilization in turbulent, lifted-jet flames", *Combustion and Flame,* vol. 112, no. 4, pp. 559-574.

Schneider, C., Dreizler, A., Janicka, J. and Hassel, E. P. (2003), "Flow field measurements of stable and locally extinguishing hydrocarbon-fuelled jet flames", *Combustion and Flame,* vol. 135, no. 1-2, pp. 185-190.

Seiser, R., Truett, L. and Seshadri, K. (2002), "Extinction of partially premixed flames", *29th International Symposium on Combustion,* Vol. 29, Jul 21-25 2002, Hokkaido University Sapporo Japan, Combustion Institute, Sapporo, Japan, pp. 1551.

Sivashinsky, G. I. (2002), "Some developments in premixed combustion modeling", *29th International Symposium on Combustion,* Vol. 29, Jul 21-25 2002, Hokkaido University Sapporo Japan, Combustion Institute, Sapporo, Japan, pp. 1737.

Soloff, S. M., Adrian, R. J. and Liu, Z. -. (1997), "Distortion compensation for generalized stereoscopic particle image velocimetry", *Measurement Science & Technology,* vol. 8, no. 12, pp. 1441-1454.

Syred, N. (2006), "A review of oscillation mechanisms and the role of the processing vortex core (PVC) in swirl combustion systems", *Progress in Energy and Combustion Science,* vol. 32, no. 2, pp. 93-161.

Tanahashi, M., Fukuchi, Y., Choi, G. -., Fukuzato, K. and Miyauchi, T. (2004), "The time-resolved stereoscopic digital particle image velocimetry up to 26.7 kHz", *12th International Symposium Applications of Laser Techniques to Fluid Mechanics,* Lisbon, Portugal, 12-15 July 2004, Lisbon, Portugal, pp. Paper n. 8.1.

Tanahashi, M., Murakami, S., Choi, G. -., Fukuchi, Y., Miyauchi, T., Meier, W. and Agarwal, A. K. (2005), "Simultaneous CH-OH PLIF and stereoscopic PIV measurements of turbulent premixed flames", *30th Symposium (International) on Combustion the Combustion Institute,* Vol. 30, Elsevier Ltd, Oxford, OX5 1GB, United Kingdom, pp. 1665.

Thurber, M. C. and Hanson, R. K. (1999), "Pressure and composition dependences of acetone laser-induced fluorescence with excitation at 248, 266, and 308 nm", *Applied Physics B: Lasers and Optics,* vol. 69, no. 3, pp. 229-240.

Vervisch, L. (2000), "Using numerics to help the understanding of non-premixed turbulent flames", *28th International Symposium on Combustion,* Vol. 28, Jul 30-Aug 4 2000, Combustion Institute, Edinburgh, United Kingdom, pp. 11.

Veynante, D. and Vervisch, L. (2002), "Turbulent combustion modeling", *Progress in Energy and Combustion Science,* vol. 28, no. 3, pp. 193-266.

Wang, S., Yang, V., Mongia, H., Hsieh, S. -. and Hsiao, G. (2002), "Modeling of gas turbine swirl cup dynamics. V - Large eddy simulation of cold flow", *41st AIAA Aerospace Sciences Meeting & Exhibit,* vol. AIAA Paper 2003-0485.

Wang, Y., Jacobitz, F. and Rutland, C. (2003), "Large eddy simulation of homogeneous shear flow", *41st AIAA Aerospace Sciences Meeting & Exhibit,* vol. AIAA Paper 2003-0779.

Westerweel, J. (1997), "Fundamentals of digital particle image velocimetry", *Measurement Science & Technology,* vol. 8, no. 12, pp. 1379-1392.

Won, S. H., Chung, S. H., Cha, M. S. and Lee, B. J. (2000), "Lifted flame stabilization in developing and developed regions of co-flow jets for highly diluted propane", *28th International Symposium on Combustion,* Vol. 28, Combustion Institute, Edinburgh, United Kingdom, pp. 2093.